Mechanistic-Empirical Failure Prediction Models for Spring Weight Restricted Flexible Pavements in Manitoba Using Manitoba and MnROAD Instrumented Test Sites

by:

Leonnie N. Kavanagh, P. Eng.

A Thesis submitted to the Faculty of Graduate Studies of

The University of Manitoba

In partial fulfillment of the requirements of the degree of

DOCTOR OF PHILOSOPHY

Department of Civil Engineering

University of Manitoba

Winnipeg

ABSTRACT

Pavement damage due to heavy loads on thaw weakened flexible pavements is a major concern for road agencies in Western Canada. To protect weaker, low volume roads, agencies impose spring weight restrictions (SWR) during the spring thaw to reduce pavement damage. While SWR may be cost effective for highway agencies, reducing the spring weight allowances can have a major impact on truck productivity and shipping costs. Therefore an improved process that links SWR loads to pavement damage, and based on limiting failure strain, is required.

This thesis developed Local mechanistic-empirical damage models to predict fatigue and rutting failure on two spring weight restricted (SWR) flexible pavements in Manitoba. The Local damage models were used to assess the SWR loads that regulate commercial vehicle weights in Manitoba based on a limiting strain relationship between truck loads and damage. The Local damage models and a calibrated Finite Element Model (FEM) were used to predict the equivalent single axle load (ESAL) repetitions to fatigue and rutting failure at varying B-Train axle loads at the Manitoba sites. The Local model predictions were compared to predictions from the Asphalt Institute (AI) and Mechanistic Empirical Design Guide (MEPDG) damage models. The results of the analysis showed that for each 1% increase in load, there was a corresponding 1% increase in strain, and up to 3% decrease in ESAL repetitions to failure, depending on the Local, AI, or MEPDG damage models. The limiting failure strains, computed from the Local model for design ESALs of 100,000, were 483μm/m and 1,008μm/m for fatigue and rutting failure, respectively. For the Manitoba sites, the predicted FEM strains at B-Train normal and SWR loads were higher than the Local model limiting strains. Therefore the Manitoba

SWR loads regulating B-Train operations on the two pavements during the spring period appeared to be reasonable. It is recommended that the research findings be verified with further calibration and validation of the Local damage model using a larger data set of low volume flexible pavements. A strain-based concept on how to manage the SWR regime in Manitoba based on the limiting strains was developed and presented.

ACKNOWLEDGEMENTS

This thesis would not have been possible without the assistance of many individuals. I would like to extend my sincere thanks to my advisor Dr. A. Shalaby, P. Eng. for his continued support, encouragement, and technical guidance during this research. Many thanks to the members of my advisory committee: Professor A. Clayton, P. Eng., Dr. P. Rasmussen, P. Eng., and Dr. Y. Luo, P. Eng, and external examiner Dr. J. Zaniewski for their technical advice and comments.

Special thanks to my colleagues in the Pavement Research Group University of Manitoba Civil Engineering Department and staff at Manitoba Infrastructure and Transportation Materials Engineering Branch, and FP Innovations FERIC, for carrying out the instrumentation and their assistance during field and lab testing. Thank you to the staff at the Minnesota Department of Transportation for access to their cold research pavement test sites and research database, and to Dr. G. Ganapathy for his technical comments and suggestions.

Finally, I would like to thank my family for their support and unfailing encouragement.

TABLE OF CONTENTS

LIST OF TABLES

LIST OF FIGURES

TERMINOLOGY

Asphalt Concrete (AC) – a designed mixture of asphalt cement and graded coarse and fine aggregates usually used in the surface layer of an asphalt pavement

Asphalt Pavement – a pavement consisting of an asphalt concrete surface layer on a base or sub-base layer placed over an underlying subgrade soil

Damage – the effect of repetitive load applications in contributing to the loss of serviceability in a pavement

Distress – the cumulative effect of damage in a pavement that is observable and quantifiable (such as cracking or rutting).

Equivalent Single Axle Load (ESAL) – a concept developed from the AASHTO road test which converts the damage of axle configurations and axle loads of various magnitudes and repetitions ('mixed traffic') to the damage of an equivalent 80 kN single axle load (normally designated as ESAL).

Failure – the state when cumulative distress in the pavement reaches a pre-assigned value.

Falling Weight Deflectometer (FWD) – a device used to measure the surface deflection of a pavement under an impulse load in order to evaluate its structural adequacy

Fatigue Cracking - interconnected cracking in the wheel path of a pavement caused by repetitive loading

Finite Element Model (FEM) - a model based on a numerical analysis technique for finding approximate solutions to engineering problems, by breaking the system into elements that are interconnected at discrete node points

Gross Vehicle Weight (GVW) – the allowable total weight of a loaded vehicle and trailers

Low Volume Road – a roadway generally subject to low levels of traffic (typically <400 vehicles per day) and with design ESAL of 50,000-1,000,000 for flexible pavements with AC surface and 10,000-100,000 for gravel/AST surface

Mechanistic Model – a model based on fundamental engineering principles as determined by pavement response to load and/or environment

Resilient Modulus (M_r) – the measure of the stiffness of a material under repeated applied loads, and estimated by the applied stress divided by the recoverable strain

Rutting - a transverse depression or permanent deformation in the wheelpath of an asphalt pavement due to loading

Spring Weight Restriction (SWR) – weight limits that are applied systematically by road agencies during the spring thaw period to restrict truck operation to lower than normal weight limits

ACRONYMS

AASHTO	American Association of State Highway and Transportation Officials
AC	Asphalt Concrete
AI	Asphalt Institute
AST	Asphalt Surface Treated
BBR	Benkelman Beam Rebound
ELMOD	Evaluation of Layer Moduli and Overlay Design
ESAL	Equivalent Single Axle Load
FEM	Finite Element Model
FHWA	Federal Highway Administration
FWD	Falling Weight Deflectometer
GVW	Gross Vehicle Weight
MEPDG	Mechanistic Empirical Pavement Design Guide
MIT	Manitoba Infrastructure and Transportation
PTH	Provincial Trunk Highway
PR	Provincial Road
RTAC	Roads and Transportation Association of Canada
SWR	Spring Weight Restriction

CHAPTER 1 - INTRODUCTION

Spring weight restrictions (SWR) are currently a major challenge in Western Canada because of their impact on highway infrastructure costs and on commercial user competitiveness.

SWRs are weight limits that are applied systematically on roads during the spring period to restrict truck operations to lower than normal weights. Road agencies impose lower truck weights to reduce pavement damage and to protect weaker, low volume roads (typically <400 vehicles per day) during the spring thaw.

During the four seasons in frost areas, the strength of flexible pavements vary. The variation of strength in the spring season is the most critical for weaker pavements. Flexible pavements are designed to transfer loads vertically through each layer to the subgrade in order to avoid deterioration [Yoder, 1975; AASHTO, 1993; Huang, 2004; Papagiannakis and Masad, 2008; NCHRP, 2007]. However, in frost areas, the base and soil freeze in the winter and then thaw in early to late spring. During the spring thaw, weaker pavements reach a critical state where the upper layer is thawed, while the lower layers remain frozen or partially frozen. Water trapped within, and between, the base and subgrade layers, saturates the structure making it incapable of transferring loads effectively and avoiding deterioration. The saturated layers along with high pore water pressures reduce the strength of the structure. Under these conditions the pavement bearing capacity decreases compared to other seasons. The structure remains in the weakened state until the moisture dissipates and strength recovery begins. Heavy loads

driving on the road under these spring conditions cause more damage to the structure than during other seasons of the year.

Ovik et al [2000] conducted a study of flexible pavements in Minnesota and at three Long Term Pavement Performance (LTPP) seasonal monitoring sites in the US to characterize the seasonal variation of layer material modulus. The modulus is the stiffness of the material under repeated loads and is estimated by the applied stress (load) divided by recoverable strain. Ovik et al used the Minnesota mechanistic-empirical pavement design procedure to relate changes in temperature and moisture in the base and subgrade to the modulus at the sites over five seasonal phases; frozen, spring thaw, spring recovery, summer, and fall. Ovik et al found that compared to the fall modulus factor of 1, the spring thaw modulus factor for granular base was approximately 0.65, and the subgrade modulus factor ranged from 0.43 to 0.65 depending on the monitoring site.

While the alternative to mitigate this seasonal loss of strength is to design and construct stronger pavements to carry full loads, even during the spring thaw period, agencies tend not to design full structures on low volume roads due to competing cost and resource allocation to high volume routes.

Compared to designing and constructing low volume pavement to carry full loads even during the spring thaw, agencies enforce temporary weight restrictions as a cost effective way of ensuring acceptable pavement life. This philosophy is supported by a study of the US Federal Highway Administration [FHWA, 1990] which found that a 20% and 50% weight reduction during the spring thaw could increase pavement life by 62% and 95% respectively. By decreasing the loads on weakened roads during the spring, agencies can

significantly reduce the deterioration of the infrastructure and the associated costs for rehabilitation and maintenance on the restricted road.

Levinson et al [2005] and Smalkowski et al [2006] conducted similar studies to determine the economic benefits and costs of spring weight restrictions in Minnesota. Levinson et al employed pavement performance model to predict expected pavement life based on truck flows, pavement conditions, and seasonal variation of material properties over several counties and state-aid paved roads in Minnesota. The performance model was coupled with a freight demand model to predict truck flows in the network. Levinson et al estimated that a 9% and 14% reduction in annual pavement facility cost could be realized by implementing spring restrictions on 9-ton roads, by reducing the loads to those of 7-ton and 5-ton roads, respectively.

While SWR may be cost effective for highway agencies, reducing the spring weight allowances can have major impacts on truck productivity and shipping costs. Montufar et al [2002] showed that seasonal weight limits on prairie highways can have a major financial impact on Western Canadian commercial users and ultimately on the regional economies. Since the region moves large quantities of low-value, dense commodities associated with key industries such as forestry, mining, petroleum, and agriculture, usually on lower strength pavements, SWR can limit truck productivity because the heavier and larger the truck, the lower is the per unit payload cost of handling these commodities. The study also found that, for example, the "first level of SWRs on state highways in North Dakota, USA, reduced the allowable gross vehicle weight (GVW), and in turn payload potential, of a 6-axle tractor semi-trailer by 14%".

The western provincial road agencies in Alberta, Saskatchewan, Manitoba, as well as the frost zone in the US states of Minnesota and North Dakota have annual SWRs in place for two to four month periods, starting in March and terminating as late as June 30 (Appendix A and B). For approximately 30% of the year Montufar et al [2002] noted that SWR "plays a part in managing the balance between protecting the regions' highway infrastructure and influencing commercial vehicle characteristics and operations".

SWRs affect approximately 26% of the Manitoba provincial network or 4,800 kilometers of low volume asphalt concrete and asphalt surface treated (AST) roads, usually for a fixed period from March 18 to May 31 [MIT, 2009]. Since a significant number of Manitoba's key regional industries (forestry, mining, and agriculture) use these secondary roads to reach their markets, the level of SWR is a major and influential issue from a political, economic, and road user perspective.

The most common method used by highway agencies to establish their SWR programs is limiting maximum pavement deflections. Pavement deflections are measured by applying a standard load to the pavement and recording the corresponding maximum surface rebound or deflection under the load. Agencies use deflections because it provides a relative measure of the strength of the pavement and is easy to obtain.

Pavement deflection equipment measures the vertical rebound of the pavement as a result of an applied static or dynamic load. Static deflection equipment measures the pavement deflection in response to a static load. The more advanced measurement devices record the vertical deflection in multiple locations, which provides a more

complete characterization of pavement deflection. The area of pavement deflection under and near the load application is collectively known as the "deflection basin". The general principle is to apply a load of known magnitude to the pavement surface and analyze the shape and magnitude of the deflection basin to assess the strength of the pavement structure.

Figure 1.1 shows a typical deflection basin from an applied load on a flexible pavement. The figure shows the deflection measurements and deflection basin at multiple locations (D_1-D_7) from the load. The deflection under the load (D_1) is the maximum deflection and provides information about the overall pavement strength. A surface curvature index (SCI $=D_1-D_3$) can be related to the relative stiffness of the upper layer of the pavement. A base damage index (BDI=D_3-D_5) can be related to the relative stiffness of the base layer of the pavement. The deflection towards the end of the basin (D_6) tends to indicate the condition (modulus) of the subgrade layer [Van Duesen et al, 2002].

Figure 1.1: Typical Deflection Basin from Applied Load on Flexible Pavement [after TXDOT, 2008]

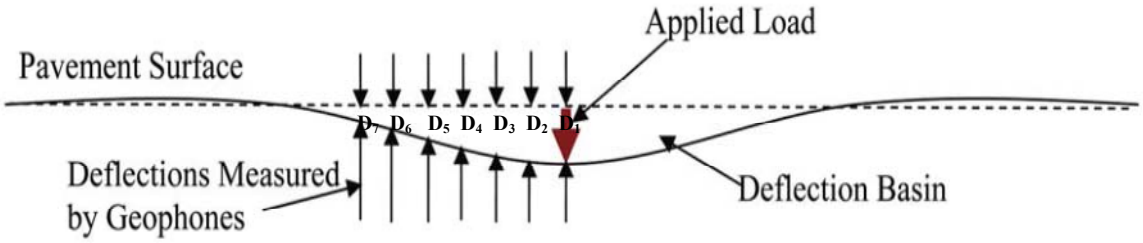

The two most common pavement deflection measuring devices are the Benkelman Beam (BBR) and the Falling Weight Deflectometer (FWD). The BBR device, developed at the Western Association of State Highway Organizations (WASHO) Road Test in 1952, is a

simple beam that operates on the lever arm principle. The BBR beam is used with a loaded truck, at standard AASHTO 80 kN (18kip) load on a single axle with dual tires. The measurement is made by placing the tip of the beam between the dual tires and measuring the pavement surface rebound as the tires of the loaded truck slowly moves away. While the Benkelman Beam is a low cost device, it is slow and labor intensive and does not produce a deflection basin to better characterize pavement deflection. The standard Benkelman Beam Rebound tests are described in the test method of AASHTO T 256 "Standard Method of Test for Pavement Deflection Measurements" [AASHTO, 2001].

The Falling Weight Deflectometer (FWD) is an impact load device that delivers a transient impulse load to the pavement surface. The subsequent pavement response (deflection basin) is measured by a series of sensors. The FWD can either be mounted in a truck or on a trailer and is equipped with a load plate, weight, and several velocity transducer sensors (geophones). To perform a test, the loading plate is positioned over the desired location, the geophones are lowered to the pavement surface and the weight is dropped. During testing, multiple tests can be performed on the same location at different loads, depending on the weight drop height. The advantage of the FWD impact device, over the BBR static device, is that it records the deflection in multiple locations in the deflected basin, the impact load can be easily varied and it more accurately simulates the transient loading of traffic. The standard FWD test method is ASTM D 4694: Standard Test Method for Deflections with a Falling-Weight-Type Impulse Load Device [ASTM, 2009].

Figure 1.2 shows a truck mounted FWD featuring the loading plate and seven geophone locations on a flexible pavement in Manitoba.

Figure 1.2: Truck Mounted Falling Weight Deflectometer (FWD) with Loading Plate and Geophones

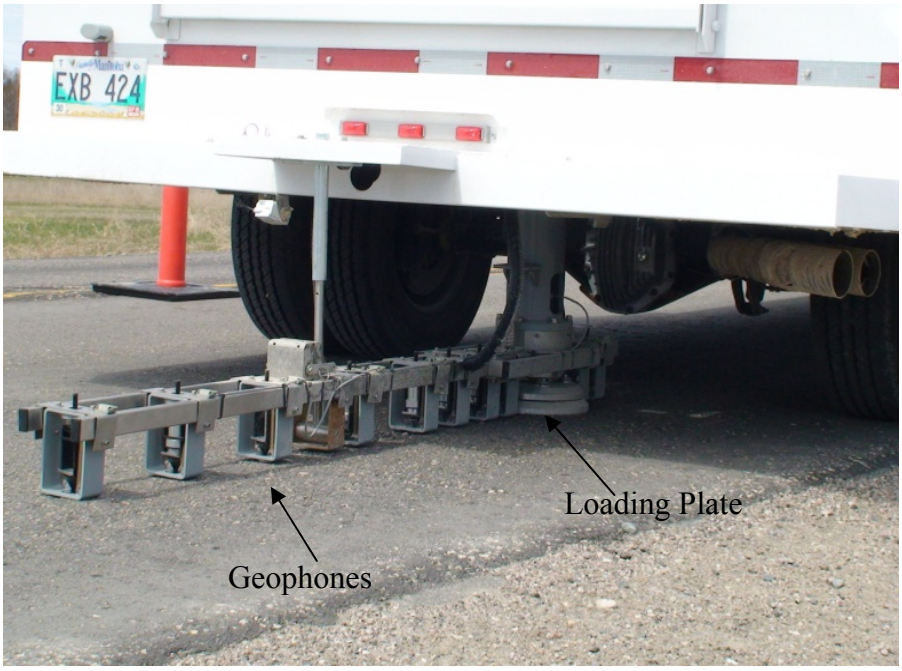

In general, Western Canadian agencies rely almost exclusively on limiting deflection for their SWR program. A market scan, to document the methods for determining SWR by Canadian and International agency practices, was conducted by Bullock et al [2006]. The market scan was conducted as part of a research and development project to determine opportunities for intelligent transportation systems to assist with SWR.

Table 1.1 presents the results of the market scan of SWR determination by Western Canadian and Minnesota road agencies from Bullock et al [2006].

Table 1.1: SWR Determination by Western Canadian and Minnesota Road Agencies

Jurisdiction	SWR Level	Determination of Restriction
Alberta	90%, 75% of Load	Deflection
Saskatchewan	90%, 75% of Load	Road Condition, Deflection
Manitoba	90%, 65% of Load	Deflection, Experience
Minnesota	5-Ton, 7-Ton and 9-Ton Loads	Deflection, Design Testing[1], Experience

Note: [1] Based on cumulative thawing index from air temperature weather forecast

In Manitoba, SWR levels on thaw-weakened roads are based on limiting deflection, and also on past experience. Manitoba's SWR program uses a formula of 90% and 65% of the normal axle loads in an attempt to limit deflections and to "provide higher truck loads where possible and protect pavements where necessary" [MIT, 2009]. Manitoba collects BBR deflections during the spring thaw and recovery periods and uses the data to select the roads that are to be restricted, and the level of restrictions.

The limiting deflection criteria used by western agencies for establishing their SWR programs are either the American Association of State Highway & Transportation Officials (AASHTO) method, or the Roads and Transportation Association of Canada (RTAC) method, or simply based on their experience. The AASHTO and RTAC limiting deflection criteria are based on empirical relationships between the number of applications of an equivalent single axle load (ESAL) and the maximum spring Benkelman Beam Rebound (BBR) deflection, after the disappearance of frost.

The AASHTO limiting deflection criterion was developed in 1962 and originated from data obtained at the 1959 AASHO Road Test in Ottawa, Illinois [AASHTO, 1962]. The AASHTO criterion is based on the number of ESALs sustained by a pavement to the lowest serviceability, or level of pavement distress that a road user will tolerate, before rehabilitation or reconstruction of a pavement is required. The ESAL concept was developed from the AASHO Road Test results which converts the damage of axle configurations and axle loads of various magnitudes and repetitions ('mixed traffic') to the damage of a 'standard' or 'equivalent' 80 kN single axle load [AASHTO, 1993].

The AASHTO limiting deflection criteria is shown in Equation 1.1 [AASHTO, 1962]:

$$logW = 9.40 + 1.32logL_1 - 3.25logd_{sn} \qquad (1.1)$$

Where:

W=number of applications of axle load, L_1, sustained by the pavement to the terminal serviceability index of 2.5

L_1=single axle load (kips)

d_{sn}=Benkelman beam springtime measured surface deflection, in 0.001 inch, measured at AASHO Road Test after disappearance of frost

The RTAC deflection criterion is calculated from the RTAC study in 1977 and later updated by Haas et al in 1994 [RTAC, 1997; Haas et al, 1994]. The RTAC criterion is similar to the AASHTO criteria and is an empirical relationship between the maximum deflection (normalized to a standard temperature of 21^{o}C), and the ESALs sustained by the pavement.

The RTAC limiting deflection criteria is shown in Equation 1.2 [Hass et al, 1994]:

$$BBR = 10^{(0.40824 - 0.30103 log ESAL)} \qquad (1.2)$$

Where:

BBR = Maximum springtime Benkelman Beam Rebound (in.)

(defined as the mean rebound deflection plus 2 standard deviations, and temperature corrected to 70^{o}F (21^{o}C));

For ESALs ≤ 47,651 BBR=0.10 in. (2.5mm); and ESAL >10,000,000 BBR=0.02 in (0.5mm)

ESAL = Equivalent single axle load repetitions to failure based on a 80 kN (18 kip) single axle load

Table 1.2 presents the AASHTO and RTAC limiting spring deflections for a range of ESAL repetitions to failure. The AASHTO deflections were calculated from Equation 1.1 and L_1=18Kip (80kN) single axle load. The RTAC deflections were calculated from Equation 1.2.

Table 1.2: AASHTO and RTAC Limiting Deflection Criteria

ESAL Repetitions to Failure	BBR Limiting Spring Deflection (mm)	
	AASTHO	RTAC
10,000	3.7	2.5
100,000	1.8	2.0
1,000,000	0.9	1.0
10,000,000	0.5	0.5

The results show that for very strong pavements with 10 million or more repetitions, both the AASHTO and RTAC criteria predict the same limiting deflection of 0.5 mm. However for very weak pavements, with 100,000 or less repetitions, and which are often subject to thaw weakening during the spring, there is a 10-30% difference between the deflection criteria.

In addition, the RTAC criterion is more conservative and limits the deflection to a lower level than AASHTO. This may be due to different environment between the AASHO Test Road and RTAC. Ultimately the same road may be restricted to different deflection levels based solely on the method selected by the road agency.

While the use of limiting surface deflection is advantageous, in that it's easy to obtain in the field, it is not an accurate measure of pavement failure or damage. The carrying capacity of the pavement is better characterized by the strains at critical points in the pavement than surface deflections. Huang [2004] and Schwartz and Carvalho [2007] emphasizes that it is widely understood that "pavement failures are caused by excessive stress and strains instead of deflections'. Two pavements can have the same deflections, but different strain responses and different failure rates. Additionally, Kersten and Skok [1968] found that the use of deflection in establishing the effect of loads on pavement life produced the most conservative estimate resulting in thicker pavements when compared to other design methods.

Since the current system for limiting SWR damage in western Canada is not based on failure strains, but on deflections, and no agency policy was found that uses limiting

strain for SWR levels, there is a need to improve the relationship between SWR, failure strain, and pavement damage.

The need to improve the understanding between SWR and damage was further emphasized in the findings of two studies on harmonization and rationalization of seasonal weight limits in the Canadian prairie region by Clayton et al [2001] and Montufar et al [2000 and 2002]. The studies found a serious void in the understanding of the relationship between truck loads and damage to highway infrastructure during the critical thaw periods. The studies further noted that decisions were based mostly on empirical research that was carried out over 30 years ago, and that changes to truck tire types, tire pressures, axle configurations, axle loads, and the large increase in truck volumes, including on low volume roads, "may have rendered at least some, and possibly much, of the old research obsolete".

Given the current methodologies for determining SWR in Western Canada, road users continue to challenge SWR programs, with ongoing requests to develop updated methods for balancing the needs of the industry.

In March 2006, Bradley et al [2007] and the Manitoba forestry industry delivered a report to the Manitoba Government on the competitiveness of on-road transport for the Manitoba forest industry. A major objection of the report was the length of the trucking haul season. The report noted that "Manitoba's hauling season was 59 days shorter than the Canadian average". The average was based on a combination of the long spring restriction period as well as the relatively low gross vehicle and axle loads allowed during the SWR period. The report further cited the negative "impacts on the

competitiveness of the Manitoba transportation industry as well as on the quality of living of those reliant on this industry".

The changing nature of the transportation industry further reinforces the need for an updated technical rationale for SWR. Between 1982 and 2002, Montufar et al [2002] noted that the western Canadian provinces experienced a significant increase in allowable axle loads, changes in truck configurations, growth of commodity exempt vehicles, and a huge increase in truck volumes, often on roads with light pavement structures.

A complementary study by Clayton et al [2005] found that approximately 36.2 million tonnes of goods per year were moved or originate from the three Prairie Provinces, with Manitoba accounting for over 18% of that movement of goods. Axle loads and commodity growth have continued to increase and on-going changes in the trucking industry have accelerated within Manitoba. The Transport Institute [TI, 2010] reported that between 2004 and 2008, the gross domestic product (GDP) for Manitoba derived solely from trucking activities rose by 34%.

Therefore, road agencies need improved tools, based on fundamental engineering and state-of-the-art techniques, to establish SWR levels that fully balance pavement life and economic impacts, while remaining transparent and rational to industry. Therefore an improved process that links or establishes SWR levels to fundamental principles of limiting or failure strains and pavement damage is required in Manitoba.

This thesis investigates the strain-based relationship between truck loads and pavement damage during the spring thaw in Manitoba. The thesis presents the results of

mechanistic-empirical damage models that were developed to predict failure and damage on thaw-weakened flexible pavements in Manitoba. The damage models were used to establish limiting failure strains for low volume roads during the spring period.

1.1 RESEARCH OBJECTIVES AND SCOPE

The objectives of this research are to develop Local calibrated damage models to predict fatigue and rutting failure on thaw-weakened flexible pavement in Manitoba and to investigate if the current SWR load levels are valid based on limiting strain between truck loads and damage. In addition, to establish a strain-based decision regime for SWR load levels using the Local model.

The specific objectives of this thesis are to:

1. Demonstrate and communicate an understanding of the research need and the relationship between truck loads and pavement damage based on literature review and the author's engineering experience,

2. Calibrate structural response models and develop Local damage models based on Manitoba Infrastructure and Transportation (MIT) and Minnesota Department of Transportation (MnDOT) instrumented test sites,

3. Determine the limiting strains that cause fatigue and rutting failure for the spring conditions on low volume SWR asphalt concrete (AC) and asphalt surface treated (AST) roads in Manitoba using the Local damage model,

4. Use the Local damage model to develop a strain-based decision regime for SWR load levels in Manitoba, and

1.2 ORGANIZATION OF THESIS

Chapter 1 of this thesis discusses the rationale for the study, along with the objectives and scope of the research.

Chapter 2 presents the background and relationship between loads, material characterization, pavement structural response, failure modes, and mechanistic-empirical pavement damage models. The discussion includes a review of relevant studies on pavement response and damage analysis to prevent duplication, to identify gaps in previous works, and to point the way forward for future research. Discussions and comments on current or emerging research, within the context of this thesis, are presented.

Chapter 3 presents the research methodology and analytic approach developed and used to meet the objectives of this thesis.

Chapter 4 describes the experimental design and instrumentation of pavement test sites in Manitoba and at the Minnesota Road Research (MnROAD) facilities that were selected for this research. The chapter describes the test vehicles and pavement response data obtained from the instrumented test sites.

Chapter 5 reports on the data trends and variability analysis from the measured pavement responses and field performance data at the test sites.

Chapter 6 presents critical strain predictions from a calibrated Finite Element Model (FEM) and layered elastic (KENLAYER) structural model with comparisons to the measured field strains.

Chapter 7 presents the development of Local Manitoba/MnROAD damage models and comparisons with two mechanistic-empirical damage models from literature; Asphalt Institute (AI) and Mechanistic Empirical Pavement Design Guide (MEPDG).

Chapter 8 presents the limiting strains computed from the Local model for the Manitoba sites. The chapter also presents a strain-based decision regime for SWR load levels based on the Local model relationship between truck load and damage.

Finally, Chapter 9 presents the conclusion of this research and recommendations for future work.

CHAPTER 2 – BACKGROUND AND LITERATURE REVIEW

How pavements respond to applied loads and the environment determines how it will behave structurally. The stresses and resultant pavement response are the combined results of load, moisture conditions, and material layer characteristics. Therefore, the development of models to predict pavement behavior requires mechanistic relationships that relate loads to structural response, and empirical relationships that relate structural response to pavement damage.

This chapter presents the background relationship between loads, material characterization, pavement structural response, failure modes, and pavement damage. Studies and emerging research on pavement response predictions and damage analysis are presented and discussed within the context of this thesis.

The response of flexible pavements to loading has been of interest to researchers since the early 1930's when Burmister developed a theory to predict stresses and strains in layered elastic flexible pavements based on Boussinesq expressions for stresses and strains in homogenous earth fill using the theory of elasticity [Brown, 1997]. Flexible pavements are layered structures consisting of a wearing surface of asphalt concrete (AC) or asphalt surface treatment (AST), on granular and/or stabilized base and/or subbase, over a subgrade. The pavement is designed to distribute loads through the layers to the subgrade, so that the stress at the subgrade does not exceed the subgrade bearing capacity [Huang, 2004].

Since the early American Association of State Highways and Transportation Officials (AASHTO) road test sites in the US, studies have been on-going to further refine pavement response predictions, pavement performance, and pavement damage analysis.

Early researchers and studies contributed greatly to the gradual move from empirical to mechanistic analysis of flexible pavements. Work by Dorman [1962] bridged the gap between empirical and theoretical analysis of flexible pavements. Dorman's research derived the two classical failure design criteria, compressive strain at the top of the subgrade and horizontal tensile strain at the bottom of the asphalt layer of a three layer flexible pavement structure. The analysis was based on the assumption of linear elastic materials subjected to a circular uniformly distributed load. The tensile strain criterion was based on Dorman's research with the Asphalt Institute and Shell laboratories, and parallel with work by Monismith et al [1961] at the University of California [Brown, 1997]. The early work by Dorman and Monismith has remained the basis for on-going research on mechanistic analysis for flexible pavements.

Figure 2.1 shows the critical tensile strain at the bottom of the surface layer (ε_t), and critical vertical compressive strain at the top of the subgrade (ε_v) due to a dual-tire axle load on a three layer flexible pavement.

Figure 2.1: Critical Tensile and Vertical Strains in Flexible Pavement

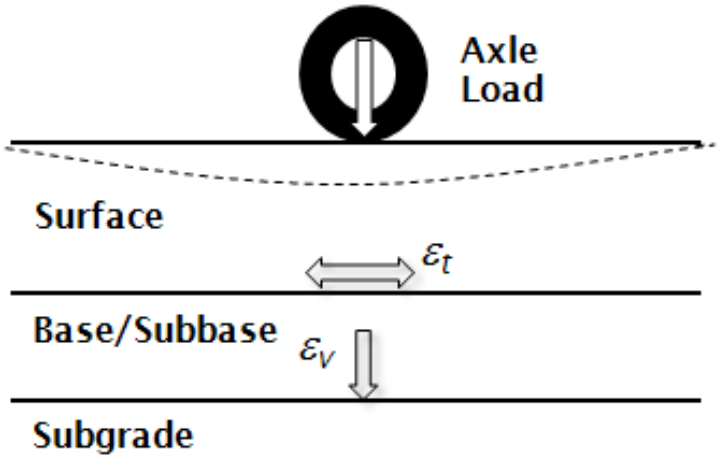

These critical strains are the mechanical responses of a material to loads. They can be related to the rate at which pavements deteriorate, and then calibrated against the performance of in-service or test pavements [Huang, 2004; Wardle et al, 2003]. The critical tensile strain at the bottom of the asphalt layer (ε_t) is related to fatigue cracking. Fatigue cracking is interconnected cracks in the AC layer caused by repeated load repetitions. The critical compressive strain at the top of the subgrade (ε_v) is related to rutting, which is permanent deformation in the material layers caused by repeated loads. Rutting is manifested in the pavement surface.

The critical strains are of particular importance during the spring thaw-weaken period, when the potential for pavement damage exists. Fatigue cracking and rutting distresses can compromise the structural integrity and safety of a roadway, and can result in major infrastructure damage during the spring period. The failure criteria for these two pavement distresses during the spring thaw are the focus of this thesis.

Of considerable importance in pavement response analysis is characterizing material mechanical properties which allows for predictions of how structures will response to different load and environment. Researchers use the elastic or resilient modulus of asphalt concrete, bound or unbound granular bases, and soils under repeated loading to characterize material behavior and predict pavement structural response to load.

The elastic or resilient modulus is the measure of the stiffness of a material under repeated applied loads. The resilient modulus is the stress generated by an impulse load, similar to those experienced from a wheel load, divided by the recoverable strain after a loading cycle [Huang, 2004]. The resilient modulus is used in structural response models to predict the pavement response to load. Poisson's ratio, μ, which is lateral strain divided by axial strain, is also used with the resilient modulus in structural models.

The general form of the elastic or resilient modulus is shown in Equation 2.1 [after Newcomb and Birgisson, 1999].

$$E = M_r = \frac{\sigma}{\varepsilon_R} \qquad (2.1)$$

Where:

$E=M_r$=elastic or resilient modulus

σ = applied stress

ε_R = recoverable strain

Figure 2.2 shows the resilient modulus as determined from a simplified load and unload stress-strain diagram.

Figure 2.2: Resilient Modulus from Simplified Stress-Strain Diagram

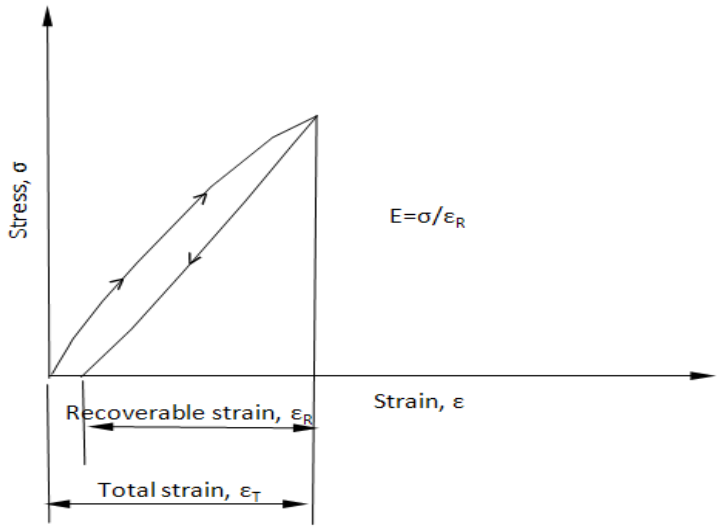

Within the linear range of the stress-strain behavior of a material, strain is proportional to stress; this allows the prediction of the behavior of the material. This property is important when characterizing the ability of a material to return to its original shape and size immediately after deformation. The stress-strain diagram for soils and granular materials is often determined from the repeated load triaxial test. The stress-strain test for asphalt materials can be determined from the indirect tensile Protocol P07 Test Method for Determining Resilient Modulus for Asphalt Materials (FHWA, 2010]. The uniaxial/triaxial tests from the simple performance test for Superpave mix design [NCHRP 9-29, 2002] may also be used to determine the resilient characteristics of asphalt concrete materials.

Figure 2.3 shows the principal stresses acting on unbound granular aggregate and soils for the triaxial test conditions. In the triaxial test, the resilient modulus for bases and

soils depends on the material type, vertical pressure (σ_1), confining pressure (σ_3), deviator stress ($\sigma_d=\sigma_1-\sigma_3$), and the moisture content and density of the sample.

Figure 2.3: Principal Stresses Acting on Unbound Base or Soil for Triaxial Test Conditions [after Ovik et al]

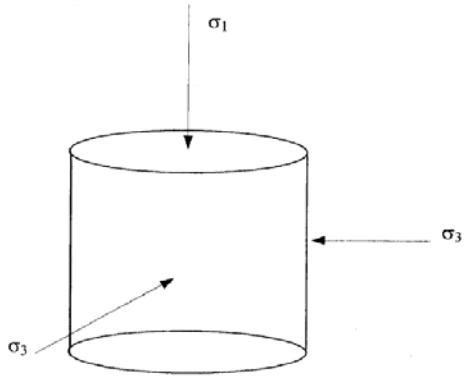

The resilient modulus of unbound granular aggregate and soil materials can be non-linear and stress dependent. Brown [1997] demonstrated the non-linear elastic behavior of granular base and soils both from in-situ measurements of stress and strain, using field instrumentation, and through back-calculation of surface deflection bowls measured with the falling weight deflectometer (FWD). Back-calculation is an iterative process that assigns layer modulus (stiffness) that theoretically matches computed deflections to measured deflections.

Ovik et al [2000] characterized the seasonal trends in pavement layer moduil using data from the Minnesota Road Research Project (MnROAD) and long term pavement performance (LTPP) sites in the US. The relationships between climate factors, subsurface environmental conditions, and pavement material mechanical properties were investigated. The layer moduli were back-calculated from FWD deflections of the pavement using the back-calculation program EVERCAL Version 5.01. Ovik et al related

changes in layer temperature and moisture in the base and subgrade to layer modulus at the sites over five seasonal phases; frozen, spring thaw, spring recovery, summer, fall, and using the Minnesota mechanistic-empirical pavement design procedure.

Ovik et al found that pavement layer stiffness was highly responsive to changes in the average daily temperature and moisture content. The resilient modulus of a granular material typically increased with increasing density and confining pressure, and decreasing moisture content. The modulus of fine-grained soils typically decreased with increasing deviator stress, but was dependent on the soil type, moisture content and density.

Figure 2.4 presents the seasonal variations in aggregate base and subgrade back-calculated layer modulus compared to the volumetric moisture content at 290 mm in the base layer at a Minnesota site by Ovik et al [2000].

Figure 2.4: Seasonal Variations in Aggregate Base and Subgrade Back-Calculated Layer Moduli Compared to Volumetric Moisture Content for a Minnesota site [after Ovik et al, 2000]

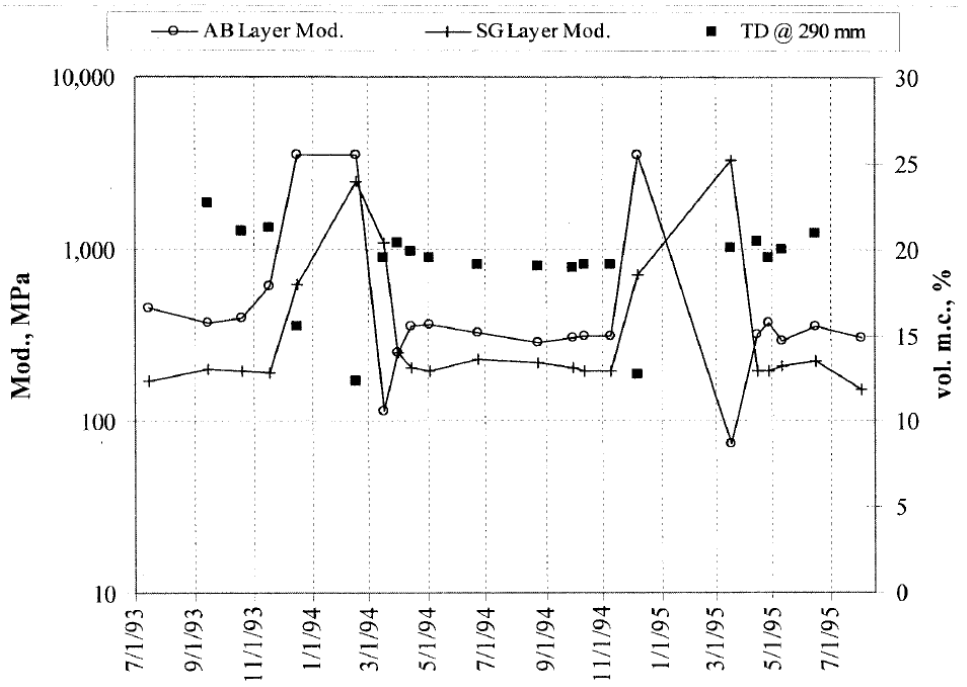

Note: AB=aggregate base, SG=subgrade, TD=volumetric moisture content

The graph shows that the base stiffness decreased when the early spring thaw occurred and rebounded to a near constant value in the summer months. The base modulus decreased as the unfrozen volumetric moisture content increased. The subgrade layer thawed after the base layer and stayed at the same relative stiffness value through the summer. Both layers reached a maximum stiffness in the winter when the layers were frozen.

Ovik et al found that the asphalt layer modulus was at a minimum in the summer when temperatures were high. The granular base layer moduli was at a minimum during the early spring thaw when excess moisture is unable to drain, and the fine-grained subgrade

layer moduli was at a minimum in late spring and summer due to the low permeability and slow recovery of the material. The study found that a seasonal trend between the base moduli and the state of moisture in the base layer can be used to characterize the seasonal changes in the base and subgrade strengths.

Several constitutive models were developed to estimate the resilient modulus of aggregate base and fine-grained soils.

Table 2.1 presents the generalized resilient modulus model used for aggregate base and fine-grained soils in the Mechanistic Empirical Pavement Design Guide (MEPDG) models [NCHRP, 2007]. Soliman [2010] developed local k_1, k_2, k_3, regression constants for the MEDPG equations shown in Table 2.1 for high plastic clays in Manitoba. The deviator stress model for fine grain soils [after Levinson, 2005] is also presented.

Table 2.1: Generalized Models used to Estimate Aggregate Base and Fine-Grained Subgrade Resilient Modulus

Type	Protocol	Model
Generalized Model	Mechanistic Empirical Design Guide (MEPDG) [NCHRP, 2007] Granular Bases and Fine Grained Soils AASHTO T-307 or NCHRP 1-28A	$M_r = k_1 P_a \left(\frac{\theta}{P_a}\right)^{k_2} \left(\frac{\tau_{oct}}{P_a} + 1\right)^{k_3}$ Where M_r=resilient modulus, psi θ=bulk stress=(σ_1+$\sigma_{2+}\sigma_3$) σ_1=major principal stress σ_2=intermediate principal stress σ_3=minor principal stress, confining pressure τ_{oct}=octahedral shear stress= $\frac{1}{3}\sqrt{(\sigma_1-\sigma_2)^2+(\sigma_1-\sigma_3)^2+(\sigma_2-\sigma_3)^2}$ P_a= atmospheric pressure (normalizing stress) k_1, k_2, k_3 = regression constants
	Regression coefficients for Manitoba high plastic clay subgrade [Soliman, 2010]	k_1=$1.1911 - 0.01525(MC - OMC)$ k_2=$0.4560 - 0.0039\left(\frac{MC \times \%Clay}{OMC}\right)$ k_3=$4.1319 - 0.0696\left(\frac{MC \times \%P200}{OMC}\right)$ MC=moisture content OMC=optimum moisture content P200=% passing #200 sieve
Deviator Stress Model	Fine Grained Soils [Levinson, 2005]	$M_r = k_1 \sigma_d^{k_2}$ M_r=resilient modulus, psi σ_d=deviator stress=σ_1-σ_3 σ_1=vertical pressure σ_3=confining pressure k_1, k_2 = regression constants depend on material

Note: AASHTO=American Association of State Highway and Transportation Officials, NCHRP=National Corporative Highway Research Program

Dai and Zollars [2002] compared repeated triaxial tests on soil specimens to determine the resilient modulus at the Minnesota road research facility (MnROAD). The objectives of the research were to compare different constitutive models for describing subgrade soil resilient behavior and to study the effects of material properties on resilient modulus

(M_r). Dai and Zollars experimental results showed that the generalized resilient model (in Table 2.1) described the subgrade modulus slightly better than the deviator stress model (in Table 2.1). The coefficients k_1, k_2, k_3 in the resilient modulus generalized model were found to have good correlation to moisture content and density of the materials.

2.1 THEORY OF ELASTICITY AND STRUCTURAL RESPONSE MODELS

It is generally accepted that flexible pavements are best modeled as a layered system, with a wearing surface, base or subbase, resting on a natural subgrade [Yoder 1975; Huang, 2004]. Therefore, flexible pavement structures are typically analysed using layered elastic theories to calculate critical stresses and strains under applied loads.

THEORY OF ELASTICITY

The most widely used model for pavement analysis is based on the theory of elasticity and the state of stress and strain in a continuous body. In the basic linear elastic theory, it is assumed that loading is static, that deformations are continuous (compatibility between normal and shear strains) and that all materials are homogeneous, isotropic and linear elastic [Timoshenko and Goodier, 1951]. For isotropic, linear elastic materials, the theory is based on three assumptions:

1. Equilibrium (Surface forces = 0),

2. Compatibility between normal and shear strains (deformations are continuous),

3. Hooke's law.

Figure 2.5 shows the elastic parameters for a material (cube) subject to a uniform axial stress, σ_z, in the vertical direction, z. The applied uniform stress results in a change in length of the sides of the cube, *dW*, *dU*, and *dV*.

Figure 2.5: Elastic Parameters for Material Subject to Uniform Axial Stress

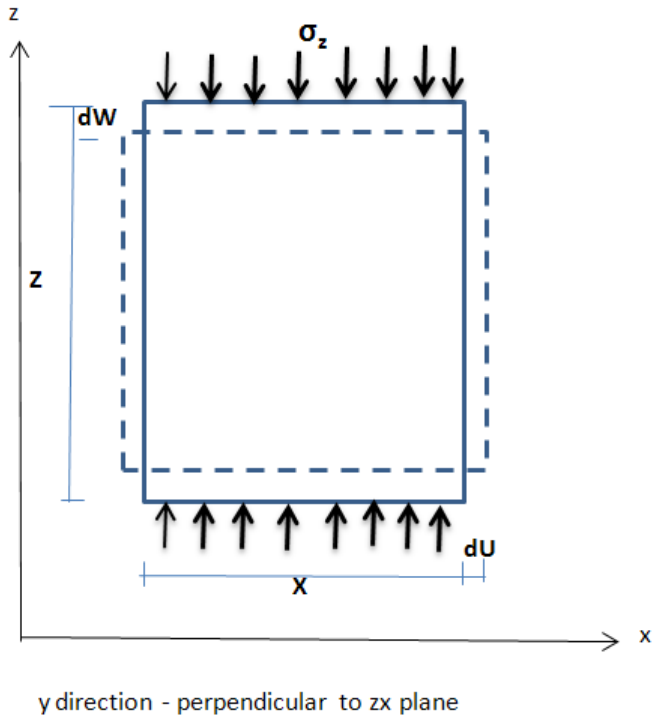

When the displacements are very small compared to the dimensions of the cube, the strains will be equal to the relative change of length. The cube may experience displacements U, V, W in the X, Y, and Z directions, respectively. A normal stress, σ, will produce a normal strain, ε, and a shear stress, τ, will produce a shear strain, γ. The equations relating normal strains and shear strains to displacements are shown in Equation 2.2 [Timoshenko and Goodier, 1951].

Strain-Displacement Equations:

Normal strains: $\varepsilon_x = \frac{dU}{dX}$ *(2.2)*

$$\varepsilon_y = \frac{dV}{dY}$$

$$\varepsilon_z = \frac{dW}{dZ}$$

Shear Strains: $\gamma_{xy} = \frac{dU}{dY} + \frac{dV}{dX}$

$$\gamma_{yz} = \frac{dV}{dZ} + \frac{dW}{dY}$$

$$\gamma_{zx} = \frac{dW}{dX} + \frac{dU}{dZ}$$

If the material is linear elastic, then the ratio of vertical stress, σ_z, to vertical strain, ε_z, will be a constant. This constant or coefficient of elasticity or Young's modulus (E) is known as Hooke's law, and is shown in Equation 2.3.

$$E = \frac{\sigma_z}{\varepsilon_z} \qquad \text{Hooke's Law} \qquad (2.3)$$

The ratio between the horizontal strains (ε_x and ε_y) and the vertical strain, ε_z, is also a constant, known as Poisson's ratio (ν), and is shown in Equation 2.4. A stress in one direction produces a strain, proportional to $-\nu/E$, in a perpendicular direction. This relationship is also shown in Equation 2.4.

$$\nu = -\frac{\varepsilon_x}{\varepsilon_z} \qquad \text{Poisson's Ratio} \qquad (2.4)$$

$$\varepsilon_x = \frac{-\nu\sigma_z}{E}$$

For three-dimensional loading of an isotropic material, Hooke's Law (Equation 2.3) can be written for the normal strains. For the isotropic material, the shear stress will produce a shear strain that is a constant shear modulus, G. The shear strain does not affect the normal strains. The stress-strain relationships for normal and shear strains are shown in Equation 2.5 [Timoshenko and Goodier, 1951].

Stress-Strain Equations:

$$\text{Normal strains: } \varepsilon_x = \frac{\sigma_x}{E} + \frac{-v\sigma_y}{E} + \frac{-v\sigma_z}{E} \qquad (2.5)$$

$$\varepsilon_y = \frac{-v\sigma_x}{E} + \frac{\sigma_y}{E} + \frac{-v\sigma_z}{E}$$

$$\varepsilon_z = \frac{-v\sigma_x}{E} + \frac{-v\sigma_y}{E} + \frac{\sigma_z}{E}$$

$$\text{Shear strains: } \gamma_{xy} = \frac{\tau_{xy}}{G}$$

$$\gamma_{yz} = \frac{\tau_{yz}}{G}$$

$$\gamma_{zx} = \frac{\tau_{zx}}{G}$$

$$\text{Where G= shear modulus, } G = \frac{E}{2(1+v)}$$

In general, highway pavement materials are not linear elastic. However, if the basic assumptions with respect to materials and boundary conditions are correct, structural models can be used to predict pavement responses for any combination of loads, climatic effects and materials.

For the special case of a point load, P, and at the centerline of the load, the vertical stress, σ_z, vertical strain, ε_z, and vertical displacement, d_z, reduces to Equation 2.6 [Huang, 2004]:

$$\sigma_z = \frac{3P}{2\pi z^2 E} \qquad (2.6)$$

$$\varepsilon_z = \frac{(1+v)(3-2v)P}{2\pi z^2 E}$$

$$d_z = \frac{(1+v)(3-2v)P}{2\pi z E}$$

Equation 2.6 reveals why Huang [2004] and Schwartz and Carvalho [2007] emphasize that "pavement failures are caused by excessive stress and strains instead of deflections. In Equation 2.6 the displacement, d_z, is inversely proportional to the depth, z, while stress and strain are inversely proportional to the square of the depth, z. One of the consequences of this difference is that surface deflection on a layered system is poorly correlated to the stresses and strains in the individual layers [ELMOD5, 2007]. Surface deflection is, therefore, a poor substitute for stresses and strains. Since pavement deterioration is related to the stresses or strains in the individual layers, it is unfortunate that surface deflection is still used in Canada for evaluating pavement failure.

STRUCTURAL RESPONSE MODELS

Researchers use the theory of elasticity in structural response models to analyse and refine flexible pavement responses due to loads. The structural response models are

mechanistic equations that use material layer modulus and layer thickness to predict stresses and strains in the pavements.

The two most common structural response models used to calculate induced stresses and strains in flexible pavements are layered elastic models (LEM) and finite element models (FEM).

LEM models are based on the classic layer elastic theory published by Burmister in 1945 [Huang, 2004]. The layered elastic approach is a mechanistic procedure capable of determining pavement responses in flexible pavements. The layered elastic model can compute stresses, strains, and deflections at any point in a pavement structure resulting from the application of a surface load.

The layered elastic approach works with simple closed-form mathematical models that assume that each pavement layer is homogenous, isotropic, and linear elastic. That is the layer materials are the same in all directions and will rebound to their original form once the load is removed. The layers are assumed to extend infinitely in the horizontal direction (a limitation since fatigue failure frequently starts or is more predominant in the wheelpath near the edge), the subgrade extends infinitely in the downward direction, and the materials are not stressed beyond their elastic range. The surface load is represented by a uniformly distributed stress, superimposed for multiple loads over a circular contact area [Huang, 2004].

LEM requires the layer thickness and modulus to adequately characterize the pavement structure and its response to loading. The advantage of the layered elastic system is the short computation time due to the simplified assumptions. The disadvantage is the

reduced accuracy depending on the assumptions of the structural response predictions when compared to actual field conditions.

Figure 2.6 shows the layered elastic model inputs for a 3-layer flexible pavement structure. The material layer is characterized by the modulus of elasticity, E, Poisson's ratio, ν, finite thickness, h, except the subgrade layer, which is semi-infinite. The surface load, P, is represented by a uniformly distributed vertical stress, p, over a circular contact area, with radius, a. The stresses and strains are in the horizontal (radial), r, and vertical, z, directions. The selection of the layer thicknesses and materials is based on limiting the critical strains, and the associated distresses expected in each layer [Huang, 2004].

Figure 2.6: Layered Elastic Model Inputs for 3-Layer Flexible Pavement Structure

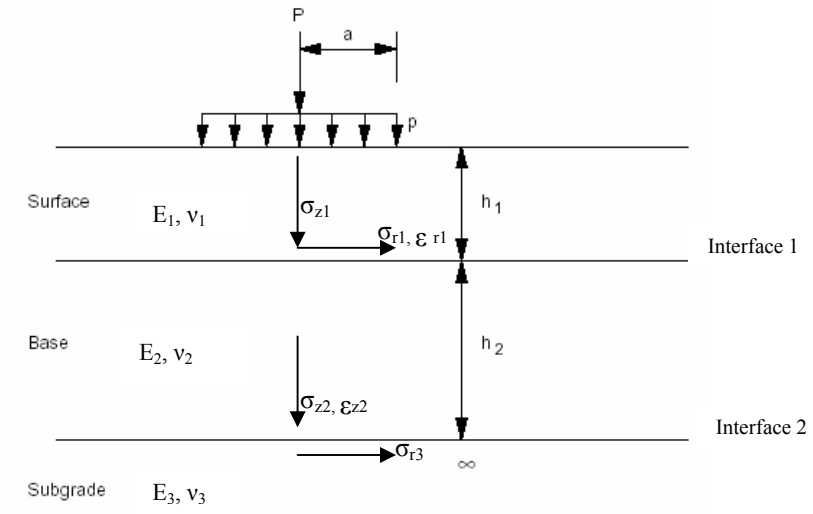

The critical horizontal tensile strains at the bottom of the AC layer, ε_{r1}, and vertical compressive strains at the top of the subgrade, ε_{z2}, are expressed by Equations 2.7 and 2.8, respectively [Huang, 2004].

$$\varepsilon_{r1} = \frac{\sigma_{r1}}{E_1} - v_1 \frac{\sigma_{r1}}{E_1} - v_1 \frac{\sigma_{z1}}{E_1} \quad (2.7)$$

$$\varepsilon_{z2} = \frac{1}{E_3}(\sigma_{z2} - \sigma_{r3}) \quad (2.8)$$

Where:

ε_{r1} = horizontal tensile strain at the bottom of the asphalt layer 1

ε_{z2} = vertical compressive strain at the top of the subgrade layer 3

σ_{r1} = horizontal stress at the bottom of the asphalt layer 1

σ_{z1} = vertical stress at the at the bottom of the asphalt layer 1

σ_{z2} = vertical stress at the bottom of the base layer 2

σ_{r3} = horizontal stress at the top of the subgrade layer 3

E_1 and E_3 = Modulus of Elasticity of layers 1 and 3

ν_1 = Poisson's ratio of layer 1

Unlike the closed-form layered elastic model, the FEM model is a numerical analysis technique for obtaining approximate solutions to pavement structures. The FEM works with more complex mathematical models than the LEM, and makes fewer assumptions about the material properties, particularly in how the domain and computation of the resilient modulus, M_r, are treated.

The FEM analysis discretizes the pavement and subgrade into a number of elements with the load at each node of the element. The finite element extends horizontally and vertically from the influence of the load and assumes boundary conditions in the area of interest. The assumed boundary conditions and element geometry (size and shape) of the FEM can have a major influence on the overall performance of the model.

Figure 2.7 shows an example of a flexible pavement with Everflex 3D FEM discretized element mesh as adapted from Wu [2001]. Everflex is an FEM program developed by Wu and Turkiyyah at the University of Washington. The figure shows the discretized element mesh, wheel loads, modeled crack, and slip interface on the pavement.

Figure 2.7: Example of Flexible Pavement with Everflex 3D FEM Discretized Element Mesh, [after Wu, 2001]

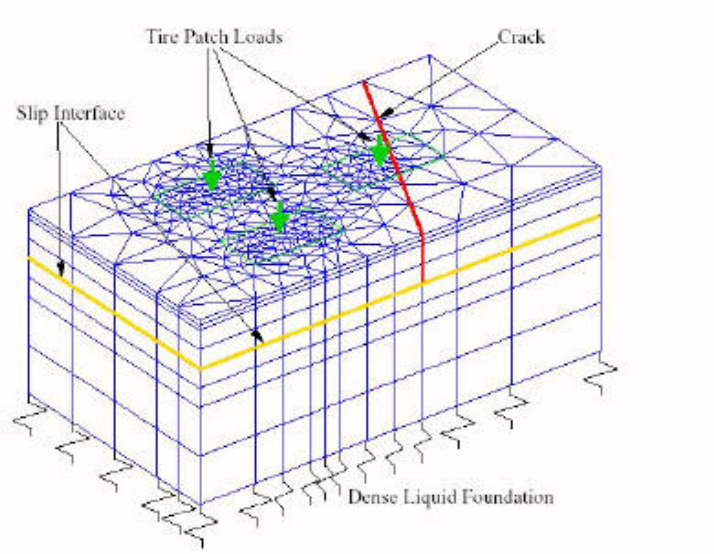

The FEM model is capable of accounting for time- and temperature-based strain relations of materials, any configuration of layer strengths, boundary conditions and loading arrangements. The FEM can model static or dynamic loading and elastic or visco-elastic representations of the pavement structure. This approach involves the determination of material parameters for the analysis at conditions as close as possible to field conditions [Huang, 2004].

The advantage of the FEM is improved structural response predictions and representation of field conditions. The disadvantage is greater computational effort and more detailed material parameters and field condition inputs into the model.

For this thesis, an FEM developed by Liu [2011] was used to predict the pavement response at the Manitoba test sites.

2.2 LITERATURE REVIEW OF FAILURE MODES AND DAMAGE PREDICTION MODELS

Pavement structural responses can be related to pavement failure through damage models. Damage models are mechanistic-empirical (M-E) equations that predict repetitions to pavement failure based on critical structural responses to loads. The primary failure criteria considered in most mechanistic-empirical damage models are fatigue cracking and rutting [Huang, 2004].

Figure 2.8 shows the schematic of a mechanistic-empirical damage model and the relationship between the pavement responses and pavement failure modes. The M-E model equations are empirically derived by relating mechanistic parameters, such as structural response, to observed performance of pavements and the type and extent of the failure to cumulative load repetitions.

Figure 2.8: Schematic of Mechanistic-Empirical Damage Model

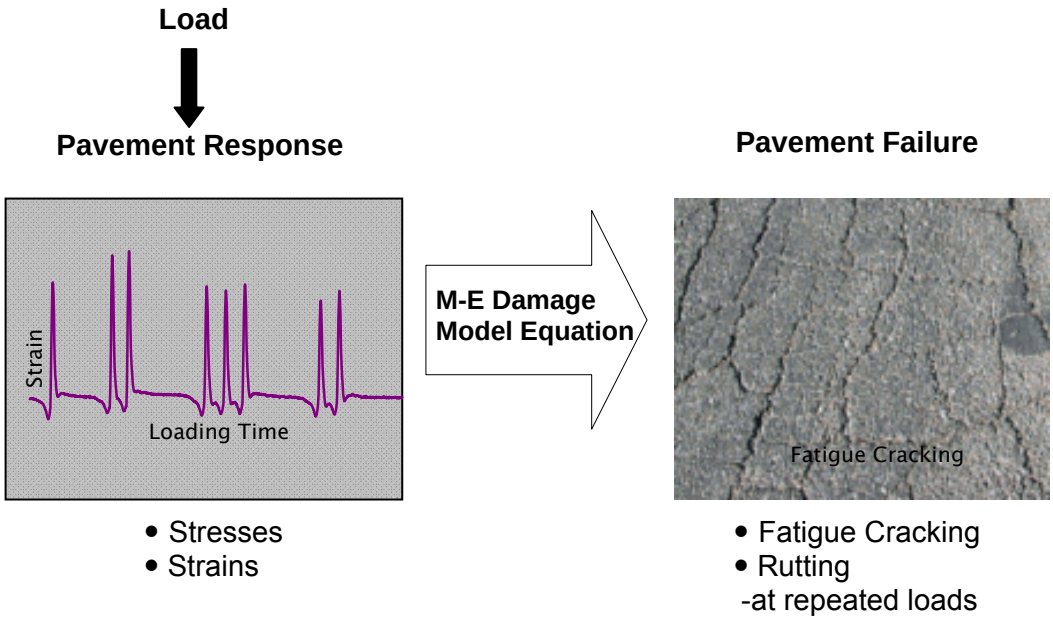

2.2.1 AI AND MEPDG DAMAGE MODELS

Several damage models are available in the literature. The two damage models selected for comparison in this thesis are the Asphalt Institute model [AI, 1982] and the Mechanistic Empirical Pavement Design Guide model, MEPDG [NCHRP, 2007]. The AI and the MEPDG damage models are global mechanistic-empirical equations that incorporate pavement strain responses to loads, translate them into damage, and accumulate the damage into distresses over time [Huang, 2004].

A review of the studies currently using fatigue prediction models developed by the Asphalt Institute [AI, 1982] and MEPDG [NCHRP, 2007] were based on laboratory fatigue relationships obtained in controlled stress or controlled strain loading of asphalt beams in flexure. These models were valid only within the global range of mix types, volumetric composition and loading conditions investigated, and the extent of field

validation carried out. Therefore field validation of predicted results using local conditions was of utmost importance.

From the literature, there are two approaches to account for surface rutting in the damage models. The first approach is rutting in the surface caused by vertical compressive strains at the top of the subgrade. This approach was used by Dorman [1962] and the Asphalt Institute researchers, who assumed that if vertical strains at the top of the subgrade are controlled, the rut depth in the pavement surface can be limited. The advantage of this approach is that rutting damage models do not require a large number of layer parameters. The main drawback is that the rutting models may not properly account for the permanent deformation in the other pavement layers, and errors in estimation of the pavement life can occur when large seasonal variations occur in the material properties. However, Levinson et al [2005] found that if the subgrade rutting model is calibrated for a region, the errors can be minimized and the rutting models can be used for any type of regional flexible pavement and traffic load.

The second approach is rutting in the surface caused by permanent deformation in each layer of the pavement (AC, base, and subgrade) [NCHRP, 2007]. This approach accounts for permanent deformation in each layer, but requires a larger number of layer parameters to improve the estimate of pavement damage.

For this thesis, rutting based on vertical compressive strains at the top of the subgrade was selected for the damage analysis during the spring thaw.

AI DAMAGE MODELS

The AI fatigue and rutting damage models were based on mechanistic-empirical and multi-layer theory in conjunction with empirical failure criteria. The AI damage models include equations to predict load repetitions to fatigue cracking and to rutting failures. The models were calibrated with data from the AASHO Road Test and a number of British test roads, and subsequently compared with the design procedures from the US. Army Corps of Engineers and several state agencies [Huang, 2004].

AI Fatigue Model

The AI fatigue damage model is a global mechanistic-empirical equation between the critical tensile strain at the bottom of the asphalt layer (due to bending) and load repetitions to fatigue failure. The relationship is based on bottom-up fatigue cracking which initiates at the bottom of the AC layer due to repeated loads, and propagates to the surface. The AI fatigue failure criterion is fatigue cracking in the wheelpath area, greater than 10% [AI, 1982].

The AI bottom-up fatigue cracking model is shown in Equation 2.9 [AI, 1982].

Fatigue Cracking:

$$N_f = 0.0796\,\varepsilon_t^{-3.291} E_1^{-0.854} \qquad (2.9)$$

Where:

N_f = the predicted number of load repetitions to fatigue failure

ε_t = load-induced horizontal tensile strain at the bottom of asphalt layer

E_1 = stiffness or moduli of asphalt layer (psi), with typical asphalt properties for the AC layer of 10% asphalt by volume and 4% air voids

Figure 2.9 illustrates the AI fatigue damage model. The graph (log-log scale) shows the horizontal tensile strains at the bottom of the AC layer versus the number of axle load repetitions to fatigue failure. Typical AC modulus of 500,000psi (3,500MPa) from AASHTO [1993] and a lower AC modulus of 200,000psi (1,350MPa) were used to show the variation of AC modulus on the fatigue model.

Figure 2.9: Illustration of AI Fatigue Damage Model

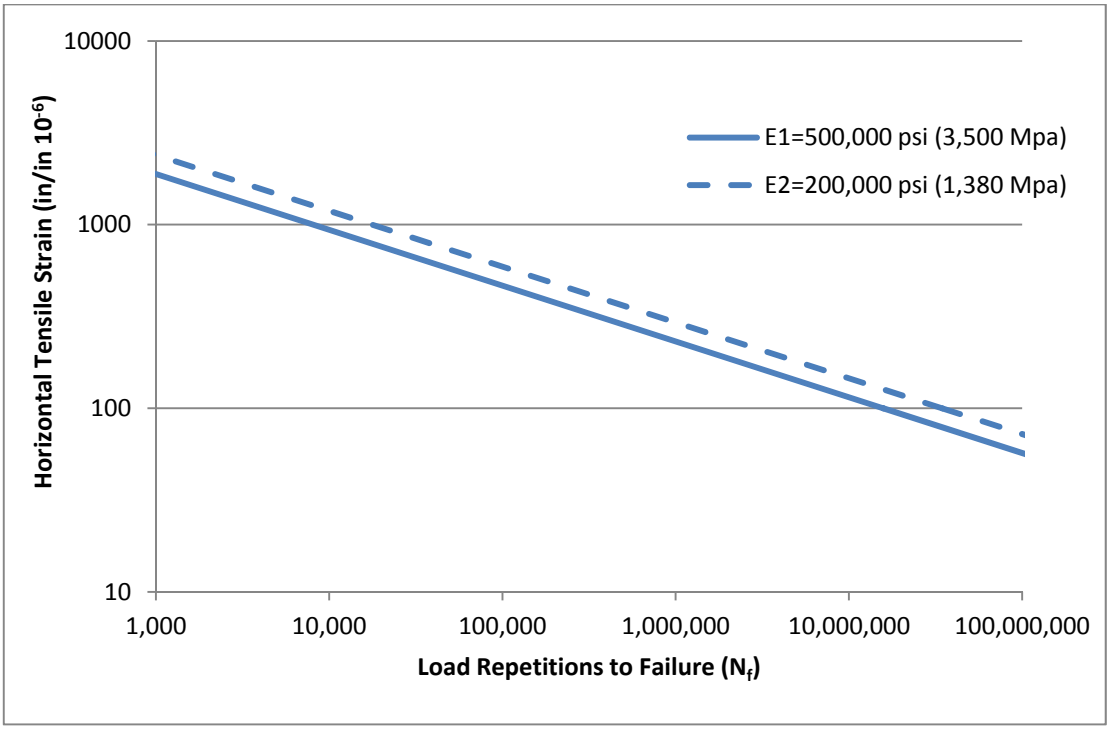

The AI fatigue model in Figure 2.9 shows that as horizontal tensile strains increase at the bottom of the AC layer, the number of load repetitions required to cause fatigue failure decreases. For the same horizontal strain, the number of repetitions to fatigue failure decreases with increase in the AC modulus.

Monismith et al [1969] has shown that for extremely low strains, the slope of the repetitions to failure line flattens out, resulting in near infinite loads to failure. Monismith et al suggested that the relationship between strain at the bottom of the AC layer and repetitions to fatigue failure seems to undergo a significant slope change lower than approximately 70 microstrains. Below this strain level, the asphalt layer can undergo infinite repetitions without fatigue failure.

Carpenter et al [2003] also hypothesized that at low strains around 70 microstrains, asphalt mixtures have infinite fatigue. Carpenter et al suggested that a continuous physical-chemical healing reaction in the AC is occurring at low strain levels. Since research into the fatigue of asphalt mixtures has been limited to strain levels well above the hypothesized value of 70 microstrains, work is currently underway by the National Cooperative Highway Research Program, NCHRP 9-38, to identify the endurance limit of AC mixtures in flexible pavements [NCHRP, 2010].

AI Rutting Model

The AI rutting damage model is a global mechanistic-empirical equation between the vertical compressive stain at the top of the subgrade and load repetitions to rutting

failure. The AI relationship is based on permanent deformation in the subgrade, and manifested at the pavement surface. By limiting the strains on the subgrade, the strains in other layers in the pavement structure will also be limited, and the magnitude of permanent deformation on the pavement surface will be limited [Huang, 2004]. The failure criterion for rutting is rut depths greater than 12.5 mm (0.5 in) in the pavement surface [AI, 1982].

The AI rutting model is shown in Equation 2.10 [A1, 1982].

Rutting:

$$N_f = 1.36 \times 10^{-9} \varepsilon_v^{-4.477} \qquad (2.10)$$

Where:

N_f = the predicted number of load repetitions to rutting failure

ε_v = load-induced vertical compressive strain at top of subgrade

Figure 2.10 illustrates the AI rutting damage model. The graph (log-log scale) shows the vertical compressive strains at the top of the subgrade versus the number of axle load repetitions to rutting failure.

Figure 2.10: Illustration of AI Rutting Damage Model

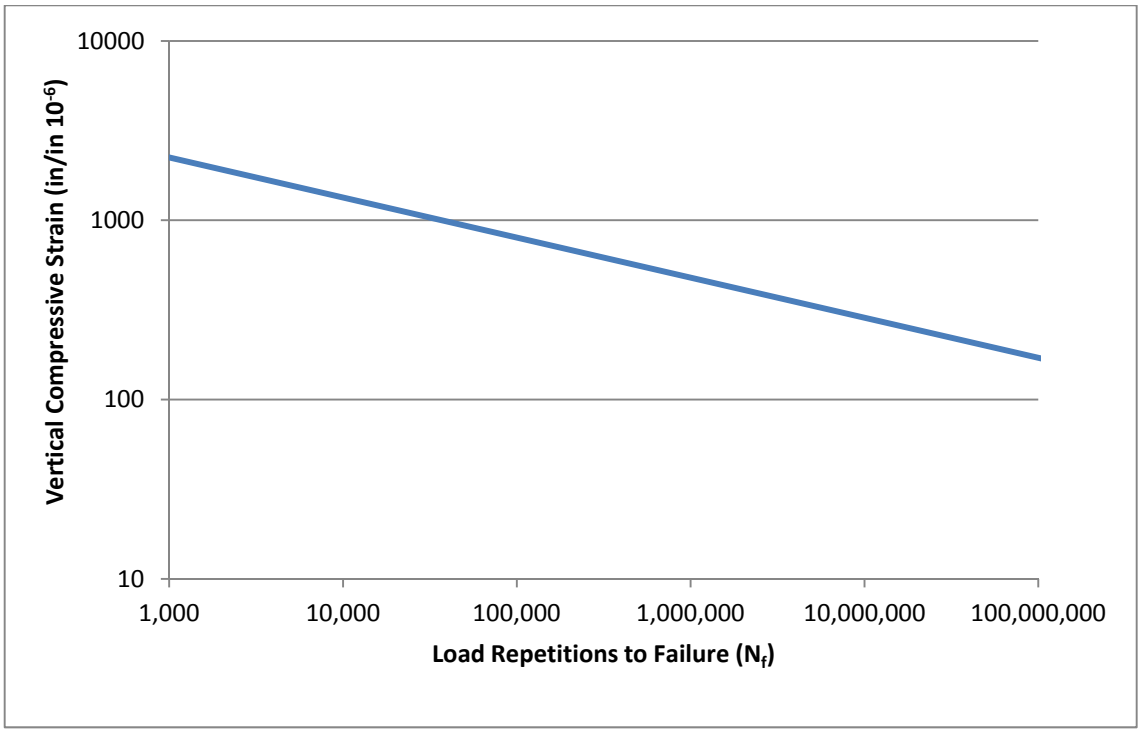

The AI rutting model in Figure 2.10 shows that as the compressive strains at the top of the subgrade increases, the numbers of load repetitions required to cause failure decreases. Because subgrade moduli are relatively low compare to base or AC modulus, the AI rutting model is not sensitive to modulus.

MEPDG DAMAGE MODELS

The Mechanistic Empirical Design Guide (MEPDG) is a mechanistic-empirical system of structural response and damage models that relate critical structural responses and distresses, to load repetitions to failure in flexible pavements. The MEPDG damage models use mechanistic-empirical transfer functions and regression equations to predict

load repetitions to fatigue cracking and rutting failures, at levels of reliability and failure limits specified by the user.

The MEPDG was developed by the Joint Task Force on Pavements of the American Association for State Highway and Transportation Officials (AASHTO) and in cooperation with the US National Cooperative Highway Research Program (NCHRP) and the US Federal Highways Administration (FHWA) [NCHRP, 2007]. The MEPDG models were calibrated with global data from the long term pavement performance (LTPP) and other pavement test sites in the US. Calibration of the MEPDG models for local conditions is recommended for road agencies [NCHRP, 2007].

The MEPDG structural response model uses the multi-layer linear elastic program JULEA to calculate structural responses (stresses, strains, and deflections) based on axle loads, and material properties and environment conditions. A 2-D finite element program, DSC2D which is recommended only for researchers, is also available for considering non-linear responses of bases, subbases, and subgrades [Schwartz and Carvalho, 2007].

MEPDG Fatigue Model

The MEPDG fatigue damage model is a global mechanistic-empirical equation between the critical tensile strain at the bottom of the asphalt layer and load repetitions to fatigue failure. The same AI fatigue failure criteria of 10% bottom-up fatigue cracking in the wheelpath area was selected for the MEPDG model

The MEPDG bottom-up fatigue cracking model is shown in Equation 2.11 [NCHRP, 2007].

Fatigue Cracking:

$$N_f = 0.007566\, CC_H \beta_{f1} \varepsilon_t^{-3.9492\beta_{f2}} E_{HMA}^{-1.281\beta_{f3}} \qquad (2.11)$$

$$C = 10^{4.84\left(\frac{V_{be}}{V_a + V_{be}} - 0.69\right)}$$

$$C_H = \frac{1}{0.000398 + \frac{0.003602}{1 + e^{(11.02 - 3.49 H_{HMA})}}}$$

Where:

N_f = allowable number of axle load repetitions to fatigue failure

ε_t = horizontal tensile strain at the bottom of the asphalt layer

E_{HMA} = dynamic modulus of the hot mix asphalt layer (psi)

β_{f1} *and* β_{f2}, β_{f3} = local or mixture specific field calibration parameters

C = factor for asphalt mixture properties based on percent effective asphalt content (V_{be}) and percent air voids (V_a)

C_H = thickness correction factor for bottom-up fatigue cracking based on asphalt layer thickness (H_{HMA}) in inches

The factors for the asphalt properties, C, and thickness correction for bottom-up cracking, C_H, for the Manitoba mixtures were calculated and used as input into the MEPDG fatigue model. The fatigue calibration parameters β_{f1}, β_{f2}, and β_{f3} in the MEPDG fatigue model

were set to the global constant of 1, due to the absence of local field calibration parameters for the Manitoba mixtures.

MEPDG Rutting Model

The MEPDG rutting damage model is a global mechanistic-empirical equation between the critical vertical compressive strains at the top of the subgrade and load repetitions to rutting failure. The MEPDG rutting model contains two permanent deformation equations related to vertical compressive strains in each layer of the pavement; one for the AC layer and the other for base and/or subgrade layers. For this thesis, only the permanent deformation equations related to vertical compressive strains at the top of the subgrade was selected for the spring thaw condition. Odermatt et al [1999] reported that approximately 70% of the rutting occurred in the subgrade, and that the permanent strain/rut depth relationship was more likely to be significant at higher moisture contents, such as during thaw weakening periods. The MEPDG rutting failure criteria was selected at the same level as the AI model, and for surface rut depths greater than 12.5 mm (0.5 in).

The MEPDG rutting model (based on vertical compressive strain at the top of the subgrade) is shown in Equation 2.12 [NCHRP, 2007].

Rutting:

$$\varepsilon_p = \beta_{s1} k_{s1} \varepsilon_v \left(\frac{\varepsilon_o}{\varepsilon_r} \right) e^{-\left(\frac{\rho}{N_f} \right)^{\beta}} \qquad (2.12)$$

Where:

N_f = allowable number of axle load repetitions to rutting failure

ε_p =permanent plastic strain; which is the permanent deformation, Δ_{soil} (in.), divided by *thickness* of soil layer, h_{soil} (in.)

k_{s1} = global calibration coefficients for soil type

β_{s1} = local calibration constant for rutting

ε_v = vertical elastic strain in the soil layer

ε_o = lab permanent strain at number of load cycles

ε_r = lab resilient strain at number of load cycles

$$\frac{\varepsilon_o}{\varepsilon_r} = 0.5\left(0.15e^{\rho^\beta} + 20e^{\left(\frac{\rho}{10^9}\right)^\beta}\right)$$

β = local constant based on soil volumetric moisture content, %

ρ =local constant based on soil moisture content and resilient modulus

The cumulative pavement damage can be computed from the AI and MEPDG predicted number of load repetitions to fatigue and rutting failure using a damage ratio based on Miner's hypothesis. Miner's hypothesis assesses the proportional life consumed during a period divided by the sum of the proportional life over all periods [Huang, 2004].

The damage ratio, based on Miner's hypothesis, is computed from the expected load repetitions, divided by the predicted load repetitions to fatigue or rutting failure, over a given time period (*i*).

The damage ratio, D_r, is shown in Equation 2.13 [Huang, 2004]. In order to avoid failure, the damage ratio should be less than one.

$$D_r = \sum_{i=1}^{k} \frac{N_i}{N_{fi}} \qquad (2.13)$$

Where:

D_r = damage ratio, failure is generally reached when $D_r = 1$

N = number of expected axle load repetitions in a given period (*i*)

N_f = number of predicted axle load repetitions to failure in a given period (*i*)

k=number of time periods

The expected pavement life, which is the inverse of the damage ratio, can be evaluated for fatigue and rutting failures. The failure mode with a shorter life controls the analysis. The expected pavement life is shown in Equation 2.14.

$$Expected\ Pavement\ Life = \frac{1}{D_r} \qquad (2.14)$$

Various studies were found in the literature on structural response and damage model predictions of flexible pavements.

Odermatt et al [1999] determined subsurface dynamic stresses and strains on the subgrade of flexible pavements subjected to accelerated loading. Permanent strains and rut depths were measured. Odermatt et al found that the stresses and strains increased rapidly during the early loading cycles, and then continued to increase at a much slower rate. The study found that the permanent strain at the top of the subgrade can be used to relate to surface rutting. Odermatt et al reported that approximately 70% of the rutting occurred in the subgrade, and that the permanent strain/rut depth relationship was significant at higher moisture contents, such as during thaw weakening periods.

Boa [2000] selected and evaluated an elastic layered mechanistic model (WESLEA) and a finite element model (ILLI-PAVE) to investigate load responses flexible pavements in Minnesota. WESLEA is a linear elastic layered program developed by the U.S. Army Corps of Engineers, and ILLI-PAVE is a finite element program developed at the University of Illinois. The study compared the predicted strains by the models to the measured field responses at MnROAD during the pilot testing. Bao found the two programs provided equivalent results. Bao used WESLEA to predict the horizontal strains at the bottom of the asphalt layer to compare with strains that were measured at MnROAD during the summer. Bao concluded that the ratios of predicted strains from WESLEA to measured field strains was close to one for factors such as axle loads, tire pressure, vehicle offset position, and asphalt layer thickness. The exception was strains relating to vehicle speed, which varied due to visco-elastic effects.

Moreno [2000] developed mechanistic-empirical procedures for the determination of load equivalency factors (LEF) from data at the MnROAD test facility in Minnesota. The LEF represents the damage caused by a particular axle configuration relative to the damage caused by a standard AASHTO 80kN (18-kip) single axle at a terminal serviceability value, p_t, when the pavement reaches the end of its service life. The higher the LEF, the greater is the damage relative to the standard 80kN (18-kip) single axle load. Moreno used the structural linear elastic model BISAR and FWD back-calculated layer moduli to predict strain at the bottom of the asphalt layer. The fatigue cracking equation from several damage models (Asphalt Institute, Shell, Transportation Research Lab Britain (TRL) and Spain Centro de Estudios y Experimentacion de Obras Publicas (CEDEX)), were used to develop the LEF. The LEF values from the models were compared to the values provided by the AASHO Road Test empirical equations at different terminal serviceability indices, p_t. Moreno concluded that the LEF obtained for different fatigue models underestimated the AASHTO LEF values, and the larger the load, the greater the underestimation.

Figure 2.11 shows the LEF for varying tandem axle loads using several fatigue damage models [after Moreno, 2000]. The plot shows that for a range of tandem axle loads, the LEF increases as loads increase. The plot also shows that the higher the load, the greater the difference in LEF predictions between the various fatigue damage models. For practical purposes, LEF greater than 10 may be unlikely since tandem axle loads in Minnesota are typically less than 50kips.

Figure 2.11: Load Equivalency Factor (LEF) for Varying Tandem Axle Loads [after Moreno, 2000]

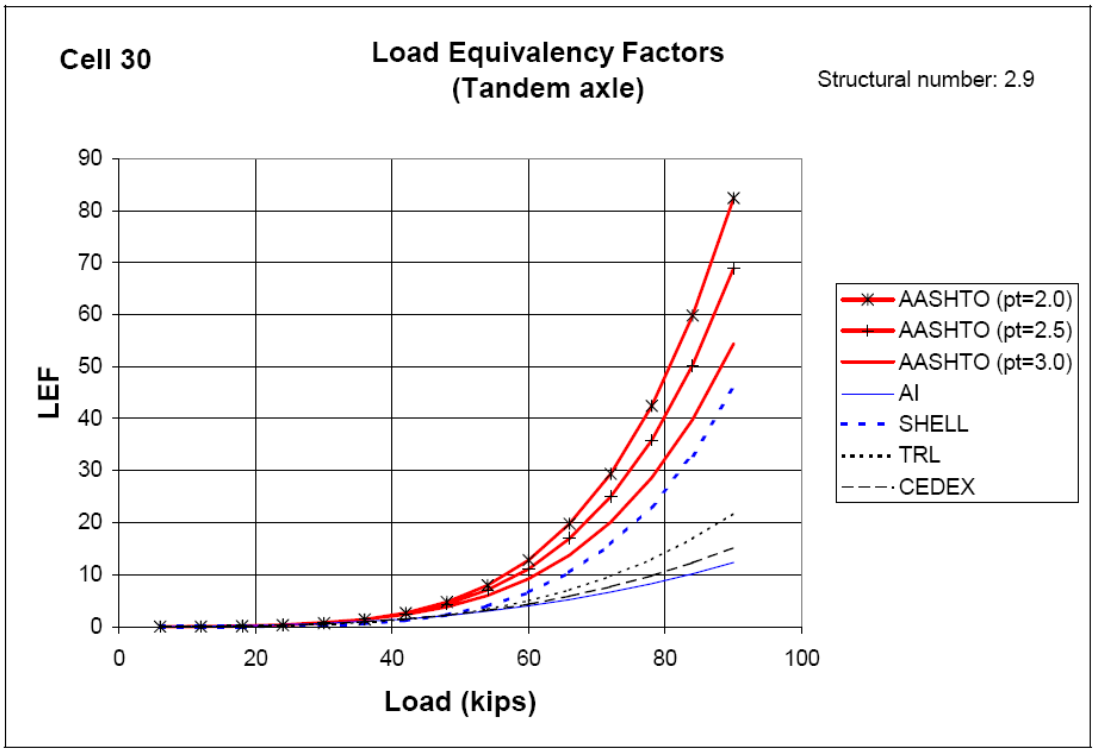

Note: LEF=Load equivalency factor

Several studies investigated the environmental influence of temperature and moisture, particularly extended freezing of subgrades in northern climates and the weakening effects caused by spring thaw.

Cowe-Falls et al [2006] investigated and presented strain results on the Nisku Test Road in Edmonton, Alberta during the spring and fall of 2005. The study was conducted in response to a round table discussion of the 2005 Transportation Association of Canada highlighting the wide range of approaches to overload permits across Canada, regardless of season. Arrays of strain gauges and pressure cells were placed in the asphalt-base interfaces to measure longitudinal and transverse strains, and pressure cells installed at

the subgrade to measure vertical stress. Deflection, temperature and soil moistures were also measured at the site. Test vehicles with a standard single and tandem axle loads were run in the spring of 2005 at legal allowable loads and at 25% overload in the fall of 2005. The vehicle was tested at different speeds. Cowe-Falls et al found that the vertical pressure on the subgrade and the longitudinal strain under the AC layer increased under the 25% overload. Load equivalency factors (LEF) were calculated using the AASHTO-method and a theoretical method by Christison [1978] using tensile strain under the AC layer. The LEF reflected the expected damage caused by the single or tandem axle load, relative to a standard 80kN equivalent single axle load (ESAL). The LEF was found to be highly variable and between 1.64 (AASHTO method) and 9.9-25.3 (Christison method). LEF was dependent on whether the mean or maximum strain values were used for the calculation and on the method chosen (AASHTO or Christison). Depending on the method, the high variability in the LEF analysis by Cowe-Falls et al could result in significant overestimation or underestimation of the damage to pavement.

Bayat et al [2010] investigated the environmental and load associated responses on asphalt pavements due to a variety of loads and tire pressures at the instrumented Center for Pavement and Transportation Technology (CPATT) test track in southern Ontario. Strain gauges and pressure cells were installed in the test track. A series of controlled loading tests were performed to investigate pavement dynamic response to a variety of wheel and tire pressure loadings. The data were used to determine the impacts of wheel wander on sensor readings and temperature effects on measured AC longitudinal strains. Bayat et al found that 160 mm of wheel wander can reduce asphalt longitudinal strain by 36% and that daily temperature fluctuations can result in a 200% increase in asphalt

longitudinal strain. The study did not investigate the impacts of vehicle loads and limiting strain during the spring thaw/recovery period.

Figure 2.12 shows the CPATT longitudinal strain response from a 44.4kN wheel load under different lateral wheel wander or offset [after Bayat, 2010]. The longitudinal strain response was at a speed of 25km/hr, directly over the strain gauge, and 8cm and 16cm of offset. The pavement structure was 185mm AC layer, 1400 mm granular base, on clayey silt subgrade.

Figure 2.12: CPATT Longitudinal Strain Response from 44.4 KN Wheel Load under Different Lateral Wheel Wander or Offset [after Bayat, 2010]

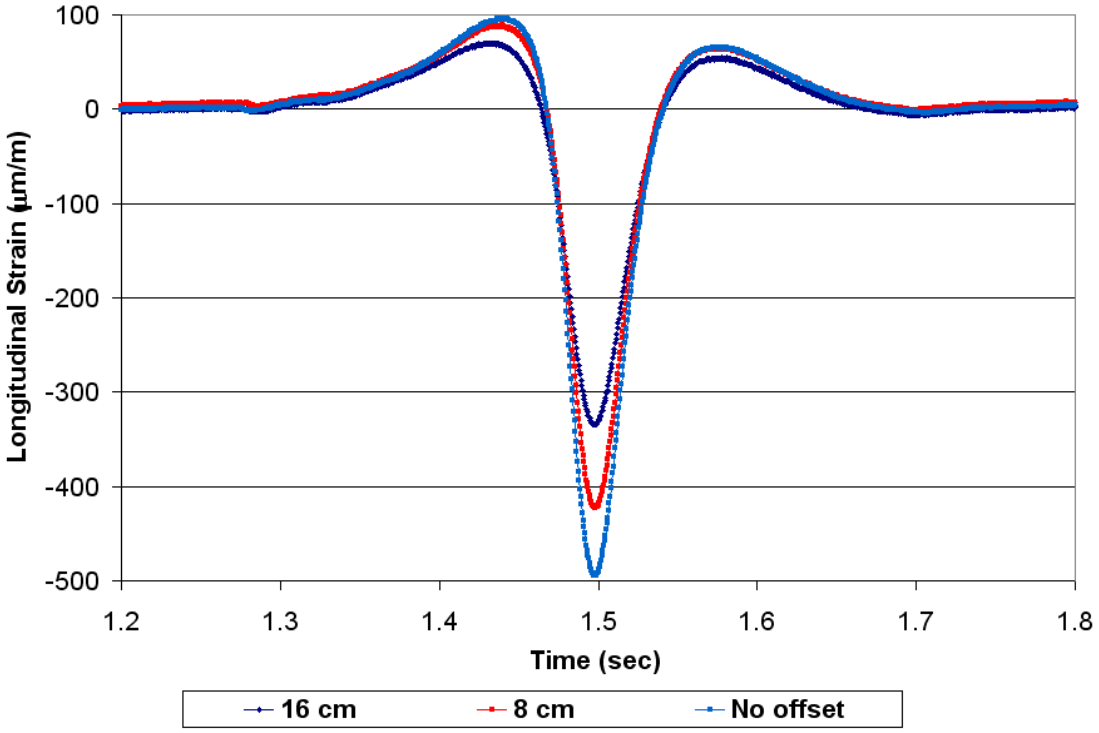

Ghuzlan and Carpenter [2003] studied the traditional fatigue damage analysis of 78 asphalt concrete and 6 polymer modified AC mixtures. They investigated the effects of

mixture variables on fatigue performance as well as the mode of loading and testing temperature using laboratory flexural fatigue testing. Ghuzlan and Carpenter concluded that different mixtures parameters alter the fatigue model coefficients. The mode of loading, testing temperature and asphalt content had a significant effect on the fatigue coefficients. Ghuzlan and Carpenter found that asphalt type, air void and aggregate gradations had no significant effect on the fatigue model coefficients.

Wu and Hossain [2003] analysed the relative pavement damage at different axle loads and configurations at two instrumented Superpave asphalt test sections constructed at the Kansas accelerated testing laboratory (K-ALT). Stress and strain responses were measured during K-ALT wheel loading and data collected from a falling weight deflectometer (FWD). Theoretical pavement responses were also calculated with a multi-layer elastic analysis program (ELSYM-5) and compared to the test results. Wu and Hossain found that the measured vertical stresses at the top of the subgrade and tensile strains at the bottom of the asphalt layer due to FWD loads were generally very close to those calculated by ELSYM5 (ratio of calculated to measured values of 0.8-1.5). However the measured tensile strains and stresses under the wheel loads were found to be higher than those calculated by ELSYM5 (ratio of calculated to measured values of 1.9). Wu and Hossain also found that the measured tensile strains under the wheel loads increased with increasing number of repetitions, but the measured vertical stresses remained relatively constant. Fatigue and rutting damage analysis were also conducted on a set of test beams sawed from the asphalt sections. The rutting and fatigue lab results were consistent with observed and predicted damage.

Hoegh et al [2010] used time history rutting performance data for pavement sections at the Minnesota Department of Transportation (MnDOT) full-scale pavement research facility (MnROAD) to evaluate local calibration of the MEPDG rutting model. Hoegh et al compared the predicted total rutting, asphalt layer rutting, and measured rutting. The comparison of the predicted and measured rutting showed the need for a recalibration of the MEPDG rutting model that did not involve an adjustment of the calibration parameters as typically recommended. Forensics showed that the granular base was mostly unaffected by rutting for the pavement sections evaluated in the study. The MEPDG models predicted unrealistically high rutting in the base and subgrade in the first month of pavement life. Hoegh et al discussed why a conventional MEPDG model calibration was not found to be feasible and recommended a modification of the rutting model. A modified MEPDG model was created to account for the forensic and predictive evaluations for the local conditions. The locally calibrated rutting predictions were found to be less biased, with lower rutting, than the predictions using the nationally calibrated rutting model.

Several studies investigated the influence of tire pressure on pavement response, particularly in the upper layers of flexible pavement structures [Bradley, 2006; Wang and Machemehl, 2006; Smith, 1993; Park, 2008; Fernando, 2006, Raad et al, 1998].

Smith [1993] conducted an analysis of pavement data using design models which accounted for the effects of variable tire pressures (690 kPa and 276 kPa) on low-volume aggregate surfaced and AC-surfaced roads. Smith found that when tire pressures were reduced, a 37% reduction in base thickness could be realized for an aggregate

surfaced road and a 10% to 12% reduction in base thickness for asphalt surfaced roads to reach an equivalent terminal serviceability level for the pavement.

Park [2008] studied the effects of different tire types on pavement fatigue and rutting service life. Park used three types of tires; radial, bias ply and wide-based tires to study the effects of tire pressures (520 kPa, 690 kPa, and 820 kPa) on pavement service life. Park predicted pavement fatigue and rutting life using a 3D Finite element model of asphalt pavements to investigate the influence of 3D tire types on pavement service life. Park found differences in the predicted pavement performance with wide-base and radial tires and that the effects of tire contact pressure distributions were seen near the surface and diminished with depth.

Fernando [2006] also found that the effects of the differences in tire contact pressure distributions were mainly seen near the surface and diminished with depth.

Bradley [2006] theorized that tire pressure reduction, or in combination with payload reduction, could reduce fatigue cracking more effectively than reducing payloads alone on haul roads in British Columbia.

Wang and Machemehl [2006] conducted an analysis of the effects of truck tire pressure (483 kPa, 690 kPa, and 896 kPa) on pavement performance using tire contact stresses. Wang and Machemehl showed that increased tire pressure can cause more fatigue cracking and rutting on flexible pavement performance.

Raad et al [1998] evaluated the effect of tire pressure (412 kPa and 756 kPa) on flexible pavement damage during spring-thaw. Raad et al evaluated pavement damage using ELSYM5 multi-layer elastic analysis software and the Asphalt Institute fatigue and

rutting damage equations. The analysis evaluated different wheel loads, asphalt thickness, thaw depth, and open-graded versus dense-graded bases. Raad et al found that the number of repetitions to failure was most critical in the unbound granular base in the pavement structure, and that the critical thaw depth for maximum damage started at the onset of base thawing and to a depth of 450 mm in the base. The study also found that the influence of tire pressure decreased with increasing asphalt thickness and that a decrease in tire pressure was most significant for asphalt layers thinner than 150 mm.

DISCUSSION OF EMERGING ISSUES AND GAPS IN RESEARCH

Several issues and gaps emerged from the studies on pavement structural response and pavement damage analysis.

Some of the studies related to SWR and vehicle loading in Canada focused on determining the start and end of SWR using thawing indices from frost probes, pavement temperature, and moisture conditions. The studies were unrelated to axle loads and damage based on limiting failure strain during the SWR periods.

Heun et al [2006] described ongoing studies in Ontario which involved the installation of thermistor probes in the pavement. The studies related road weather information to observed pavement structure and suggested a preliminary thaw index for seasonal load restrictions.

Chapin et al [2009] investigated models that could be used to estimate pavement strength as a function of the frost/thaw depths, the characteristics of the pavement structure and

other variables. Among the findings, Chapin et al suggested the FWD deflections can be used to approximate the thawing front depth during the spring period. However the research found large variations in the FWD pavement stiffness due to the presence of frost in the pavement.

Mabood et al [2008] investigated whether reduced tire pressure could be used to mitigate load damage to load restricted secondary roads of two pavement test sites in Dryden and Chapleau, Ontario. Repeated Light Weight Falling Weight Deflectometer (FWD) testing was carried out at the sites to monitor pavement strength and identification of the SLR period. The study found that light weight FWD can be used to determine in-situ strength, along with pavement temperature and moisture, but needed to be examined over a range of pavement conditions.

Wardle et al [2003] echoed the importance of validation as one of the current issues facing users of mechanistic-empirical models. Wardle et al noted that because failure criterion is derived in its own context, predictions will be consistent and appropriate when used as part of the same procedure. If a failure criterion was used in conjunction with a different procedure, the vital empirical link between the design and the original performance data used to calibrate the criterion was broken.

Baburamani [1999] found that the differences between laboratory and in-service pavement fatigue lives can be attributed to differences in loading conditions including vehicle type and axle configurations, rest periods between vehicle loads, vehicle wander in the wheelpaths, environmental factors, aging and micro damage healing in the asphalt pavement, crack propagation mechanism, and asphalt compaction and properties. The

differences between laboratory and field conditions required the use of a "calibration factor" in the prediction of field fatigue life. The magnitude of the factor applied was generally between 10 and 20, depending on the level of cracking in the pavement, the thickness of the asphalt layer and the field environment. The literature reported that calibration factors of 13.0 and 18.4 were used for fatigue failure criterion of 19% and 45%, respectively. Baburamani [1999] noted that these shift factors were comparable to the shift factors suggested for the US Strategic Highway Research Program (SHRP) fatigue life prediction models.

Rutherford [1989] found that many thin pavements (50 mm AC thickness) reached critical conditions by the time of base thawing in the spring, and asphalt tensile strain was the critical response parameter for the majority of these pavements in the spring. Rutherford reported that thicker AC pavements (100 mm thickness) did not experience strains or deflections in excess of those in summer until some subgrade thawing occurred; and subgrade vertical strain was the critical parameter for these pavements. Rutherford also found that deflections were not a reliable indicator of when critical conditions are realized in a thaw weakened pavement.

Huang [2004] reported that tensile strain and asphalt mix stiffness were the two main variables which influence fatigue life. Huang noted that the exponents for these variables in prediction equations vary according to the laboratory test method, loading conditions, and the asphalt mixtures used in the investigation.

Research Need

Based on gaps identified in the literature and given the limited numbers of studies related to the use of limiting strain criteria for SWR, the investigation of a calibrated local failure strain model for SWR loads in Manitoba was relevant for this thesis.

CHAPTER 3 - RESEARCH METHODOLOGY AND ANALYTIC APPROACH

This chapter presents the research methodology and analytic approach used to meet the objectives of this thesis.

The analytic approach included five phases; the experimental design and selection of test sites with instrumentation and data collection; calibration of pavement response models to predict critical strains in the pavements at various loads; development of local damage models to predict axle repetitions to failure; computation of damage accumulation, and investigation of whether SWR loads were valid in Manitoba based on limiting strains.

Figure 3.1 shows the flowchart of the research methodology and analytic approach developed for this thesis. The methodology was developed to be universal in nature. The approach could be used to evaluate any pavement structure, vehicle loads including overloads, tire pressure, axle configurations, and tire contact areas, based on the relationship between load, pavement damage, and limiting strain.

A discussion of the research analytic approach follows.

FIGURE 3.1: Flow Chart of Research Methodology and Analytic Approach

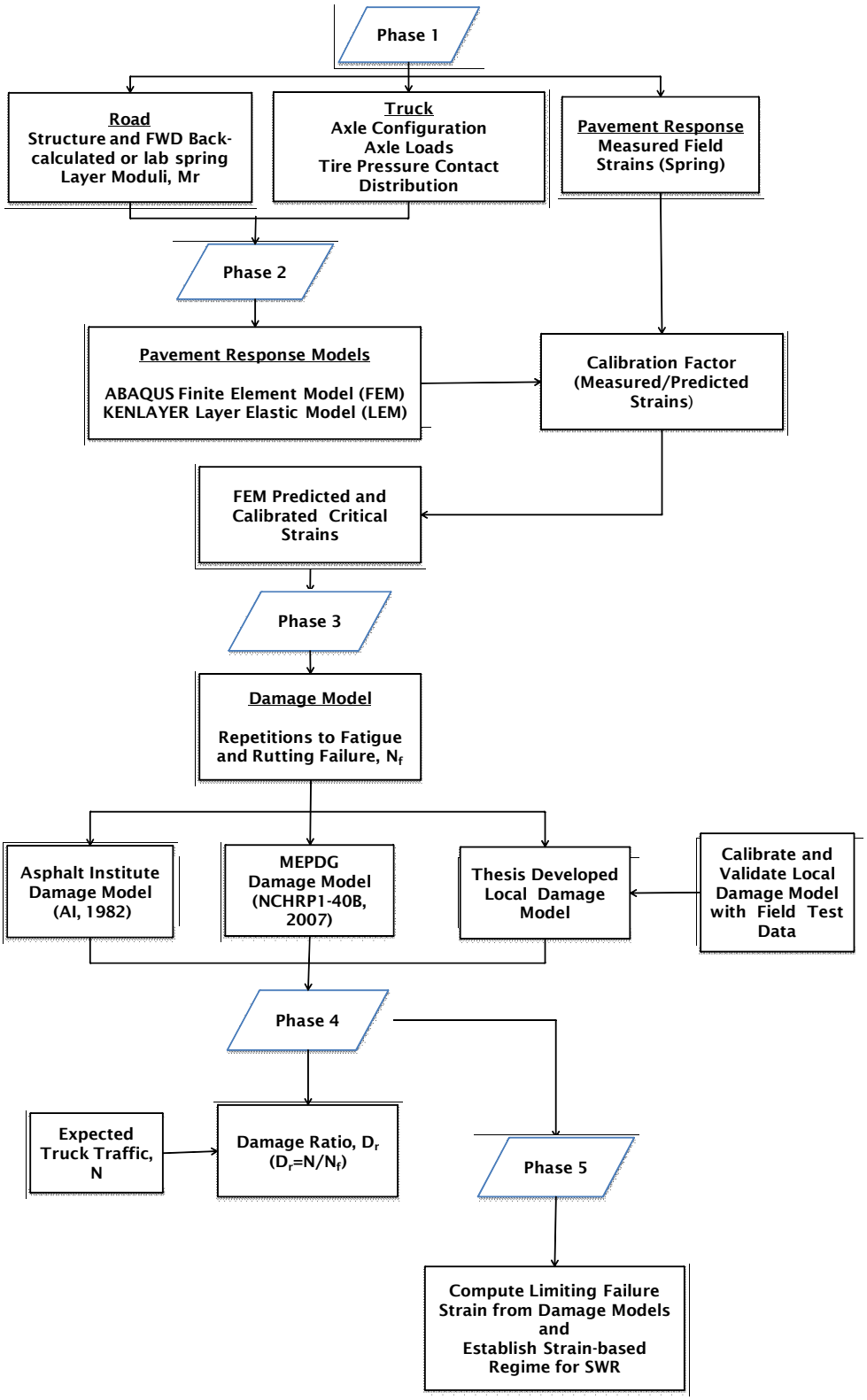

RESEARCH METHODOLOGY

Phase 1 of the research methodology was the experimental design of two instrumented flexible pavement sites in Manitoba, and selection of seven flexible pavements from the MnROAD low volume road facility. Phase 1 also included the collection of field and pavement response testing data from the sites.

The data collection included pavement structures and material layer characterization, vehicle axle loads and axle configuration, and pavement structural responses.

The material characterization included determination of the resilient modulus (M_r) of the layers in the pavement. Two methods were selected to determine the modulus of the pavement layers at the Manitoba sites: (1) back-calculation of the modulus from Falling Weight Deflectometer (FWD) deflections taken on the road using the evaluation of layer moduli and overlay design (ELMOD) software Version 5.1.72 [ELMOD5, 2007], and (2) lab testing of field samples of layer materials using standard lab modulus test methods.

The FWD back-calculation process is a mechanistic evaluation that attempts to match measured deflections with calculated deflections (to within ±2%) generated from a "seed" or starting layer moduli. The approach in ASTM D5858 "Standard Guide for Calculating in Situ Equivalent Elastic Moduli of Pavement Materials Using Layered Elastic Theory" [ASTM, 2008] was used for back-calculating the layer moduli. Since the back-calculated method can be highly dependent on the initial assumed moduli, lab testing of the layer materials was also conducted to estimate the moduli. The back-calculated or lab modulus that produce resilient modulus values that best correlated to measured field strains were used to characterize the layer materials in this thesis.

The trends and variability in the field data collected from the Manitoba and MnROAD sites were analysed to determine their suitability for calibrating and validating the structural response and damage models.

Phase 2 of the research methodology was the structural response model predictions of critical strains in the pavement layers at the Manitoba sites. The strain predictions were performed using the ABAQUS-based FEM developed by Liu in 2010 [Liu, 2011]. Calibration factors for the FEM were developed using the predicted and measured strains at the Manitoba sites.

To assess the underlying assumptions of the pavement response and to evaluate whether the FEM was necessary, a layered elastic model (LEM) was compared to the FEM. The LEM model predictions were performed using KENLAYER Pavement Analysis software, developed by Huang [2004]. KENLAYER is a multi-layer computer program which uses a layered elastic model applied to pavements under single and dual wheel loads.

Phase 3 of the research methodology was the development and validation of local damage models to predict load repetitions to pavement failure, at normal and SWR loads during the spring period in Manitoba. Local damage models were developed based on field data obtained from the MnROAD low volume road facility. The Local model predictions were compared to two available damage models; the Asphalt Institute [AI, 1982] and the Mechanistic Empirical Pavement Design Guide, MEPDG, [NCHRP, 2007].

Phase 4 of the research methodology was the determination of damage ratio based on the expected ESAL repetitions, and the predicted ESAL repetitions to failure, on the pavements using Miner's hypothesis.

Finally, Phase 5 of the research methodology was computing limiting strains for the Manitoba sites and establishing a strain-based criteria and decision regime for SWR load levels using the Local model developed between truck load and damage.

CHAPTER 4 - INSTRUMENTED TEST SITES, TEST VEHICLES, AND FIELD DATA COLLECTION

Field data, measured under real loads, is often required to validate structural response and damage model predictions. For this thesis, field data collected under loading at instrumented flexible pavement sites were used to validate pavement response and damage models that could not have been validated using theoretical analysis alone.

Two sources of field data from flexible pavements in Manitoba and the Minnesota Road Research (MnROAD) facility were used for this thesis. A field experiment was designed and instrumentation carried out on two low volume flexible pavements in Manitoba to measure pavement responses due to loading and environment during the spring thaw.

This chapter presents the design of the Manitoba and MnROAD test sites, the general descriptions of the pavement structures and material characterizations, instrumentation and sensor layout, material layer properties, control test vehicle, vehicle weights and axle configurations, and the collection of pavement response and other field data. The chapter reports on the Manitoba tasks carried out mainly by the author and supplemented with additional reports and research from the Manitoba experiment. The chapter also presents the MnROAD experiment carried out by the Minnesota Department of Transportation.

The flexible pavements in Manitoba and MnROAD were selected based on their weak structures, susceptibility to thaw-weakening during the spring, and availability of field response and performance monitoring data from instrumentation at the sites. The MnROAD low volume pavements were selected to augment the field data required for developing and calibrating local failure models for this thesis. The MnROAD sites have

pavement response, loading, and field performance data over the life of the pavements, from construction to demolition, which the Manitoba sites do not.

The MnROAD field data was considered appropriate for this analysis because the pavement structures at the low volume road were comparable to the structures at the Manitoba sites. In addition, both jurisdictions have SWR programs operating under similar climatic and axle load conditions.

4.1 MANITOBA INSTRUMENTED TEST SITE, TEST VEHICLE, AND FIELD DATA COLLECTION

A field experiment was designed and instrumentation carried out on two low volume flexible pavements in Manitoba. The roads were instrumented in October 2008 with strain gauges, deflection gauges, and moisture and temperature probes to measure responses under real load and environmental conditions during the SWR period. The field data was to evaluate structural response to loading and to predict pavement damage during the spring thaw.

The Manitoba test sites are located on secondary Provincial Trunk Highway (PTH) 11, and Provincial Road (PR) 304, approximately 110 kilometers northeast of the City of Winnipeg, Manitoba. The roads are logging routes that supported a former pulp and paper mill and are subject to annual SWR.

Figure 4.1 shows the instrumented test sections locations on PTH 11 and PR 304. The test section on PTH 11 is located 2.7 kilometers south-east of the intersection of PTH 11

and PR 304. The test section on PR 304 is 2.4 kilometers north-east of the intersection of PTH 11 and PR 304. The two sites have similar commercial vehicle types, climatic, and subgrade conditions.

Figure 4.1: Manitoba Instrumented Test Site Locations [MIT, 2009]

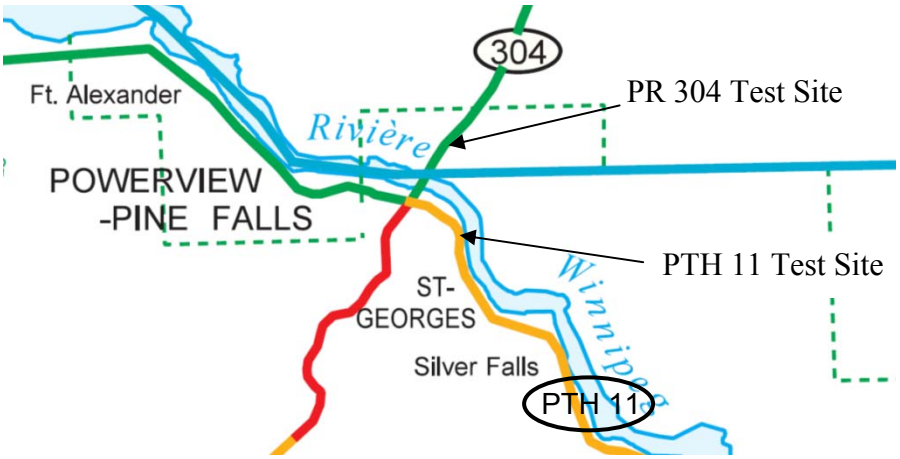

The instrumentation of the two haul roads in Manitoba was part of a larger, 3-year study by Manitoba Infrastructure and Transportation, University of Manitoba, and FP Innovations on improving truck productivity during the spring period [Bradley et al, 2007; Kavanagh et al, 2010; Liu, 2011; Kavanagh et al, 2011]. The objective of the larger study was to provide tools and develop policies that incorporated reduced tire pressures in combination with higher SWR loads during the spring thaw period.

The larger study included instrumentation of the pavement test sites in October 2008, pavement response data collection during the spring of 2009, and structural response modeling of thaw weakened pavements, and damage analysis using information from the test sites. A controlled test truck, with known weights and axle configurations similar to

typical vehicles operating on SWR roads in Manitoba, was used to test different axle loads and tire pressure combinations on each road.

The analysis of the data trends and pavement damage modeling from the larger study was completed by the author of this thesis. The results from the reports [Kavanagh et al, 2010; Kavanagh et al, 2011] are included in the thesis.

PTH 11

PTH 11 is a flexible pavement consisting of an asphalt concrete (AC) wearing surface on granular base. Constructed in 1964, the pavement structure is 130 mm AC, on 335 mm of granular base, and on a high-plastic clay subgrade.

The AC surface consists of two (52 mm) lifts of original asphalt concrete mix laid in 1964, and a 26 mm lift of patching mix laid in 2008. Laboratory analysis of the original (as built) mixture obtained from MIT [MIT, 1964] shows that the asphalt concrete consisted of a Bituminous 'A' surface lift and Bituminous 'B' bottom lift. The Bituminous 'A' and 'B' designations are MIT classes of asphalt mix types. Bituminous 'B' mixture is a coarser mix with maximum aggregate size of 19 mm. Bituminous 'A' mixture is a finer mix with maximum aggregate size of 16 mm. The densities of the original Bituminous 'A' and 'B' mixtures were an average 2,340 kg/m^3 and 2,300 kg/m^3 respectively. The average air voids in the Bituminous 'A' and 'B' mixes were 5.0% and 7.5%, respectively, with the target air void of 4%. The asphalt binder type used in both original mixtures was a 150/200 penetration grade asphalt, which was a moderately soft

asphalt binder. The asphalt contents (by weight of aggregate) in the Bituminous 'A' and 'B' mixtures were an average of 5% and 4.5%, respectively.

The granular base layer of PTH 11 is an aggregate base, designated as 'A' Base by MIT, with a maximum aggregate size of 19 mm. A soil survey conducted by MIT in October 2008 [MIT, 2008] describes the base layer as a non-frost susceptible granular aggregate with 4% average moisture content during the fall of 2008.

The subgrade is described as an organic, firm, black clay, with average moisture content of 27% and an organic content of 6.6%. The subgrade is classified as an A-7-6 soil, based on the American Association of State Highway and Transportation Officials (AASHTO) soil classification system. The AASHTO system classifies soils based on gradation and Atterberg limits (plastic limit and liquid limits), which can be used to quantify the quality of the soil as a construction material. The A-7-6 soil on PTH 11 is considered as a fair to poor embankment construction material [Yoder and Witczak, 1975].

MIT classifies PTH 11 as a key secondary arterial with a maximum allowable gross vehicle weight (GVW) of 56,500 kg. MIT considers the structure as relatively weak, with average BBR rebounds over 2.5mm (at 80kN standard load) and subject to annual SWR during the spring period.

PR 304

PR 304 is a flexible pavement with a double asphalt surface treatment (AST) on granular base, and a rock-filled sub-base on a clay subgrade. The AST surface is a thin layer of fine aggregate embedded in liquid asphalt on top of the granular base. Constructed in 1976, the pavement structure is 30 mm AST, 200 mm granular base, 500 mm rock sub-base on high-plastic clay subgrade. The roadway was built on a previously drained swamp, with a high water table at approximately 1.8 meters below the pavement surface.

The granular base layer of PR 304 is an 'A' base with a maximum aggregate size of 19 mm. The rock-filled sub-base is a crushed granite with maximum aggregate size of 50 mm. The 2008 soil survey from MIT [MIT, 2008] describes the base layer as a non-frost susceptible granular aggregate, and sub-base as rock fill aggregate with 90% fines. The subgrade is described as soft, grey, silty clay, with a moisture content of 24% (during fall 2008) and organic (peat) content of 7.3%. The subgrade is classified as A-6 soil based on the AASHTO classification. Similar to the A-7-6 subgrade on PTH 11, the A-6 soil on PR 304 is also considered as a fair to poor construction embankment material.

MIT classifies PR 304 as a secondary arterial with an allowable GVW of 47,630 kg. MIT considers the structure as a moderately strong AST, with sections that are subject to annual SWR during the spring period.

Figure 4.2 shows the two Manitoba pavement structures and cross-sections of the layer thicknesses and layer material types.

FIGURE 4.2: Manitoba Pavement Structures

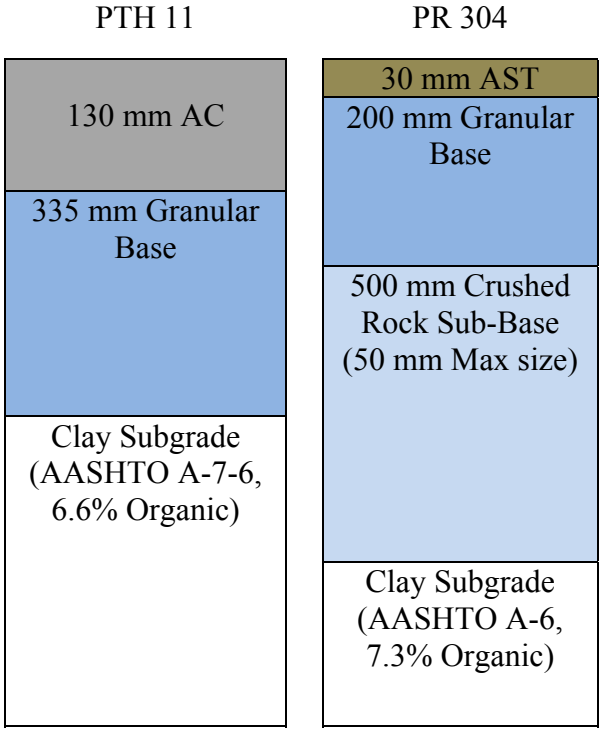

Note: AC=Asphalt Concrete, AST=Asphalt Surface Treatment, Cross section not to scale

ROADWAY AND TRAFFIC INFORMATION

Roadway and traffic information were obtained for PTH 11 and PR 304 to estimate loading on the pavements since construction. The traffic information included average annual daily traffic (AADT) and the percent trucks on each roadway. The AADT and percent trucks were obtained and estimated by MIT from yearly traffic counts conducted for a mix of vehicles and truck types.

Table 4.1 presents the roadway and traffic information at the Manitoba test sites. The road information includes the pavement structure, maximum allowable gross vehicle weight (GVW), SWR status, 2008 average annual daily traffic (AADT) and percent

trucks, and 2008 average annual daily truck traffic (AADTT). The AADTT is the AADT multiplied by the percent trucks. A comparison of the AADTT on both roads shows approximately two and a half times more daily truck traffic on PTH 11 than on PR 304. The higher maximum GVW allowed on PTH 11 does not imply that MIT considers the structure on PTH 11 to be stronger than PR 304. Other factors in the classification and designation of the highway include proximity and access to communities based on population.

Table 4.1: Roadway and Traffic Information at Manitoba Test Sites

Road	Year Built	Structure	Maximum Allowable GVW (kg)	Road Subject to Annual SWR	2008 AADT	% Trucks	2008 AADTT
PTH 11	1964	130mm AC 335mm Base Clay Subgrade	56,500	Yes	1,210	3.2	39
PR 304	1976	30mm AST 200mm Base 500mm Sub-base Clay Subgrade	47,630	Yes	265	5.5	15

Note: GVW=Gross vehicle weight, SWR=Spring weight restriction,
AADT=Average annual daily traffic, AADTT=Average annual daily truck traffic

MANITOBA TEST SITE INSTRUMENTATION

The Manitoba test sites were instrumented with structural response gauges and environmental sensors to measure pavement responses under real loads and road conditions. The instrumentation was installed in October 2008 and included asphalt strain gauges, soil compression gauges, multi-depth deflection gauges, and environmental

temperature and moisture probes. A description of the experiment, instrumentation and sensor layout is presented.

PTH 11 INSTRUMENTATION

Horizontal asphalt strain gauges (Model ASG-152 by Construction Technology Laboratories (CTL)), were installed at the bottom of the AC layer of PTH 11. The ASG were used to measure longitudinal and transverse strains from dynamic traffic loading. The configuration of the ASG-152 gauge is a 350 Ω Wheatstone Bridge mounted on a 203 mm long by 152 mm wide I-beam. The maximum range of the ASG was ± 1500 microstrains, which is within the expected range for most flexible pavements.

The asphalt strain gauges were installed parallel to the direction of travel to measure longitudinal strains, and perpendicular to the direction of travel to measure transverse strains. The strain gauges were positioned in three rows in the outer wheel path of the test lane.

Figure 4.3 shows the sensor layout at the Manitoba test sites. The layout shows the locations of the longitudinal and transverse asphalt strain gauges, MDD, and SCG sensors in the outer wheel path of the test lane.

Figure 4.3 Sensor Layouts at Manitoba Test Site

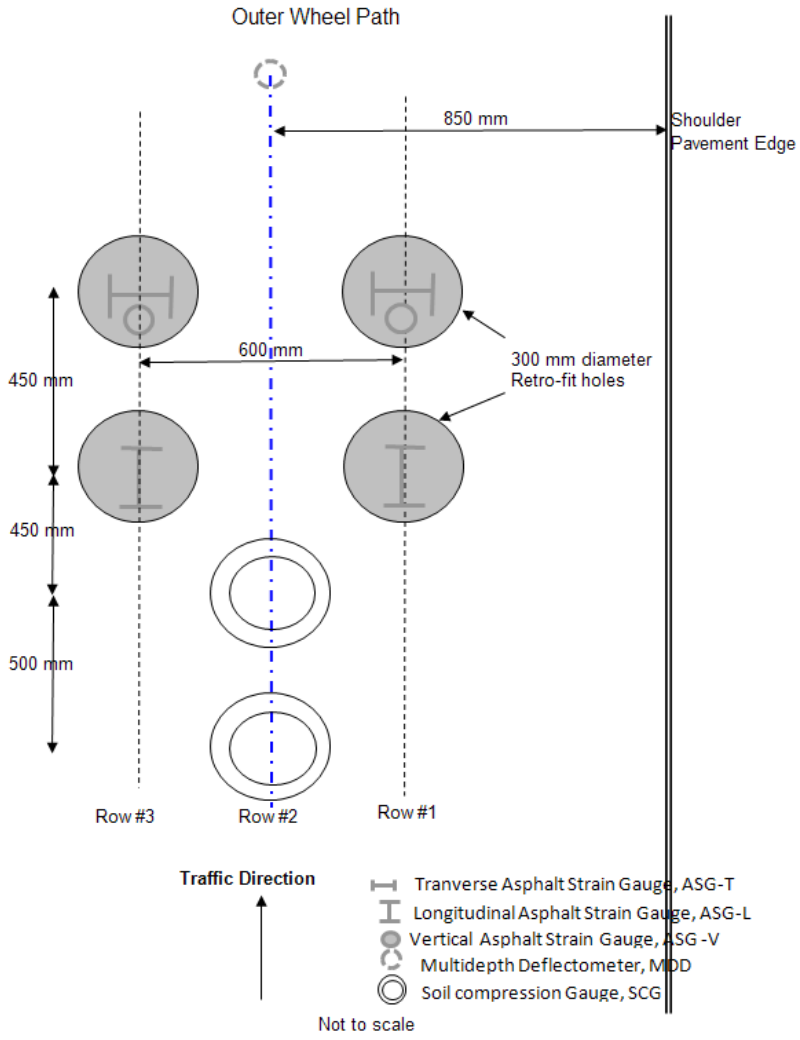

Several alternative procedures were considered for the asphalt strain gauge installation. One procedure included removing a full lane width of AC slab from the pavement to expose the base, install the sensors, and fill and compact the lane with AC. The other procedure was a retrofit installation, which included coring the AC surface at the sensor locations only, installing the sensors at the bottom of the hole, and filling and compacting the hole with AC. The retrofit procedure was ultimately selected for the installation since

it was quicker than removing the full lane width and did not require overnight lane closure. Overnight lane closure was not allowed on the road.

For the retrofit installation, the asphalt strain gauges were installed at the bottom of 300 mm diameter holes. The holes were cored through the AC layer to the top of the base in the outerwheel path of the test lane. After the strain gauges were installed, the holes were filled with new AC mix and hand compacted. A tack coat was used to bond the new AC to the old.

Figure 4.4 shows the installation of the asphalt strain gauges at the Manitoba test sites. The photographs show the retrofit installation in the outerwheel path of the test lane and the horizontal and vertical asphalt strain gauges at the bottom of the surface layer.

Figure 4.4: Installation of Asphalt Strain Gauges at Manitoba Test Sites

(a) Retrofit installation

(b) Horizontal and vertical strain gauges

There were concerns that the new AC in the retrofit installation could significantly influence the pavement response over the strain gauges. However, it was theorized that the influence of the dual tires would extend significantly beyond the AC in the retrofit

hole. The response of the tire loads would be greater on the existing AC pavement, thereby minimizing the impacts of the retrofit hole on the strain gauges.

Soil compression gauges (SCG) (manufactured by CTL) were installed on PTH 11 to measure the vertical strains at the top of the subgrade due to loading. The SCG consists of a top and bottom plate, 150 mm apart that use a four-wire thermal resistor (potentiometer) to measure soil deformation up to 25 mm. While the installation of the SCG was completed on PTH 11, field testing of the gauges produced inconsistent deformation readings and ultimately the gauges stopped working. The subgrade deformations from the SCG were not used in this thesis.

A multi-depth deflectometer (MDD) (manufactured by CTL) was installed on PTH 11 to measure subgrade deflection under loading. The MDD measures vertical deflection at multiple depths in a pavement from a reference head (linear potentiometer) near the top surface of the pavement, to predetermined depths. The overall vertical deflection is referenced to a fixed anchor in the subgrade. As the pavement deflects, the reference head moves downward compressing the potentiometer. Vertical strains at various depths in the subgrade can be obtained by dividing the MDD deflection at the top of the subgrade, by the length of the reference head.

CTL installed the MDD in a 75 mm diameter bore hole on PTH 11, from the pavement surface to a depth of 2.2 meters into the subgrade. During installation of the MDD, CTL used silica sand to backfill the space between the ribbed exterior of the device casing and the clay subgrade to ensure good soil interface.

Environmental sensors were installed on PTH 11 to measure layer material conditions during spring testing. Time domain reflectometers (TDR) (Model CS616 by Campbell Scientific) were installed under the base and subgrade, to measure changes in moisture content in the base and subgrade. The TDR probe consists of an epoxy head and two parallel conducting rods that measure changes in conductivity of the material surrounding the conducting rods based on the dielectric constant. The device is excited by a high frequency electromagnetic pulse along the rods. The velocity of the reflected wave is measured and correlated to soil moisture content. The relationship between the volumetric moisture content and the dielectric constant is determined through regression equations provided by the gauge supplier. The TDRs were installed on PTH 11 at various depths in the base, at the top of the subgrade and to a depth of 2.4 meters into the subgrade.

Thermocouple (TC) probes (Model 107B by Campbell Scientific) were installed under the base and subgrade, to measure temperature changes in the base and subgrade. The TC sensor is a pair of dissimilar metal alloy wires connected together near the point of measurement. The TC generates an open-circuit voltage which is proportional to the temperature difference between the hot end and a reference junction. A thermocouple string with seven probes was installed in a vertical borehole in the outer wheelpath of PTH 11 to determine the temperature profile and depth of frost/thaw in the pavement structure, to a depth of 2.4 meters.

PR 304 INSTRUMENTATION

The same procedure as PTH 11 was used to install the instrumentation on PR 304. The asphalt strain gauges were installed using the retrofit installation and oriented in the longitudinal and transverse directions of the test lane, at a depth of 140 mm below the AST surface. Normally, asphalt strain gauges are not installed under AST surfaces because of the thin layer thickness. However the strain gauges were installed at this site in an attempt to obtain relative magnitudes of longitudinal and transverse strains under the AST layer.

Soil compression gauges were installed in the subgrade on PR 304 to measure subgrade deformation from loading. Similar to the experience on PTH 11, the SCG produced inconsistent deformation readings during field testing and ultimately the gauges stopped working. The subgrade deformations from the SCG on PR 304 were not used in this thesis.

Attempts to install an MDD on PR 304 to obtain vertical deflections in the subgrade were unsuccessful. CTL found it impossible to grout and anchor the MDD rod in the subgrade due to the high water table at the site.

Environmental sensors were installed on PR 304 to measure material conditions during testing. Time domain reflectometers (TDR) and thermistors were installed under the base and subgrade, to measure changes in moisture content and temperature. The TDR and thermistors probes were located at various depths in the base, at the top of the subgrade, and to a depth of 2.4 meters into the subgrade.

Installation of the pavement sensors at the two sites was completed over a four-day period. All cables and wires from the sensors were buried and directed to data loggers in a data acquisition panel box along the right-of-way of each road. The Campbell Scientific D1-718Bx and D1715B data loggers were used to collect the asphalt strain gauge responses and MDD deflections, respectively, at the sites. A Campbell Scientific CR100 data logger was used to collect moisture and temperature data.

Table 4.2 presents the pavement sensor types and sensor depths at the Manitoba test sites. The information includes the type of sensors, the hole diameter and sensor depths in the outer wheelpath of each test lanes on PTH 11 and PR 304. The depth of the sensors varied with the pavement structure, type of instrumentation and pavement responses expected at specific locations in the structure.

Table 4.2: Pavement Sensor Types and Sensor Depths at Manitoba Test Sites

Road	Sensors	Hole Diameter (mm)	Sensor Depth (mm)
PTH 11	ASG-T, ASG-L	300	145
	MDD	75	2200
	SCG	75	735 & 945
PR 304	ASG-T, ASG-L	300	140
	SCG	75	871 & 925

Note: ASG-T=Transverse Asphalt Strain Gauge, ASG-L= Longitudinal Asphalt Strain Gauge, MDD=Multi-Depth Deflectometer, SCG=Soil Compression Gauge

MANITOBA TEST VEHICLE

A control test vehicle was used for pavement response testing under real loads and road conditions at the Manitoba sites. An 8-axle tractor double trailer (or B-Train) was

selected as the control vehicle. The B-Train was representative of the typical commercial vehicle type used for heavy commodity hauls on low volume SWR roads in Manitoba.

The B-Train configuration consists of a tractor with a steering and drive tandem axle, a lead trailer with a tridem axle, and rear trailer with a tandem axle. The B-Train is equipped with dual-tire assemblies of standard 11R22.5 tire size (11inch tread radial tire and 22.5 inch diameter rim) on all except the steering axle.

Figure 4.5 shows the schematic of the 8-axle B-Train configuration. For this analysis, the single axle on the tractor of the B-train was designated as 'Steering', the tandem axle on the tractor was designated as 'Drive', the tridem axle on the lead trailer was designated as 'Trailer1', and the tandem axle on the rear trailer was designated as 'Trailer2'. Details of the vehicle dimensions can be found in Appendix C.

FIGURE 4.5: Schematic of 8-Axle B-Train Configuration [after MIT, 2009]

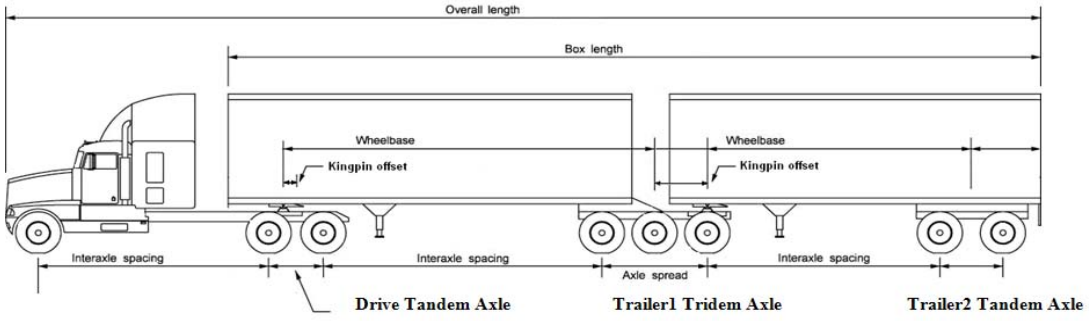

Table 4.3 presents the B-Train dual tire spacing and axle group spacing. The axle and dual tire spacings were measured from center-to-center of each tire in the group.

Table 4.3: B-Train Dual Tire Spacing and Axle Group Spacing

Axle Group	Dual Tire Spacing (mm)	Axle Group Spacing (mm)
Drive Tandem	340	1320
Trailer1 Tridem	338	1520
Trailer2 Tandem	334	1520

B-TRAIN AXLE GROUP LOADS AND TIRE LOADS

Three combinations of axle loads were used in the research to measure the pavement response to truck loading during the SWR period. The three load combinations included a maximum allowable load, one level higher than the maximum allowable load, and the SWR load allowed on each road during the spring period.

Maximum vehicle and axle loads are governed by Manitoba provincial regulations on primary and secondary roads. There are three provincial load designations in Manitoba: B1N, A1N, and RTAC (Roads and Transportation of Canada).

B1N designations are the lowest loads in Manitoba and are generally applied on low volume weak gravel and AST roads. A1N designations are intermediate loads and are generally applied on secondary roads. RTAC loads are the highest loads and are generally applied on primary roads and key secondary roads in Manitoba [MIT, 2009].

Manitoba applies SWR to B1N and A1N roads at two restriction levels. Level 1 SWR is 90% of normal maximum allowable load, and Level 2 SWR is 65% of normal maximum

allowable load. Level 1 SWR is designated as L1, and Level 2 SWR is designated as L2. Provincial regulators affix a suffix (L1 or L2) to the normal maximum allowable load to signify the level of load restrictions on selected roads during the spring. For example, a road designated as B1L1 is subject to Level 1 spring restriction (90% of normal B1 loads). The level of restrictions can increase from Level 1 to Level 2 as the pavement weakens during the spring thaw.

Table 4.4 presents the Manitoba load designations and SWR restrictions levels. RTAC designated roads are strong pavements and are not restricted during the spring period.

Table 4.4: Manitoba Load Designations and SWR Restriction Levels

Load Designations	SWR Restriction Level
B1N	Level 1 - 90% of Normal Legal Loads
A1N	Level 2 – 65% of Normal Legal Loads
RTAC	No Restriction

A combination of three B-Train axle loads was used for the research testing on PTH11 and PR 304. The SWR loads were selected based on the levels designated by MIT for each road. The loads were:

PTH 11

- A1L1 (SWR Level 1 - 90% of A1 Normal load)
- A1N (Normal Load)
- RTAC (One load level higher than normal)

PR 304

- B1L2 (SWR Level 2 - 65% of B1 Normal load)
- B1N (Normal Load)
- A1N (One load level higher than normal)

Table 4.5 presents the B-Train maximum allowable axle and tire loads (and gross vehicle weights) used for the research on PTH 11 and PR 304. The maximum allowable loads (under Manitoba provincial regulations in Appendix B) were targeted for the field testing.

Table 4.5: B-Train Maximum Allowable Axle and Tire Loads

Maximum Allowable Axle and Tire Loads (kg)									
Load Level	Steering		Drive		Trailer1		Trailer2		B-Train
	Axle Load (kg)	Tire Load (kg)	Axle Load (kg)	Tire Load (kg)	Axle Load (kg)	Tire Load (kg)	Axle Load (kg)	Tire Load (kg)	GVW (kg)
PTH 11									
A1L1	5,500	2,750	14,400	1,800	20,700	1,725	14,400	1,800	55,000
A1N	5,500	2,750	16,000	2,000	23,000	1,917	16,000	2,000	56,500[1]
RTAC	5,500	2,750	17,000	2,125	23,000	1,917	17,000	2,125	62,500
PR 304									
B1L2	3,575	1,788	9,425	1,178	13,000	1,083	9,425	1,178	35,425
B1N	5,500	2,750	14,500	1,813	20,000	1,667	14,500	1,813	47,630[1]
A1N	5,500	2,750	16,000	2,000	23,000	1,917	16,000	2,000	56,500[1]

Note: [1]Maximum GVW less than sum of individual axle loads,
GVW=Gross Vehicle Weight

MANITOBA FIELD TESTING

Pavement response testing at the Manitoba sites was conducted during the late spring of 2009. The testing was conducted over four day, from May 19-22, 2009 after frost had disappeared from the subgrade. The data collected during testing included pavement strains and deflections at the three B-Train loads and two tire pressures (690 kPa standard pressure and 345 kPa low pressure), and three truck speeds (static, 20 km/hr, and 70 km/hr). The B-Train was equipped with a tire pressure control system that allowed the truck operator to conveniently monitor and vary the tire pressures while driving.

The B-Train combination of axle loads, tire pressures, and vehicle speeds used for testing on PTH 11 and PR 304 were:

<u>PTH 11</u>

- Axle Group Loads
  - A1L1, A1N, RTAC
- Tire Pressures
  - 690 kPa, 345 kPa
- Vehicle Speeds
  - Static, 20 km/hr, 70 km/hr

<u>PR 304</u>

- Axle Group Loads
  - B1L2, B1N, A1N
- Tire Pressures
  - 690 kPa, 345 kPa
- Vehicle Speeds
  - Static, 20 km/hr, 70 km/hr

During the four days of B-Train trafficking, strain and deflection measurements were taken over three ‘good’ runs of the steering tires on the target sensors.

A good run was defined as the ‘wander’, a distance less than 30 mm, from the outer edge of the steering tire and the outer edge of the target sensor. A video camera and pavement markings were used to verify that the steering tire was within the prescribed ‘wander’ limit. Repeat runs of the B-Train were made if the tire ‘wander’ was outside the prescribed limit.

Figure 4.6 shows the B-Train trafficking over the pavement sensors at the Manitoba sites. The photograph shows one run of the B-Train and the video and pavement markings used to verify the tire offset over the sensors.

Figure 4.6: B-Train Trafficking Over Pavement Sensors at Manitoba Site

The loads on the B-train loads were incrementally increased after each combination of runs. The truck operator incrementally loaded the B-Train trailers with wood chips and weighed the vehicle on platform scales in order to achieve the target loads. Pavement temperatures were monitored closely during testing to ensure pavement responses under similar environmental conditions. Pavement temperatures at 200mm depths ranged from 10°C to 15°C, while air temperatures ranged from 17°C to 20°C. The B-Train runs were conducted only when pavement temperatures were within 2°C-3°C of each test runs.

Table 4.6 presents the B-Train actual (measured) axle and tire loads achieved for the field testing on PTH 11 and PR 304.

Table 4.6: B-Train Actual (Measured) Axle and Tire Loads Achieved for Testing on PTH 11 and PR 304

Load Level	Actual (Measured) Axle and Tire Loads (kg)								
	Steering		Drive		Trailer1		Trailer2		B-Train
	Axle Load (kg)	Tire Load (kg)	Axle Load (kg)	Tire Load (kg)	Axle Load (kg)	Tire Load (kg)	Axle Load (kg)	Tire Load (kg)	GVW (kg)
PTH 11									
A1L1	4,897	2,449[1]	15,176	1,927	20,856	1,765	15,136	1,829[1]	56,065
A1N	4,944	2,472[1]	15,192	1,930	21,084	1,785	15,392	1,924[1]	56,612
RTAC	4,837	2,419[1]	17,072	2,173	24,504	2,079	16,568	2,071[1]	62,981
PR 304									
B1L2	4,525	2,263[1]	10,576	1,322[1]	14,940[2]	1,245	10.104[2]	1,263	40,145
B1N	4,715	2,358[1]	13,904[2]	1,738	17,700	1,475[1]	14,072	1,650	50,391
A1N	4,890	2,445[1]	15,224	1,903	21,108	1,759[1]	15,392	1,924[1]	56,614

Note: [1]Tire load was estimated from measured axle group load
[2]Axle group load was estimated from measured tire load
GVW=Gross Vehicle Weight

While major efforts were made by the truck operator to achieve the maximum loads during weighing, differences arose between the maximum loads (in Table 4.5) and the actual (measured) loads achieved in Table 4.6.

A statistical comparison was conducted to assess whether the B-Train actual (measured) loads were representative of the maximum allowable loads. The GVW was not included in the statistical comparison, because unlike bridges, pavement damage is affected by axle loads not gross vehicle loads.

A t-test was selected to determine whether the means of the maximum allowable and the actual (measured) axle loads (at one sample location) were the same, at 95% confidence level, α. The t-test assumes the null hypothesis (H=0); that the difference between the means (μ_d) of the two samples is zero, and that the mean of sample one ($\bar{X}_1$) is equal to the mean of sample two ($\bar{X}_2$) (i.e. Null hypothesis H=0; $\bar{X}_1 = \bar{X}_2$; $\mu_d = 0$).The t-test calculates a t-statistic value from the two samples, and compares it to a t-critical value obtained from statistical tables at the confidence limit, α, and the degree of freedom of the data points. If the calculated t-statistic for the paired differences is less than t-critical, the null hypothesis is not rejected, and it can be concluded that the two samples are not statistically different, at the specified confidence limit.

The t-statistic, t, for paired-sample test and normal distribution is shown in Equation 4.1 [Groebner et al, 2008]:

$$t = \frac{\bar{d} - \mu_d}{\frac{s_d}{\sqrt{n}}} \qquad (4.1)$$

$$S_d = \sqrt{\frac{\sum(d-\bar{d})^2}{n-1}}$$

Where:

t= t-statistic

$\bar{d}=\frac{\sum d}{n}$ = mean of paired differences

d=differences between paired values in the samples

μ_d=0, Hypothesized mean paired differences

S_d=standard deviation of paired differences in the samples

n=number of paired values in the samples

$df = n - 1$=degree of freedom

Figure 4.7 shows a t-test normal distribution curve and the region where the null hypothesis would be accepted or rejected, at specified confidence level. T-critical is the cut-off between rejecting and accepting the null hypothesis, at the selected confidence limit, α. The one-tail t-critical is used if the t-statistic is expected to be only positive or negative, while the two-tailed t-critical is used if the t-statistic is expected to be either positive or negative.

Figure 4.7: T-test Normal Distribution Curve and Region Where Null Hypothesis Would be Accepted or Rejected [after Groebner et al, 2008]

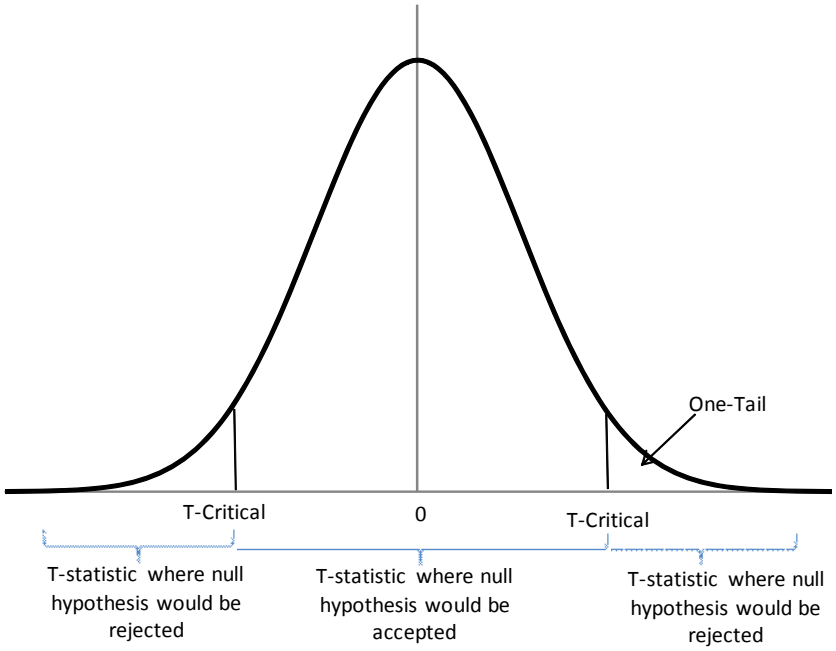

The ρ-value is an additional approach to conducting hypothesis testing. The ρ-value is the probability that the null hypothesis would be accepted or rejected. If the ρ-value is greater than the specified confidence level (e.g. α=0.05), the null hypothesis is not rejected. The advantage of the ρ-value is that it provides a measure of the extent to which the data disagrees with the null hypothesis, not just whether they disagree [Groebner et al, 2008].

Table 4.7 presents the t-test parameters of the B-Train maximum allowable axle loads versus the actual (measured) axle loads. The two tailed t-critical was used since a number of the actual (measured) axle loads were either higher or lower than the maximum allowable axle loads. The ρ-value was also calculated.

TABLE 4.7: T-test Parameters of B-Train Maximum Allowable versus Actual (Measured) Axle Loads

Road	t-Critical d_f=11 (2-Tail)	t-Statistic (α=0.05, *n*=12)	Probability, ρ (α<0.05) (2-Tail)	Not Rejected/ Rejected Null Hypothesis
PTH 11	2.20	1.47	0.4698	Not Rejected
PR 304	2.20	1.40	0.1891	Not Rejected

From the t-test results, the t-statistics for both PTH 11 and PR 304 were less than t-critical. Therefore the null hypothesis was not rejected and it was concluded that the maximum allowable and actual (measured) axle loads were not statistically different, at the 95% confidence level.

Based on the results of the t-test, the B-Train actual (measured) axle loads were judged to be representative of the maximum allowable loads and acceptable for trafficking during the spring field testing.

MEASURED B-TRAIN TIRE FOOTPRINTS AND TIRE CONTRACT PRESSURES

One of the major assumptions of the traditional layered elastic models is a uniformly loaded contact area with circular tire footprint on a pavement. To check this assumption and to evaluate the pressure distribution and contact area during loading, the B-Train tire footprints and contact areas were measured for each change in load and tire pressure.

An I-Scan pressure mat was used to measure the tire-pavement contact pressure (stress) distributions at the three B-Train axle loads and two tire pressures on PTH 11 and PR 304. The tire pressures were the standard 690 kPa commonly used by commercial trucks in western Canada, and 345 kPa (or 50% reduced) pressure. The tire-pavement pressure distributions were measured on the outside dual tire of the 'Drive', 'Trailer1' and 'Trailer2' axle group assemblies. The pressure on the single 'Steering' axle tire remained at 690 kPa during testing, because the steering tires carry a fixed heavy load and require a relatively high inflation pressure at all travel speeds.

Figure 4.8 shows the tire-pavement contact pressure distribution testing with the I-Scan pressure mat at the Manitoba site. The pressure distribution measurements were taken after each change in axle loads and tire pressure during the spring testing.

Figure 4.8: Tire-Pavement Contact Pressure Distribution Testing with I-Scan Pressure Mat at Manitoba Test Site

Data of the numerical pressure distribution and screen shots from the pressure mat software were obtained during testing. The pressure distribution identified the shape of the measured contact area and the magnitude of the stress distributions at each tire pressure setting and B-Train load.

Figure 4.9 shows a comparison of the measured tire footprints under the standard 690 kPa and low 345 kPa tire inflation pressures from the B-Train RTAC load at the Manitoba site. The pressure mat software was set to imperial units of pressure (stress) distribution in the images.

FIGURE 4.9: Comparison of Measured Tire Footprints under Standard 100 PSI (690 kPa) and Low 50 PSI (345 kPa) Tire Inflation Pressure from B-Train RTAC Load at Manitoba Site [after Kavanagh et al, 2011]

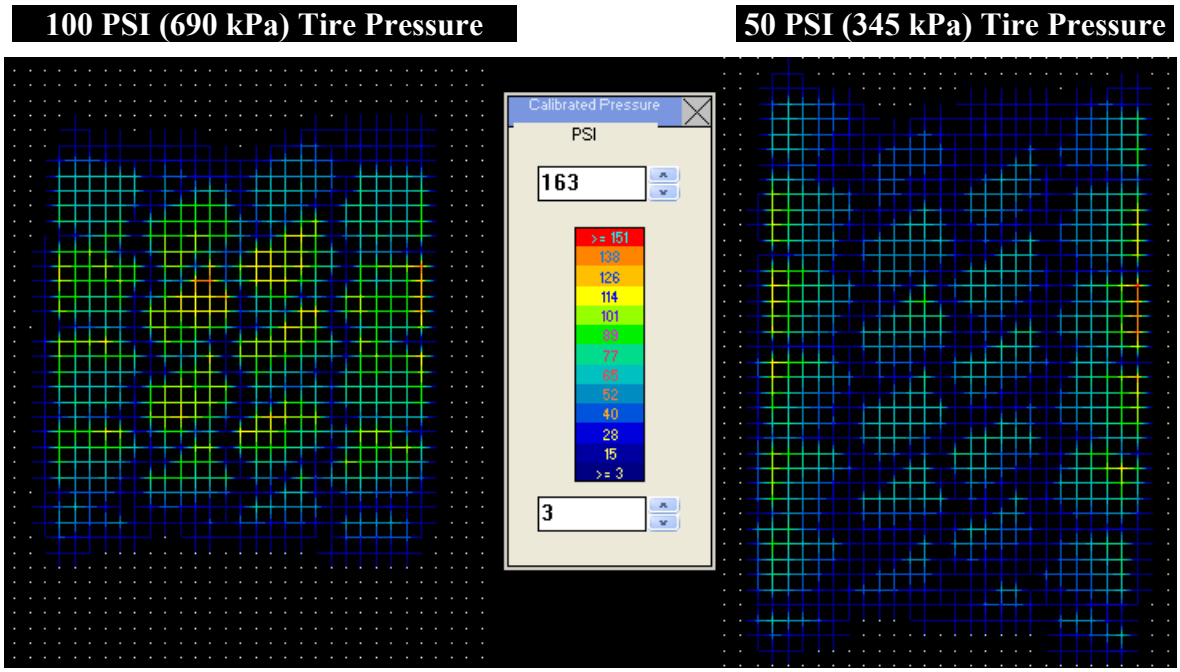

The footprints show that the tire pressure distributions are not uniform and not circular, (closer to a rectangle) and contrary to the simplified assumptions in traditional layered

elastic models of a uniform, circular area. Liu and Shalaby [2013] found that the distribution of contact stresses and the shape of the tire footprint were different from the traditional assumptions. The study found that the tensile strains at the bottom of the surface layer were mainly affected by the shape and contact stresses and diminished with depth.

The images show that the standard 690 kPa tire footprint was smaller than the 345 kPa footprint. For the same load, the contact area at the standard 690 kPa tire pressure was 15% smaller on average than at the 345 kPa tire pressure. The 690 kPa tire footprint had higher pressure (stress) distributions at the interior of the tire, while the 345 kPa tire pressure had lower pressure distributions at the interior of the tire. However, the 345 kPa tire pressure produced higher pressure distributions at the sidewall. The higher pressure distributions at the sidewall were caused by confinement of the steel in the sidewall of the tire.

For this research, the measured shape and size of the B-Train tire contact area and the numerical values of the measured tire pressure (stress) distributions were used as inputs into an FEM structural response model.

Figure 4.10 shows a numerical example of the measured tire-pavement contact pressure distributions (in kPa) used as input into the FEM. The numerical pressure distributions were obtained from the pressure mat scans at the B-Train, Drive axle, A1N tire load and 690 kPa tire pressure.

FIGURE 4.10: Measured Tire-Pavement Contact Pressure Distribution (in kPa) used as Input into FEM for B-Train Drive Axle at A1N Load and 690kPa Tire Pressure

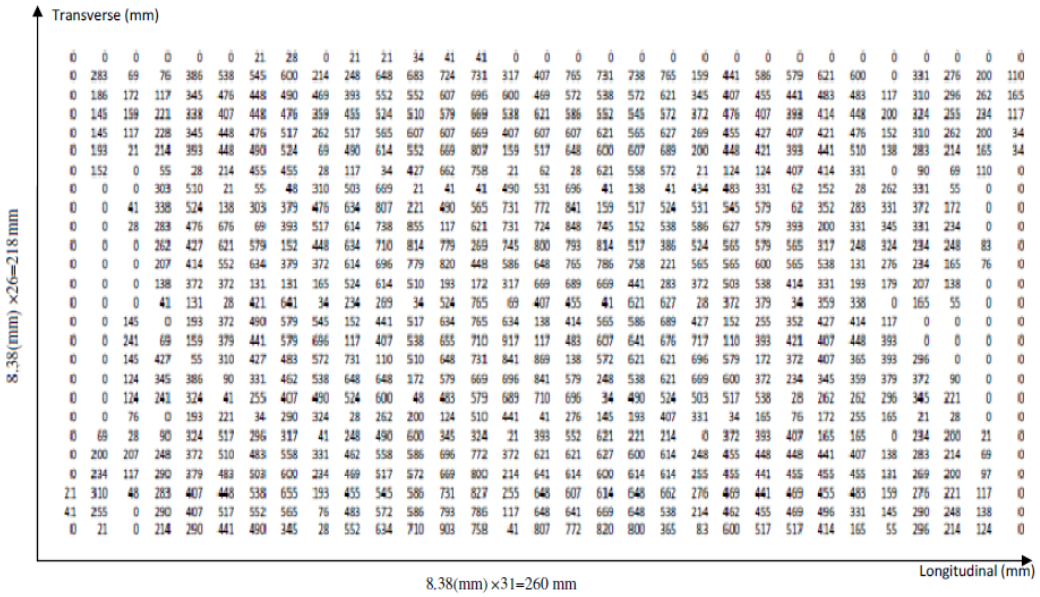

Each numerical value in Figure 4.10 represented a stress distribution element in the contact area at the load and tire pressure. The dimension of each element was 8.38 mm by 8.38 mm and was based on the pressure mat setting. The area of each element was 70.2 mm^2. The total number of elements on the pressure mat was 806, with 31 elements in the longitudinal direction (with traffic) and 26 elements in the transverse direction (perpendicular to traffic). The dimension of the contact area was 218 mm by 260 mm.

ADDITIONAL FIELD TESTING

During the 2009 field testing, pavement deflection testing was conducted at the Manitoba sites using a Falling Weight Deflectometer (FWD). The FWD testing was conducted on

the same days as B-Train trafficking to ensure that the pavement responses were taken under similar moisture and temperature conditions.

The FWD deflections were taken directly on the strain gauges and at 300 mm offset from the strain gauges. FWD deflections at a standard load of 40 kN were used to back-calculate the in-situ resilient modulus for each pavement layer.

Pavement temperature and moisture content were continuously measured in the base and subgrade layers during the 2009 spring testing. The layer temperatures and moisture contents were measured from the thermocouples and TDR sensors installed at the sites.

Rutting and fatigue cracking distresses were measured on PTH 11 and PR 304. Rut depths were obtained from MIT in June 2010. The rut depths were measured using a high-speed, Class 1, laser profiler which measured the transverse depression in the wheelpaths of each lane at highway speed. A manual fatigue cracking survey was conducted in October 2010 using the SHRP procedure in the 'Distress Identification Manual for the Long Term Pavement Performance Project Protocol [SHRP, 2001]. The extent of fatigue cracking in the wheelpaths was mapped over 150 meters of representative sections of each roadway.

INVENTORY OF PAVEMENT RESPONSE AND FIELD DATA FOR MANITOBA SITES

Table 4.8 presents an inventory of the pavement response and field data selected for the Manitoba sites. The data included longitudinal and transverse strains at the bottom of the surface layers, vertical deformations at the top of the subgrade, back-calculated layer

modulus, laboratory AC layer moduli, layer moisture content and temperature, FWD pavement deflections, and fatigue cracking and rutting distresses.

Table 4.8: Inventory of Pavement Response and Field Data at Manitoba sites

Roadway	Road Structure	Selected Field Data
PTH 11	130 mm AC 335 mm Base Clay Subgrade	Pavement Response • Horizontal Strains (Longitudinal and transverse strains at bottom of AC and AST layers) • FWD Deflection (Back-calculation of AC, Base, Subgrade Modulus) • MDD Deflection (Subgrade) • Lab AC Modulus Environmental • Pavement Moisture Content (Base, Subgrade) • Pavement Temperature (Base, Subgrade) Pavement Distress • Fatigue Cracking • Wheelpath Rutting Vehicle • Tire Pressure Distribution and Contact Area • Axle group loads • Tire loads
PR 304	30 mm AST 200 mm Base 500 mm Rock Subbase Clay Subgrade	

4.2 MNROAD TEST SITES, TEST VEHICLE, AND DATA COLLECTION

The field data from seven flexible pavements at the Minnesota Road Research facility (MnROAD) low volume road were also selected for evaluation under real loads during the SWR period, and to validate model predictions. The MnROAD flexible pavements were instrumented with structural response and environmental sensors at the time of construction and were based on a 5-year accelerated design life. MnROAD collected data from the pavement construction to end of pavement life.

Built in 1994 by the Minnesota Department of Transportation (MnDOT), the MnROAD test facility was designed to investigate pavement performance under real traffic, environment, and materials conditions and to validate prediction models with field performance data. The facility is a cold region laboratory with instrumented asphalt and concrete pavements at the site. MnROAD is located 64 kilometers northwest of Minneapolis, on I-94 near Albertville, Minnesota [Cline and Worel, 2009].

The MnROAD facility consists of a mainline interstate roadway and a low volume road loop. The mainline and low volume roads are divided into test cells representing varying combinations of materials and designs.

The mainline roadway is a 5.6 kilometers long section of high volume traffic diverted from Interstate I-94. The low volume road is a two-lane, 4.0 kilometer closed loop, trafficked by a controlled 5-axle tractor semi trailer.

Figure 4.11 shows the MnROAD test facility with the low volume road loop and mainline I-94 roadways.

Figure 4.11: MnROAD Test Facility [after Cline and Worel, 2009]

The low volume road was originally constructed with 20 asphalt and concrete cells of varying lengths, and combinations of materials and designs. The numbers of cells have increased to 24, as original cells were replaced at the end of their design life and reconstructed with different designs and materials and given new cell designations.

Figure 4.12 shows the layout of the low volume road test cells at the MnROAD facility. The layout shows the number designation of each cell and where original cells were replaced and re-numbered with new cell designations.

Figure 4.12: Layout of Low Volume Road Test Cells at MnROAD Facility [after MnROAD, 2009]

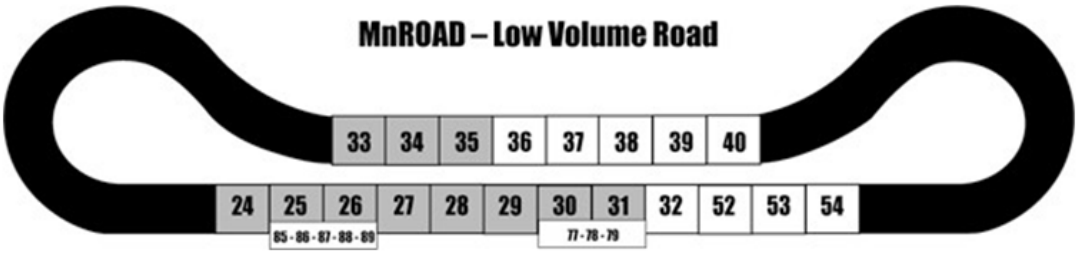

MnROAD collects pavement materials, dynamic response, and performance data from the pavements and makes the data available through the MnROAD database. The MnROAD database includes, but is not limited to, static and dynamic strain response data, material laboratory test results, and field distress surveys.

Field data was requested for selected flexible pavements from the MnROAD low volume road and used for this thesis.

MNROAD FLEXIBLE PAVEMENTS CELLS

Seven flexible pavement cells were selected from the MnROAD low volume road for analysis. The cells were chosen during a site visit at the facility on October 15, 2009. The selection was based on pavement structures and subgrade types similar to the Manitoba sites. The selection was also based on cells that had data over a complete history of failure, from construction to demolition.

The selected pavement structures along with their asphalt binder types, classes of aggregate bases and subgrade profiles were obtained from the MnROAD database [MnROAD, July 2010]. The flexible pavements consisted primarily of asphalt concrete (AC) surface on granular base on subgrade; asphalt surface treated (AST) surface on granular base on subgrade; and stabilized road mix asphalt surface on granular base on subgrade.

The asphalt binder in the AC mixes was the standard MnDOT 120/150 penetration asphalt. MnDOT also graded the asphalt binders using the newer Performance Graded (PG) system developed and implemented in 2002 under the US Strategic Highway Research Program [NCHRP, 2007]. The PG grade is a system of test method and specifications based on the high and low pavement temperatures under which the asphalt binder is expected to perform. The system was designed to control rutting at high temperature, fatigue cracking at intermediate temperature, and thermal cracking at low temperature, at selected levels of reliability. MnROAD graded the asphalt binder in the selected asphalt pavement cells at PG58-28, or high pavement temperature up to 58^{o}C and to a low temperature of -28^{o}C, at 95% reliability. It should be noted that rutting and fatigue cracking in asphalt mixtures are also dependent on the aggregate type, density, and thickness of the AC layer.

The granular bases for the MnROAD cells were either crushed stone or granular material conforming to MnDOT aggregate base classes; Class 5, Class 6, and crushed stone specifications. The Class 5 granular bases were sandy gravel, with 6% fines passing the 75 um sieve, maximum dry density of 2,130 kg/m^3 and optimum moisture content of 8%. Class 6 granular bases were sandy gravel, with 5% fines passing the 75 um sieve,

maximum dry density of 2,032 kg/m^3, and optimum moisture content of 7%. The crushed stone bases had maximum dry density of 1,952 kg/m^3 and optimum moisture content of 6%. MnDOT considered the Class 6 granular bases as the strongest and least susceptible to changes in moisture content.

The subgrade at the MnROAD site is a low strength silty-clay with California Bearing Ratio (CBR) of 1 to 2, and AASHTO soil classification of A-6. Similar to the subgrades at the Manitoba sites, the MnROAD A-6 subgrade is considered as a fair to poor embankment construction material [Yoder and Witczak, 1975].

Figure 4.13 shows the MnROAD pavement structures. The schematic shows the seven flexible pavement cells, layer thicknesses, construction and demolition dates, cell lengths, and experimental design life.

Figure 4.13: MnROAD Pavement Structures

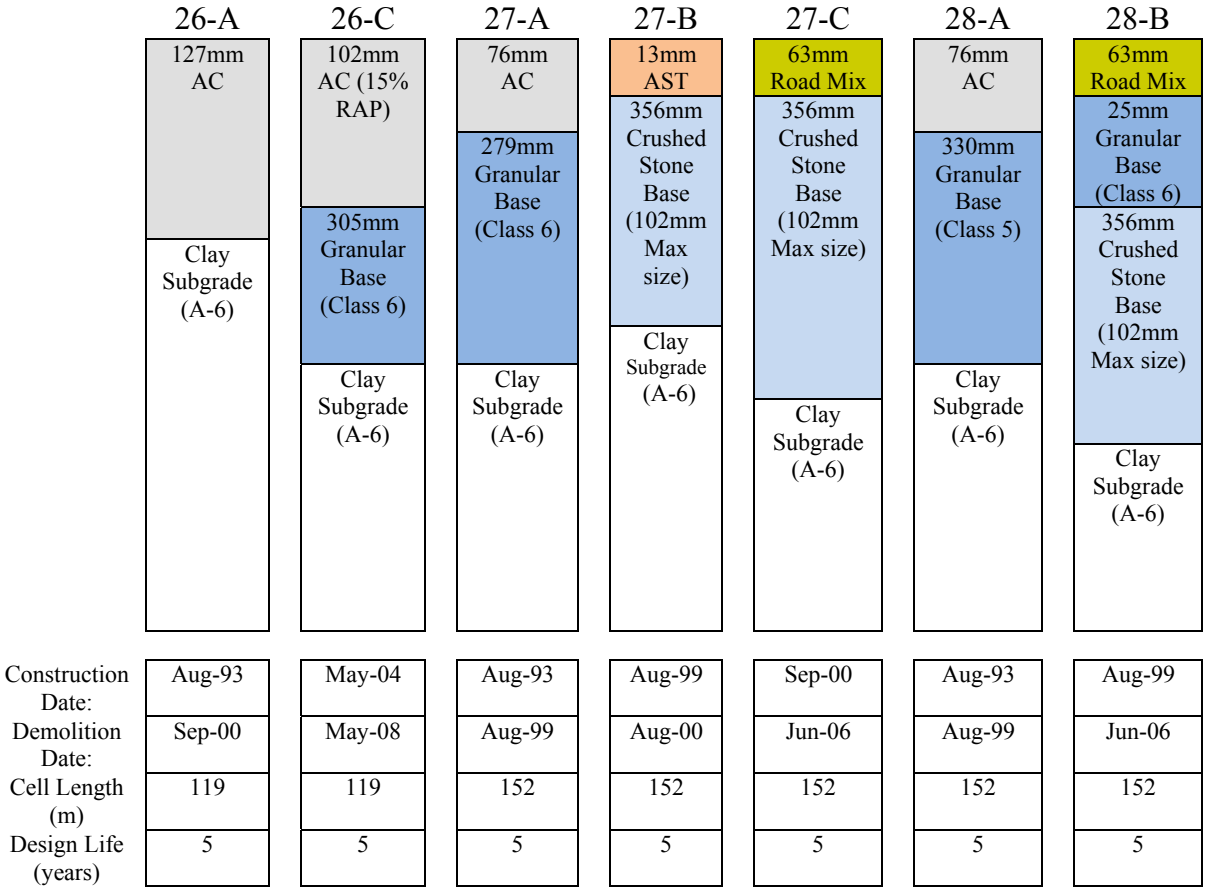

Note: AC=Asphalt Concrete, RAP=Recycled Asphalt Product, AST=Asphalt Surface Treatment

MnROAD numbered and designated each flexible pavement cell by 'A' indicating the original construction, 'B' indicating the second re-construction, and 'C' indicating the third re-construction of the pavement at that location. The seven flexible pavements were built between 1993 and 2000, and demolished between 1999 and 2006.

MnROAD constructed each pavement cell on the low volume road with a driving (inside) lane and a passing (outside) lane. The driving and passing lanes of each cell had the same structures, material types, and layer thicknesses.

MNROAD TEST SITE INSTRUMENTATION

MnROAD instrumented the flexible pavements on the low volume road with structural response gauges and environmental sensors to provide pavement data under real loads and road conditions. The instrumentation included asphalt embedment strain gauges, dynamic soil pressure cells, and thermocouple gauges embedded throughout the pavement and subgrade layers of each cell.

The asphalt embedment strain gauges (Dynatest Model 2AC) were installed at the bottom of the AC layers in the driving and passing lanes of each cell to measure longitudinal and transverse strains due to loading. The asphalt strain gauges consists of electrical resistance gauges embedded in fiber reinforced epoxy, with transverse steel anchors at each end. The gauges were oriented longitudinally (LE) in the direction of traffic, and transversely (TE) perpendicular to the direction of traffic.

Dynamic soil pressure gauges (PK) (Kulite Model 0234) were installed at the top of the subgrade, and to various depths into the subgrade, to measure vertical pressures on the subgrade due to loading. The PK gauge is a soil stress cell consisting of a liquid-filled hollow steel cell, with an electrical transducer housed within the cell. The pressure cell responded to changes in pressure applied to the surface of the sensor by the material in which the sensor was embedded [MnROAD, 2010].

Thermocouples (TC) and Time Domain Reflectometers (TDR) were installed at various depths under the pavement to measure temperatures and moisture content throughout the structure.

Figure 4.14 shows the asphalt strain gauge and dynamic soil pressure gauge used at the MNROAD facility. Figure 4.14 (b) shows the asphalt strain gauge installation at the bottom of the asphalt layer of the pavement.

Figure 4.14: Asphalt Strain Gauge and Dynamic Soil Pressure Gauge Used at MnROAD Facility [after MnROAD, 2010]

(a) Asphalt Strain Gauge

(b) Asphalt Strain Gauge Installation

(c) Dynamic Soil Pressure Cell (PK)

MnROAD installed the asphalt strain gauges and soil pressure gauges at three locations in the wheelpath of the driving and passing lanes. The sensors were located at the inside edge of the wheelpath and designated with the suffix '1', the center of the wheelpath

and designated with the suffix ‘2’, and the outside edge of the wheelpath and designated with the suffix ‘3’.

Figure 4.15 shows the sensor layout and designations in the outer wheelpath of the MnROAD lane. The schematic shows the longitudinal (LE) and transverse (TE) asphalt strain gauges and soil pressure gauges (PK) in the three rows of the wheelpath in the driving lane. The sensors were installed approximately 304 mm apart across the wheelpath, and at various distances along the lane.

Figure 4.15: Sensor Layout and Designations in Outer Wheelpath of MnROAD Lane

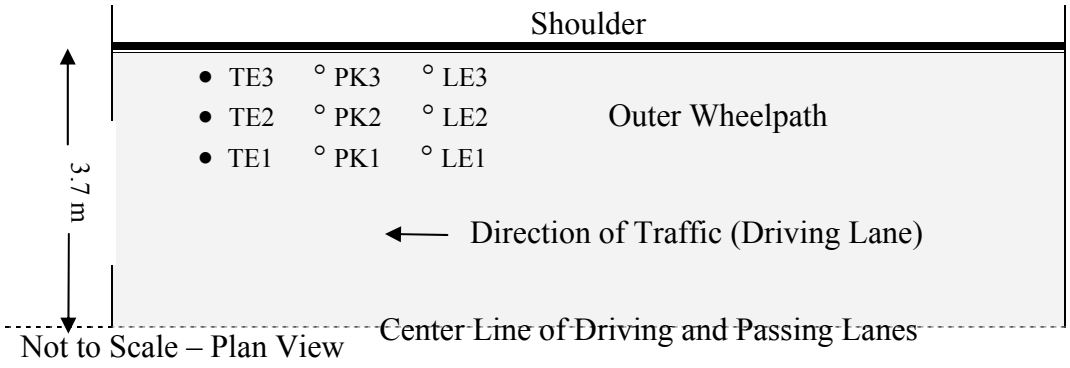

Note: TE=Transverse asphalt strain gauge, LE=Longitudinal asphalt strain gauge, PK=Soil pressure gauge

The same layout convention was used for sensor installations in the passing lane. However the designations of sensors located at the inside edge of the wheelpath were designated with the suffix ‘4’, sensor at the center of the wheelpath were designated with the suffix ‘5’, and sensors at the outside edge of the wheelpath designated with the suffix ‘6’.

Table 4.9 presents the pavement sensor types and average sensor depths in the MnROAD low volume cells. The strain gauges (LE/TE) and pressure sensors (PK) data were available only for Cells 26-A, Cell 27-A, and Cell 28-A. The depth of the sensors varied with the pavement structure, type of instrumentation, and responses required at specific locations in the structure. Details of the sensor layout and depths for each cell can be found in Appendix E.

Table 4.9: Pavement Sensor Types and Depths in MnROAD Low Volume Cells

Cell	Sensors	Average Sensor Depths from Pavement Surface (mm)	
		80KIP Driving Lane	102KIP Passing Lane
26-A	LE/TE	156/165	134/135
	PK	199	179
27-A	LE/TE	72/82	79/86
	PK	378	378
28-A	LE/TE	Na/84	Na/86
	PK	Na	Na

Note: LE= Longitudinal asphalt strain gauge, TE=transverse Asphalt Strain Gauge, PK=Soil pressure gauge, Na=data not available

MnROAD manually collects pavement response data from the embedded sensors in each cell during the early spring, late spring, summer, and fall of each year. Minnesota defines early spring as when the thawing index (TI) reaches 15^{o}C-days, which is a when spring load restriction levels in Minnesota are in place. The TI is the cumulative number of average daily air temperature above 0^{o}C, after the winter freeze. During the early spring, the base is thawing but the subgrade is frozen. The early spring ends 28 days after the TI reaches 15^{o}C-days. Minnesota defines late spring as the end of early spring and the period when the subgrade thaws. Late spring ends when the average 3-day mean daily air temperature is

greater than 17°C. Minnesota uses a reference temperature to account for the increasing intensity of the sun during the spring thaw period. As the sun's daily duration and intensity increases the air temperature at which thawing may occur in the pavement's structure reduces [Ovik et al, 2000].

Table 4.10 presents the Minnesota criteria for determining the early and late spring. The early and late spring layer modulus, relative to the fall standard modulus, is also presented.

Table 4.10: Minnesota Criteria for Determining Early and Late Spring

Minnesota Criteria for Early and Late Spring		
Duration	Early Spring	Late Spring
	Base thaws, Subgrade frozen	Base recovers, Subgrade thaws
Start	TI>15°C_Days	End of early Spring
End	Approximately 28 days	3-day T_{avg}>17°C
Layer Modulus[1]		
AC	High	Standard
Base	Low	Low
Subgrade	High	Low

Note: [1]Relative to fall standard modulus [Ovik et al, 2000]
TI=thawing index
T_{avg}=average air temperature

Table 4.11 presents the early and late spring dates at the Manitoba and MnROAD sites. The dates were determined based on air temperature obtained at the sites and the Minnesota's reference temperatures and criteria for calculating thawing and freezing index [MnDOT, 2009]. The Minnesota procedure for calculating starting and ending

dates based on the thawing and freezing index is presented in Appendix G. The late spring season, as defined by Minnesota, was the period selected for the damage analysis for this thesis.

Table 4.11: Early and Late Spring Dates at Manitoba and MnROAD Sites based on Minnesota Reference Temperatures and Criteria for Calculating Thawing and Freezing Index

Minnesota Criteria	Duration	Manitoba and MnROAD Early and Late Spring Dates	
		Cell 26-A, Cell 27-A, Cell 28-A (1996)	PTH 11 and PR 304 (2009)
Early Spring[1]	Start	March 12	March 21
	End	April 8	April 17
Late Spring[2]	Start	April 8	April 17
	End	May 16	May 26
Freezing Index (FI)	Degree_Days_°C	1,230	1,790

Note: [1] TI>15°C_Days to approximately 28 days; base thaws, subgrade frozen;
[2] End of early spring to 3-day T_{avg}>17°C; base recovers, subgrade thaw
FI=freezing index
T_{avg}=average air temperature

MNROAD TEST VEHICLE

MnROAD uses a 5-axle tractor semi trailer as the control vehicle to provide known loads to test the sensor instrumentation and for long term trafficking on the low volume road.

The MnROAD semi trailer has a steering axle, tandem drive axle on the tractor, and rear tandem axle on the trailer. The tandem drive axle and trailer tandem axles are fitted with dual 11R24.5 tire size, and at the standard 690 kPa tire pressure [MnROAD, June 2009].

Figure 4.16 shows a schematic of the MnROAD 5-axle semi trailer configuration. For this thesis, the steering axle was designated as 'Steering', the tandem axle on the tractor designated as 'Drive', and the rear tandem axle on the trailer designated as 'Trailer'.

Figure 4.16: Schematic of MnROAD 5-Axle Semi Trailer Configuration [after MnROAD, June 2009]

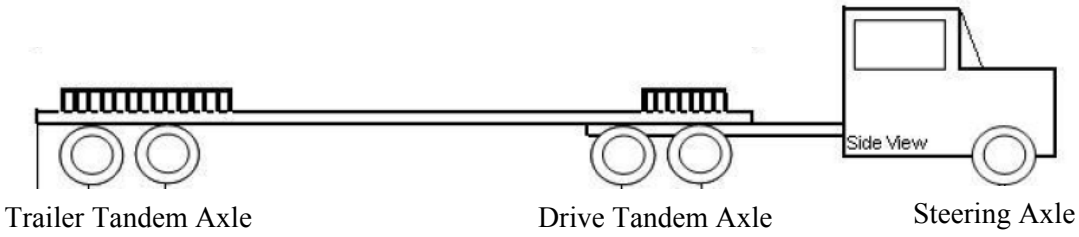

Table 4.12 presents the 5-axle semi trailer dual tire spacing and axle group spacing. The spacing was measured from center to center of each tire in the axle group. Details of the dimensions of the MnROAD 5-axle semi trailer are presented in Appendix D.

Table 4.12: 5-Axle Semi Trailer Dual Tire Spacing and Axle Group Spacing

Axle Group	Dual Tire Spacing (mm)	Axle Group Spacing (mm)
Drive Tandem	381	1320
Trailer Tandem	381	1219

MnROAD started operating the semi trailer on the low volume road on June 16, 1994. The control vehicle was driven on the loop an average 6 hours per day (80 laps per day) and 5 days per week [MnROAD, June 2009].

Figure 4.17 shows the 5-axle semi trailer trafficking on the MnROAD low volume road.

Figure 4.17: 5-Axle Semi Trailer Trafficking on MnROAD Low Volume Road

(a) 5-Axle Semi on Flexible Cell

(b) 5-Axle Semi Trailer Loading

5-AXLE SEMI TRAILER AXLE LOADS AND TIRE LOADS

MNROAD used two different semi trailer loads for trafficking on the low volume road and to measure dynamic pavement responses; a 'legal' load and a 'heavy' load.

The 'legal' semi trailer load had a GVW of 36,364 kg (80,000 lb or 80 KIP) and the 'heavy' semi trailer load had a GVW of 46,364 kg (102,000 lb or 102 KIP). The 80KIP 'legal' load was applied on the inside (driving) lane, while the 102KIP 'heavy' load was applied on the outside (passing) lane of the low volume road.

MnROAD varied the number of semi truck passes during trafficking on the 'legal' and 'heavy' lanes to produce similar numbers of equivalent single axle loads (ESALs) on both lanes. To produce this comparable number of ESALs, approximately 3 times more truck passes were made on the 'legal' lane, compared to the 'heavy' lane.

Figure 4.18 shows the layout of the 80KIP 'legal' driving lane and 102KIP 'heavy' passing lane on the MnROAD low volume road.

Figure 4.18: Layout of 80KIP 'Legal' Driving Lane and 102KIP 'Heavy' Passing Lane on MnROAD Low Volume Road

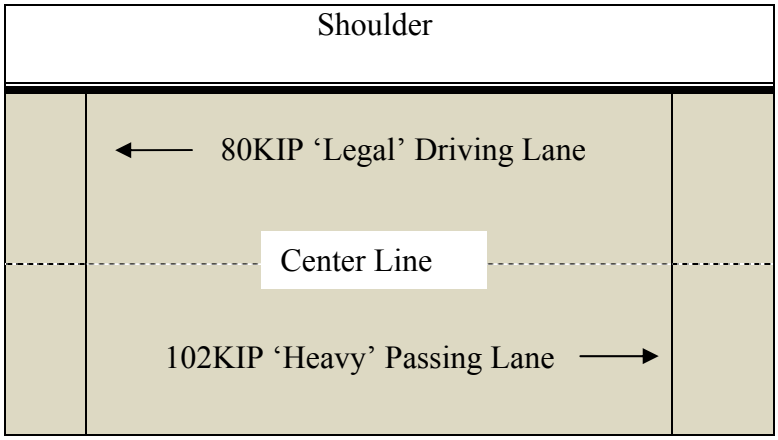

Note: Not to scale

Table 4.13 presents the 5-axle semi trailer tire load and axle group loads that were used for trafficking and dynamic testing on the low volume road.

Table 4.13: 5-Axle Semi Trailer Axle and Tire Loads used for Trafficking on MnROAD Low Volume Road

Loading	5-Axle Semi Trailer Measured Axle Weight (kg)						
	Steering		Drive		Trailer		
	Axle Load (kg)	Tire Load[1] (kg)	Axle Load (kg)	Tire Load [1] (kg)	Axle Load (kg)	Tire Load [1] (kg)	GVW[2] (kg)
Legal 80 KIP	5,454	2,727	15,455	1,932	15,455	1,932	36,364
Heavy 102 KIP	5,682	2,841	20,341	2,543	20,341	2,543	46,364

Note: [1]Tire loads calculated from measured axle load
[2]GVW=Gross Vehicle Weight

On average, the 102KIP load was 4% higher on the ‘Steering’ axle than the 80KIP load, and 31% higher on the ‘Drive’ and ‘Trailer’ tandem axles than the 80KIP load.

A comparison of the MnROAD and Manitoba maximum allowable axle loads revealed that the MnROAD 80KIP legal ‘Steering’ and ‘Drive’ axle loads were similar to the Manitoba A1N ‘Steering’ and ‘Drive’ axle loads.

MNROAD DATABASE AND INVENTORY OF SELECTED FIELD DATA

MnROAD collects, reviews, and enters pavement response, environmental, traffic loading, and distress performance data from the low volume road into an Oracle database with ancillary information in an offline database.

Table 4.14 presents an inventory of the pavement response and field data for the MnROAD cells. The data included longitudinal and transverse strains at the bottom of the surface layers, vertical pressures at the top of the subgrade, laboratory testing of layer moduli, moisture content and temperature, FWD deflections, traffic loading, and fatigue cracking and rutting distresses.

Table 4.14: Inventory of Pavement Response and Field Data for MnROAD Cells

Low Volume Road Cell	Year	Road Structure	Selected MnROAD Field Data
26-A	1993-2000	127 mm AC Clay Subgrade	Pavement Response • Horizontal Strains (Longitudinal and transverse strains at bottom of AC layer) • Vertical Subgrade Pressure • FWD Deflection • Lab Modulus (AC, Base, Subgrade) Environmental • Pavement Moisture Content (Base, Subgrade) • Pavement Temperature (Base, Subgrade) Pavement Distress • Fatigue Cracking • Wheelpath Rutting Vehicle • Axle group loads • Traffic (number of passes, ESAL)
26-C	2004-2008	102mm AC with RAP 305mm Granular Base Clay Subgrade	
27-A	1993-1999	76 mm AC 279mm Granular Base Clay Subgrade	
27-B	1999-2000	13 mm AST 356mm Crushed Stone Base Clay Subgrade	
27-C	2000-2006	63mm Road Mix 356mm Crush Stone Base Clay subgrade	
28-A	1993-1999	76 mm AC 330mm Granular Base Clay Subgrade	
28-B	1999-2006	63.5mm Road Mix 25mm Granular Base 356 mm Crush Stone Base Clay Subgrade	

Note: AC=Asphalt Concrete
RAP=Recycled Asphalt Product
FWD=Falling Weight Deflectometer
AST=Asphalt Surface Treatment
ESAL=Equivalent Single Axle Load

CHAPTER 5 - FIELD DATA TREND AND VARIABILITY ANALYSIS

An important aspect of pavement analysis is the quality, repeatability, and variability of measured field data. Reliable and consistent data are an important and necessary component to adequately model pavement behavior, calibrate structural models, and validate damage predictions.

This chapter presents the variability and trend analysis in the measured field data from the Manitoba and MnROAD flexible pavement sites. The measured traffic loads, pavement response, and distress data were analysed to verify whether the values conformed to conventional variability and trend assumptions, and therefore suitable for model calibration and validation.

The coefficient of variation (COV) was used to measure the variability of the data relative to the mean. Generally, the higher the COV, the greater is the variability and uncertainty in the data. The coefficient of variation is shown in Equation 5.1 [Groebner el al, 2008].

$$COV = \frac{\sigma}{\mu} \times 100 \qquad (5.1)$$

Where:

COV=coefficient of variation

σ = standard deviation of the data

μ = mean of the data

5.1 MANITOBA FIELD DATA TREND AND VARIABILITY

5.1.1 TRAFFIC LOADS AND ESAL TREND

The traffic and ESALs on PTH 11 and PR 304 were analysed for data trends and variability from construction to 2009. The ESALs were estimated from available truck data, since detailed truck types and loads were not available throughout the life of the pavements.

The cumulative ESALs were calculated using Equation 5.2 [AASHTO, 1993].

$$ESAL = AADT \times T \times TEF \times G \times L \times D \times d \times Y \qquad (5.2)$$

Where:

$$TEF = \sum_{i=1}^{m} p_i F_i$$

ESAL=cumulative equivalent single axle load

AADT=average annual daily traffic

T=percent trucks

TEF= Truck equivalency factor or damage of mix of axle groups and loads versus the damage of a standard 80 kN single axle load [AASHTO, 1993]

m=number of truck types in traffic stream

p=percent of truck type, *i,* in traffic stream

F_i=truck equivalent factor for truck type, i

G=growth factor $G = (1 + r)^Y$ where, r, is growth rate and, Y, is number of years

L=lane factor

D=direction factor

d=number of days per year

Y=number of years

Table 5.1 presents the estimated cumulative and design ESALs on PTH 11 and PR 304. The cumulative ESALs were calculated, from construction to 2009, using Equation 5.2 and the traffic data in Table 4.1. The estimated 20-year design ESALs are also presented.

TABLE 5.1: Estimated Cumulative and Design ESALs on PTH 11 and PR 304

Road	Estimated Cumulative ESAL from Construction	Estimated 20-Year Design ESAL
PTH 11	642,000	222,000
PR 304	178,000	95,000

For the ESAL calculations, a traffic growth rate of 1% per year was assumed. A truck equivalency factor (TEF) of 2.0 was used for the typical mix of truck types and empty/loaded trucks on PTH and PR 304 [MIT, 2009]. A direction factor of 0.5 was used to split the truck traffic in both directions of the roads. A lane factor of 1 was used since each road was undivided. The 365 days of truck operation per year were assumed for each road.

The results show PTH 11 and PR 304 exceeded their 20-year design ESAL by approximately 3 and 2 times, respectively.

5.1.2 FATIGUE CRACKING AND RUTTING DISTRESS TREND

Fatigue cracking and rutting distress data from PTH 11 and PR 304 were summarized and analysed for trends and data variability.

Table 5.2 presents the average rut depths and percent fatigue cracking in the wheelpath area of PTH 11 and PR 304. The rut depths were averaged over a distance of 5 km (2.5 km on either side of the sensor locations on PTH 11 and PR 304) from measurements taken by MIT with a high-speed, Class 1, laser profiler. The profiler measurements were taken at 10 meter increments across the outer and inner wheelpaths of each lane. The areas of fatigue cracking were manually measured using the "SHRP Distress Identification Manual for the Long Term Pavement Performance Project Protocol" [SHRP, 2001]. Fatigue cracking was measured in the outer and inner wheel path of a 150-meter length of each test lane. The 150m section was selected to be representative of the distress in the rest of the roadway as per the SHRP protocol..

TABLE 5.2: Average Rut Depths and Percent Fatigue Cracking in Wheelpath Area of PTH 11 and PR 304

Road	Average Rut Depth in Outer Wheel Path			Fatigue Cracking (% Wheelpath Area)
	Rut Depth (mm)	Standard Deviation (mm)	COV %	
PTH 11	15	5	33	6
PR 304	12	6	50	0

Note: Fatigue cracking and rut data collected in October 2010

The results show that average rut depths were higher on PTH 11 than PR 304, likely due to the higher loads and number of load repetitions on PTH 11. The variability of the rut depths on the AST surface of PR 304 was higher than on PTH 11, with a COV of 50%.

The results also show that the fatigue cracking in the wheelpath was higher on PTH 11 than on PR 304. No fatigue cracking was observed on PR 304. This is typical of thin AST surfaces which tend to exhibit rutting more than fatigue cracking.

5.1.3 MEASURED PAVEMENT STRAIN TREND

The measured longitudinal and transverse strains on PTH 11 and PR 304 were summarized and analysed for trends and data variability. The strains were measured at three B-Train axle loads, two tire pressures, and three vehicle speeds. Only strains measured at 20 km/hr were used for the trend analysis. The strains measured under the static loads exceeded the upper limits of the range of the strain gauges and were unusable. The measurements at 20km/hr were as close to static as was achievable. The strains measured at high speed (70km/hr) were also not used because the models selected for structural response predictions (applied later in the thesis) were developed for the static conditions.

Figure 5.1 shows a plot of the measured longitudinal and transverse strains at the bottom of the AC layer from one run of the B-Train axle groups during the spring testing on PTH 11. The B-Train was at RTAC load, 20 km/hr, and 690 kPa tire pressure. The shift in the transverse and longitudinal strains was due to offset of the strain gauges in the wheelpath.

Figure 5.1: Measured Longitudinal and Transverse Strains at Bottom of AC layer from B-Train Axle Groups during Spring Testing on PTH 11

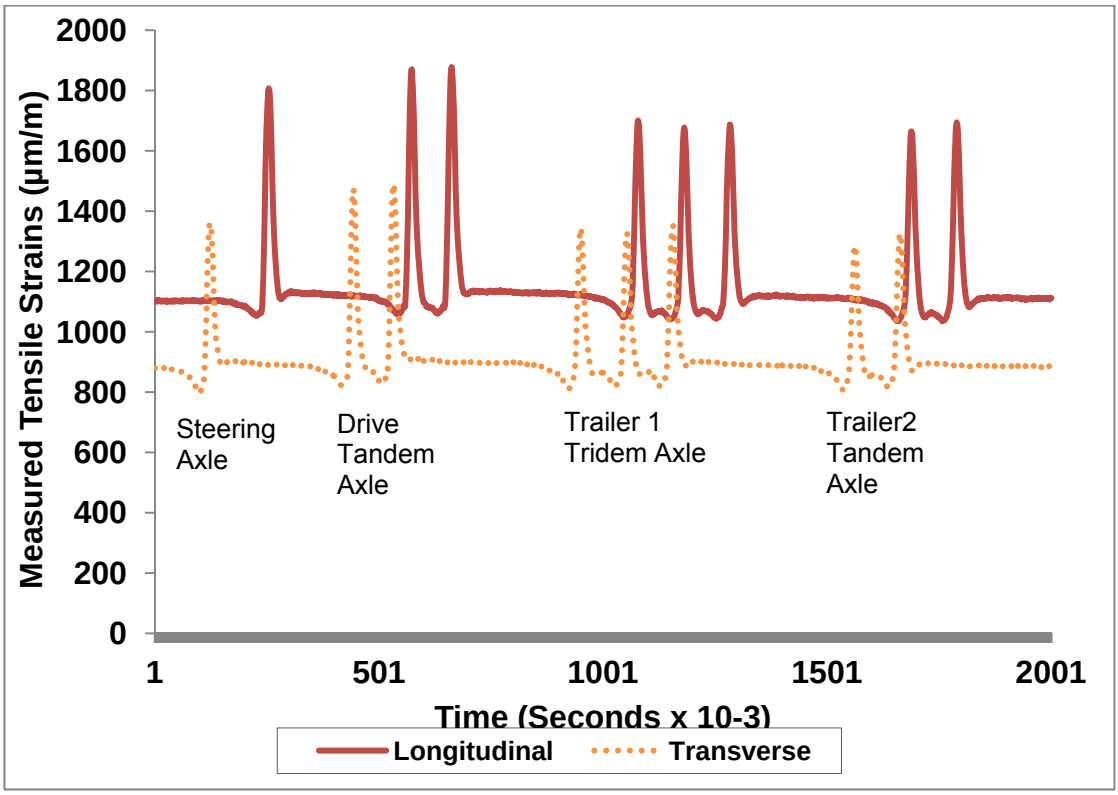

The plot shows a good representation of the strain responses for each axle group, with the 'Steering', 'Drive', 'Trailer1', and 'Trailer2' axles clearly depicted by the strain gauges.

NORMALIZED MAXIMUM MEASURED STRAINS

Tire offset or 'wander' from pavement sensors is one of the main sources of variability in vehicle testing. Bayat et al [2010] investigated the load associated responses on flexible pavements due to wheel wander at the Center for Pavement and Transportation Technology (CPATT) test track in southern Ontario. Bayat et al found that 160 mm of

wheel wander from the sensors reduced the measured longitudinal strains under the AC layer by 36%.

Since the B-Train tires did not consistently pass directly on the strain gauge during the Manitoba testing, the measured transverse and longitudinal strains on PTH 11 and PR 304 were normalized to obtain maximum measured strains at zero tire offset. A linear regression model was used to determine the relationship between the measured strains and tire 'wander', or offset, from the strain sensors. The linear relationship for this analysis was valid only for offsets less than 200 mm. For cases in which larger wheel offsets were encountered, the relationship was nonlinear and similar to the approximation of a second-order polynomial for offsets of 200 to 1000 mm as found by Timm and Priest [2004].

Figure 5.2 shows the relationship between the measured longitudinal and transverse strains versus tire offset for the B-Train at 20 km/hr and 345 kPa tire pressure on PTH 11. The linear regression equations are shown at A1L1, A1N, and RTAC loads.

Figure 5.2: Relationship between Measured Longitudinal and Transverse Strains Versus Tire Offset for B-Train at 20 km/hr and 345 kPa tire Pressure on PTH 11 [after Liu et al, 2011]

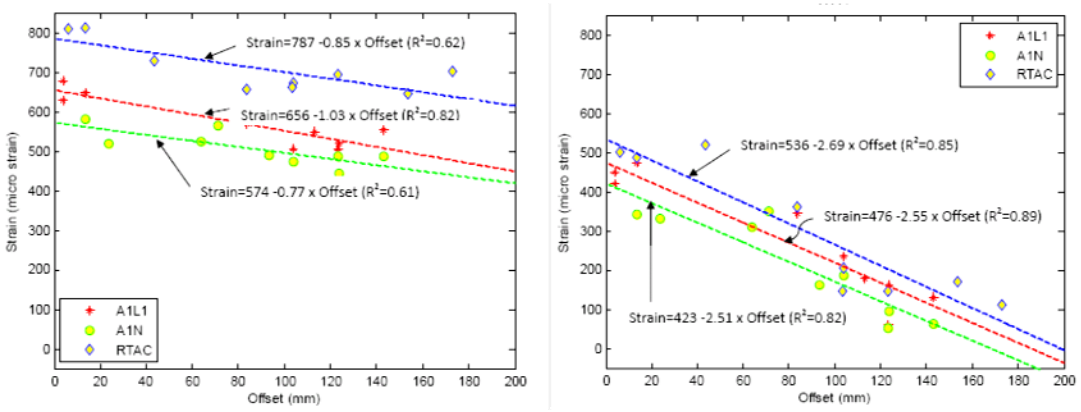

a) Longitudinal Strain gauge

b) Transverse Strain Gauge

The plots show that the transverse and longitudinal strains decreased with tire offset, for all loads. The A1L1 loads however produced higher strains than the A1N loads. This was unexpected, because heavier loads should produce higher tensile strains.

One explanation for this occurrence may have been the result of changes in pavement temperature during testing. Although the pavement temperatures were monitored closely during testing and the testing was conducted only when temperatures were similar at each test run, a 2 to 3^{o}C difference between the A1N and A1L1 tests still occurred. The lower temperature of the AC layer during the A1N testing may have resulted in a slightly higher stiffness in the AC layer and therefore lower strains at that loading. Additionally, the difference in the measured tire loads between A1L1 and A1N was approximately 10%. The small load difference between A1L1 and A1N loads may also have contributed to the lack of a clear trend in the pavement responses at those loads.

The measured strains on PTH 11 and PR 304 were normalized to a maximum strain, at zero offset, using Equation 5.3 [Liu et al, 2011]:

$$Normalized\ strain = measured\ strain + \beta \times offset \qquad (5.3)$$

Where:

β is the slope of the regression line.

The F-test statistical analysis was conducted to determine the significance of the regression parameters in the linear relationships, at the 95% confidence level, α. The null hypothesis was used to test whether the regression parameters were not statistically different from zero (H=0).

If the f-statistic was greater than f-critical at 95% confidence level, it could be concluded that the regression parameters were statistically different from zero, and could be used to predict the normalized strains. The ρ-value, or probability that f-critical is greater than f-statistic, was also calculated.

Table 5.3 shows the regression and f-test parameters for the measured longitudinal and transverse strains versus tire offset at the B-Train loads and 20 km/hr during the spring testing on PTH 11. The f-critical value was 5.59 at the 95% confidence level (α=0.05).

Table 5.3: Regression and F-test Parameters for Measured Longitudinal and Transverse Strains versus Tire Offset at B-Train Loads and 20 km/hr during Spring Testing on PTH 11 [after Liu et al., 2010]

Strain Gauge	Tire Pressure (kPa)	Load Rating	β	R^2	F-Critical	F-Statistic	Probability (ρ<0.05)	Pass/ Fail Null Hypothesis
Transverse	345	A1L1	-2.55	0.89	5.59	54.21	0.0002	Fail
		A1N	-2.51	0.82		32.42	0.0007	Fail
		RTAC	-2.69	0.85		38.79	0.0004	Fail
	690	A1L1	-4.57	0.96		150.84	0.0000	Fail
		A1N	-3.68	0.70		16.17	0.0050	Fail
		RTAC	-3.46	0.91		69.67	0.0001	Fail
Longitudinal	345	A1L1	-1.03	0.82		31.47	0.0008	Fail
		A1N	-0.77	0.61		10.99	0.0128	Fail
		RTAC	-0.85	0.62		11.30	0.0121	Fail
	690	A1L1	-2.17	0.95		129.43	0.0000	Fail
		A1N	-0.74	0.27		2.53	0.1557	Pass
		RTAC	-2.01	0.73		19.02	0.0033	Fail

The results show the β coefficients, or slope of the regression line, were consistently negative for the transverse and longitudinal strains, indicating decreased strains as tire offset increased.

The β coefficients for the transverse strains were generally higher than the corresponding longitudinal strain coefficients. This indicated a steeper slope of the regression line and that the transverse strains were more sensitive to the tire offset than the longitudinal strains. This may be due to the time of loading on the gauge and the capture rate of the sensor.

For the transverse gauge, the tire traveled perpendicular to the gauge and produced a short waveform, resulting a shorter loading time. The shorter load time resulted in lower strains. For the gauge in the longitudinal direction, the tire traveled parallel to the gauge and produced a longer waveform, resulting in a longer loading time. The longer loading time on the longitudinal gauge produced higher strains than the transverse gauge, at the same offset. This observation agreed with the findings of Willis and Timm [2008].

The f-statistics of the regression equations were greater than f-critical for all but one of the longitudinal and transverse strains. This indicated that the regression parameters were statistically different from zero, at 95% confidence level and could be used to normalize the strains. Only the f-statistic for the regression equation for the longitudinal strain at A1N and 690kPa was less than f-critical, and therefore not statistically significant at 95% confidence limit. The ρ-value also indicted that the A1N at 690kPa regression equation was not statistically significant at the 95% confidence limit. The longitudinal strains at the A1N load at 690kPa were checked but there was no obvious error found in the data.

Table 5.4 shows the regression and f-test parameters for the measured longitudinal and transverse strains versus tire offset at the B-Train loads and speed of 20 km/hr during the spring testing on PR 304.

Table 5.4: Regression and F-test Parameters for Measured Longitudinal and Transverse Strains versus Tire Offsets at B-Train Loads and 20 km/hr during Spring Testing on PR 304 [after Kavanagh et al., 2010]

Sensor	Tire Pressure (kPa)	Load Rating	β	R^2	F-Critical	F-Statistic	Probability (ρ<0.05)	Pass/ Fail Null Hypothesis
Transverse	345	B1L2	-	-	5.59	-	-	-
		B1N	3.09	0.51		8.228	0.0240	Fail
		A1N	5.11	0.80		24.343	0.0026	Fail
	690	B1L2	1.66	0.15		1.052	0.3445	Pass
		B1N	3.79	0.62		11.529	0.0115	Fail
		A1N	4.50	0.82		28.266	0.0011	Fail
Longitudinal	345	B1L2	-	-		-	-	-
		B1N	-0.94	0.62		10.965	0.0129	Fail
		A1N	-0.83	0.11		0.866	0.3830	Pass
	690	B1L2	-6.52	0.65		9.762	0.0205	Fail
		B1N	-1.14	0.39		4.330	0.0759	Pass
		A1N	-1.48	0.42		4.395	0.0742	Pass

Note: '-'=not applicable, field strains not measured at this load and tire pressure

As expected, the results show the β coefficients for the longitudinal strains were consistently negative, indicating decreased strains as tire offset increased. However the signs of the β coefficients for the transverse strains were positive, indicating increased strains as tire offset increased. This was contrary to expectations, since strains typically decrease as tire offset increase. A review of the transverse strains did not indicate errors within the data.

The results also show three of the five longitudinal strain parameters and one of the five transverse strain parameters had f-statistics less than f-critical and was therefore not statistically significant at 95% confidence level. The corresponding ρ-value also indicted those parameters were not statistically significant at the 95% confidence level.

It may be argued that the longitudinal and transverse strains measured by the asphalt strain gauges in the base of the AST did not adequately characterize the strain behavior of the thin surface, making it difficult to portray the strains in a simple way.

The regression β coefficients and measured longitudinal and transverse strains were used to normalize the strains at zero offset for PTH 11 and PR 304. Equation 5.3 and the statistically significant β coefficients from Table 5.3 were used to normalize the strains for PTH 11. Equation 5.3 and the statistically significant β coefficients from Table 5.4 were used to normalize the strains for PR 304. Due to the discrepancy in the sign convention, the β coefficients for the transverse strains on PR 304 were not used to normalize the strains. Instead, the average measured transverse strains from three repeat runs of the B-Train 'Drive' axle were used to approximate the normalized transverse strains on PR 304. The 'Drive' axle produced the most consistent responses on the transverse strain sensors.

Table 5.5 presents the normalized maximum longitudinal and transverse strains and vertical strains at the B-Train loads and 20km/hr from the spring testing on PTH 11. The normalized longitudinal and transverse strains were at the bottom of the AC layer. The vertical strains were at the top of the subgrade. The subgrade strains were calculated using measured deflections from the MDD at the top of the subgrade, and divided by the length of the MDD reference head.

TABLE 5.5: Normalized Maximum Longitudinal and Transverse Strains, and Vertical Strains at B-Train Loads and 20km/hr from Spring Testing on PTH 11

Axle Group	Load Rating	Axle Load (kg)	Tire Load (kg)	Normalized Maximum Strain (μm/m)					
				Transverse[1]		Longitudinal[1]		Vertical[2]	
				20 km/hr					
				690kPa	345kPa	690kPa	345kPa	690kPa	345kPa
Steering	AlL1	4,897	2,449	680	-	756	-	n/a	n/a
	A1N	4,944	2,472	551	-	721	-	n/a	n/a
	RTAC	4,837	2,419	869	-	1000	-	n/a	n/a
Drive	A1L1	15,176	1,927	741	509	820	684	-1277	-1293
	A1N	15,192	1,930	775	530	-	621	n/a	n/a
	RTAC	17,072	2,173	586	638	941	827	n/a	n/a
Trailer1	A1L1	20,856	1,765	797	561	787	658	-1277	-1293
	A1N	21,084	1,785	586	472	-	574	n/a	n/a
	RTAC	24,504	2,079	579	589	869	777	n/a	n/a
Trailer2	A1L1	15,136	1,829	740	496	830	703	-1277	-1293
	A1N	15,392	1,924	623	422	-	598	n/a	n/a
	RTAC	16,568	2,071	615	579	948	850	n/a	n/a

Note: [1]Bottom of AC layer
[2]Top of Subgrade
n/a=data not available
'-'=not applicable, regression equation not statistically significant

The results show the normalized longitudinal strains were 15% higher on average than the normalized transverse strains, over all loads and axle groups, on PTH 11.

Table 5.6 presents the normalized maximum longitudinal and transverse strains at the B-Train loads and 20km/hr from the spring testing on PR 304. For the longitudinal and transverse strains at the bottom of the AST layer where regression equations were not

significant or the sign of β coefficients were positive, the longitudinal and transverse strains were based on the average of three repeat runs of the B-Train. Vertical strains at the top of the subgrade were not available on PR 304.

TABLE 5.6: Normalized Maximum Longitudinal and Transverse Strains at B-Train Loads and 20km/hr from Spring Testing on PR 304

Axle Group	Load Rating	Axle Load (kg)	Tire Load (kg)	Normalized Maximum Strain (μm/m)					
				Transverse[1]		Longitudinal[1]		Vertical[2]	
				20 km/hr					
				690kPa	345kPa	690kPa	345kPa	690kPa	345kPa
Steering	B1L2	4,525	2,263	n/a	n/a	n/a	n/a	n/a	n/a
	B1N	4715	2,358	n/a	n/a	n/a	n/a	n/a	n/a
	A1N	4,890	2,445	n/a	n/a	n/a	n/a	n/a	n/a
Drive	B1L2	10,576	1,322	-	-	902	-	n/a	n/a
	B1N	13,904	1,738	475[3]	450[3]	725[3]	473	n/a	n/a
	A1N	15,224	1,903	590[3]	550[3]	769[3]	478[3]	n/a	n/a
Trailer1	B1L2	14940	1,245	-	-	681	-	n/a	n/a
	B1N	17,700	1,475	-	-	722[3]	459	n/a	n/a
	A1N	21,108	1,759	-	-	688[3]	574[3]	n/a	n/a
Trailer2	B1L2	10,104	1,263	-	-	696	-	n/a	n/a
	B1N	14,072	1,650	-	-	653[3]	429	n/a	n/a
	A1N	15,392	1,924	-	-	640[3]	496[3]	n/a	n/a

Note: [1]Bottom of AST layer
[2]Top of Subgrade
[3] Values based on average of three repeat runs.
n/a=data not available
'-'=not applicable, regression equation not statistically significant

Figure 5.3 illustrates the normalized maximum longitudinal and transverse strains (given in Table 5.5) for the B-Train loads and 20km/hr spring testing on PTH 11. The graph

shows the longitudinal strains consistently higher than the transverse strains, over all loads and tire pressures.

Figure 5.3: Normalized Maximum Longitudinal and Transverse Strains from B-Train Loads and 20km/hr Spring Testing on PTH 11

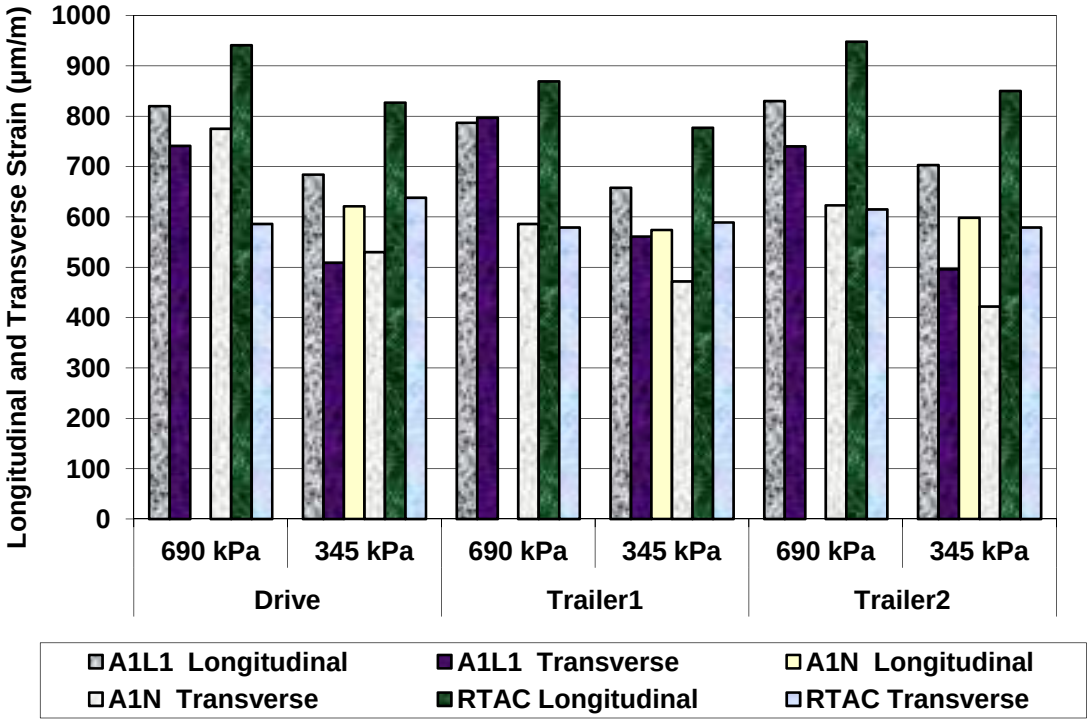

Figure 5.4 illustrates the normalized maximum longitudinal and transverse strains (given in Table 5.6) from the B-Train loads and 20km/hr spring testing on PR 304. The graph shows an inconsistent trend between longitudinal and transverse strains on PR 304, where the longitudinal strains were not always higher than the transverse strains.

Figure 5.4: Normalized Maximum Longitudinal and Transverse Strains from B-Train Loads and 20km/hr Spring Testing on PR 304

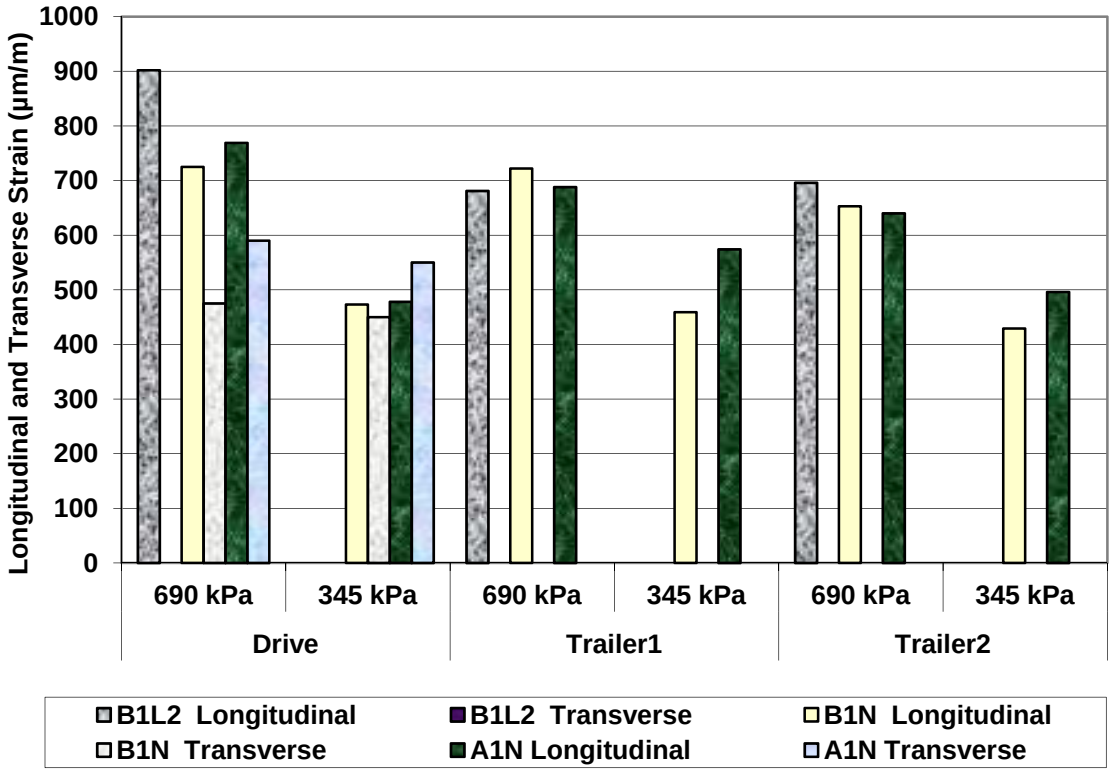

In general, the trend analysis of the PTH 11 data indicated the measured longitudinal and transverse at the bottom of the AC layer, and vertical strains at the top of the subgrade were suitable for calibrating structural response models in this thesis.

However, the trend analysis of the PR 304 data indicated that the measured longitudinal and transverse strains under the AST surface were not considered suitable. The discrepancies in the trends in the tensile strains obtained under the AST did not appear to adequately characterize the behavior of that pavement.

Since fatigue cracking was not observed on the AST surface of PR 304, and this type of pavement tends to fail in rutting rather than in fatigue, the measured longitudinal and transverse strains on PR 304 were not used for further analysis in this thesis.

5.2 MNROAD FIELD DATA TREND AND VARIABILITY

A trend analysis was conducted of the measured field data from the MnROAD low volume road. Annual and cumulative 5-axle semi loads, rut depths, fatigue cracking, and pavement strain data obtained from construction to demolition, were analyzed for trends and data variability. The analysis was conducted to determine the suitability of the MnROAD data in developing local damage models, and to determine whether the data trends observed for the MnROAD pavements were appropriate for Manitoba conditions.

5.2.1 TRAFFIC LOADS AND ESAL TREND

Table 5.7 presents the annual and cumulative 5-axle semi trailer loads and ESAL repetitions on the 80KIP and 102KIP lanes of MnROAD Cell 26, Cell 27, and Cell 28.

MnROAD calculated the ESALs and truck equivalency factors (TEF) using the 1993 AASHTO Design Guide [AASHTO, 1993]. The AASHTO methodology accounts for the pavement structure, pavement terminal serviceability, and truck axle configuration and weight in the calculation. The 5-axle semi loads were applied and recorded from construction to demolition of each pavement cell.

Table 5.7: Annual and Cumulative 5-Axle Semi Trailer Loads and ESAL Repetitions on 80KIP and 102KIP Lanes of MnROAD Cell 26, Cell 27 and Cell 28

Pavement Age[1] (Years)		Annual Number of Truck Loads and ESAL Repetitions							Total Cumulative Repetitions
		1	2	3	4	5	6	7	
Cell		80KIP Lane							
26-A	Loads	-	8,265	8,479	9,140	7,361	5,666	8,177	47,088
	ESALs	-	19,430	19,937	21,487	17,300	13,262	19,282	110,698
26-C	Loads	3,924	6,365	6,410	3,917	-	-	-	20,616
	ESALs	9,222	14,959	15,074	9,213	-	-	-	48,468
27-A	Loads	-	8,265	8,479	9,140	7,361	5,642	-	38,887
	ESALs	-	19,430	19,937	21,487	17,300	13,262	-	91,416
27-B	Loads	7,637	-	-	-	-	-	-	7,631
	ESALs	17,956	-	-	-	-	-	-	17,956
27-C	Loads	9,818	8,268	6,372	4,849	5,711	4,906	-	39,924
	ESALs	23,076	19,438	14,977	11,397	13,423	11,529	-	93,840
28-A	Loads	-	8,265	8,479	9,140	7,361	5,642	-	38,887
	ESALs	-	19,430	19,937	21,487	17,300	13,262	-	91,416
28-B	Loads	8,201	9,291	8,009	6,624	5,398	5,513	5,134	48,170
	ESALs	19,282	21,837	18,829	15,569	12,717	12,930	12,064	113,228
		102KIP Lane							
26-A	Loads	-	2,804	3,073	2,515	1,435	2,323	2,188	14,338
	ESALs	-	19,628	21,511	17,605	10,045	16,261	15,316	100,366
26-C	Loads	1,371	2,206	1,913	57	-	-	-	5,547
	ESALs	9,597	15,442	13,391	399	-	-	-	38,829
27-A	Loads	-	2,804	3,073	2,515	1,435	2,323	-	12,150
	ESALs	-	19,628	21,511	17,605	10,045	16,261	-	85,050
27-B	Loads	2,041	-	-	-	-	-	-	2,041
	ESALs	14,287	-	-	-	-	-	-	14,287
27-C	Loads	3,044	1,787	1,726	1,501	1,965	1,760	-	11,783
	ESALs	21,308	12,509	10,976	11,613	13,755	12,320	-	82,481
28-A	Loads	-	2,804	3,073	2,515	1,435	2,323	-	12,150
	ESALs	-	19,628	21,511	17,605	10,045	16,261	-	85,050
28-B	Loads	2,188	2,979	1,852	1,493	1,734	1,806	1,919	13,971
	ESALs	15,316	20,853	12,964	10,451	12,138	12,642	13,433	97,797

Note: [1] Number of years after construction
'-'=not applicable, no semi loads applied
Cell 26-A - 127 mm AC, clay subgrade
Cell 26-C - 102 mm AC, 305 mm granular base Class 6, clay subgrade
Cell 27-A - 76 mm AC, 279 mm granular base Class 6, clay subgrade
Cell 27-B – 13 mm AST, 356 mm crushed stone base, clay subgrade
Cell 27-C - 63 mm road mix, 356 crushed stone base, clay subgrade
Cell 28-A - 76 mm AC, 330 mm granular base Class 5, clay subgrade
Cell 28-B – 63 road mix, 25 mm granular base Class 6, 356 crushed stone base, clay subgrade

The results show that the traffic sustained by each pavement structure at demolition was significantly different, despite each cell having the same 5-year design.

For the 80KIP lane, an average 7,200 semi trailer loads were applied annually on the lane. Cell 26-A and Cell 28-B had the highest total cumulative semi trailer loads at approximately 50,000. Cell 27-B, which failed after the first year of trafficking, had the lowest total cumulative semi trailer loads at approximately 8,000.

For the 102KIP lane, an average 2,200 semi trailer loads were applied annually on the lane. Cell 26-A and Cell 28-B had the highest total cumulative semi trailer loads at 15,000. Cell 27-B had the lowest total cumulative semi trailer loads at 2,000. Approximately one third the numbers of semi trailer loads were applied on the 102KIP lane, compared to the 80KIP lane.

While the numbers of semi trailer loads were different on the 80KIP and 102KIP lanes, the ESAL repetitions were similar on the lanes. There was an average 16,900 ESAL repetitions applied annually on the 80KIP lane, and an average 15,400 ESAL repetitions applied annually on the 102KIP lane. MnROAD used a TEF of 2.35 for the 80KIP semi trailer load, and TEF of 7.0 for the 102KIP semi trailer load to calculate the ESAL repetitions on each lane. The ratio of the TEF indicates that each 102KIP semi trailer load was estimated to be 3 times more damaging than the 80KIP semi trailer load.

Figure 5.5 and Figure 5.6 illustrates the cumulative 5-axle semi trailer ESAL repetitions versus pavement age (given in Table 5.7) on the 80KIP and 102 KIP lanes, respectively, of MnROAD Cell 26, Cell 27, and Cell 28.

Figure 5.5: Cumulative 5-Axle Semi Trailer ESAL Repetitions versus Pavement Age on 80KIP Lane of MnROAD Cell 26, Cell 27, and Cell 28

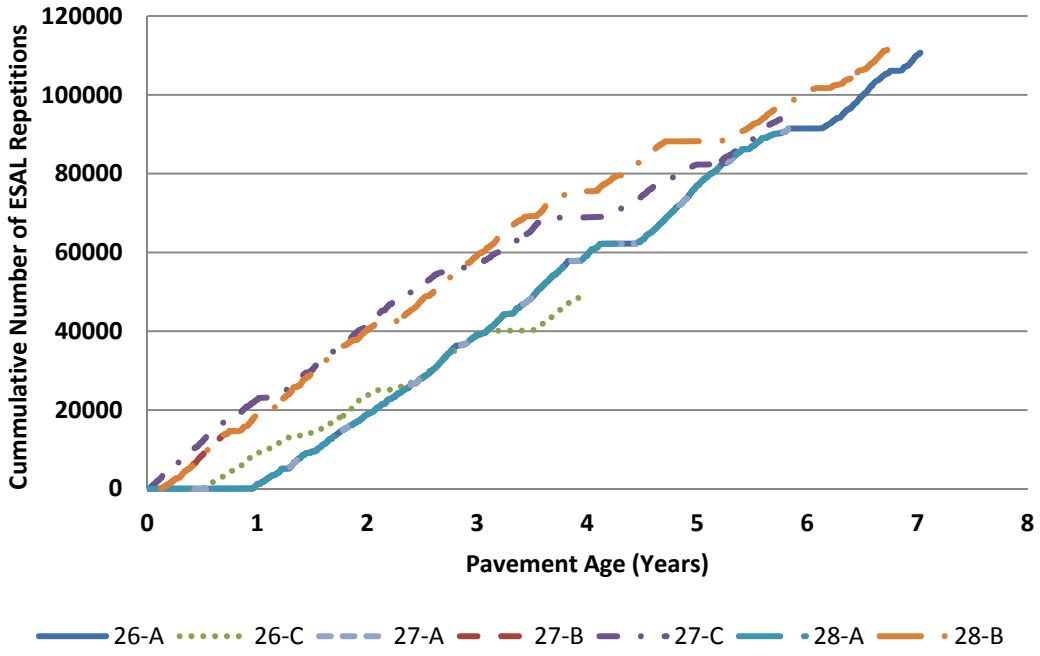

Figure 5.6: Cumulative 5-Axle Semi Trailer ESAL Repetitions versus Pavement Age on 102KIP Lane of MnROAD Cell 26, Cell 27, and Cell 28

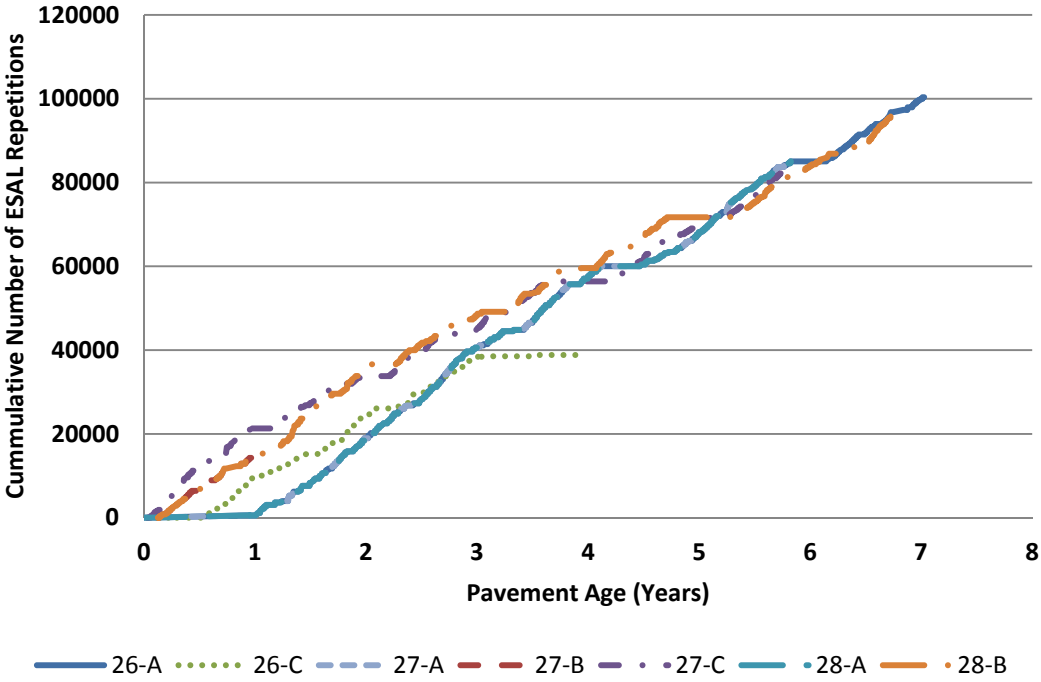

The plots show similar magnitudes of ESAL repetitions on the 80KIP and 102KIP lanes, (as per the MnROAD experimental design) even though the semi load repetitions on each lane were different. Due to the same magnitude of ESALS and assuming the correct AASHTO TEF, comparisons of the performance of the 80KIP and 102KIP lanes were made for this analysis.

5.2.2 FATIGUE CRACKING AND RUTTING DISTRESS TREND

The measured rut depths and percent fatigue cracking on the MnROAD pavement cells were summarized and analysed for trend and data variability. MnROAD mapped and recorded rut depths and fatigue cracking annually on each pavement cell, from construction to demolition.

RUTTING DISTRESS TREND

Table 5.8 presents the average rut depths versus pavement age in the outer wheelpath of the 80KIP and 102KIP lanes on MnROAD Cell 26, Cell 27, and Cell 28. The rut depths in the outer wheelpath of the lane were selected because rutting was higher in the outer wheelpath than the inner wheelpath. The average rut depths were measured with a 1.83-meter straight edge across the wheelpath of each lane, and at 10-meter increments along the length of the pavement cell. The standard deviation (STD) of the rut depth over the length of the cell is also shown.

Table 5.8: Average Rut Depths versus Pavement Age in Outer Wheelpath of 80KIP and 102KIP Lanes on MnROAD Cell 26, Cell 27, and Cell 28

		Average Rut Depths in Outer Wheelpath (mm)							Final Rut Depth
Pavement Age (Years)		**1**	**2**	**3**	**4**	**5**	**6**	**7**	
Cells					80KIP Lane				
26-A	Mean	-	8	8	10	9	14	10	10
	STD		1	1	2	1	2	3	
26-C	Mean	6	9	10	10	-	-	-	10
	STD	2	3	3	3				
27-A	Mean	-	9	11	15	18	19	-	19
	STD		1	1	1	3	4	-	
27-B [1]	Mean	>13	-	-	-	-	-	-	>13
	STD								
27-C	Mean	5	4	5	-	-	-	-	5
	STD	2	2	3					
28-A	Mean	-	12	16	20	22	21	-	21
	STD		0	1	6	4	8		
28-B	Mean	9	13	10	12	-	-	-	12
	STD	5	5	2	1				
					102KIP Lane				
26-A	Mean	-	9	12	13	11	11	11	11
	STD		2	2	2	2	5	3	
26-C	Mean	7	11	12	11	-	-	-	11
	STD	2	3	2	2				
27-A	Mean	-	6	8	11	14	13	-	13
	STD		1	1	1	5	3	-	
27-B [1]	Mean	>13	-	-	-	-	-	-	>13
	STD								
27-C	Mean	10	10	12	-	-	-	-	12
	STD	3	3	3					
28-A	Mean	-	9	12	17	16	18	-	18
	STD		1	1	2	5	5		
28-B	Mean	9	11	13	14	-	-	-	14
	STD	3	4	5	4				

Note: [1]Cell 27-B failed within first year,
STD=standard deviation
'-'=not applicable, rut data not measured
Cell 26-A - 127 mm AC, clay subgrade
Cell 26-C - 102 mm AC, 305 mm granular base Class 6, clay subgrade
Cell 27-A - 76 mm AC, 279 mm granular base Class 6, clay subgrade
Cell 27-B – 13 mm AST, 356 mm crushed stone base, clay subgrade
Cell 27-C - 63 mm road mix, 356 crushed stone base, clay subgrade
Cell 28-A - 76 mm AC, 330 mm granular base Class 5, clay subgrade
Cell 28-B – 63 road mix, 25 mm granular base Class 6, 356 crushed stone base, clay subgrade

Figure 5.7 and Figure 5.8 show the average rut depths versus pavement age (given in Table 5.8) on the 80KIP and 102KIP lanes, respectively, of MnROAD Cell 26, Cell 27, and Cell 28. The rutting failure limit of 12.5 mm rut depth is shown in the plots.

Figure 5.7: Average Rut Depths versus Pavement Age on 80KIP Lane of MnROAD Cell 26, Cell 27, and Cell 28

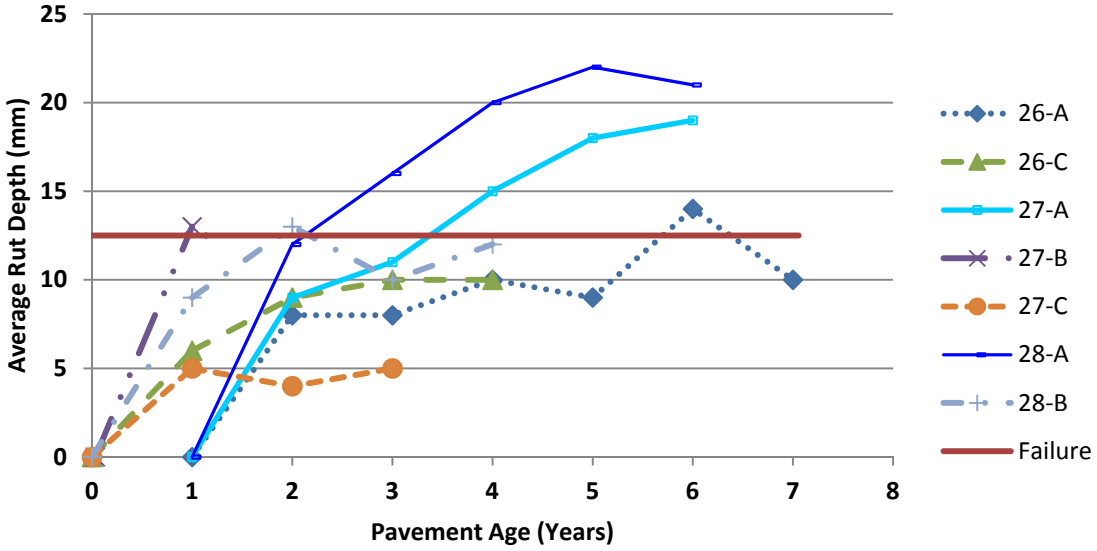

Figure 5.8: Average Rut Depths versus Pavement Age on 102KIP Lane of MnROAD Cell 26, Cell 27, and Cell 28

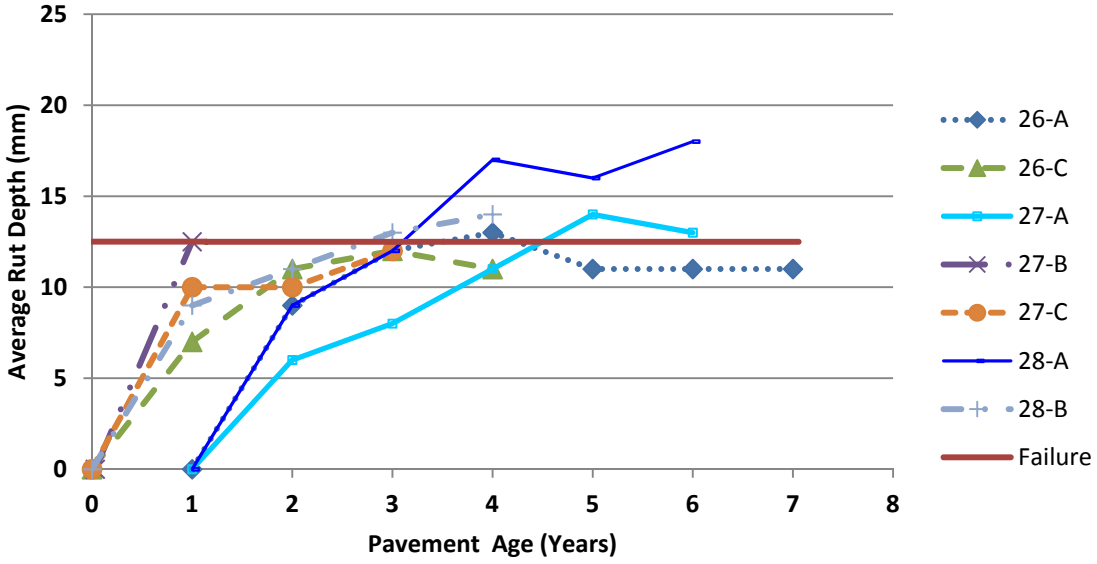

Figure 5.9 and Figure 5.10 show the average rut depths versus cumulative ESAL repetitions on the 80KIP and 102KIP lanes, respectively, of MnROAD Cell 26, Cell 27, and Cell 28.

Figure 5.9: Average Rut Depths versus Cumulative ESAL Repetitions on 80KIP Lane of MnROAD Cell 26, Cell 27, and Cell 28

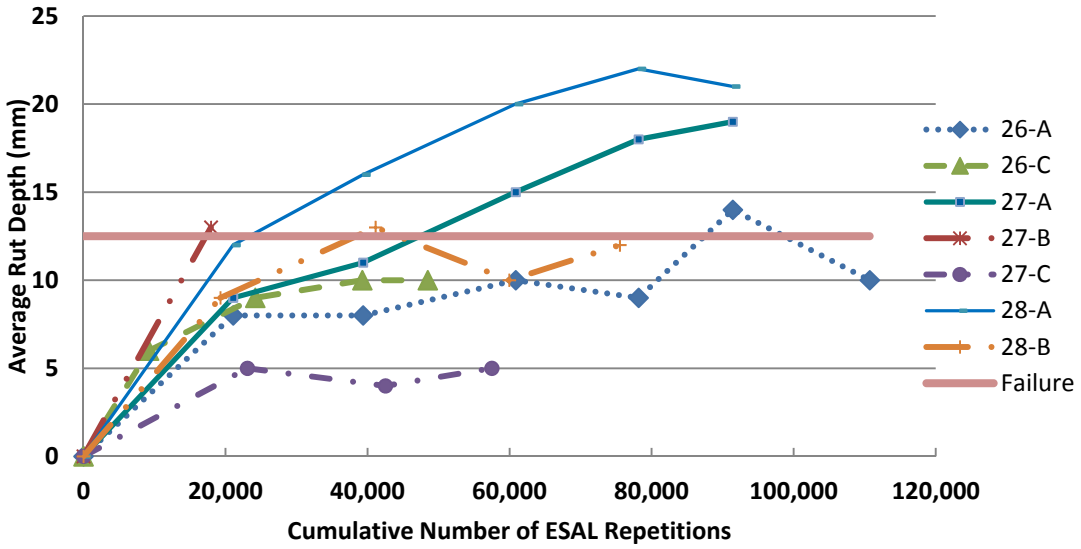

Figure 5.10: Average Rut Depths versus Cumulative ESAL Repetitions on 102KIP Lane of MnROAD Cell 26, Cell 27, and Cell 28

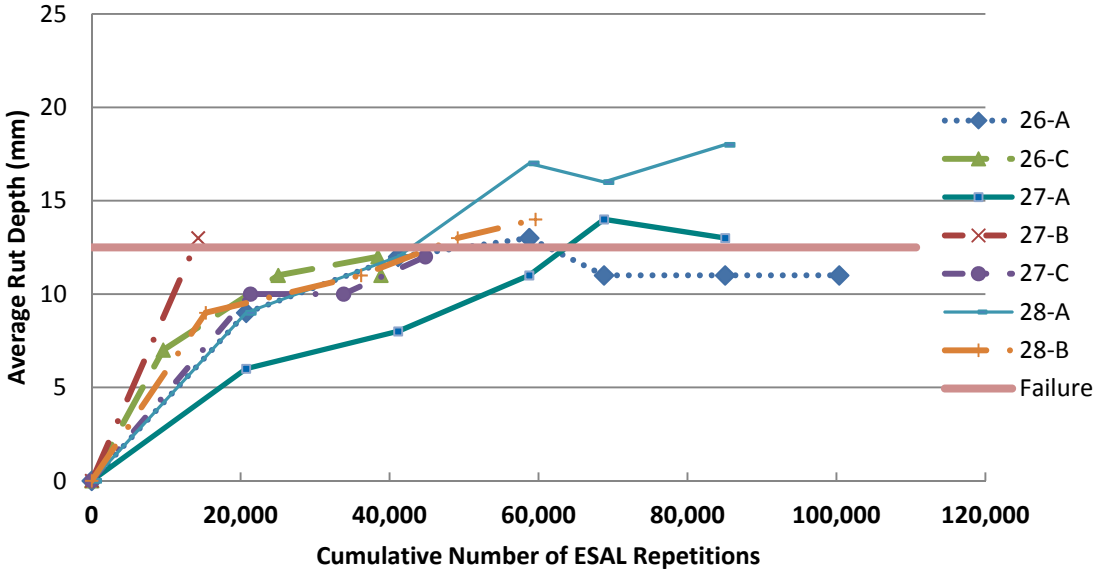

The results show that average rut depths increased as the cumulative ESAL repetitions increased on both the 80KIP and 102KIP lanes. The rut depth increased quickly with loading, and plateau over time for some of the pavement cells.

The results also show that on Cell 27-A and Cell 28-A the average rut depths were generally higher in the 80KIP lane than the 102KIP lane, despite the relatively similar ESAL repetitions in each lane. According to current damage analysis, the same number of ESALs should produce the same amount of rutting for each lane, which is not the case. A review of the ESAL repetitions in Table 5.7 showed that the ESALs applied on the 80KIP lane of Cell 27-A and Cell 28-A were 7% higher on average than the 102KIP lane, which may be a factor in the higher rut depth in the 80KIP lanes. In addition, the semi trailer loads were applied 4 day of the week on the 80KIP lane and 1 day of the week on the 102KIP lane. Given the similar numbers of ESAL repetitions and the same pavement structures, it was possible that how the pavement was loaded (i.e. 4 day rest period between loads) may explain the lower rut depths on the 102KIP lane.

FATIGUE CRACKING DISTRESS TREND

Table 5.9 presents the percent fatigue cracking in the wheelpath areas versus pavement age on the 80KIP and 102KIP lanes of MnROAD Cell 26, Cell 27, and Cell 28. The percent fatigue cracking was calculated by dividing the measured area of fatigue cracking in the wheelpaths, by the total area of the wheelpaths in each lane.

Table 5.9: Fatigue Cracking in Wheelpath Areas versus Pavement Age on 80KIP and 102KIP Lanes of MnROAD Cell 26, Cell 27, and Cell 28

	Percent Fatigue Cracking (%)							Final Fatigue Cracking (%)
Pavement Age (Years)	**1**	**2**	**3**	**4**	**5**	**6**	**7**	
Cell	80KIP Lane							
26-A	-	0	0	0	0	2	2	2
26-C	0	0	0	0	-	-	-	0
27-A	-	0	0	1	5	11	-	11
27-B [1]	-	-	-	-	-	-	-	-
27-C	9	14	7	24	19	31	-	31
28-A	-	0	0	6	20	21	-	21
28-B	0	0	0	0	1	2	9	9
	102KIP Lane							
26-A	-	0	0	0	0	1	1	1
26-C	0	0	0	-	-	-	-	0
27-A	-	0	0	0	3	6	-	6
27-B [1]	-	-	-	-	-	-	-	-
27-C	0	0	0	5	4	7	-	7
28-A	-	0	0	2	9	15	-	15
28-B	0	0	1	1	3	4	4	4

Note: [1]Cell 27-B failed in first year,
'-'=not applicable, fatigue data not measured
Cell 26-A - 127 mm AC, clay subgrade
Cell 26-C - 102 mm AC, 305 mm granular base Class 6, clay subgrade
Cell 27-A - 76 mm AC, 279 mm granular base Class 6, clay subgrade
Cell 27-B – 13 mm AST, 356 mm crushed stone base, clay subgrade
Cell 27-C - 63 mm road mix, 356 crushed stone base, clay subgrade
Cell 28-A - 76 mm AC, 330 mm granular base Class 5, clay subgrade
Cell 28-B – 63 road mix, 25 mm granular base Class 6, 356 crushed stone base, clay subgrade

Figure 5.11 and Figure 5.12 show the percent fatigue cracking versus pavement age on the 80KIP and 102KIP lanes, respectively, of MnROAD Cell 26, Cell 27, and Cell 28. The fatigue failure limit of 10% cracking in the wheelpath area is shown in the graphs.

Figure 5.11: Percent Fatigue Cracking versus Pavement Age on 80KIP Lane of MnROAD Cell 26, Cell 27, and Cell 28

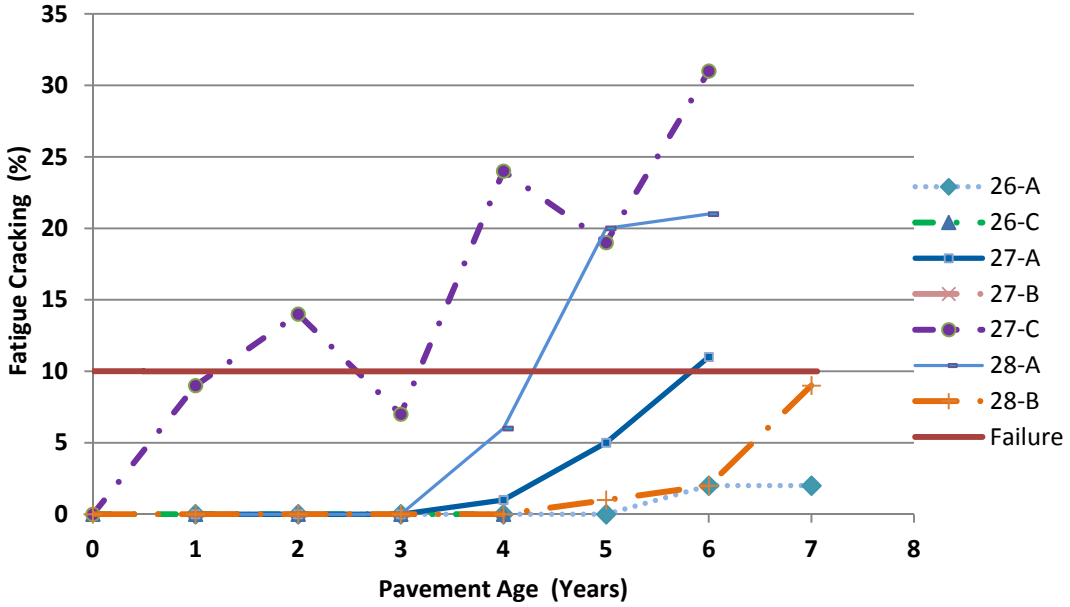

Figure 5.12: Percent Fatigue Cracking versus Pavement Age on 102KIP Lane of MnROAD Cell 26, Cell 27, and Cell 28

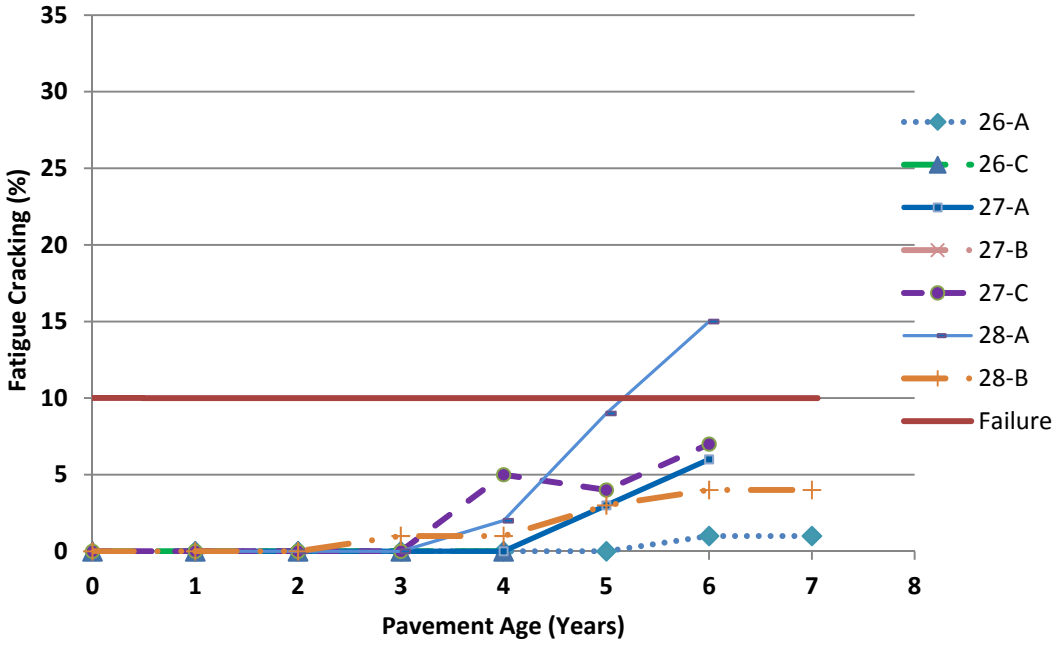

Figure 5.13 and Figure 5.14 show the percent fatigue cracking versus the cumulative ESAL repetitions on the 80KIP and 102KIP lanes, respectively, of MnROAD Cell 26, Cell 27, and Cell 28.

Figure 5.13: Percent Fatigue Cracking versus Cumulative ESAL Repetitions on 80KIP Lane of MnROAD Cell 26, Cell 27, and Cell 28

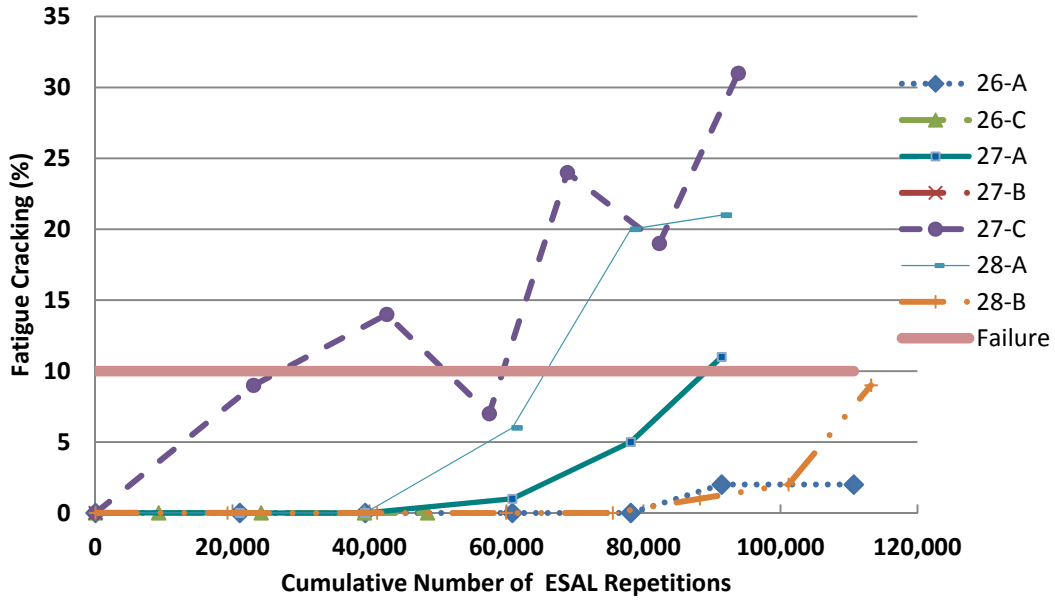

Figure 5.14: Percent Fatigue Cracking versus Cumulative ESAL Repetitions on 102KIP Lane of MnROAD Cell 26, Cell 27, and Cell 28

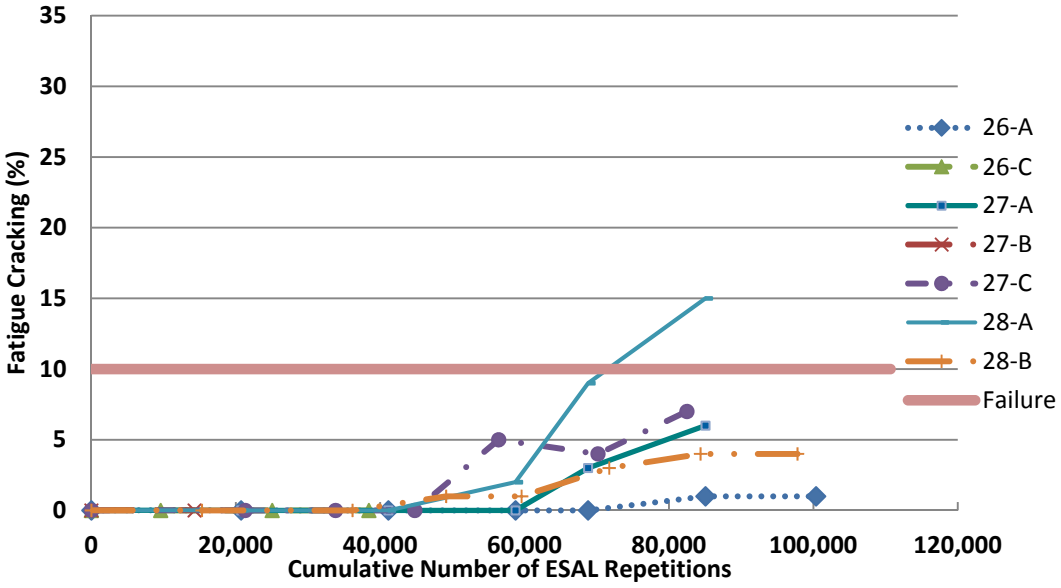

The graphs show that fatigue cracking generally developed later in the pavement life and then increased with increasing ESAL repetitions. The exception was Cell 27-C which was the road mix surface over granular base on subgrade. The structure on Cell 27-C had significant, and highly variable, fatigue cracking as ESAL repetitions increased. This variation in the road mix fatigue cracking was not unusual. The material consistency of road mixes allow for 'healing' of the cracks at high summer temperatures, thereby causing large variability in fatigue crack detection. The standard fatigue equations would not apply for this type of pavement.

The results also show overall lower fatigue cracking on the 102KIP lane compared to the 80KIP lane, which was unexpected. This may be due to the 7% higher ESAL repetitions applied on the 80KIP lane, and the application of the semi trailer loads four days of the week on the 80KIP lane and one day of the week on the 102KIP lane. It was possible that given similar numbers of ESAL repetitions and the same pavement structure, how the pavement was loaded (i.e. 4 day rest period between loads) may explain the lower fatigue cracking on the 102KIP lane. Beranek and Carpetner [2004] studied laboratory fatigue algorithms for IDOT asphalt mixtures at full scale test sections. The test sections were trafficked over a two-year period, and cracking and rutting were recorded throughout the testing along with the strains and temperatures. Laboratory fatigue test data was used to prepare laboratory fatigue curves. Additional healing fatigue testing that applied a rest period between the load pulse was conducted to develop a relation between the rest period and the fatigue life extension provided by the rest period. Bernaek and Carpenter found that IDOT may expect a level of conservatism in HMA pavements in the field due to the healing effects provided by the rest periods between heavy loads. The factor of

safety may be between 4 to 10 times the numbers of loads to produce cracking failure, compared to the design.

5.2.3 MEASURED PAVEMENT STRAIN AND SUBGRADE PRESSURE TREND

The MnROAD longitudinal and transverse strains and subgrade stresses during late spring were analysed for data trends and variability. The analysis was at the semi trailer 80KIP and 102KIP loads, 690 kPa standard tire pressure, and average speed of 60km/hr. Static strains from the semi trailer pass were not available from the MnROAD database.

MnROAD conducted multiple passes of the 5-Axle semi trailer over the sensors during dynamic response testing at the sites. A video camera was installed on the drive axle of the truck to determine the offset of the axle with respect to the strain sensor for each pass of the vehicle [Moreno, 2000; Dai et al, 2000; Lukanen, 2005].

MnROAD extracted the peak strains from the raw data of each pass of the semi trailer using a computer program for selecting peak dynamic sensor responses developed by the University of Minnesota [Burnham et al, 2007]. The raw dynamic strain data was stored offline while the peak strains were filtered by MnROAD and stored in the database.

Figure 5.15 shows the longitudinal strain responses (and peak strains) from one pass of the 5-axle semi trailer axle groups on a MnROAD pavement cell. The trace shows good representation of the strain responses from the Steering axle, Drive and Trailer1 tandem axle groups.

Figure 5.15: Longitudinal Strain Response and Peak Strains from a Pass of 5-Axle Semi Trailer Axle Groups on MnROAD Pavement Cell [after Burnham et al, 2007]

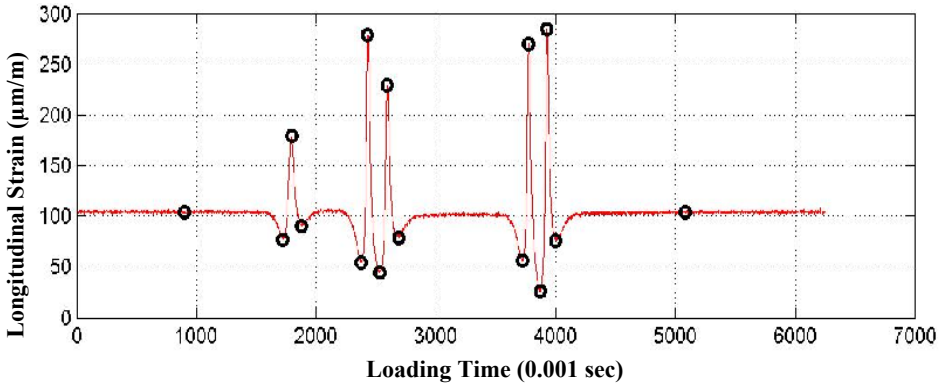

While the MnROAD database contains extensive dynamic response data, there were limitations on the strain data available for the seven cells selected for this analysis.

Cell 26-A, Cell 27-A, and Cell 28-A had strain and pressure data available from 1994 to 1996. Only a few cells from the original 1993 installation had strain gauges that provided meaningful data after 1996. The measured strains from 1996 were selected since complete longitudinal and transverse strains were available for that year. The peak strains (from early to late spring of 1996) for Cell 26-A, Cell 27-A, and Cell 28-A are presented in Appendix F.

Strain data were not available for Cell 26-C, Cell 27-B, Cell 27-C, and Cell 28-B, which were constructed in 1999 and 2004. After the initial data request, MnROAD indicated that strain gauges and pressure cells were not installed on these cells.

NORMALIZED MAXIMUM STRAINS

Since tire 'wander' from sensors is one of the main sources of variability in pavement response testing, a regression analysis was conducted to normalize the 1996 measured peak strains on Cell 26-A, Cell 27-A, and Cell 28-A. The regression analysis was conducted to correct the tire to zero offset from the strain sensors. The regression parameters were determined for the longitudinal and transverse strains versus semi trailer tire offset for each pavement cell. The tire offsets were available from the MnROAD database.

Figure 5.16 shows the relationship between the peak longitudinal and transverse strains versus tire offset for the 5-axle semi trailer on the 102KIP lane of MnROAD Cell 26-A during late spring. The strains were from the LE5 and TE5 strain sensors in the center of the wheelpath of the 102KIP lane. The semi trailer was at 690 kPa standard tire pressure and speed of 64 km/hr.

Figure 5.16: Relationship between Peak Longitudinal and Transverse Strains versus Tire Offset for 5-Axle Semi Trailer on 102KIP Lane of MnROAD Cell 26-A during Late Spring

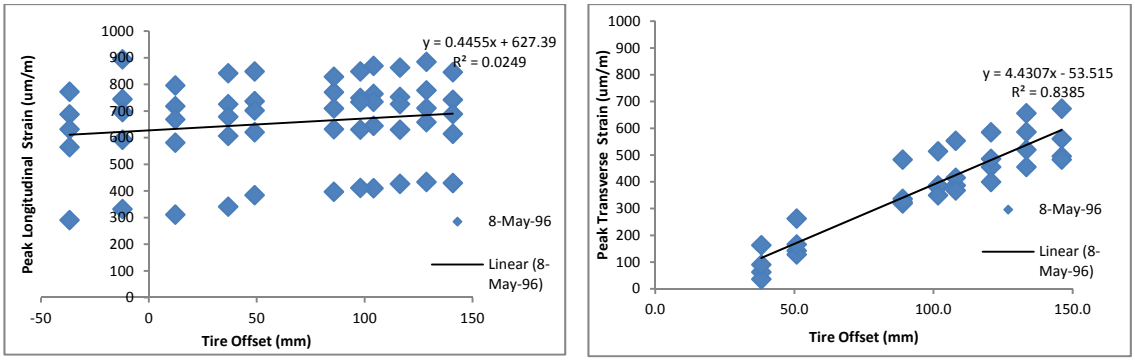

a) Longitudinal LE5 Peak Strain

b) Transverse TE5 Peak Strain

The results show a steeper slope of the regression line for the transverse strains which were more sensitive to the tire offset than the longitudinal strains. However, the results show poor correlation (R^2=0.02) between the peak longitudinal strains versus tire offsets. In addition, the transverse strains relationship showed increasing strain as the tire offset increased. This was contrary to expectations, since strains typically decrease as tire offset increase. A review of the longitudinal and transverse strains does not indicate errors in the data.

Table 5.10 shows the regression parameters for the longitudinal and transverse strains versus tire offset for the 5-axle semi trailer loads and late spring conditions on MnROAD Cell 26-A, Cell 27-A, and Cell 28-A. The strains were from the center sensors (LE5 and TE5) in the wheelpaths of the 80KIP and 102KIP lanes and at semi trailer speeds of 60-64km/hr and 690kPa standard tire pressure.

Table 5.10: Regression Parameters for Peak Longitudinal and Transverse Strains versus Tire Offsets for 5-Axle Semi Trailer Loads and Late Spring Conditions on MnROAD Cell 26-A, Cell 27-A, and Cell 28-A

Sensor	Cell	Load Rating	β	R^2
Transverse	26-A	80KIP	0.44	0.10
		102KIP	4.43	0.84
	27-A	80KIP	1.06	0.30
		102KIP	-	-
	28-A	80KIP	-5.05	0.24
		102KIP	3.45	0.15
Longitudinal	26-A	80KIP	-0.02	0.00
		102KIP	0.44	0.02
	27-A	80KIP	0.13	0.01
		102KIP	-	-
	28-A	80KIP	-	-
		102KIP	-	-

Note: '-'=not applicable

The regression parameters show the inconsistency in the trends between the longitudinal and transverse strains and tire offset. The signs of the β coefficients were both negative and positive for the strains versus tire offset. This was contrary to the expected trend of only negative β coefficients. The R^2 were also low, indicating poor fit of the regression equations between the peak measured longitudinal and transverse strains and the tire offsets.

Given the inconsistency of the regression parameters, the regression equations were not used to normalize the peak strains for the MnROAD cells. Instead, the average peak strains from three runs of the semi tires closest to the sensors were selected for Cell 26-A, Cell 27-A, and Cell 28-A.

Table 5.11 presents the peak longitudinal and transverse strains at the 5-axle semi trailer loads and late spring conditions on the 80KIP and 102KIP lanes of MnROAD Cell 26-A, Cell 27-A and cell 28-A. The strains were the average peak strains measured from multiple passes (from the same day) of the semi trailer on Cell 26-A, Cell 27-A, and Cell 28-A.

Table 5.11: Peak Longitudinal and Transverse Strains at 5-Axle Semi Trailer Loads and Late Spring Conditions on 80KIP and 102 KIP Lanes of MnROAD Cell 26-A, Cell 27-A, Cell 28-A

Axle Group	Tire Load (kg)	Strain Orientation	Longitudinal and Transverse Strains (μm/m)		
			26-A [1]	27-A[2]	28-A[3]
			80KIP Lane		
Steering	2,727	Longitudinal	384	n/a	n/a
		Transverse	405	n/a	567
Drive	1,932	Longitudinal	503	350	n/a
		Transverse	447	531	601
Trailer	1,932	Longitudinal	514	360	n/a
		Transverse	442	523	748
			102KIP Lane		
Steering	2,841	Longitudinal	411	n/a	n/a
		Transverse	456	n/a	n/a
Drive	2,543	Longitudinal	n/a	n/a	n/a
		Transverse	486	n/a	n/a
Trailer	2,543	Longitudinal	n/a	n/a	n/a
		Transverse	585	n/a	621

Note: [1]26A-80KIP – May 13, 1996; Air Temp=13.5°C; Speed=64km/hr
26A-102KIP – May 8, 1996; Air Temp=12.5°C; Speed=64km/hr
[2]27A-80KIP – May 13, 1996; Air Temp=13.5°C; Speed=64km/hr
[3]28A-80KIP – May 13, 1996; Air Temp=13.5°C; Speed=64km/hr
28A-102KIP – May 8, 1996; Air Temp=12.5°C; Speed=64km/hr
'n/a'=data not available

Table 5.12 presents the peak vertical subgrade pressures (stresses) at the 5-axle semi trailer loads and late spring conditions on the 80KIP and 102KIP lanes of MnROAD Cell 26-A, Cell 27-A, and Cell 28-A. MnROAD measured the vertical pressures from pressure plates installed in the subgrade.

Table 5.12: Peak Vertical Pressures at 5-Axle Semi Trailer Loads and Late Spring Conditions on 80KIP and 102 KIP Lanes of MnROAD Cell 26-A, Cell 27-A, Cell 28-A

Axle Group	Stress Orientation	Vertical Pressure (kPa)		
		26-A [1]	27-A[2]	28-A
80KIP Lane				
Steering	Vertical	39	n/a	n/a
Drive	Vertical	65	118	n/a
Trailer	Vertical	70	137	n/a
102KIP Lane				
Steering	Vertical	n/a	55	n/a
Drive	Vertical	119	90	n/a
Trailer	Vertical	125	100	n/a

Note: [1]26A-80KIP – May 13, 1996; Air Temp=12.5°C; Speed=64km/hr
26A-102KIP – May 13, 1996; Air Temp=12.5°C; Speed=64km/hr
[2]27A-80KIP – May 13, 1996; Air Temp=13.5°C; Speed=64km/hr
27A-102KIP – May 15, 1996; Air Temp=12.5°C; Speed=64km/hr
n/a=data not available

In general, the analysis of the pavement structures, semi trailer loading and environmental conditions from the MnROAD cells were considered representative of the Manitoba SWR pavement conditions. The trend and variability analysis of the pavement performance from the rut depths and fatigue cracking distresses and the pavement responses from the peak longitudinal and transverse strains (from average semi trailer passes on the strain sensors) were used to develop the local damage models for the spring conditions.

CHAPTER 6 - CRITICAL STRAIN PREDICTIONS AND STRUCTURAL MODEL CALIBRATION

The relationship between vehicle loads and material behavior is important in modeling the structural response of pavements. Heavy loads result in stresses and strains at critical locations in the pavement layers, which accumulate over time resulting in pavement deterioration such as rutting and fatigue cracking. Structural response models are often used to predict these critical stresses and strains in the pavements.

This chapter presents and compares critical strain predictions from two structural response models; a Finite Element Model (FEM) and layered elastic KENLAYER model for the Manitoba pavements. The chapter also presents the calibration of the FEM predictions using measured field strains from the Manitoba sites.

6.1 FEM CRITICAL STRAIN PREDICTIONS

A finite element model (FEM) is a powerful tool for evaluating the response of pavements to vehicle loadings. A three-dimensional FEM was calibrated and used to predict the critical strains at different B-Train loads and tire pressures during the late spring of 2009 on PTH 11 and PR 304.

The FEM was developed by Liu [2011] for a static analysis using the ABAQUS numerical analysis software. The analysis discretized the pavement and subgrade into a number of elements with the wheel load at the top of the structure. The elements extended horizontally and vertically from the influence of the load, and boundary

conditions in the area of interest were assumed. The analysis focused on the critical strains under the center of one tire, under the edge of one tire, and under the center-to-center midpoint of dual tires.

FEM ASSUMPTIONS AND INPUTS

The methodology used to develop the FEM included meshing the pavement layers into a suitable number of elements and nodes; defining the stress-strain equation which described the stress or strain responses to the applied load for each layer of the structure; assembling a matrix of equations and boundary conditions to sum the responses for each element; calculating strains, stresses or displacements based on the equations; interpolating the model output response at desired locations within the pavement structure; and calibrating the FEM using measured field strains.

A number of inputs and assumptions were made in the development of the FEM and in mapping the Manitoba pavement structures and B-Train axle loads. An eight-node linear brick element was used for the finite element analysis. A symmetrical elemental block (between dual tires) with X, Y, and Z coordinates of 2200mm, 4400mm, and 6000mm respectively, was used to compute the pavement response for the dual-tired tandem and tridem axles. The coordinates were defined by the orthogonal coordinate system where the X and Y axes were parallel to the pavement surface, with X in the transverse direction of the truck movement, Y in the longitudinal of that movement; and the Z (or vertical) axis perpendicular to the pavement surface. The minimum boundary conditions were selected based on previous pavement response studies [Duncan, 1968; Kim, 2007;

NCHRP, 2004; Park, 2008; Wang and Machemehl, 2006], which produced reasonably accurate results [Liu, 2011].

Figure 6.1(a) shows the ABAQUS FEM eight-node linear brick element (in the X-Y-Z orthogonal coordinate system) and Figure 6.1(b) the labeling of displacement components at the element nodes. The horizontal displacement, U, and vertical displacement, W, in the X, Z directions, respectively, of the nodes on 'face 3' of the element is shown.

Figure 6.1: ABAQUS FEM 8-Node Linear Brick Element [after Johnson, 2006] and Labeling of Displacement Components at Element Nodes

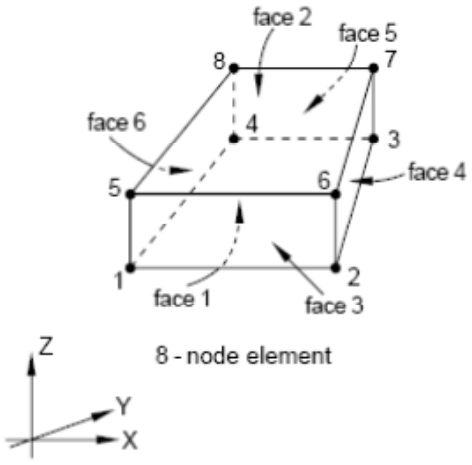

a) 8-Node Linear Brick Element

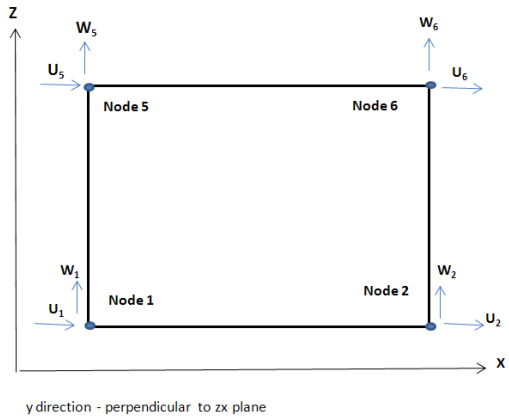

b) Labeling of Displacement at Nodes on Face 3

A linear displacement shape function was selected so that straight lines remained straight within the element. The strain-displacement equations (Equation 2.2) and shape functions for the elements were used to approximate the strains and displacements at the nodes in the element. Hooke's law (Equation 2.3), elastic material properties, and stress-strain equations (Equation 2.5) were used to approximate the stress solutions at the nodes in the

element. The constitutive Hooke's law and function matrices relationship are given in Equation 6.1.

$$\{\varepsilon\} = [D]\{\sigma\} \qquad \text{Constitutive Law} \qquad (6.1)$$

Where: D is the stiffness matrix that represents the linear equations given in Equation 2.5.

$$[D] = \begin{bmatrix} \frac{1}{E} & \frac{-v}{E} & \frac{-v}{E} & 0 & 0 & 0 \\ & \frac{1}{E} & \frac{-v}{E} & 0 & 0 & 0 \\ & & \frac{1}{E} & 0 & 0 & 0 \\ & & & \frac{1}{E}\frac{2(1+V)}{E} & 0 & 0 \\ & & & & \frac{2(1+v)}{E} & 0 \\ & symmetry & & & & \frac{2(1+v)}{E} \end{bmatrix}$$

and {ε} and {σ} matrices:

$$\{\varepsilon\} = \begin{bmatrix} \varepsilon_x \\ \varepsilon_y \\ \varepsilon_z \\ \gamma_{xy} \\ \gamma_{yz} \\ \gamma_{zx} \end{bmatrix} \qquad \{\sigma\} = \begin{bmatrix} \sigma_x \\ \sigma_y \\ \sigma_z \\ \tau_{xy} \\ \tau_{yz} \\ \tau_{zx} \end{bmatrix}$$

LIMITATION OF ABAQUS FEM

While the ABAQUS FEM by Liu [2011] was used for structural response predictions in this research, there were a number of limitations. The FEM was a static, linear model which could not account for the non-linearity of the layer materials and vehicle speed. In addition, triaxial tests were not conducted for the base and subgrade on PTH 11 and PR 304 and the resilient modulus-deviator stress equations (in Table 2.1) could not be used.

It could be argued that had lab triaxial test been conducted, the results may not fully characterize the in-situ non-linear behavior of the base and subgrade because samples tended to be disturbed and reconstituted for the test. Von Quintus and Killingsworth [1998] found differences in laboratory and field moduli that were related to the inability of the laboratory tests to simulate the actual in-situ confinement and effect of the surrounding materials in both the lateral and vertical direction.

For this research, the non-linearity in the FEM was mitigated by modeling fully thawed pavement layers, and using measured strains from the Manitoba sites to calibrate the FEM predictions. By calibrating the FEM to measured strains, this accounted for variables (such as non-linearity) that may not be captured by the model. Therefore, the FEM could be used to predict strains on SWR roads in Manitoba with similar structures.

FEM CRITICAL STRAIN PREDICTIONS ON PTH 11 AND PR 304

The ABAQUS FEM was used to simulate and compute the critical strains on PTH 11 and PR 304 at three B-Train loads and two tire pressures during the spring thaw.

The pavement structures of PTH 11 and PR 304 were meshed into the 8-node elements with a displacement shape function. The FEM was focused on simulating the B-Train dual tires on the tandem and tridem axle groups. These axle groups were chosen because the maximum measured strains were produced either by the Drive tandem or Trailer1 tridem axle, for all load and tire pressure combinations.

Figure 6.2 shows the FEM elemental mesh and boundary conditions for simulation on PTH 11. A fine mesh was used around the tire contact area, with the element dimension chosen to equal 8.38 mm, which was the size of the pressure mat footprint setting. A larger mesh size was used away from the contact areas, with a bias ratio of 0.9, to minimize the computation time. Full interface bonding was assumed between the different layers.

Figure 6.2: FEM Elemental Mesh and Boundary Conditions for Simulation on PTH 11 [after Liu, 2011]

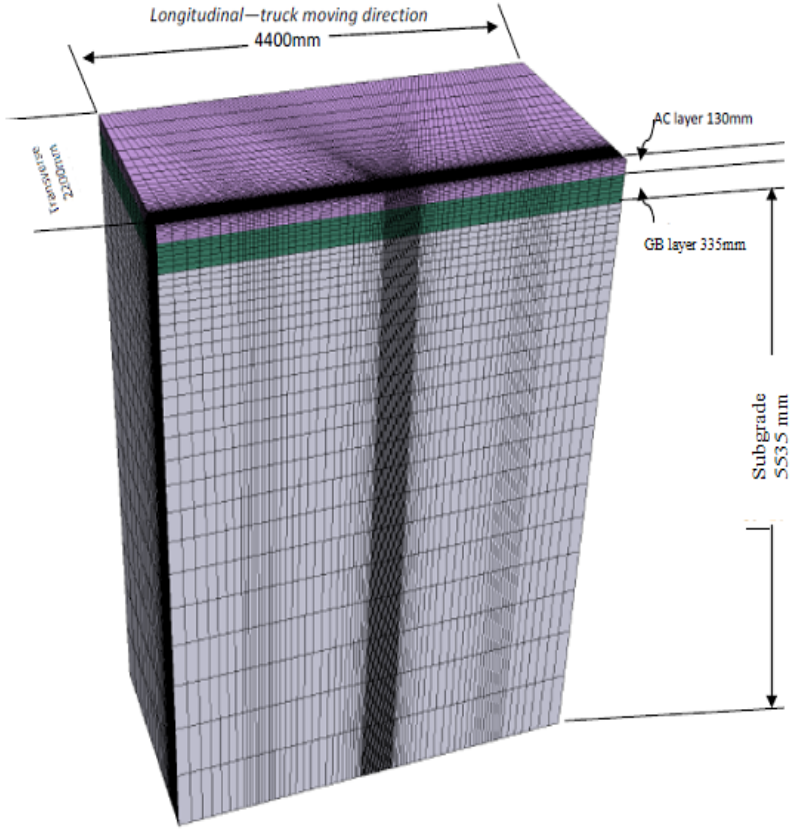

Figure 6.3 shows the FEM modeling areas and tandem and tridem axle analysing configurations for the simulation on PTH 11. The plan view of the FEM boundary conditions and tandem and tridem axle configurations are shown. The boundary

conditions were for the 4400mm x 2200mm elemental block, where the bottom half (dashed line) of the block is symmetrical to the top half. Due to this symmetry, only the bottom half of the block was analysed to reduce model computation. The axle configuration represented a tridem axle with dual tires. The first axle 'Axle3' is the lead axle, the 'Analysing Axle' is the center axle, and 'Axle1' is the trailing axle. To simulate the FEM responses for a tandem axle configuration with dual tires, 'Axle3' was removed, leaving the 'Analysing Axle' and 'Axle1'. For all axle configurations, the FEM responses were simulated under the center of the 'Analysing Axle' and center of the dual tire.

Figure 6.3: FEM Modeling Areas and Tandem and Tridem Axle Analysing Configurations for Simulation on PTH 11 [after Liu, 2011]

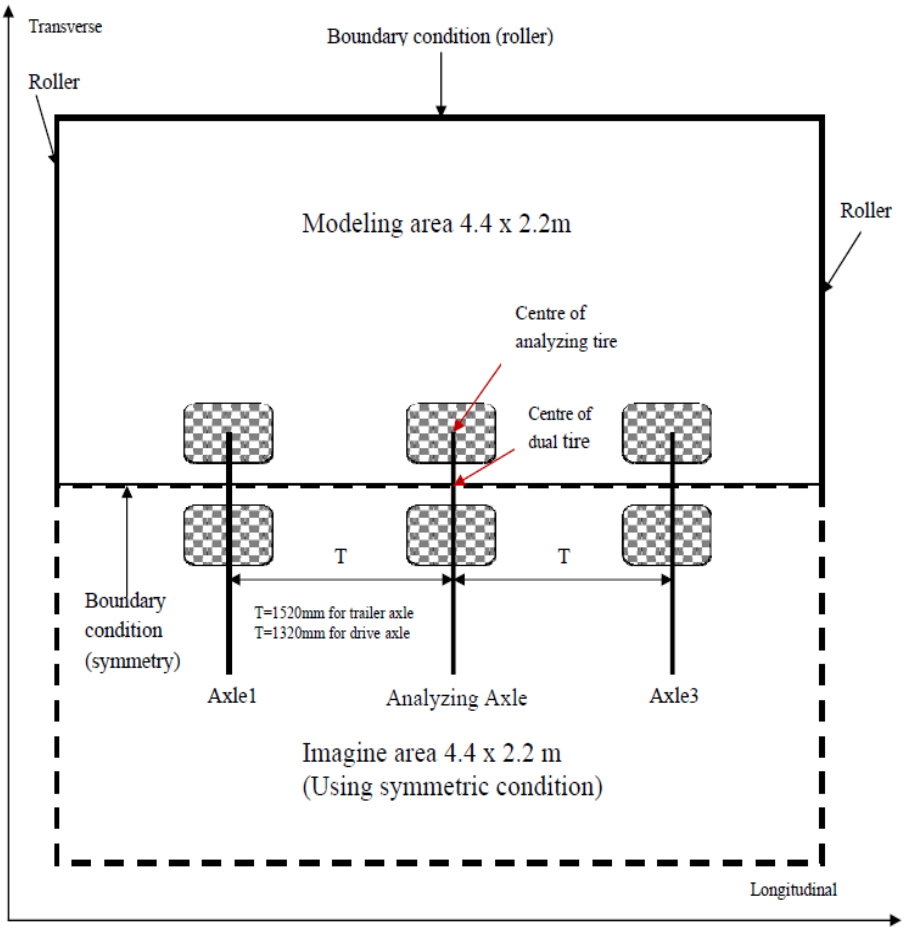

The measured numerical tire pressure distribution and shape of the footprints (shown in Figure 4.9 and Figure 4.10) were direct inputs into the FEM. The footprints were measurements of the tire-contact stresses due to loads at the top of the pavement surface. Tires were analyzed for each axle group using symmetric boundary condition in the longitudinal and vertical (Y-Z) surfaces, and under the centre of the tires, and center of the dual tire assembly, to reduce model computation times.

The pavement structure, thicknesses, and layer modulus properties were inputs into the FEM. The layer thicknesses were measured from cores and borehole drilling at the sites. The layer moduli were back-calculated from FWD deflections using the ELMOD software Version 5.1.72 [ELMOD, 2007].

Table 6.1 presents the back-calculated layer modulus used in the FEM for the spring condition on PTH 11 and PR 304. The measured spring moisture content (from Time Domain Reflectometer in the base and subgrade), and typical values of Poisson's ratio for the spring condition are also shown. Poisson's ratio was obtained from Huang [2004] using reasonable values for AC mixes at 25^{o}C and saturated bases and clay subgrade. The typical values of Poisson's ratio were considered appropriate for the analysis. Christopher et al [2006] and Huang [2004] found that the influence of Poisson's ratio on computed pavement response was normally small, and the assumed values often gave satisfactory results.

TABLE 6.1: Back-Calculated Layer Modulus used in FEM for Spring Conditions on PTH 11 and PR 304

Road	Layer	Thickness (mm)	TDR Volumetric Moisture Content (%)	ELMOD Back-Calculated Modulus (MPa)	Poisson's Ratio[1]
PTH 11	AC	130	-	2,700[2]	0.35
	Base	335	20	250	0.40
	Clay Subgrade	semi-infinite	35	35	0.45
PR 304	AST&Base	140	n/a	236[3]	0.40
	Rock Subbase	590	n/a		
	Clay Subgrade	semi-infinite	35	24	0.45

Note: TDR=Time Domain Reflectometer
[1]Typical values of Poisson's ratio [Huang, 2004]
[2]Revised back-calculated modulus
[3]AST/Base/Subbase back-calculated as one layer
n/a=data not available
'-'=not applicable

The AC layer modulus of 2,700MPa on PTH 11 was adjusted from the ELMOD back-calculated value of 745 MPa which was considered to be unusually low for late spring. Typical AC modulus of 3,500MPa at 25^{o}C is often reported [AASHTO, 1993]. It was possible that the low back-calculated AC modulus was due to imperfect bonding between the new and old asphalt used in the retrofit installation of the strain gauges.

The AC modulus on PTH 11 was adjusted through an iterative process that matched measured strains from FWD drops on the strain sensors. KENLAYER was used to predict strains at varying modulus inputs. The modulus that matched the predicted strains to the measured strains from the FWD drops on the sensors was found at 2,700 MPa. It was assumed that in using the strain measured from the FWD drops on the sensor, the curvature of the deflection basin under the FWD loads would be close to the true value.

Laboratory AC Resilient Modulus Testing on PTH 11

To confirm the adjusted AC modulus of 2,700MPa, laboratory resilient modulus testing was conducted on specimens from three cores extracted from PTH 11.

The LTPP Protocol P07 "Test method for Determining the Creep Compliance, Resilient Modulus and Strength of Asphalt Materials using the Indirect Tensile Test Device" was used for the resilient modulus testing [FHWA, 2010].

The testing device was an MTS model (407 Controller with 651 Environmental Chamber, 858 Table Top System Load Frame and Hydraulic Pump) top loading, closed-loop, servo-hydraulic universal testing machine, capable of providing a fixed or constant load with a resolution of at least 4.45 KN and constant ram displacement between 12 and 75 mm/minute.

A dynamic cyclic stress and constant stress of fixed amplitude, with duration of 0.1 second and a rest period of 0.9 seconds, was applied to 150 mm diameter by 50 mm thick test specimen for the resilient modulus testing. Loads were selected to keep horizontal deformations between 0.038 and 0.089 mm. The deformation responses of the specimen were measured near the center of the specimen with gauge point mounted extensometers. The resilient modulus was calculated both as instantaneous and total resilient modulus.

Figure 6.4 shows the schematic of the instantaneous and total resilient deformation for a resilient modulus loading cycle. The instantaneous resilient modulus was calculated from the instantaneous resilient deformation. The total resilient modulus was calculated using the total resilient deformation, which includes both the instantaneous recoverable and the

time-dependent continuing recoverable deformation, during the rest-period of one cycle [FHWA, 2010].

FIGURE 6.4: Schematic of Instantaneous and Total Resilient Deformation for a Resilient Modulus Loading Cycle [after FHWA, 2010]

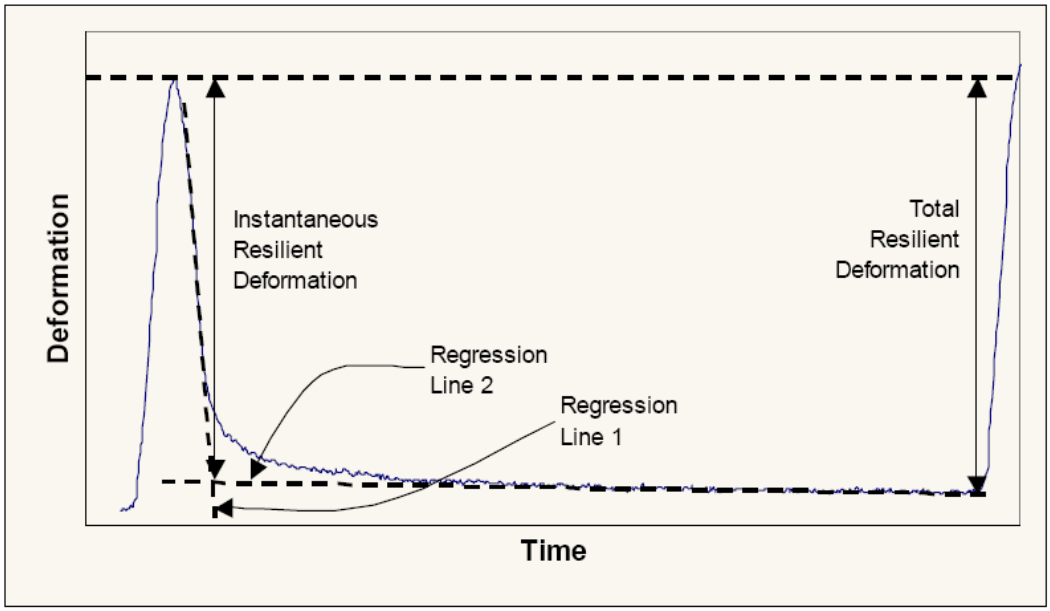

The resilient modulus testing of three cores from PTH 11 was conducted in February 2012. Specimens were taken from the top and bottom layers of the 130mm cores, and sawn and trimmed to the required test heights. The specimen densities were determined using ASTM D1188 "Test Method for Bulk Specific Gravity and Density of Compacted Bituminous Mixtures using Coated Samples". The specimen air voids were determined using ASTM D3203 "Standard Test Method for Percent Air Voids in Compacted Dense and Open Bituminous Paving Mixtures" and maximum specific gravity (specific gravity without air voids) for the mixes. Maximum specific gravity of 2.50 and 2.45 were

obtained for the Bituminous "A" and "B" mixes, respectively, from the original construction reports on PTH 11 [MIT, 1964].

The specimens were conditioned overnight in an environmental chamber set to the desired test temperature. Four extensometers were mounted on each specimen (two on top and two on bottom) at a gauge length of 50mm, and in the horizontal and vertical direction to measure the deformations.

Figure 6.5(a) shows the PTH 11 specimen mounted in the loading device and Figure 6.5(b) the extensometer configuration for the resilient modulus testing.

FIGURE 6.5: PTH 11 AC Specimen Mounted in Loading Device and Extensometer Configuration for Lab Resilient Modulus Testing

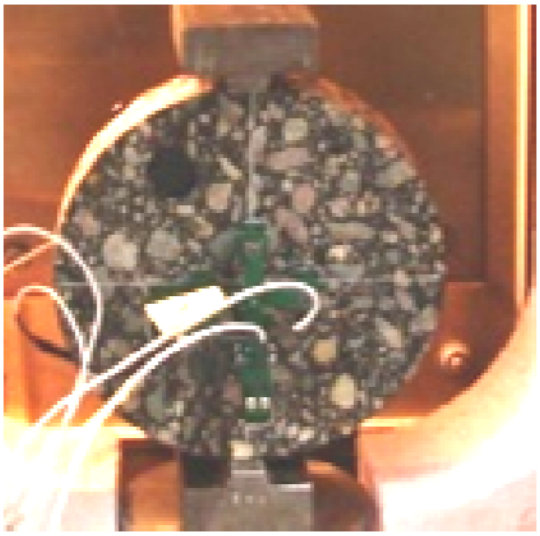

a) PTH 11 Specimen in Loading Device

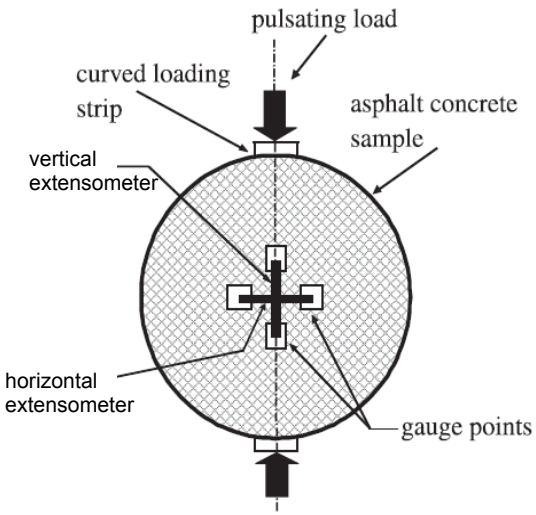

b) Extensometer Configuration[Shalaby, 2004]

The resilient modulus tests were performed at test temperatures of 5°C and 25°C. During the testing at 5°C, the first specimen (Core#1) became brittle and broke prematurely before the test was completed. No data was obtained for that specimen. Because of the

possibility of premature breakage, the remaining three specimens were tested at 25°C only, and not at 5°C. The cyclic loading, horizontal, and vertical deformations for each specimen were obtained from the test.

Figure 6.6(a) shows the cyclic loading, Figure 6.6(b) the horizontal deformation, and Figure 6.6(c) the vertical deformation at 25°C versus loading time for the resilient modulus testing of Core #3 from PTH 11. Horizontal extensometers 1 and 2 measured deformations at the top and bottom of the specimen, respectively. Vertical extensometers 1 and 2 measured deformations at the top and bottom of the specimen, respectively.

FIGURE 6.6: Cyclic Loading and Horizontal and Vertical Deformation at 25°C versus Loading Time for Resilient Modulus Testing of Core #3 from PTH 11

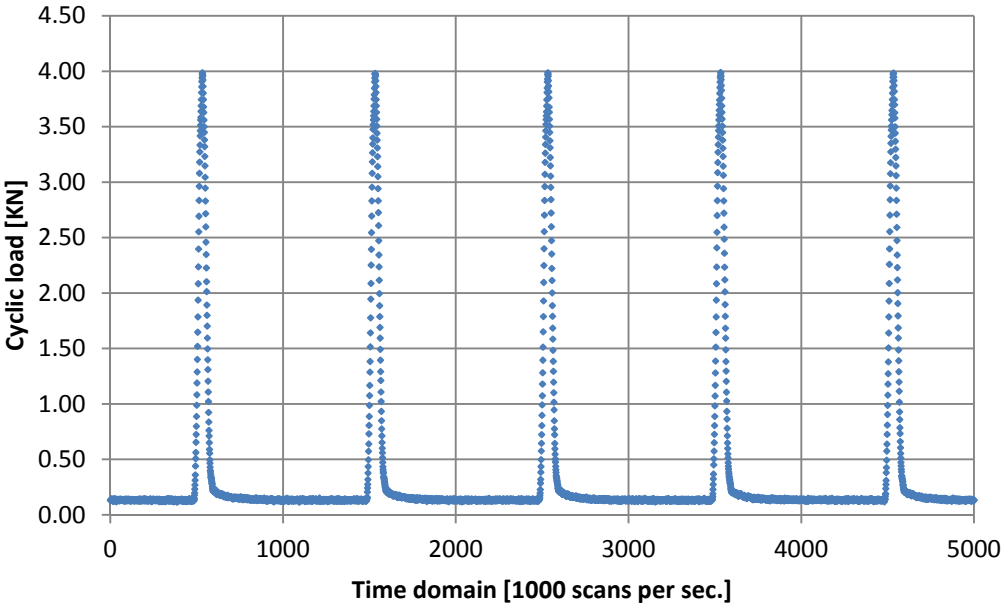

a) Cyclic Loading versus Time for Core #3

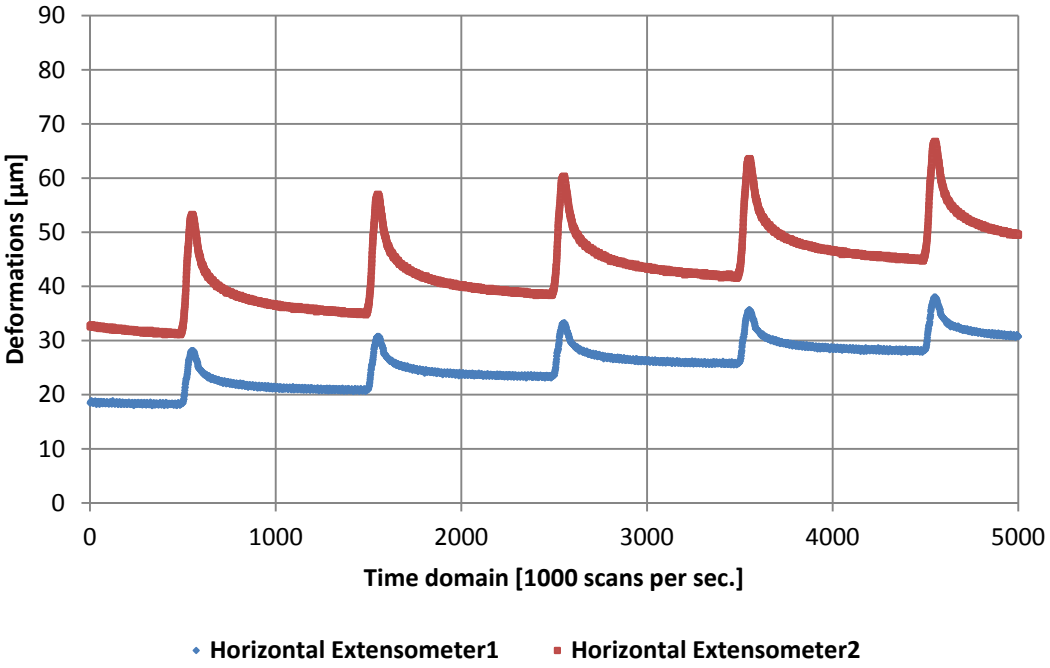

b) Horizontal Deformations versus Time for Core #3

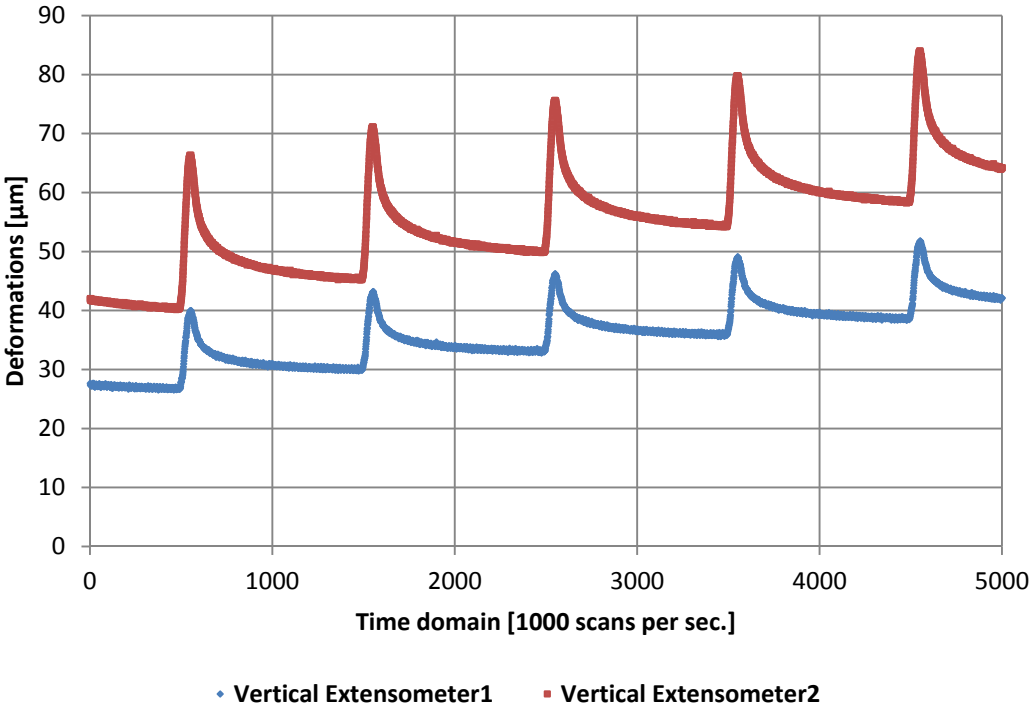

c) Vertical Deformations versus Time for Core #3

Table 6.2 presents the laboratory resilient modulus at 25°C and Poisson's Ratio calculated for the AC specimens from PTH 11. The specimen densities and percent air voids are also shown. The surface patch on specimen#2A was included in the resilient modulus testing because the B-Train response testing included all AC layers (including the patch) on PTH 11. Air voids were not calculated for specimen#2A since the maximum specific gravity for the patching mix was not available.

During loading, the horizontal extensometer deformations recorded on the bottom of specimen#2 were lower than the minimum 0.038mm required by the test protocol. The extensometers on the top and bottom of the specimen were reversed, and the test rerun, to check whether the extensometers were malfunctioning. The horizontal deformations on the bottom of the specimen still remained low. It was concluded that the specimen response caused the low deformation, not the extensometer. The resilient modulus for specimen#2 was calculated with the deformations recorded from the top of the specimen.

TABLE 6.2: Laboratory Resilient Modulus at 25°C and Poisson's Ratio of AC Core Specimen from PTH 11

Core Specimen #	Specimen Height (mm)	Density (kg/m^3)	Air Void (%)	Test Temp (°C)[2]	Poisson's Ratio		Resilient Modulus (MPa)	
					Instant-aneous	Total	Instant-aneous	Total
1[1]	46	2,403	1.9	25	n/a	n/a	n/a	n/a
2[3]	48	2,398	2.2	25	0.247	0.242	1795	1536
2A[4]	43	2,219	-	25	0.383	0.406	2211	2169
3	48	2,426	2.9	25	0.474	0.484	4015	3575
				Average	0.368	0.377	2674	2427

Note: [1] Core 1 was brittle and broke during testing at 5°C
[2]Cores 2, 2A, and 3 tested at 25°C and not 5°C to avoid brittle breakage
[3]Core 2 extensometers recorded very low deformation on one side of specimen
[4]Core 2A had 25 mm of patching mix on surface
n/a=data not available

The results of the resilient modulus testing showed the average total resilient modulus for the three AC specimens on PTH 11 was 2,427 MPa, with a standard deviation of 1,043 MPa and COV of 43%. The average Poisson's ratio was 0.38 with a standard deviation of 0.12 and COV of 32%. Variations in the lab resilient modulus were due in part to the unexpected response from specimen#2 and the lower modulus of specimen#2A. Since the average laboratory modulus obtained for the AC specimens on PTH 11 was comparable to the adjusted modulus of 2,700 MPa (given in Table 6.1), the AC modulus of 2,700MPa was used in the FEM.

FEM CRITICAL STRAIN PREDICTIONS

The FEM was used to simulate and compute the critical strains on PTH 11 and PR 304. The measured tire contact areas, measured tire contact stresses, and material properties were used in the FEM

Figure 6.7 shows the FEM simulated longitudinal stress and deformation from the B-Train Drive axle dual tire load on PTH 11. The simulation is shown in the longitudinal direction and at the center of the dual tire assembly.

Figure 6.7: FEM Simulated Longitudinal Stress and Deformation from B-Train Drive Axle Dual Tire Load on PTH 11 [after Liu, 2011]

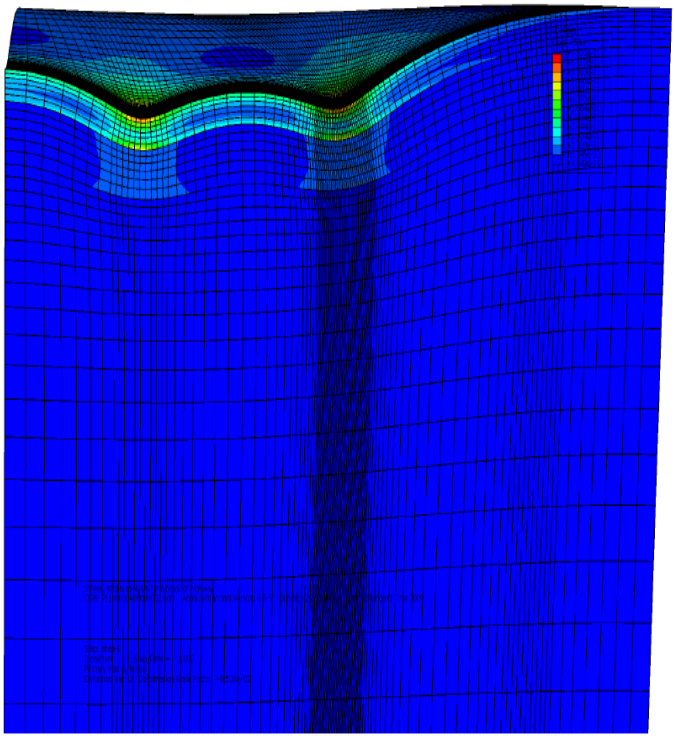

The simulation in the plot showed highest stress distributions at the surface of the pavement and directly under the 'analyzing' tire load.

Table 6.3 presents the FEM predicted longitudinal and transverse strains and vertical strains from the B-Train actual (measured) tire loads and measured tire-pavement pressure distributions on PTH 11. The steering axle loads were not included in the predictions since the steering axle loads and tire pressures did not vary from the summer and fall seasons and the SWR period in Manitoba.

TABLE 6.3: FEM Predicted Longitudinal and Transverse and Vertical Strains from B-Train Actual (Measured) Tire Loads and Tire-Pavement Pressure Distribution from Spring Testing on PTH 11

Axle Group	Load Rating	Axle Load (kg)	Tire Load (kg)	FEM Predicted Strain (µm/m)					
				Bottom of Surface				Top of Subgrade	
				Transverse		Longitudinal		Vertical	
				690kPa	345kPa	690kPa	345kPa	690kPa	345kPa
Steering	AlL1	4,897	2,449	-	-	-	-	-	-
	A1N	4,944	2,472	-	-	-	-	-	-
	RTAC	4,837	2,419	-	-	-	-	-	-
Drive	A1L1	15,176	1,927	112	95	180	151	-439	-432
	A1N	15,192	1,930	112	95	180	151	-439	-432
	RTAC	17,072	2,173	127	106	205	168	-495	-486
Trailer1	A1L1	20,856	1,765	120	107	167	150	-390	-386
	A1N	21,084	1,785	120	107	167	150	-390	-386
	RTAC	24,504	2,079	143	125	202	177	-458	-453
Trailer2	A1L1	15,136	1,829	123	109	183	162	-436	-433
	A1N	15,392	1,924	123	109	183	162	-436	-433
	RTAC	16,568	2,071	124	111	193	172	-457	-452

Note: '-'=not applicable, steering axle not included in analysis

The results show that the FEM predicted strains increased with increasing loads on PTH 11. When the 'Drive' axle tire load was increased from A1L1 to RTAC (a 13% load increase), there was a 12% increase on average in the predicted longitudinal and transverse strains at the bottom of the AC layer, and a 13% increase on average in the predicted vertical strains at the top of the subgrade. Since the FEM predictions were based on linear model the increase in load produced a proportional increase in strains in the pavement structure.

The results also show that the predicted longitudinal strains were 33% higher on average than the transverse strains, for each load and and tire pressure. This result was consistent with the trend from the measured field strains.

The FEM predicted strains decreased with reductions in tire pressure. When the 'Drive' axle tire pressure was reduced from 690kPa to 345kPa (a 50% pressure decrease), there was a 15% decrease on average in the predicted longitudinal and transverse strains at the bottom of the AC layer which was considered significant. There was a 1% decrease on average in the vertical strains at the top of the subgrade, which was not considered significant. This was expected since the effect of tire pressure decreased with depth.

Tables 6.4 presents the FEM predicted vertical strains from the B-Train actual (measured) tire load and spring testing on PR 304. The FEM predictions were at the measured tire-pavement pressure distributions from the spring testing.

TABLE 6.4: FEM Predicted Vertical Strains from B-Train Actual (Measured) Tire Load and Tire-Pavement Pressure Distribution from Spring Testing on PR 304

Axle Group	Load Rating	Axle Load (kg)	Tire Load (kg)	FEM Predicted Strain (μm/m)	
				Top of Subgrade	
				Vertical	
				690kPa	345kPa
Steering	B1L2	4,525	2,263	-	-
	B1N	4,715	2,358	-	-
	A1N	4,890	2,445	-	-
Drive	B1L2	10,576	1,322	-257	-256
	B1N	13,904	1,738	-335	-330
	A1N	15,224	1,903	-365	-361
Trailer1	B1L2	14940	1,245	n/a	n/a
	B1N	17,700	1,475	-279	-278
	A1N	21,108	1,759	-332	-329
Trailer2	B1L2	10,104	1,263	n/a	n/a
	B1N	14,072	1,650	-306	-303
	A1N	15,392	1,924	-360	-357

Note: '-'=not applicable
n/a=data not available; contact pressures not measured at load and tire pressure

The results show that the FEM predicted vertical strains increased with increasing loads, on PR 304. When the 'Drive' tire load was increased from B1N to A1N (a 10% load increase), there was a 9% increase on average in the predicted vertical strains at the top of the subgrade.

The FEM predicted vertical strains decreased with decreasing tire pressure on PR 304. When the 'Drive' axle tire pressure was reduced from 690kPa to 345kPa (a 50% pressure

decrease), there was a 1% decrease on average in the predicted vertical strains at the top of the subgrade, which was not considered significant.

6.2 COMPARISON OF FEM AND KENLAYER LEM CRITICAL STRAIN PREDICTIONS

While the FEM is a powerful tool for evaluating the response of pavements to vehicle loadings, FEMs require considerable training to build and long computational times to run. To evaluate whether the FEM was necessary for this analysis, the layered elastic model (LEM) in the KENLAYER software was used to compare the predict pavement responses on PTH 11 and PR 304.

KENLAYER Pavement Analysis Software was developed by Huang [2004] at the University of Kentucky. The LEM structural response models in KENLAYER assumed the materials were not stressed beyond their elastic range (e.g. yield strength), and the load at the surface was represented by a uniformly distributed stress over a circular contact area.

KENLAYER was used to predict the horizontal strains at the bottom of the AC layer, and vertical strain at the top of the subgrades on PTH 11 and PR 304. The layer modulus, thickness, and Poison's ratio (given in Table 6.1) were used to characterize the materials of each pavement structure. The predicted strains were compared at six grid points and the maximum strain selected for the analysis.

Figure 6.8 shows an example of the pavement structure layout and KENLAYER strain response locations for the B-Train drive axle dual tires at RTAC load on PTH 11. The six grid points for the analysis are shown in the plan view of the layout. The units are shown in the standard SI units required for inputs into KENLAYER.

Figure 6.8: Pavement Structure Layout and KENLAYER Strain Response Locations for B-Train Drive Axle Dual Tires at RTAC Load on PTH 11

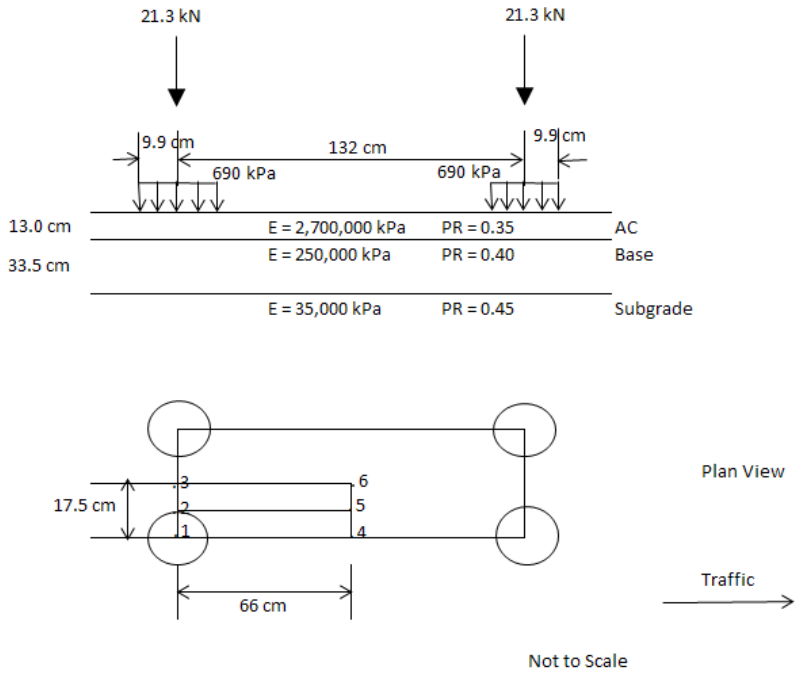

The example layout shows the B-Train drive dual tire at 21.3kN RTAC load with a tire contact radius of 99 mm, and tire inflation pressure (stress) of 690 kPa. The AC layer modulus was 2,700 MPa with Poisson's ratio of 0.35, and thickness of 130 mm. The granular base modulus was 250 MPa with Poisson's ratio of 0.4, and thickness of 335 mm. The subgrade modulus was 35 MPa with Poisson's ratio of 0.45 and semi-finite layer thickness.

For this analysis, two procedures were used to calculate the tire contact radius for KENLAYER;

a) the contact radius (CR), the conventional procedure of calculating the circular loaded area by dividing the load by the tire inflation pressure, and

b) the equivalent contact radius (ECR), the alternate procedure of calculating the circular loaded area by using measured contact areas to determine the uniform circular pressure distributions.

The equivalent tire contact radius (ECR) was developed for this thesis to assess whether the ECR was more representative of the true tire-pavement contact area than the CR, and whether a significant difference existed in the strain predictions depending on the procedure used to calculate the contact radius.

The circular radius, CR, was calculated from the tire load and tire inflation pressure, and Equation 6.2:

$$\sigma = \frac{P}{A} \text{ And } A = \pi CR^2 \text{ therefore } \qquad CR = \sqrt{\frac{P}{\sigma\pi}} \qquad (6.2)$$

Where:

CR=circular tire contact radius (m),

σ=tire inflation pressure (stress) (kPa),

A= circular tire-pavement contact area (m^2)

P=tire load (kN),

The equivalent circular tire contact radius, ECR, was calculated from the tire load, uniform contact stresses calculated from the measured tire-pavement contact areas, and Equation 6.3.

$$\sigma_m = \frac{P}{A_m} \text{ And } A_m = \pi ECR^2 \quad \text{therefore} \quad ECR = \sqrt{\frac{P}{\sigma_m \pi}} \qquad (6.3)$$

Where:

ECR=equivalent circular tire contact radius (m),

A_m= measured tire-pavement contact area (m^2) from pressure mat

σ_m=calculated uniform tire-pavement contact pressure (stress) (kPa) from measured contact area, A_m, and tire load, P

P=tire load (kN),

Table 6.5 presents the calculated tire contact radius CR and ECR at the B-Train tire loads and tire pressures on PTH 11.

Table 6.5: Tire Contact Radius CR and ECR at B-Train Tire Loads and Tire Pressures on PTH 11

Axle Group	Load Rating	Tire Load (kg)	Tire Load, (P) (kN)	Measured Tire Contact Area, (A_m) (100 square mm)		Calculated Tire-Pavement Contact Stress, (σ_m) (kPa)		Tire-Pavement Contact Stress (σ) (kPa)		Contact Radius, (CR) (mm)		Equivalent Contact Radius, (ECR) (mm)	
				Tire Inflation Pressure, (kPa)									
				690	345	690	345	690	345	690	345	690	345
Steering	AlL1	2,449	24.0	-	-	-	-	-	-	-	-	-	-
	A1N	2,472	24.3	-	-	-	-	-	-	-	-	-	-
	RTAC	2,419	23.7	-	-	-	-	-	-	-	-	-	-
Drive	A1L1	1,927	18.9	483	582	392	325	690	345	93	132	124	136
	A1N	1,930	18.9	483	582	392	325	690	345	93	132	124	136
	RTAC	2,173	21.3	534	602	399	354	690	345	99	140	130	138
Trailer1	A1L1	1,765	17.3	429	497	404	348	690	345	89	126	117	126
	A1N	1,785	17.5	429	497	408	352	690	345	90	127	117	126
	RTAC	2,079	20.4	438	531	466	384	690	345	97	137	118	130
Trailer2	A1L1	1,829	17.9	542	631	331	284	690	345	91	129	131	142
	A1N	1,924	18.9	542	631	348	299	690	345	93	132	131	142
	RTAC	2,071	20.3	479	563	424	361	690	345	97	137	123	134

Note: '-'=not applicable, steering axle not included in analysis

The results on PTH 11 show that the contact radii (CR) were 33% smaller on average (with standard deviation of 7%) than the equivalent contact radii (ECR) for each load at 690kPa tire pressure, which was considered significant. At 345kPa tire pressure, the contact radii (CR) were 2% smaller on average (with standard deviation of 5%) than the equivalent contact radii (ECR), which was not considered significant.

Table 6.6 presents the calculated tire contact radius CR and ECR at the B-Train tire loads and tire pressures on PR 304.

Table 6.6: Tire Contact Radius CR and ECR at B-Train Tire Loads and Tire Pressures on PR 304

Axle Group	Load Rating	Tire Load (kg)	Tire Load, (P) (kN)	Measured Tire Contact Area, (A_m) (100 square mm)		Calculated Tire-Pavement Contact Stress, (σ_m) (kPa)		Tire-Pavement Contact Stress (σ) (kPa)		Contact Radius, (CR) (mm)		Equivalent Contact Radius, (ECR) (mm)	
				Tire Inflation Pressure, (kPa)									
				690	345	690	345	690	345	690	345	690	345
Steering	B1L2	2,263	22.2	-	-	-	-	-	-	-	-	-	-
	B1N	2,358	23.1	-	-	-	-	-	-	-	-	-	-
	A1N	2,445	24.0	-	-	-	-	-	-	-	-	-	-
Drive	B1L2	1,322	13.0	327	391	398	332	690	345	77	109	102	112
	B1N	1,738	17.0	417	516	408	329	690	345	89	125	115	128
	A1N	1,903	18.7	483	582	387	321	690	345	93	131	124	136
Trailer1	B1L2	1,245	12.2	n/a	n/a	n/a	n/a	690	345	75	106	n/a	n/a
	B1N	1,475	14.5	367	440	395	330	690	345	82	116	108	118
	A1N	1,759	17.3	429	497	403	348	690	345	89	126	117	126
Trailer2	B1L2	1,263	12.4	n/a	n/a	n/a	n/a	690	345	76	107	n/a	n/a
	B1N	1,650	16.2	453	544	358	298	690	345	86	122	120	132
	A1N	1,924	18.9	542	631	349	300	690	345	93	132	131	142

Note: '-'=not applicable; steering axle not included in analysis
n/a=data not available; contact area not measured at load and tire pressure

The results on PR 304 also show that the contact radii (CR) were smaller than the equivalent contact radii (ECR), and that the differences were more significant at the higher tire pressure. The contact radii (CR) were 34% smaller on average (with standard deviation of 4%) than the equivalent contact radius (ECR) for each load at 690kPa tire pressure. At 345kPa tire pressure, the contact radii (CR) were 4% smaller on average (with standard deviation of 3%) than the equivalent contact radii (ECR) for each load. The two contact radii (CR and ECR) were inputs into KENLAYER.

KENLAYER STRAIN PREDICTIONS

KENLAYER was used to predict the critical tensile and compressive strains on PTH 11 and PR 304, and at the two contact radius, CR and ECR. The computational (CPU) time in KENLAYER was approximately 10 minutes for the strain predictions at each tire load. The CPU time for KENLAYER was one sixth that of the FEM.

Based on the software version used for this analysis, KENLAYER output horizontal tensile strains at the bottom of the AC layer instead of longitudinal and transverse tensile strains. To enable direct comparison between KENLAYER and FEM, horizontal strains were determined from the FEM predictions longitudinal and transverse strains (later in this chapter).

A number of general trends were observed from the results of the KENLAYER predictions. The maximum horizontal strain at the bottom of the AC layer generally occurred under the tire at the standard 690kPa tire pressure. At the reduced 345kPa tire pressure, the maximum horizontal strain at the bottom of the AC layer generally occurred at the edge of the tire or between the dual tires. The maximum vertical strains at the top of the subgrade generally occurred between the dual tires. The vertical strains were generally affected more by the tandem and tridem axle groups, and were more pronounced at greater depths in the pavements.

Table 6.7 presents the results supporting the general trends observed from the KENLAYER predicted horizontal and vertical strains at the edge of the tire, under the tire, and between the B-Train dual tire locations on PTH 11. The predictions were at RTAC loads and contact radius, CR.

TABLE 6.7: KENLAYER Predicted Horizontal and Vertical Strains at Edge of a Tire, Under a Tire, and Between B-Train Dual Tire Locations on PTH 11

Load Rating	Axle Group	Tire Load (kg)	Strain Orientation	KENLAYER-CR Predicted Strain (μm/m)					
				690 kPa			345 kPa		
				Under Tire	Edge of Tire	Between Dual Tires	Under Tire	Edge of Tire	Between Dual Tires
RTAC	Drive	2,173	Horizontal	230	219	206	177	187	187
			Vertical	-513	-549	-556	-503	-544	-546
	Trailer1	2,079	Horizontal	225	215	201	174	183	183
			Vertical	-481	-514	-531	-479	-518	-520
	Trailer2	2,071	Horizontal	226	217	204	176	185	185
			Vertical	-487	-521	-528	-476	-515	-516

The KENLAYER predicted horizontal and vertical strains at each tire locations on PTH 11 and PR 304 were compared and the maximum strains selected for the analysis. The predictions were at each contact radius; CR (designated KENLAYER-CR) and ECR (designated KENLAYER-ECR),

Table 6.8 presents the KENLAYER-CR and KENLAYER-ECR predicted horizontal and vertical strains at the B-Train tire loads and tire pressures on PTH 11.

TABLE 6.8: KENLAYER-CR and KENLAYER-ECR Predicted Horizontal and Vertical Strains at B-Train Loads and Tire Pressures on PTH 11

Axle Group	Load Rate	Tire Load (kg)	KENLAYER-CR Predicted Strains (µm/m)				KENLAYER-ECR Predicted Strains (µm/m)			
			Horizontal		Vertical		Horizontal		Vertical	
			Tire Inflation Pressure (kPa)							
			690 kPa	345 kPa	690 kPa	345 kPa	690 kPa	345 kPa	690 kPa	345 kPa
Steering	AlL1	2,449	-	-	-	-	-	-	-	-
	A1N	2,472	-	-	-	-	-	-	-	-
	RTAC	2,419	-	-	-	-	-	-	-	-
Drive	A1L1	1,927	211	171	-492	-487	177	169	-493	-486
	A1N	1,930	211	171	-492	-487	176	169	-490	-486
	RTAC	2,173	230	187	-556	-546	193	188	-547	-545
Trailer1	A1L1	1,765	196	161	-448	-442	168	163	-448	-446
	A1N	1,785	199	163	-458	-449	170	164	-452	-451
	RTAC	2,079	225	183	-531	-520	197	188	-526	-523
Trailer2	A1L1	1,829	207	169	-466	-463	166	161	-455	-455
	A1N	1,924	214	175	-486	-480	175	170	-478	-480
	RTAC	2,071	226	185	-528	-515	193	188	-515	-518

Note: '-'=not applicable; steering axle not included in analysis
CR=circular radius
ECR=equivalent circular radius

The results on PTH 11 show that the KENLAYER-CR predicted strains increased with increasing loads. When the 'Drive' axle load was increased from A1L1 to RTAC (a 13% load increase), there was a 9% increase on average in the horizontal strains at the bottom of the AC layer, and a 13% increase on average in the vertical strains at the top of the subgrade.

The predicted strains decreased with the reduction in tire pressure. When the 'Drive' axle tire pressure was reduced from 690kPa to 345kPa, there was an 18% decrease on average in the horizontal strain at the bottom of the AC layer, and a 1% decrease on average in the vertical strain at the top of the subgrade.

In general, the difference between KENLAYER-CR and KENLAYER-ECR predictions were significant only for horizontal strains at the 690kPa tire pressure. There was a 10% average difference between the KENLAYER-CR and KENLAYER-ECR at 690kPa tire pressure, and a 1% difference on average at 345kPa tire pressure for the horizontal strains. For vertical strains, there was a 3% average difference between the KENLAYER-CR and KENLAYER-ECR predictions at 690kPa tire pressure, and a 1% average difference at 345kPa tire pressure.

Table 6.9 presents the KENLAYER-CR and KENLAYER-ECR predicted vertical strains at the B-Train loads and tire pressures on PR 304.

TABLE 6.9: KENLAYER-CR and KENLAYER-ECR Predicted Vertical Strains at B-Train Loads and Tire Pressures on PR 304

Axle Group	Load Rating	Tire Load (kg)	KENLAYER-CR Predicted Strains (μm/m)		KENLAYER-ECR Predicted Strains (μm/m)	
			Vertical		Vertical	
			Tire Inflation Pressure (kPa)			
			690 kPa	345 kPa	690 kPa	345 kPa
Steering	B1L2	2,263	-	-	-	-
	B1N	2,358	-	-	-	-
	A1N	2,445	-	-	-	-
Drive	B1L2	1,322	-289	-287	-290	-292
	B1N	1,738	-385	-376	-378	-377
	A1N	1,903	-420	-412	-415	-412
Trailer1	B1L2	1,245	-280	-278	n/a	n/a
	B1N	1,475	-335	-332	-330	-328
	A1N	1,759	-394	-391	-394	-393
Trailer2	B1L2	1,263	-274	-270	n/a	n/a
	B1N	1,650	-351	-349	-350	-352
	A1N	1,924	-409	-407	-405	-407

Note: '-'=not applicable; steering axle not included in analysis
n/a=data not available
CR=circular radius
ECR=equivalent circular radius

The results on PR 304 also show that KENLAYER-CR vertical strains increased with increasing loads. When the 'Drive' axle load was increased from B1 to A1N (a 10% load increase), there was a 10% average increase in the vertical strain at the top of the subgrade.

The results also show that when the tire pressure was reduced from 690kPa to 345kPa, there was 1% average decrease in the vertical strain.

The difference between KENLAYER-CR and KENLAYER-ECR vertical strains were not significant on PR 304. There was a 3% and 0.5% average difference in predictions at 690kPa and 345kPa tire pressure, respectively.

COMPARISON OF KENLAYER AND FEM PREDICTED STRAINS

The KENLAYER predicted tensile and compressive strains were compared to the ABAQUS FEM predicted strains on PTH 11 and PR 304. The comparisons were based on (1) FEM with measured tire contact area and measured tire pressure distributions; (2) KENLAYER-CR with conventional contact radius (CR), and (3) KENLAYER-ECR with equivalent contact radius (ECR) from measured tire contact areas.

The FEM longitudinal and transverse strains at the bottom of the AC layer were converted to horizontal strains in order to provide a direct comparison with KENLAYER horizontal strains. The horizontal strain is important in damage analysis because it is the strain that causes cracking to initiate at the bottom of the surface layer, and is the strain used to predict fatigue damage in pavements [Huang, 2004].

The horizontal tensile strains were calculated from the longitudinal and transverse strains, using Equation 6.4 [Huang, 2004].

$$\varepsilon_t = \frac{1}{2}\left(\varepsilon_{xx} + \varepsilon_{yy}\right) \pm \sqrt{\left(\frac{1}{2}\left(\varepsilon_{xx} - \varepsilon_{yy}\right)\right)^2 + \varepsilon_{xy}^{\ 2}} \qquad (6.4)$$

Where:

ε_t = horizontal principal tensile strain,

ε_{yy} = horizontal transverse tensile strain,

ε_{xx} = horizontal longitudinal tensile strain,

ε_{xy} = longitudinal shear strain in the transverse (y) plane

The shear strains, ε_{yx}, were assumed to be negligible for the calculations because the breaking or traction force of the test vehicle was zero during the field testing, and the shear forces tended to be highest at the tire-pavement interface at the surface and diminished with depth [Yoder and Witzak, 1975]. The FEM sign convention of positive for tensile strains and negative for compressive strains was used.

Table 6.10 presents the FEM predicted horizontal strains at the B-Train loads and tire pressures on PTH 11. The horizontal strains were calculated from Equation 6.3 and the FEM predicted longitudinal and transverse strains given in Table 6.3. The FEM predicted vertical strains are also shown.

TABLE 6.10: FEM Predicted Horizontal and Vertical Strains at B-Train Loads and Tire Pressures on PTH 11

Axle Group	Load Rating	Tire Load (kg)	FEM Predicted Strains (μm/m)			
			Horizontal[1]		Vertical	
			Tire Inflation Pressure (kPa)			
			690kPa	345kPa	690kPa	345kPa
Steering	AlL1	2,449	-	-	-	-
	A1N	2,472	-	-	-	-
	RTAC	2,419	-	-	-	-
Drive	A1L1	1,927	180	151	-439	-432
	A1N	1,930	180	151	-439	-432
	RTAC	2,173	205	168	-495	-486
Trailer1	A1L1	1,765	167	150	-390	-386
	A1N	1,785	167	150	-390	-386
	RTAC	2,079	202	177	-458	-553
Trailer2	A1L1	1,829	183	162	-436	-433
	A1N	1,924	183	162	-436	-433
	RTAC	2,071	193	172	-457	-452

Note: [1] Calculated from longitudinal and transverse strains
'-'=not applicable; steering axle not included in analysis

The horizontal and vertical strains from KENLAYER-CR, KENLAYER-ECR and the FEM were compared and the differences quantified.

Table 6.11 presents the average percent differences between the KENLAYER-CR, KENLAYER-ECR and FEM predicted strains on PTH 11 and PR 304. The percent differences for PTH 11 were based on the KENLAYER-CR and ECR predictions (given in Table 6.8) and the FEM predictions (given in Table 6.10). The comparisons for PR 304 were based on the KENLAYER-CR and ECR predictions (given in Table 6.9) and the FEM predictions (given in Table 6.4). Positive percent differences indicated

KENLAYER strains were higher compared to the FEM. Negative percent differences indicated KENLAYER strains were lower compared to the FEM.

TABLE 6.11: Percent Differences between KENLAYER-CR, KENLAYER-ECR and FEM Predicted Strains at B-Train Loads on PTH 11 and PR 304

Road	Structural Prediction Models	Average Percent Difference between Strain Predictions (%)			
		Horizontal		Vertical	
		Tire Inflation Pressure (kPa)			
		690 kPa	345 kPa	690 kPa	345 kPa
PTH 11	KENLAYER-CR and FEM	14	8	12	9
	KENLAYER-ECR and FEM	-3	7	11	9
PR 304	KENLAYER-CR and FEM	-	-	13	13
	KENLAYER-ECR and FEM	-	-	13	14

Note: CR=circular radius
ECR=equivalent circular radius
'-'=not applicable, horizontal strains not used for AST surface

The results show that the average percent differences were lowest between KENLAYER-ECR and FEM predictions. There was a 3% average difference between KENLAYER-ECR and FEM for the horizontal strain at 690kPa tire pressure. There was a 14% average difference between the KENLAYER-CR and FEM for the horizontal strains at the same tire pressure. However, the average percent differences were the same between KENLAYER-ECR, KENLAYER-CR and FEM predictions for horizontal strains at 345kPa tire pressure, and vertical strains at 690kPa and 345kPa tire pressures.

Figure 6.9 show a plot of the average percent differences (from Table 6.11) between the KENLAYER-CR, KENLAYER-ECR and FEM predicted horizontal and vertical strains on PTH 11 and PR 304.

Figure 6.9: Percent Differences between KENLAYER-CR, KENLAYER-ECR and FEM Predicted Horizontal and Vertical Strains on PTH 11 and PR 304

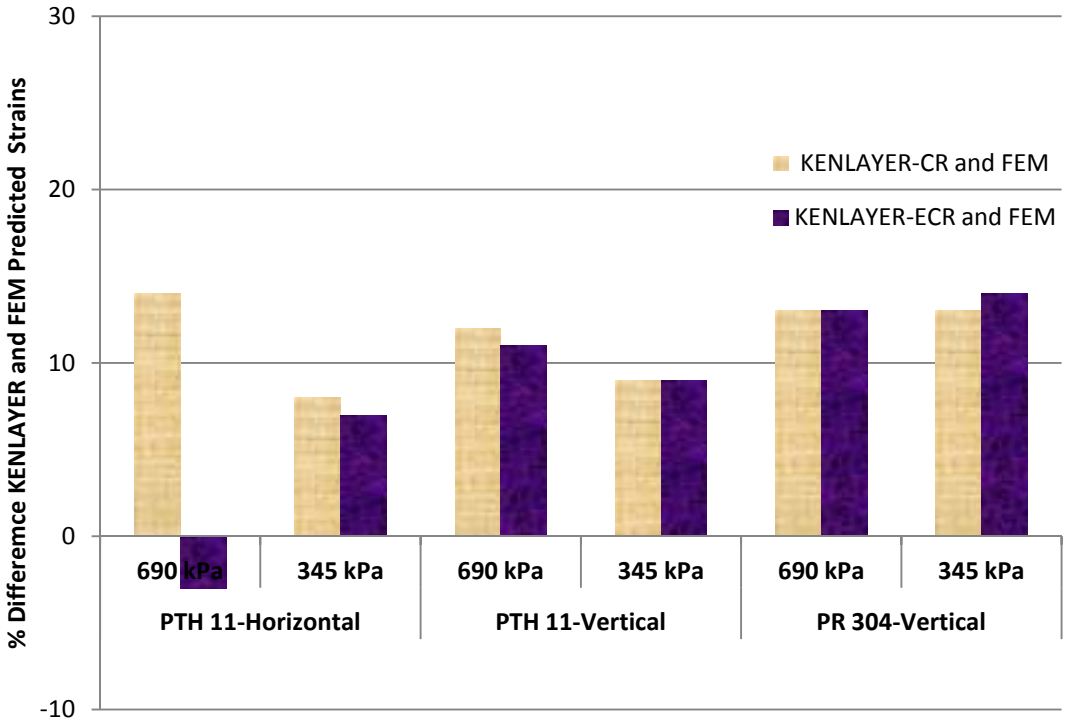

In general, the KENLAYER horizontal and vertical strain predictions were 14% higher on average than the FEM. No significant difference was found between the KENLAYER-CR and KENLAYER-ECR procedures for compressive strains at the top of the subgrade. This was because the differences in contact stress distributions were significant near the pavement surface and diminished with depth. The contact radius (CR) conventional procedure was still reasonable to predict vertical strains at the top of the subgrade and at low tire pressures. The equivalent contact radius (ECR) procedure was reasonable for predicting horizontal strains at the bottom of the AC layer at 690kPa tire pressure.

The comparisons showed KENLAYER confirmed the FEM trends of increasing strains at higher loads and higher tire pressure. Both models confirmed the positive impacts of reduced tire pressure on strains at the upper surface layer, but little impact on vertical strains at the top of the subgrade. The trends were consistent with the findings of Cowe-Falls and Knoth [2006] for overloads on pavement responses at the Nisku Test Road. Based on the similar trends and magnitude of the KENLAYER strain predictions compared to the FEM, KENLAYER could be calibrated to the measured strains and used for structural response modeling.

For this thesis, the ABAQUS FEM strains were used and calibrated for the structural response modeling at the Manitoba sites, because it incorporated the true measured tire-contact area and stress distributions on the surface of the pavement and generally considered more reliable.

6.3 FEM CALIBRATION

How well the predictions from structural response models match measured field values often determines whether calibration of the models is necessary. Predictions can be compared against measured field responses to determine the level of calibration.

The FEM predicted strains on PTH 11 and PR 304 were compared to the normalized measured strains from the spring condition. Calibration factors were calculated for the spring condition based on the ratio of the normalized measured strains divided by the FEM predicted strains, over all loads and tire pressures. The calibration factors for PTH

11 were calculated from the FEM predicted strains (given in Table 6.3), and the normalized measured strains (given in Table 5.5). For PR 304, the calibration factor for the vertical strains from PTH 11 was used because the subgrades were similar and measured vertical strains were not available for PR 304. The calibration factors were calculated using Equation 6.5.

$$C_r = \frac{\varepsilon_m}{\varepsilon_{FEM}} \qquad (6.5)$$

Where:

Cr=calibration factor

ε_m=measured strain

ε_{FEM}=FEM strain

Table 6.12 presents the average calibration factors for the FEM predicted strains at the B-Train loads and spring conditions on PTH 11 and PR 304. The calibration factors were calculated for the longitudinal, transverse, and vertical strains.

TABLE 6.12: Average Calibration Factors for FEM Predicted Strains at B-Train Loads and Spring Conditions on PTH 11 and PR 304

Road	Strain Orientation	Average Calibration Factors, C_r	
		C_r	STdev[1]
PTH 11	Longitudinal	4.2	0.4
	Transverse	5.1	0.9
	Vertical	3.1	0.2
PR 304	Longitudinal	-	-
	Transverse	-	-
	Vertical	3.1	0.2

Note: [1]Standard deviation; over all loads and tire pressures
'-'=not applicable for AST surface

The results show average calibration factors for the longitudinal and transverse strains on PTH 11, of 4.2 and 5.1. The vertical calibration factor was 3.1. Ullidtz [1998] have shown that measured vertical strain on top of the subgrade is usually twice the calculated values based on the elastic layer theory.

The high calibration factors (>2) in this research indicated that the FEM significantly under predicted the measured longitudinal and transverse strains for the spring conditions. This may be caused by a number of factors. The FEM model was static and based on idealized pavement structure and with no cracks or imperfections. This would produce stiffer pavement responses, and therefore lower predicted strains by the FEM. Additionally, the back-calculated base and subgrade modulus obtained for FWD deflections measurements during the spring period may not have adequately accounted for the FWD rapid loading and dilate effect on high pore water pressures in the base and subgrade. Finally, the effect of the retrofit installation was not modeled in the FEM.

For this analysis, the calibration factors were used to adjust the FEM predicted strains to the measured values. The calibration factors were considered to account for those factors that were not adequately captured by the material inputs in the static, linear FEM.

FEM PREDICTED AND CALIBRATED STRAINS AT MAXIMUM ALLOWABLE LOADS

The Manitoba provincial road agency bases its SWR limits on maximum allowable loads. Therefore, the FEM was used to predict the strains at the B-Train maximum allowable

and SWR loads (given in Table 4.5) on PTH 11 and PR 304. The calibration factors were applied to the FEM predictions.

The tire-pavement pressure distributions at the maximum allowable loads in the FEM were generated utilizing the measured tire pressure distributions from the B-Train standard 11R22.5 tire pressure testing during the spring of 2009. The process involved determining a tire pressure (stress) distribution factor (S_f) for the maximum allowable tire loads. S_f was obtained by dividing the maximum allowable tire load (P_{max}), by the total tire load (P_T). P_T was obtained by summing the tire load at each element (P_i) in the 2009 measured tire pressure distributions. (The tire loads in Table 4.6 were determined using this method and by summing the load in each element of the 2009 measured tire pressure distributions). The tire pressure distribution in each element (σ_{imax}) for the maximum allowable loads was determined by multiplying the stress distribution factor (S_f) by the measured pressure (stress) in each element (σ_{im}) of the 2009 distribution.

The load at each element (P_i), total load (P_T), stress distribution factor (S_f), and calculated tire pressure (stress) at each element of the maximum allowable load distribution (σ_{imax}) were calculated using Equation 6.6.

$$P_i = \sigma_{im} \times A_i \qquad (6.6)$$

$$P_T = \sum P_i$$

$$S_f = \frac{P_M}{P_T}$$

$$\sigma_{imax} = \sigma_{im} \times S_f$$

Where:

P_i=load at element (i) from 2009 measured pressure distribution, kN

σ_{im}=measured pressure (stress) at element (*i*) from 2009 pressure distribution, kPa

A_i=area of element (*i*), m^2, pressure mat element area=70.2 mm^2

P_T=total tire load, from2009 measured pressure distribution, kN

S_f=stress distribution factor

P_M=maximum allowable tire load, kN

σ_{imax}=calculated tire pressure (stress) at each element of the maximum allowable load distribution, kPa

This method can be used to generate tire pressure distributions for a standard 11R22.5 tire at any tire load and the same tire inflation pressure, assuming linear effects of tire pressure, and variation in stresses at the side wall of the tire were the same as the variation in the measured distributions.

The tire stress distributions were used in the FEM to predict the critical strains at the B-Train maximum allowable and SWR loads (given in Table 4.5) and spring conditions on PTH 11 and PR 304. The FEM predicted strains were multiplied by the calibration factors (given in Table 6.12).

Table 6.13 presents the FEM predicted and calibrated strains at the B-Train maximum allowable and SWR loads and spring conditions on PTH 11. The predictions were of the longitudinal and transverse at the bottom of the AC layer, and vertical strains at the bottom of the subgrade.

TABLE 6.13: FEM Predicted and Calibrated Strains at B-Train Maximum Allowable and SWR Loads and Spring Conditions on PTH 11

Axle Group	Load Rating	Axle Load (kg)	Tire Load (kg)	FEM Predicted and Calibrated Strains (μm/m)					
				Transverse		Longitudinal		Vertical	
				690kPa	345kPa	690kPa	345kPa	690kPa	345kPa
Steering	AlL1	5,500	2,750	-	-	-	-	-	-
	A1N	5,500	2,750	-	-	-	-	-	-
	RTAC	5,500	2,750	-	-	-	-	-	-
Drive	A1L1	14,400	1,800	577	485	760	630	-1280	-1256
	A1N	16,000	2,000	591	499	785	654	-1411	-1385
	RTAC	17,000	2,125	632	526	840	689	-1500	-1473
Trailer1	A1L1	20,700	1,725	607	530	726	647	-1188	-1172
	A1N	23,000	1,917	658	587	751	676	-1300	-1288
	RTAC	23,000	1,917	673	587	781	685	-1311	-1292
Trailer2	A1L1	14,400	1,800	540	485	726	630	-1250	-1256
	A1N	16,000	2,000	652	577	798	705	-1405	-1395
	RTAC	17,000	2,125	647	582	831	739	-1454	-1439

Note: '-'=not applicable; steering axle not included in analysis

Table 6.14 presents the FEM predicted and calibrated strains at the B-Train maximum legal and SWR loads and spring conditions on PR 304. The predictions were of the vertical strains at the top of the subgrade.

TABLE 6.14: FEM Predicted and Calibrated Strains at B-Train Maximum Legal and SWR Loads and Spring Conditions on PR 304

Axle Group	Load Rating	Axle Load (kg)	Tire Load (kg)	FEM Predicted and Calibrated Strains (μm/m)	
				Vertical	
				690kPa	345kPa
Steering	B1L2	3,575	1,788	-	-
	B1N	5500	2,750	-	-
	A1N	5,500	2,750	-	-
Drive	B1L2	9,425	1,178	-710	-707
	B1N	14,500	1,813	-1082	-1070
	A1N	16,000	2,000	-1190	-1178
Trailer1	B1L2	13,000	1,083	n/a	n/a
	B1N	20,000	1,667	-980	-973
	A1N	23,000	1,917	-1119	-1113
Trailer2	B1L2	9,425	1,178	n/a	n/a
	B1N	14,500	1,813	-1045	-1042
	A1N	16,000	2,000	-1166	-1156

Note: '-'=not applicable, steering axle not included in analysis
n/a=data not available, tire pressure distributions not measured

Figure 6.10 show the FEM predicted and calibrated longitudinal and transverse strains (given in Table 6.14) at the B-Train maximum allowable and SWR loads and spring conditions on PTH 11. Figure 6.11 show the FEM predicted and calibrated vertical strains on PTH 11.

Figure 6.10: FEM Predicted and Calibrated Longitudinal and Transverse Strains at B-Train Maximum Allowable and SWR Loads and Spring Conditions on PTH 11

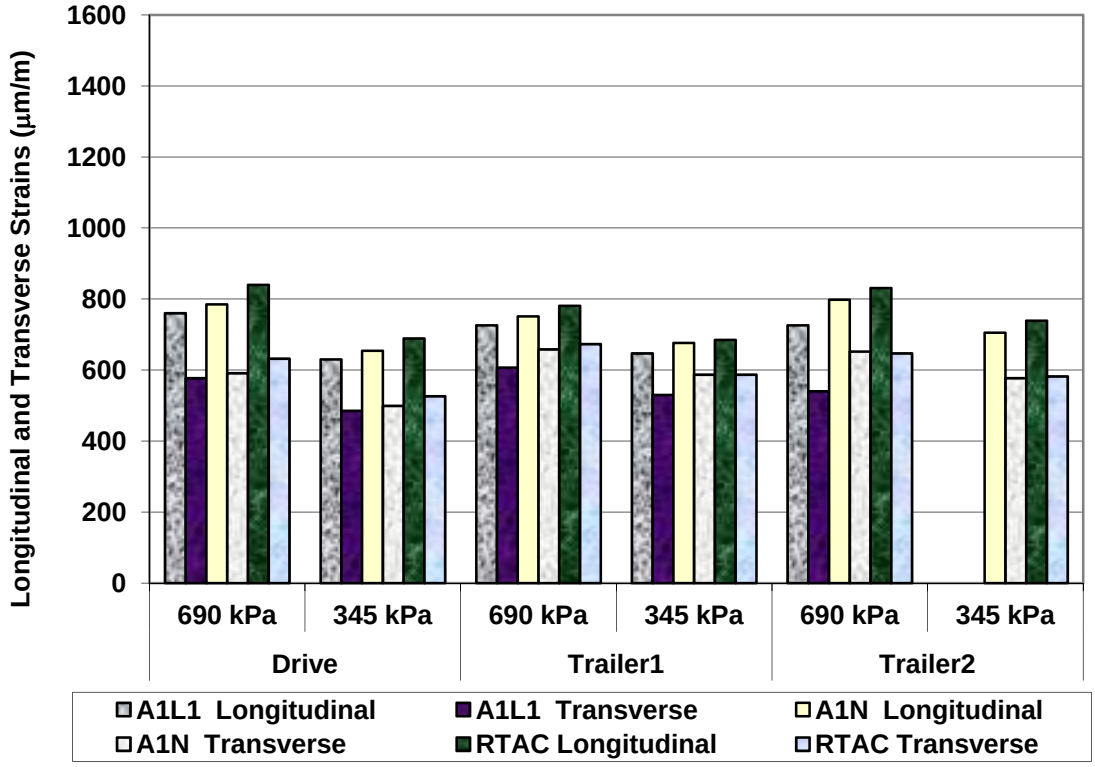

Figure 6.11: FEM Predicted and Calibrated Vertical Strains at B-Train Maximum Allowable and SWR Loads and Spring Conditions on PTH 11

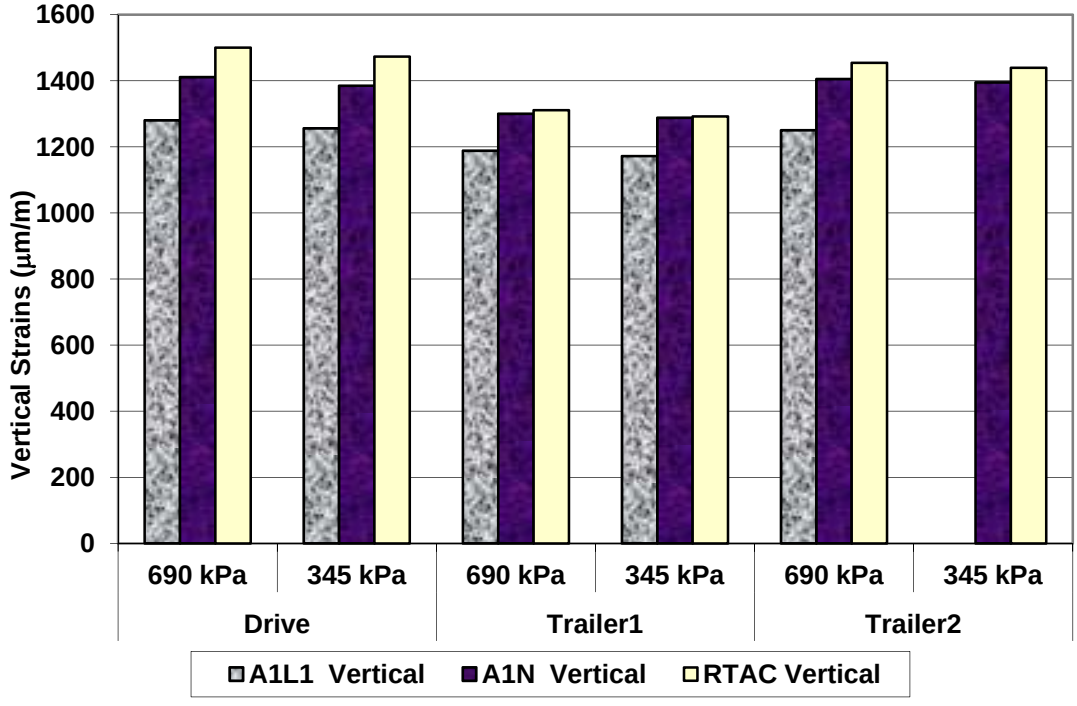

Figure 6.12 shows the FEM predicted and calibrated vertical strains (given in Table 6.15) at the B-Train maximum allowable and SWR loads and spring conditions on PR 304.

Figure 6.12: FEM Predicted and Calibrated Vertical Strains at B-Train Maximum Allowable and SWR Loads and Spring Conditions on PR 304

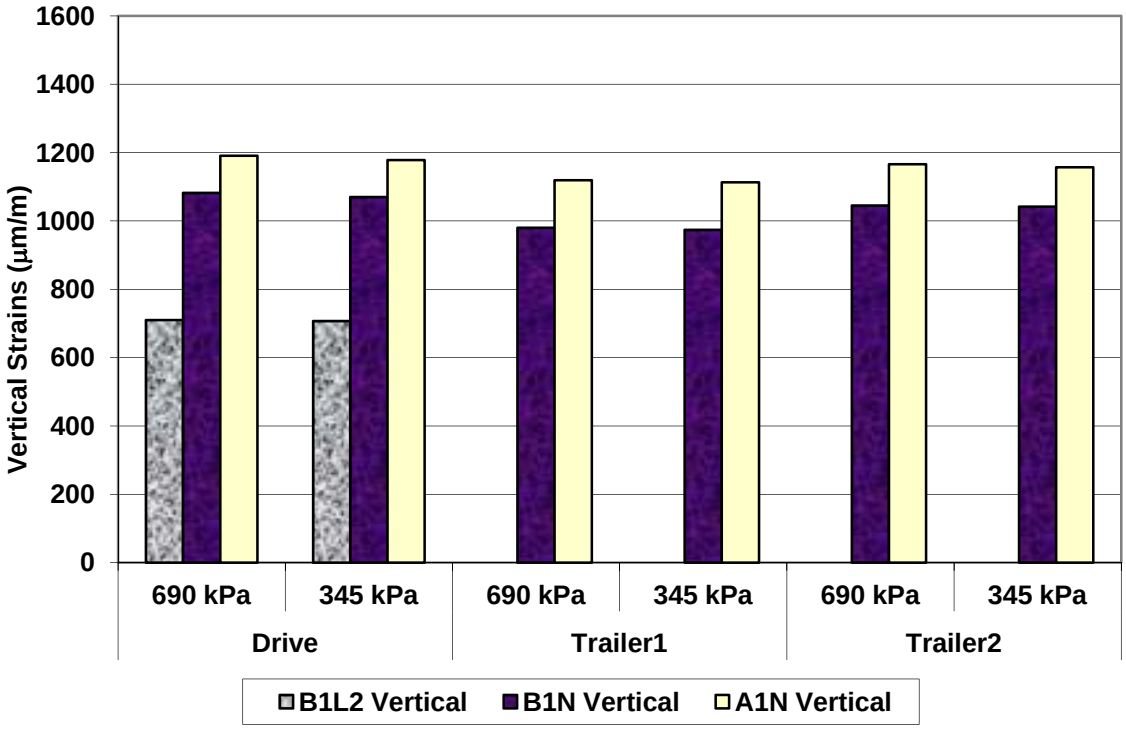

The FEM results show that the calibrated predictions produced the expected trends of increasing strains with increasing loads, and decreasing strains with reduced tire pressure. The FEM predicted and calibrated strains were used in the failure predictions and damage analysis at the Manitoba sites.

CHAPTER 7 - DAMAGE MODEL FAILURE PREDICTIONS AND DAMAGE ANALYSIS

Pavement deterioration over time is caused by repeated loads which consume pavement life. The relationship between pavement deterioration and load repetitions is important in failure predictions and damage analysis.

Damage analyses are based on the cumulative damage concept, which predict the ESAL repetitions to failure using critical strains and material properties in a pavement. Damage models are typically based on the failure criterion of fatigue cracking and rutting in flexible pavements. The fatigue damage model predicts the ESAL repetitions to failure based on the magnitude of the horizontal tensile strain at the bottom of the asphalt and the layer material properties. The rutting damage model predicts the ESAL repetitions to failure based on the magnitude of the vertical compressive strain at the top of the subgrade and the layer material properties. Damage, computed for a given period ESAL repetition, is accumulated using Miner's Hypothesis, up to a damage value of 1.0 for each distress mode.

This chapter presents the failure predictions and damage analysis for Manitoba pavements using the Asphalt Institute (AI) and Mechanistic Empirical Design Guide (MEPDG) damage models. Local damage models were also developed for this thesis using measured strains and ESAL repetitions to failure from flexible pavements at the MnROAD low volume facility.

7.1 AI AND MEPDG DAMAGE MODEL FAILURE PREDICTIONS

The AI and MEPDG damage models were used to predict the ESAL repetitions to fatigue cracking and rutting failure for the Manitoba sites at the B-Train maximum allowable and SWR loads and two tire pressures. The FEM predicted and calibrated strains were used in the damage models.

Table 7.1 presents the FEM predicted and calibrated horizontal and vertical strains at the B-Train maximum allowable and SWR loads for the spring conditions on PTH 11. The horizontal strains were calculated from Equation 6.3 and the FEM predicted and calibrated longitudinal and transverse strains (given in Table 6.14).

TABLE 7.1: FEM Predicted and Calibrated Horizontal and Vertical Strains at B-Train Maximum Allowable and SWR Loads for Spring Conditions on PTH 11

Axle Group	Load Rating	Axle Load (kg)	Tire Load (kg)	FEM Predicted and Calibrated Strains (μm/m)			
				Horizontal		Vertical	
				Tire Inflation Pressure (kPa)			
				690kPa	345kPa	690kPa	345kPa
Steering	AlL1	5,500	2,750	-	-	-	-
	A1N	5,500	2,750	-	-	-	-
	RTAC	5,500	2,750	-	-	-	-
Drive	A1L1	14,400	1,800	577	485	-1280	-1256
	A1N	16,000	2,000	591	499	-1411	-1385
	RTAC	17,000	2,125	632	526	-1500	-1473
Trailer1	A1L1	20,700	1,725	607	530	-1188	-1172
	A1N	23,000	1,917	658	587	-1300	-1288
	RTAC	23,000	1,917	673	587	-1311	-1292
Trailer2	A1L1	14,400	1,800	540	485	-1250	-1256
	A1N	16,000	2,000	652	577	-1405	-1395
	RTAC	17,000	2,125	647	582	-1454	-1439

Note: '-'=not applicable, steering axle not included in analysis

Table 7.2 presents the FEM predicted and calibrated vertical strains at the B-Train maximum allowable and SWR loads for the spring conditions on PR 304.

TABLE 7.2: FEM Predicted and Calibrated Vertical Strains at B-Train Maximum Allowable and SWR Loads for Spring Conditions on PR 304

Axle Group	Load Rating	Axle Load (kg)	Tire Load (kg)	FEM Predicted and Calibrated Strains (μm/m)	
				Vertical	
				690kPa	345kPa
Steering	B1L2	3,575	1,788	-	-
	B1N	5500	2,750	-	-
	A1N	5,500	2,750	-	-
Drive	B1L2	9,425	1,178	-710	-707
	B1N	14,500	1,813	-1082	-1070
	A1N	16,000	2,000	-1190	-1178
Trailer1	B1L2[1]	13,000	1,083	n/a	n/a
	B1N	20,000	1,667	-980	-973
	A1N	23,000	1,917	-1119	-1113
Trailer2	B1L2[1]	9,425	1,178	n/a	n/a
	B1N	14,500	1,813	-1045	-1042
	A1N	16,000	2,000	-1166	-1156

Note: '-'=not applicable
n/a=data not available, tire pressure distribution not measured

AI DAMAGE MODEL FAILURE PREDICTIONS

The AI damage models were used to predict the ESAL repetitions to fatigue and rutting failure on PTH 11 and the ESAL repetitions to rutting failure on PR 304 at the B-Train maximum allowable and SWR loads and two tire pressures. For PR 304, only the repetitions to rutting failure were predicted, since the AI fatigue model was not developed

for thin AST surfaces. The damage analysis was divided into twelve months per year, with late spring (May) selected for the SWR analysis period in Manitoba.

Table 7.3 presents the AI model predicted ESAL repetitions to fatigue cracking and rutting failures at the B-Train maximum allowable and SWR loads for the spring condition on PTH 11. The B-Train Steering axle was not included in the analysis. This was possible because the Steering axle load was not a variable during the spring period and the pavement response analysis was based on dual tires, and not the single tire on the Steering axle. The ESAL repetitions to fatigue failure were calculated from Equation 2.4, and the FEM calibrated horizontal strains (given in Table 7.1) and AC modulus (given in Table 6.1). The ESAL repetitions to rutting failure were calculated from Equation 2.5 and the FEM calibrated vertical strains (given in Table 7.1).

TABLE 7.3: AI Model Predicted ESAL Repetitions to Fatigue and Rutting Failures at B-Train Maximum Allowable and SWR Loads for Spring Conditions on PTH 11

Load Level	Strain Orientation	AI-Predicted Repetitions to Failure, $N_f \times 10^3$					
		Drive		Trailer1		Trailer2	
		690 kPa	345 kPa	690 kPa	345 kPa	690 kPa	345 kPa
Fatigue Failure							
A1L1	Horizontal	65	115	55	86	80	115
A1N	Horizontal	60	104	42	61	43	65
RTAC	Horizontal	48	88	39	61	44	63
Rutting Failure							
A1L1	Vertical	12	13	17	18	14	13
A1N	Vertical	8	9	11	12	8	8
RTAC	Vertical	6	7	11	12	7	7

The results of the AI model predictions on PTH 11 show that the ESAL repetitions to fatigue and rutting failures decreased as loads increased. When the Drive axle load at 690 kPa tire pressure was increased by two load levels, from A1L1 to RTAC (18% load increase), there was a 27% decrease in the repetitions to fatigue failure, and a 50% decrease in the repetitions to rutting failure.

The results also show that ESAL repetitions to fatigue and rutting failure increased at reduced tire pressure. When the tire pressure on the Drive axle load was reduced from 690 kPa to 345 kPa, there was a 60% increase in the repetitions to fatigue failure, and a 6% increase in the repetitions to rutting failure.

The results show that the effect of increased loads on ESAL repetitions to failure was more pronounced in the subgrade layer, while the effect of reduced tire pressure on repetitions to failure was more pronounced in the AC surface layer. This may be due to the difference in stress distribution in the pavement. At low tire pressure, the pressures were distributed over a larger surface area and created lower stresses in the surface layer. Higher loads tended to substantially increase the stresses deeper in the base and subgrade layers. This was more pronounced in the spring condition when the high moisture content in the base and subgrade tended to reduce the ability of those layers to distribute the loads over a wider area.

The AI predictions also show the greater impact of load increases on ESAL repetitions to failure, when compared to the impact of load increases on FEM predicted strains. For example on PTH 11, when the Drive axle load at 690 kPa was increased (Table 7.1) from A1L1 to RTAC (a load increase of 18%), there was a 9% increase in the horizontal strain

(related to fatigue failure), and a 17% increase in the vertical strain (related to rutting failure). For the same load level increase and tire pressure (Table 7.3) there was a 27% decrease in the ESAL repetitions to fatigue failure, and a 50% decrease in the ESAL repetitions to rutting failure.

Therefore, for each 1% increase in load, there was an approximate 0.5% and 1% increase in horizontal and vertical strains, respectively and an approximate 1.5% and 3% decrease in ESAL repetitions to fatigue and rutting failures, respectively. A small increase in strain can have a larger effect on the ESAL repetition to failure.

Table 7.4 presents the AI model predicted ESAL repetitions to rutting failure at the B-Train maximum allowable and SWR loads for the spring condition on PR 304. The repetitions to rutting failure were calculated from Equation 2.5 and the FEM calibrated vertical strains (given in Table 7.2). The B-Train Steering axle was also not included in the analysis.

TABLE 7.4: AI Model Predicted ESAL Repetitions to Rutting Failure at B-Train Maximum Allowable and SWR Loads for Spring Conditions on PR 304

Load Level	Strain Orientation	AI-Predicted Repetitions to Failure, $N_f \times 10^3$					
		Drive		Trailer1		Trailer2	
		690 kPa	345 kPa	690 kPa	345 kPa	690 kPa	345 kPa
Rutting Failure							
B1L2	Vertical	171	174	n/a	n/a	n/a	n/a
B1N	Vertical	26	27	40	41	30	31
A1N	Vertical	17	18	22	23	19	19

Note: n/a=data not available, tire pressure distribution not measured

The results of the AI predictions on PR 304 show that the ESAL repetitions to rutting failure decreased as loads increased. When the Drive axle load at 690 kPa tire pressure was increased from B1N to A1N (10% load increase), there was a 35% decrease in the repetitions to rutting failure.

The results also show that repetitions to rutting failure increased at reduced tire pressure. When the tire pressure on the Drive axle load was reduced from 690 kPa to 345 kPa, there was a 5% increase in the ESAL repetitions to rutting failure.

Similar to PTH 11, the AI predicted repetitions to rutting failure show that increased loads had a significantly negative impact on rutting, and reduced tire pressure had a minimal impact on rutting under spring conditions.

MEPDG Damage Model Failure Predictions

The MEPDG damage models were used to predict the ESAL repetitions to fatigue and rutting failure on PTH 11 and PR 304 at the B-Train maximum allowable and SWR loads and two tire pressures. Only the ESAL repetitions to rutting failure were predicted on PR 304 since the MEPDG fatigue model was not developed for thin AST surfaces.

The MEPDG model predicted ESAL repetitions to fatigue failure on PTH 11 were calculated from Equation 2.6. For the fatigue equation, the parameter for the asphalt mix property, C, and thickness correction for bottom-up cracking, C_H, were calculated using an effective asphalt content of 10% by volume, and 4% air voids on PTH 11. Therefore C was 1.31 and C_H was 250.3. The fatigue calibration parameters β_{f1}, β_{f2}, and β_{f3} were set to

the global constant of 1, due to the absence of local field calibration parameters for the MEPDG fatigue model.

The MEPDG model predicted ESAL repetitions to rutting failure were calculated from Equation 2.7. For the rutting equation, the calibration constant, β_{s1}, was set to 1 for the global setting due to the absence of a local calibration constant. The local soil constants β and ρ were calculated as 0.059 and $1.8x10^{14}$, respectively, using the additional MEPDG equations and soil volumetric moisture content of 35% and resilient modulus of 35 MPa for the local clay subgrade on PTH 11. The soil volumetric moisture content of 35% and resilient modulus of 24 MPa were used for the local clay subgrade on PR 304. The rutting calibration coefficient for soil type, k_{s1}, was set to 1.35 for a fine grained soil. The plastic strain rate in the subgrade, ε_p, was estimated at 0.006 in/in, based on the results of lab tests by Yapa and Lytton [1988] at Texas A&M University.

Yapa and Lytton's study was based on lab testing of the rutting potential in base and subgrade layers to 300,000 load repetitions and 162 different pavement sections. The subgrade plastic strain of 0.006 in/in was for rut depths of approximately 0.48 in. or 12.2 mm (based on the method of superposition) and for base modulus of 40,000 psi (275 MPa) and subgrade modulus of 5000 psi (34 MPa). Since the base and subgrade modulus on PTH 11 and PR 304 were similar in magnitude, the plastic strain was considered appropriate as input into the MEPDG rutting model.

Table 7.5 presents the MEPDG model predicted ESAL repetitions to fatigue and rutting failure at the B-Train maximum allowable and SWR loads for the spring condition on PTH 11. The B-Train Steering axle was not included in the damage analysis. The

repetitions to fatigue failure on PTH 11 were calculated from Equation 2.6 and the FEM calibrated horizontal strains given in Table 7.1 and AC modulus given in Table 6.1. The repetitions to rutting failure were calculated from Equation 2.7 and the FEM calibrated vertical strains given in Table 7.1.

TABLE 7.5: MEPDG Model Predicted ESAL Repetitions to Fatigue and Rutting Failures at B-Train Maximum Allowable and SWR Loads for Spring Conditions on PTH 11

Load Level	Orientation	MEPDG Predicted Repetitions to Failure, N_f x 10^3					
		Drive		Trailer1		Trailer2	
		690 kPa	345 kPa	690 kPa	345 kPa	690 kPa	345 kPa
Fatigue Failure							
A1L1	Horizontal	50	99	41	70	65	99
A1N	Horizontal	45	89	30	47	31	50
RTAC	Horizontal	35	72	27	47	32	48
Rutting Failure							
A1L1	Vertical	28	30	39	41	31	30
A1N	Vertical	18	20	26	27	18	19
RTAC	Vertical	14	15	25	26	16	16

The results of the MEPDG model predictions on PTH 11 show that the ESAL repetitions to fatigue and rutting failure decreased as loads increased. When the Drive axle load at 690 kPa tire pressure was increased by two load levels, from A1L1 to RTAC (18% load increase), there was a 30% decrease in the repetitions to fatigue failure, and a 50% decrease in the repetitions to rutting failure.

The results also show that ESAL repetitions to fatigue and rutting failure increased at reduced tire pressure. When the tire pressure on the Drive axle load was reduced from

690kPa to 345kPa, there was a 100% increase in the repetitions to fatigue failure, and a 7% increase in the axle repetitions to rutting failure.

Table 7.6 presents the MEPDG model predicted ESAL repetitions to rutting failure at the B-Train maximum allowable and SWR loads for the spring condition on PR 304. The fatigue failure was not included on PR 304, since the MEPDG fatigue model was not developed for thin AST pavements. The B-Train Steering axle was also not included in the analysis. The repetitions to rutting failure on PR 304 were calculated from Equation 2.7 and the FEM predicted and calibrated vertical strains (given in Table 7.2).

TABLE 7.6: MEPDG Model Predicted ESAL Repetitions to Rutting Failure at B-Train Maximum Allowable and SWR Loads for Spring Conditions on PR 304

Load Level	Orientation	MEPDG-Predicted Repetitions to Failure, N_f x 10^3					
		Drive		Trailer1		Trailer2	
		690 kPa	345 kPa	690 kPa	345 kPa	690 kPa	345 kPa
Rutting Failure							
B1L2	Vertical	480	490	n/a	n/a	n/a	n/a
B1N	Vertical	59	63	95	98	70	71
A1N	Vertical	38	40	51	52	42	44

Note: n/a=data not available, tire pressure distribution not measured

The results of the MEPDG model predictions on PR 304 show that the ESAL repetitions to rutting failure decreased as loads increased. When the Drive axle load at 690kPa tire pressure was increased from B1N to A1N (10% load increase), there was a 36% decrease in the repetitions to rutting failure. The results also show that repetitions to rutting failure increased at reduced tire pressure. When the tire pressure on the Drive axle load was

reduced from 690kPa to 345kPa, there was a 7% increase in the repetitions to rutting failure.

In general, the trends from the AI and MEPDG model predicted ESAL repetitions to fatigue and rutting failures were similar and showed that increased loads had a negative impact on repetitions to fatigue failure, while reduced tire pressure had a positive impact on repetitions to fatigue failure for the spring conditions. The model results also showed that increased loads had a significantly negative impact on ESAL repetitions to rutting failure, even at reduced tire pressure.

7.2 LOCAL DAMAGE MODEL FAILURE PREDICTIONS

The premise behind mechanistic-empirical damage models is the ability to relate pavement response to observed performance. One important aspect of model predictions is how local conditions can be related in the model to improve predictions.

Therefore local fatigue and rutting damage models were developed for this analysis using the measured strains and pavement distresses from the MnROAD flexible pavement cells. The Local model relationships were based on layer modulus, measured strains, and ESAL repetitions to fatigue cracking and rutting failure for the spring conditions.

The AC layer moduli were obtained from the MnROAD database and lab testing using the LTPP P07 resilient modulus protocol for asphalt mixtures [FHWA, 2010]. The base and subgrade modulus was obtained from triaxial testing results from the database. The

base and subgrade modulus were adjusted using the lab results by Berg et al [1996] to account for spring thaw-weakened conditions.

Berg et al [1996] tested samples of the MnROAD clay subgrade and samples of bases under seasonal frost, thawed and saturated conditions. Specimens were molded at specified moisture and density and then saturated. Once saturated, the samples were frozen. The specimens were tested using repeated-load triaxial at varying confining pressure and deviator stresses. Testing was first conducted at temperatures below freezing (-2^{o}C or lower). The specimens were allowed to thaw in the triaxial device and subsequently retested in a thawed, saturated state.

Berg et al calculated the resilient modulus from the measured resilient axial and radial strains at varying confining pressures and deviator stresses. Berg et al also developed resilient modulus regression equations from the test data to relate thawed bases and subgrades based on moisture content, confining pressure, and dry density.

Table 7.7 presents the layer modulus used for the spring conditions on the MnROAD Cell 26-A, Cell 27-A, and Cell 28-A. The resilient modulus equations from Berg et al, along with the resilient strains from the lab triaxial results from the MnROAD data base, were used to estimate the AC, base, and subgrade modulus.

TABLE 7.7: Layer Modulus Used for Spring Conditions on MnROAD Cell 26-A, Cell 27-A, Cell 28-A

Cell	Layer	Thickness (mm)	TDR Moisture Content (%)[1]	Lab Modulus (MPa)	Poisson's Ratio
26-A	AC	127	-	3,500	0.35
	Clay subgrade	Semi-infinite	36	35	0.45
27-A	AC	76	-	3,500	0.35
	Granular Base	279	17	345	0.40
	Clay subgrade	Semi-infinite	38	35	0.45
28-A	AC	76	-	3,500	0.35
	Granular Base	330	22	285	0.40
	Clay subgrade	Semi-infinite	37	35	0.45

Note: [1]Moisture content from MnROAD database measured May 2&13, 1996; TDR=time domain reflectometer
'-'=not applicable

The horizontal strains for the MnROAD pavement cells were calculated from the measured longitudinal and transverse strains at the bottom of the AC layer, since damage models use horizontal strains to predict fatigue in the AC layer. The measured vertical soil pressures at the top of the subgrade were converted to vertical strains through a proportioning process using the KENLAYER pavement analysis software. For the proportioning process, the layer modulus, MnROAD cell structures, 5-axle semi load and circular radius were input into KENLAYER. Vertical stresses and vertical strains were predicted at the location where the pressure cell was installed in the subgrade. The ratio of the predicted vertical strain and predicted vertical stress at the pressure cell location was multiplied by the measured vertical pressure, to calculate the corresponding vertical strain.

The ESAL repetitions at failure on Cell 26-A, Cell 27-A, and Cell 28-A were obtained from the plots of the rut depths and fatigue cracking versus ESALs (calculated by MnROAD using the 1993 AASHTO Design Guide) from construction to demolition.

The pavements were considered to have failed when fatigue cracking was greater than 10% of the wheelpath area, and when rut depths were greater than 12.5 mm.

Table 7.8 presents the horizontal strains and ESAL repetitions at fatigue failure for the spring conditions on the 80KIP and 102KIP lanes of the MNROAD Cell 26-a, Cell 27-A, and Cell 28-A. The ESAL repetitions at fatigue failure (cracking greater than 10% of the wheelpath area) were selected for the 80KIP lane from Figure 5.13, and the 102KIP lane from Figure 5.14. The horizontal strains for each semi trailer axle group were calculated from Equation 6.3, and the measured longitudinal and transverse strains (given in Table 5.11).

Table 7.8: Horizontal Strains and ESAL Repetitions at Fatigue Failure for Spring Conditions on 80KIP and 102 KIP Lanes of MnROAD Cell 26-A, Cell 27-A, Cell 28-A

Axle Group	Strain Orientation	Horizontal Strains and ESALs at Fatigue Failure					
		26-A		27-A		28-A	
		Horizontal Strain (μm/m)	ESALs at Failure	Horizontal Strain (μm/m)	ESALs at Failure	Horizontal Strain (μm/m)	ESALs at Failure
80KIP Lane							
Steering	Horizontal	405	>110,000	n/a	90,000	567	65,000
Drive	Horizontal	447	>110,000	531	90,000	601	65,000
Trailer	Horizontal	442	>110,000	523	90,000	748	65,000
102KIP Lane							
Steering	Horizontal	456	>100,000	n/a	100,000[1]	n/a	71,000
Drive	Horizontal	486	>100,000	n/a	100,000[1]	n/a	71,000
Trailer	Horizontal	585	>100,000	n/a	100,000[1]	621	71,000

Note: [1]Extrapolated to Failure
n/a=data not available

Table 7.9 presents the vertical strains and measured 5-axle semi trailer ESAL repetitions at rutting failure for the spring conditions on the 80KIP and 102KIP lanes of MnROAD

Cell 26-A, Cell 27-A, and Cell 28-A. The ESAL repetitions at rutting failure (rut depths greater than 12.5 mm) were selected from Figure 5.11 for the 80KIP lane and Figure 5.12 for the 102KIP lane.

Table 7.9: Vertical Strains and ESAL Repetitions at Rutting Failure for Spring Conditions on 80KIP and 102 KIP Lanes of MnROAD Cell 26-A, Cell 27-A, Cell 28-A

Axle Group	Strain Orientation	Computed Vertical Strains [1] and ESALs at Rutting Failure					
		26-A		27-A		28-A	
		Vertical Strain (μm/m)	ESALs at Failure	Vertical Strain (μm/m)	ESALs at Failure	Vertical Strain (μm/m)	ESALs At Failure
80KIP Lane							
Steering	Vertical	798	90,000	n/a	45,000	n/a	22,000
Drive	Vertical	1,182	90,000	2,878	45,000	n/a	22,000
Trailer	Vertical	1,273	90,000	3,341	45,000	n/a	22,000
102KIP Lane							
Steering	Vertical	n/a	50,000	1,499	65,000	n/a	42,000
Drive	Vertical	2,164	50,000	2,118	65,000	n/a	42,000
Trailer	Vertical	2,273	50,000	2,353	65,000	n/a	42,000

Note: [1]Vertical strains computed from vertical stresses
n/a=data not available

The vertical strains for each semi trailer axle group were computed from the measured vertical pressure. For example, the layer modulus for Cell 26-A and 80KIP steering axle tire load were input into KENLAYER (i.e. 26.8 kN load with a circular radius of 111 mm). The vertical stress and strain at the subgrade pressure cell location were predicted. The predicted vertical strain and vertical stress, at the pressure cell location were 839μm/m and 41 kPa, respectively. The ratio of the predicted vertical strain to vertical stress was 2.0×10^{-5}. The ratio was multiplied by the measured vertical pressure of 39 kPa from Table 5.12. The computed vertical strain at the pressure cell location was

798μm/m. This analysis was conducted for each semi axle group loads, and pavement cell structure to obtain the vertical strains in Table 7.9.

LOCAL FAILURE MODELS

A regression analysis was used to develop the Local fatigue and rutting failure models. The regression equations were power functions of the ESALs at fatigue and rutting failure, and the measured strains from the MnROAD cells, as given in Table 7.8 and Table 7.9. The strains from the steering axle were excluded from the regression equations because damage models are typically developed for strain measurements from dual-tired axles.

The regression equations developed for the Local fatigue and rutting failure are shown in Equation 7.1 and 7.2, respectively.

Local Fatigue Damage Model:

$$N_f = 24.089\,\varepsilon_t^{-1.091} \qquad (7.1)$$

Local Rutting Damage Model:

$$N_f = 542.57\,\varepsilon_v^{-0.756} \qquad (7.2)$$

Where:

N_f = Repetitions to failure,

ε_t = horizontal tensile strain,

ε_v = vertical compressive strain

Unlike other fatigue models, the AC modulus was not included in the Local fatigue model given in Equation 7.1. The AC modulus was not a significant variable in the equation,

because the MnROAD cells used in the model were constructed with the same asphalt mixture. Equation 7.1 would therefore be valid only for pavements with mixtures having similar AC modulus.

Figure 7.1 illustrates the Local fatigue damage model. The figure shows the negative relationship between the ESAL repetitions to fatigue failure versus the horizontal strains at the bottom of the AC layer. The regression fit is relatively good, with a coefficient of determination, R^2, of 0.76.

Figure 7.1: Illustration of Local Fatigue Damage Model

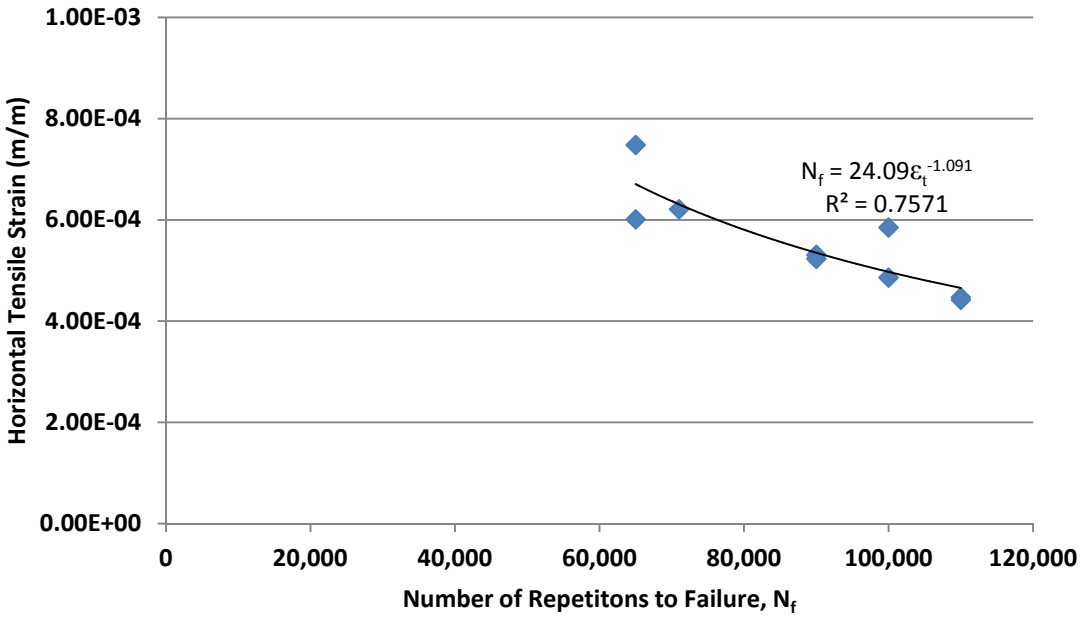

Figure 7.2 illustrates the Local rutting model. The figure also shows the negative relationship between the ESAL repetitions to rutting failure versus the vertical strains at the top of the subgrade. The regression fit is relatively good, with a coefficient of determination, R^2, of 0.81.

Figure 7.2: Illustration of Local Rutting Damage Model

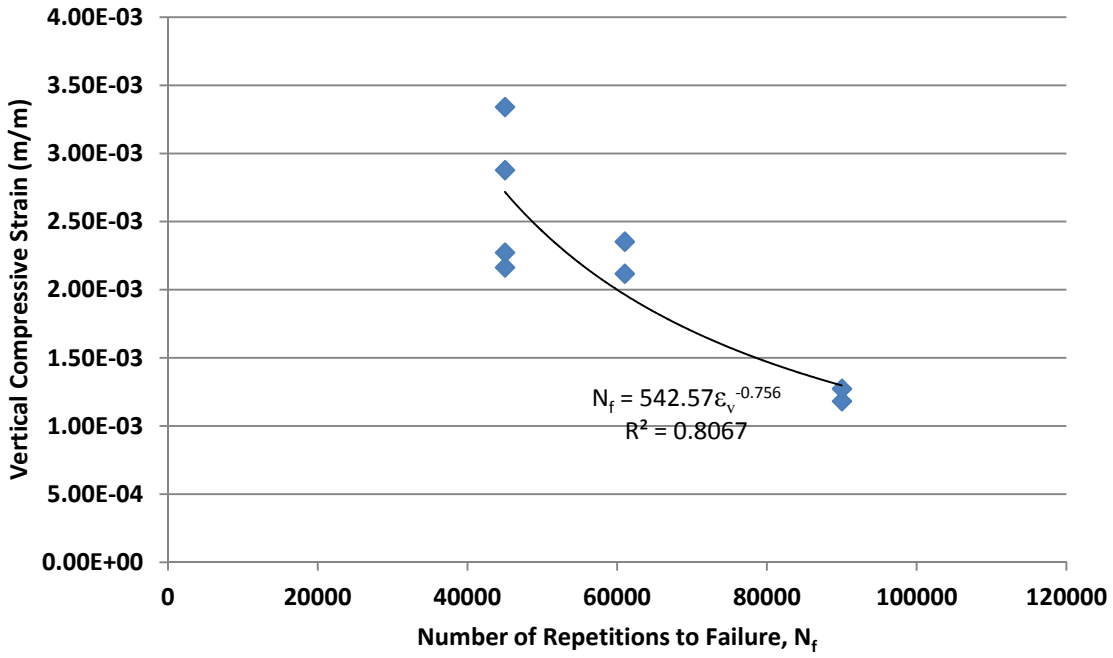

Table 7.10 compares the Local and various other fatigue and rutting damage models. The summary includes the damage models by Wu and Hossain [2003], the Minnesota pavement design guide (MnPAVE) [Levinson et al, 2005], the Asphalt Institute [AI, 1982], and the Mechanistic Empirical Pavement Design Guide (MEPDG) [NCHRP, 2007].

The Local, AI, and MnPAVE rutting models assumed that rutting in all layers was linearly proportional to the strain at the top of the subgrade, and was valid only when permanent deformation was caused by the weak subgrade (such as during the spring period) rather than by the overlying layers [Huang, 2004].

Table 7.10: Comparisons of Local and Various Other Fatigue and Rutting Damage Models

Damage Models	Regression Parameters			
	$f_{1,4}$	$f_{2,5}$	f_3	R^2
Fatigue Models $N_f = f_1 \varepsilon_t^{f_2} E^{f_3}$				
Local Damage Model	24.09	-1.091	-	0.76
MnPAVE[1] [2]AC<115 mm [2]AC≥115mm	 0.107 0.377	 -3.291 -3.291	 -0.854 -0.854	 - -
Lab Model by Wu & Hossain [2003]	18.79[3]	-1.133	-	0.98
Asphalt Institute (AI)	0.0796	-3.291	-0.854	-
MEPDG [NCHRP, 2007]	$N_f = 0.007566\, CC_H \beta_{f1} \varepsilon_t^{-3.9492\beta_{f2}} E_{HMA}^{-1.281\beta_{f3}}$ $C = 10^{4.84\left(\frac{V_{be}}{V_a+V_{be}} - 0.69\right)}$ $C_H = \frac{1}{0.000398 + \frac{0.003602}{1+e^{(11.02-3.49 H_{HMA})}}}$ β_{f1} *and* β_{f2}, β_{f3} = local or mixture specific field calibration parameters C = factor AC % effective asphalt content (V_{be}) and percent air voids (V_a) C_H = thickness correction for bottom-up fatigue cracking based on AC layer thickness (H_{HMA}) in inches			
Rutting Models $N_f = f_4 \varepsilon_v^{f_5}$				
Local Damage Model	542.57	-0.756	-	0.81
MnPAVE	0.0199	-2.350	-	-
Asphalt Institute (AI)	1.365×10^{-9}	-4.477	-	-
MEPDG [NCHRP, 2007]	$\varepsilon_p = \beta_{s1} k_{s1} \varepsilon_v \left(\frac{\varepsilon_o}{\varepsilon_r}\right) e^{-\left(\frac{\rho}{N_f}\right)^{\beta}}$ k_{s1} = global calibration coefficients for soil type β_{s1} = local calibration constant for rutting β = local constant based on soil volumetric moisture content, %			

Note: [1]MnPAVE fatigue criteria 20% of lane area
[2]AC=asphalt concrete layer thickness, HMA=hot mix asphalt
[3]Adjusted from lab coefficient of 1.879 to field coefficient of 18.79 based on transfer factor of 10 [Wu and Hossain, 2003]

The comparison of the models shows that the Local fatigue model coefficients were similar to Wu and Hossain [2003]. Wu and Hossain [2003] developed fatigue failure models from the instrumentation and lab analysis of fatigue beam samples at the Kansas accelerated testing laboratory. The laboratory fatigue test used a third-point loading model on in-situ asphalt beams sawed from asphalt pavement samples in Kansas. The lab samples were loaded to repetitions of 30,000 cycles with strain measurements taken during the lab testing.

Wu and Hossain found that the lab equations produced lower cycles than field conditions. Wu and Hossain used a transfer factor of 100 to transfer the lab fatigue model to represent the field conditions, based on previous studies of mixtures in Kansas, [Wu and Hossain, 2003]. A transfer factor of 10 more closely matched the α coefficient from Wu and Hossain fatigue equation and the Local model equation. The magnitude of the local β coefficient matched the coefficients from Wu and Hossain.

VALIDATING LOCAL DAMAGE MODEL PREDICTIONS

To validate the Local damage models, the fatigue and rutting equations were used to predict the repetitions to failure for a MnROAD pavement cell that was not used to develop the Local model.

The reconstructed pavement Cell 33-B from the MNROAD low volume road was selected for the model validation. MnROAD constructed and instrumented Cell 33-B in August 1999 and demolished the cell in June 2007.

The structure of Cell 33-B was a flexible pavement with 102 mm AC wearing surface, 305 mm Class 6 granular base, on silty-clay subgrade. The as-built average AC mixture density was 2,381 kg/m3, with an average asphalt content of 5.5%, and average air voids of 4.9%. The asphalt binder used in the AC mix was graded at a PG58-28. MnROAD characterized the asphalt layer materials through lab modulus testing based on LTPP Protocol P07 [FHWA, 2010].

Table 7.11 presents the layer modulus used for the spring condition on MnROAD Cell 33-B. The spring modulus for the AC layer was obtained from lab testing at 20°C. The moisture contents in the granular base and subgrade were not available from the MnROAD database. The spring modulus for the Class 6 granular base and subgrade from Cell 27-A was used for Cell 33-B, since both pavement cells had the same Class 6 base and subgrade materials.

TABLE 7.11: Layer Modulus Used for Spring Condition on MnROAD Cell 33-B

Cell	Layer	Thickness (mm)	Spring TDR Moisture Content (%)	Spring Modulus (MPa)	Poisson's Ratio
33-B	AC	102	-	3,900[1]	0.35
	Granular Base	305	n/a	345[2]	0.40
	Silty-Clay Subgrade	Semi-infinite	n/a	35[2]	0.45

Note: [1] MnROAD Lab modulus testing at 20°C
[2] Assumed same spring modulus as Cell 27-A, moisture content not available
'-'=not applicable
n/a=data not available

Table 7.12 presents the early and late spring dates calculated for MnROAD Cell 33-B. The dates were calculated using the Minnesota criteria for defining early and late spring given in Appendix G.

Table 7.12: Early and Late Spring Dates for MnROAD Cell 33-B

	Criteria	Early and Late Spring Dates
		Cell 33-B (2001)
Early Spring[1]	Start (*TI>15^{o}C_Days)*	March 16
	End (*Approximately 28 days)*	April 10
Late Spring[2]	Start (*End of early Spring)*	April 10
	End (*3-day T_{avg}>17^{o}C)*	April 28
Freezing Index (FI)	Degree_Days_^{o}C	1,058

Note: [1] Base Thaws, Subgrade Frozen
[2] Base Recovers, Subgrade Thaw
T_{avg}=average air temperature

Table 7.13 presents the measured annual and cumulative 5-axle semi trailer loads and ESAL repetitions on the 80KIP and 102KIP lanes of Cell 33-B. The loads and ESAL repetitions were applied over the life of the pavement. The measured rut depths in the outer wheelpath, (1.8 m straight edge) and the percent fatigue cracking in the wheelpath area are also presented.

Table 7.13: Measured Annual and Cumulative 5-Axle Semi Trailer Loads and ESAL Repetitions, Rut Depths, and Fatigue Cracking on 80KIP and 102KIP Lanes of MnROAD Cell 33-B

Cell 33-B		Annual Number of Truck Loads and ESAL Repetitions, and Rutting and Fatigue Cracking								Total
Pavement Age[1] (Years)		1	2	3	4	5	6	7	8	
Lane		Annual and Cumulative Loads and ESALs								
80KIP	Loads	7,995	9,142	8,085	6,920	5,393	5,390	5,318	6,755	54,998
	ESALs	18,797	21,486	19,009	16,265	12,677	12,669	12,497	15,886	129,286
102KIP	Loads	2,129	2,974	1,784	1,625	1,734	1,756	1,969	1,822	15,793
	ESALs	14,903	20,818	12,488	11,373	12,140	12,292	13,783	12,754	110,551
		Rut Depth in OWP (mm)								
80KIP	Mean	6	8	10	10	13	15[2]	15[2]	15[2]	15
	STD	1	1	2	2	2	-	-	-	
102KIP	Mean	4	6	6	8	8	10[2]	10[2]	10[2]	10
	STD	1	1	1	2	2	-	-	-	
		Fatigue Cracking in Wheelpath Area (%)								
80KIP		0	0	0	0	0	0	1	1	1
102KIP		0	0	0	0	0	0	0	0	0

Note: Cell 33-B Structure: 102 mm AC, 305 mm Class 6 granular base, Silty-Clay subgrade
[1] Number of years after construction
[2] Rut Depth obtained from MnROAD High Speed Profiler Data
OWP=outer wheelpath
'-'=not applicable

Figure 7.3 show the measured rut depths and percent fatigue cracking in the wheelpath area versus the cumulative ESAL repetitions on the 80KIP and 102KIP lanes of MnROAD Cell 33-B.

Figure 7.3: Measured Rut Depth and Percent Fatigue Cracking in Wheelpath Area versus Cumulative ESAL Repetitions on 80KIP and 102 KIP Lanes of MnROAD Cell 33-B

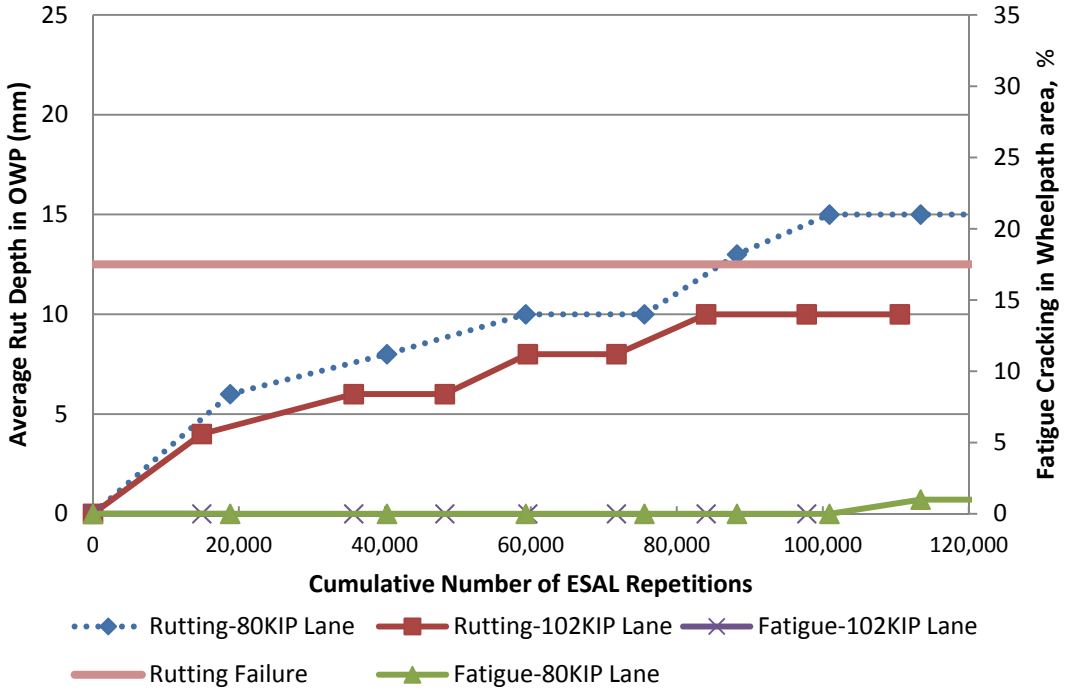

The graph shows that the average rut depths were generally higher in the 80KIP lane than the 102KIP lane, which was unexpected. However, the ESALs on the 80KIP lane of Cell 33-B were 15% higher than the 102KIP lane, which may be a factor in the higher rut depth in the 80KIP lane. Similar to the trend on the 80KIP and 102KIP lanes of Cell 26-A, Cell 27-A, and Cell 28-A, it was possible that given similar numbers of ESAL repetitions and the same pavement structure, how the pavement was loaded (i.e. 4 day rest period between loads) may explain the lower rutting on the 102KIP .

The longitudinal and transverse strains and vertical subgrade pressures, measured from the 5-axle semi trailer loads on Cell 33-B, were obtained from the MnROAD database

(2001 latest year available). The vertical pressures were converted to vertical strains using the KENLAYER proportion process described in Section 7.2.

Table 7.14 presents the measured strains and ESAL repetitions at failure, and the Local model predicted ESAL repetitions to failure on MnROAD Cell 33-B. The measured ESAL at fatigue and rutting failure were obtained from Figure 7.3. The Local model predicted ESALs were obtained using Equation 7.1 and 7.2, and the measured horizontal and vertical strains given in Table 7.14.

Table 7.14: Measured Strains and Cumulative ESAL Repetitions to Failure, and Local Model Predicted ESAL Repetitions to Failure on MnROAD Cell 33-B

Cell	Load Level	Strain Orientation	Measured Strains (μm/m)[1]		Repetitions to Failure, N_f x 10^3		
			Drive	Trailer1	Local Model Prediction		Measured
					Drive	Trailer1	
						Fatigue Failure	
33-B	80KIP	Horizontal	264	303	193,000	166,000	>120,000
	102KIP	Horizontal	346	371	144,000	133,000	>120,000
						Rutting Failure	
	80KIP	Vertical	1,290[2]	1,545[3]	83,000	72,000	87,000
	102KIP	Vertical	n/a	n/a	n/a	n/a	120,000

Note: [1]April 13, 2001; Air temperature 12°C, pavement started to re-freeze April 14-18, 2001
[2]Vertical strain estimated from measured vertical stress of 86 kPa using KENLAYER
[3]Vertical strain estimated from measured vertical stress of 103 kPa using KENLAYER
n/a=data not available

The results show that the ESAL predictions from the Local fatigue model were higher than the measured ESALs on the 80KIP and 102KIP lanes of Cell 33-B. This was expected since both lanes of Cell 33-B had minimal fatigue failure at demolition. The

ESAL predictions from the Local rutting model were an average 13% lower than the measured ESALs at rutting failure on the 80KIP lane of Cell 33-B.

Based on the relatively low difference between the Local model predictions and the measured ESALs, the Local models were considered to be valid and were used to predict the repetitions to failure at the Manitoba sites.

LOCAL DAMAGE MODEL PREDICTIONS ON PTH 11 AND PR 304

The Local damage models were used to predict the ESAL repetitions to fatigue and rutting failures at the B-Train maximum allowable and SWR loads and two tire pressures on PTH 11 and PR 304.

Table 7.15 presents the Local model predicted ESAL repetitions to fatigue and rutting failures at the B-Train maximum allowable and SWR loads for the spring condition on PTH 11. The B-Train Steering axle was not included in the analysis. The ESAL repetitions to fatigue failure were calculated from Equation 7.1 and using the horizontal strains given in Table 7.1. The ESAL repetitions to rutting failure were calculated from Equation 7.2 and using the vertical strains given in Table 7.1.

TABLE 7.15: Local Model Predicted ESAL Repetitions to Fatigue and Rutting Failures at B-Train Maximum Allowable and SWR Loads for Spring Conditions on PTH 11

Load Level	Strain Orientation	Local Model Predicted Repetitions to Failure, N_f x 10^3					
		Drive		Trailer1		Trailer2	
		690 kPa	345 kPa	690 kPa	345 kPa	690 kPa	345 kPa
Fatigue Failure							
A1L1	Horizontal	82	99	78	90	88	99
A1N	Horizontal	80	96	71	81	72	82
RTAC	Horizontal	75	91	70	81	73	82
Rutting Failure							
A1L1	Vertical	83	85	88	89	85	85
A1N	Vertical	78	79	82	83	78	78
RTAC	Vertical	74	75	82	83	76	76

Table 7.16 presents the Local model predicted ESAL repetitions to rutting failure at the B-Train maximum allowable and SWR loads for the spring condition on PR 304. The B-Train Steering axle was also not included in the analysis. The repetitions to rutting failure were calculated from Equation 7.2 and the vertical compressive strains given in Table 7.2.

TABLE 7.16: Local Model Predicted ESAL Repetitions to Rutting Failure at B-Train Maximum Allowable and SWR Loads for Spring Conditions on PR 304

Load Level	Strain Orientation	Local Model-Predicted Repetitions to Failure, N_f x 10^3					
		Drive		Trailer1		Trailer2	
		690 kPa	345 kPa	690 kPa	345 kPa	690 kPa	345 kPa
Rutting Failure							
B1L2	Vertical	130	131	n/a	n/a	n/a	n/a
B1N	Vertical	95	96	102	103	97	97
A1N	Vertical	88	89	92	93	90	90

Note: n/a=data not available

7.3 COMPARISON OF LOCAL, AI, AND MEDPG DAMAGE MODEL PREDICTIONS

The Local, AI, and MEPDG predicted ESAL repetitions to fatigue and rutting failures were compared at the maximum allowable B-train loads and two tire pressures on PTH 11 and PR 304. Additionally, the sensitivity of the AC layer modulus on the AI and MEPDG fatigue model predictions was evaluated. A statistical t-test was also conducted to determine whether the means of the three model predictions were statistically different at the 95% confidence limit.

Figure 7.4 shows the Local, AI, and MEPDG predicted ESAL repetitions to fatigue failure at the B-Train maximum allowable and SWR loads for the spring conditions on PTH 11.

FIGURE 7.4: Local, AI, and MEPDG Model Predicted ESAL Repetitions to Fatigue Failure at B-Train Maximum Allowable and SWR Loads for Spring Conditions on PTH 11

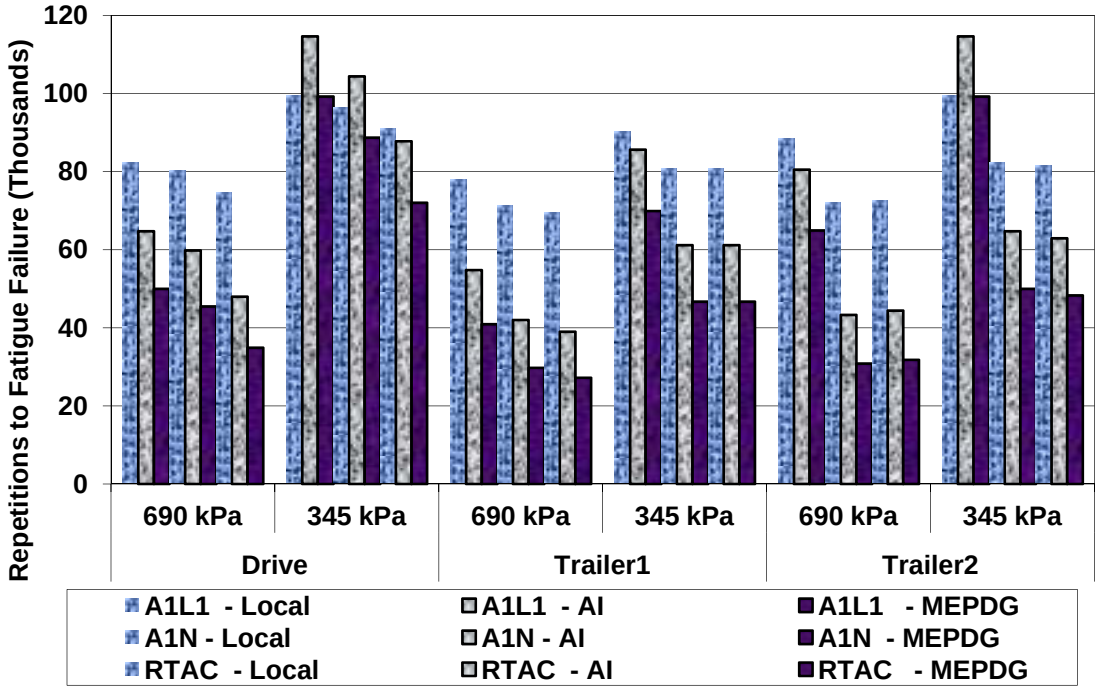

The results show that the Local model predicted ESAL repetitions to fatigue failure were higher by an average of 20% and 37% than the AI and MEPDG predictions, respectively, across all loads and axle groups.

When the loads were increased by two levels, from A1L1 to RTAC and at the same tire pressure, the Local, AI and MEPDG, predicted ESAL repetitions to fatigue failure, decreased by an average of 13%, 33%, and 38% respectively.

When the tire pressure was reduced from 690kPa to 345kPa, the Local, AI, and MEPDG predicted ESAL repetitions to fatigue failure increased by an average 17%, 60%, and 74%, respectively, over all loads and axle groups. The AI and MEPDG ESAL predictions showed that reducing tire pressure had a significantly positive impact on fatigue performance, which can more than compensate for an increase in loads by up to two levels for the spring condition. The Local model predictions were less sensitive to changes in tire pressure because the model was developed only at 690kPa which was the standard tire pressure on the MnROAD semi trailer.

Figure 7.5 shows the Local, AI, and MEPDG predicted ESAL repetitions to rutting failure at the B-train maximum allowable and SWR loads for the spring conditions on PTH 11.

FIGURE 7.5: Local, AI, and MEPDG Model Predicted ESAL Repetitions to Rutting Failure at B-Train Maximum Allowable and SWR Loads for Spring Conditions on PTH 11

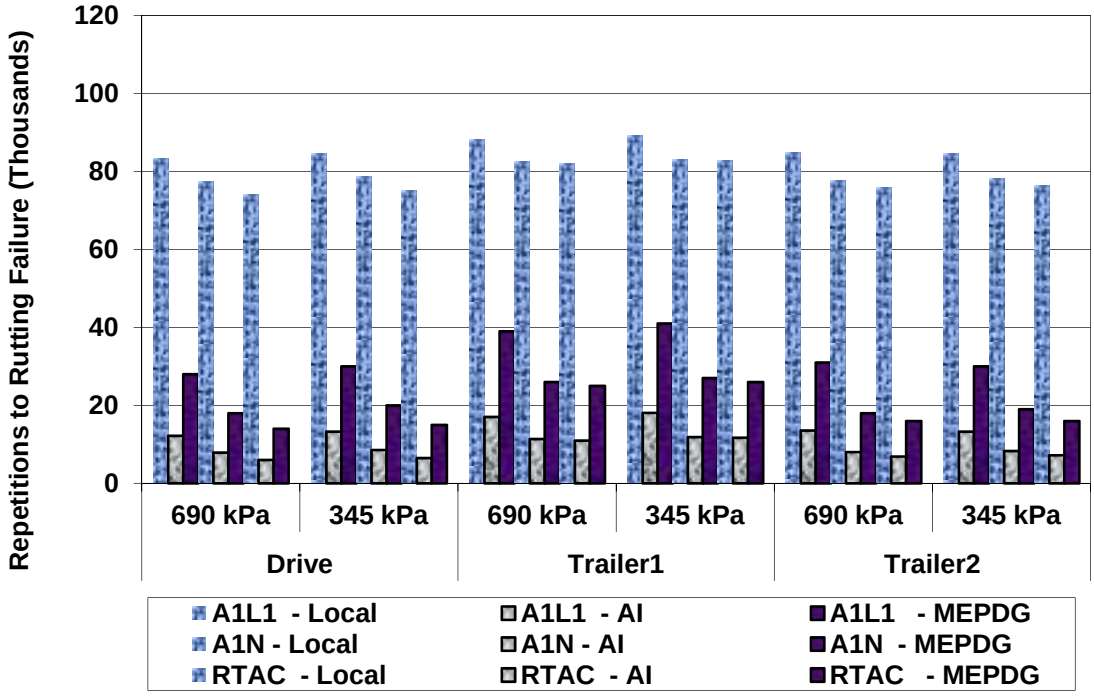

The results show that the Local model predicted ESAL repetitions to rutting failure were significantly higher than the AI and MEPDG predictions, by an average 87% and 70% respectively, across all loads and axle groups.

When the loads were increased by two levels, from A1L1 to RTAC at the same tire pressure, the Local, AI, and MEPDG predicted ESAL repetitions to rutting failure decreased by an average of 10%, 45%, and 45% respectively.

When the tire pressure was reduced from 690 kPa to 345 kPa over all loads and axle groups, the Local, MEPDG, and AI predicted ESAL repetitions to rutting failure increased by an average 1%, 5%, and 5%, respectively.

In general, the Local, AI, and MEPDG results indicated that increased loads had a moderate to significant negative impact on the repetitions to rutting failure during the spring period, while reduced tire pressure had only a minimal impact on rutting performance. The AI and MEPDG model results also indicated that subgrade rutting was the governing failure mode for PTH 11 since the ESAL repetitions to rutting failure were significantly lower than fatigue failure. This finding was similar to studies by Fernando [2006], Park [2008] and Raad [1998] who found that the effects of the differences in tire pressure were mainly seen near the surface and diminishes with depth, and that rutting was the governing failure mode for the flexible pavements.

SENSITIVITY OF AC LAYER MODULUS ON AI AND MEPDG FATIGUE MODELS

The sensitivity of the AC layer modulus on the AI and MEPDG fatigue model predictions was evaluated. The sensitivity analysis was conducted to determine how significant the AC layer modulus was on the predicted ESAL repetitions to fatigue failure. A range of AC layer modulus were input into the AI fatigue model (Equation 2.9) and MEPDG fatigue model (Equation 2.11) to predict the ESAL repetitions to fatigue failure, while holding the horizontal strain constant.

Figure 7.6 shows the effect of the AC layer modulus on the AI and MEPDG model predicted ESAL repetitions to fatigue failure using the horizontal strain from the B-Train Drive axle at RTAC load and 690 kPa tire pressure on PTH 11.

Figure 7.6: Effect of AC Layer Modulus on AI and MEPDG Model Predicted ESAL Repetitions to Fatigue Failure using Horizontal Strain from B-Train Drive Axle at RTAC Load and 690 kPa Tire Pressure on PTH 11

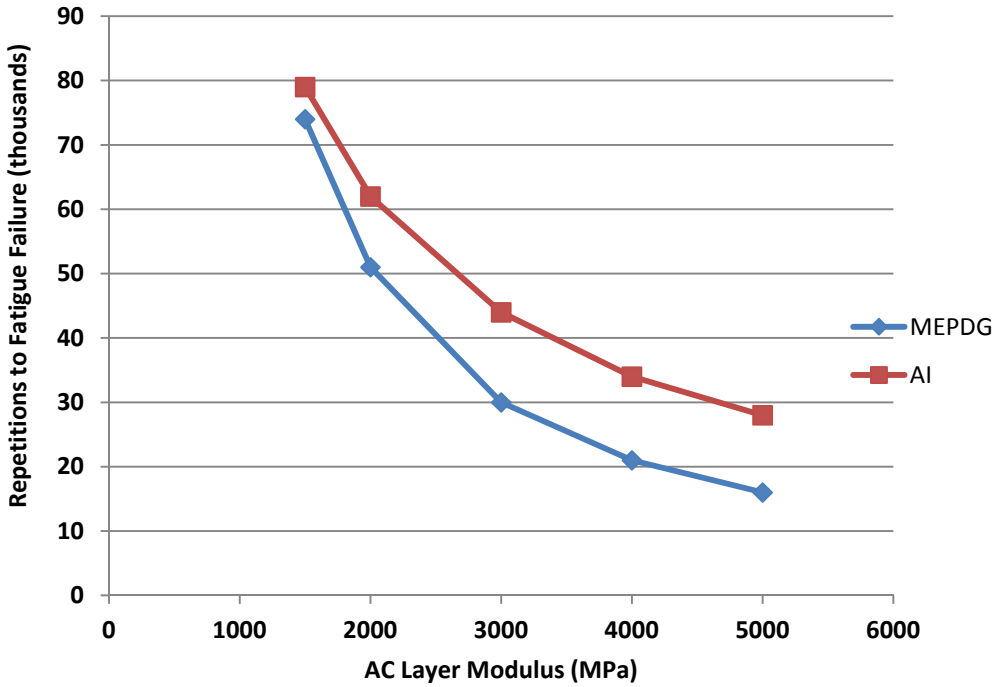

The result shows that the AI and MEPDG predicted repetitions to fatigue failure decreased as the AC layer modulus increased, indicating that the stiffer the AC layer (given the same layer thickness) the shorter the fatigue life. The results also show that the difference between the AI and MEPDG ESAL predictions were more pronounced, and more sensitive to changes, at higher AC modulus than at lower modulus.

EFFECT OF LOAD AND TIRE PRESSURE ON PREDICTED REPETITIONS TO FAILURE

To visualize the effects of the combination of tire pressures and loads on the predicted repetitions to failure, the Local and AI model predicted ESALs to fatigue and rutting

failures were plotted against the horizontal and vertical strains for the spring conditions on PTH11 and PR 304.

Figure 7.7 shows the Local model predicted ESAL repetitions to fatigue and rutting failures at the B-Train Drive axle and A1L1 to RTAC loads for the spring conditions on PTH 11. The plot shows the calibrated horizontal and vertical strains from the FEM (Table 7.1) versus Local Model ESALs (Table 7.15) for the load increase by two levels, from A1L1 to A1N, and A1N to RTAC.

FIGURE 7.7: Local Model Predicted ESAL Repetitions to Fatigue and Rutting Failure at B-Train Drive Axle and A1L1 to RTAC Loads for Spring Conditions on PTH 11

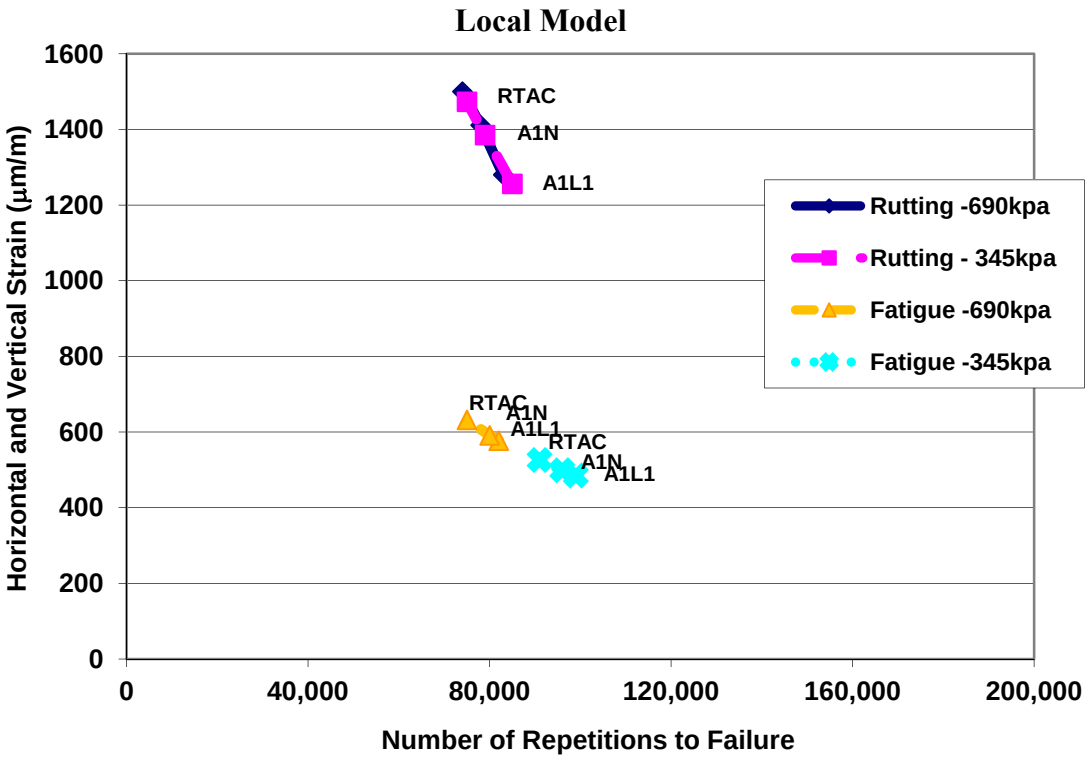

Figure 7.8 shows the AI model predicted ESAL repetitions to fatigue and rutting failures at the B-Train Drive axle and A1L1 to RTAC loads for the spring conditions on PTH 11. The plot also shows the calibrated horizontal and vertical strains from the FEM (Table 7.1) versus AI model ESALs (Table 7.3) for the load increase, from A1L1 to A1N, and A1N to RTAC.

FIGURE 7.8: AI Model Predicted ESAL Repetitions to Fatigue and Rutting Failure at B-Train Drive Axle and A1L1 to RTAC Loads for Spring Conditions on PTH 11

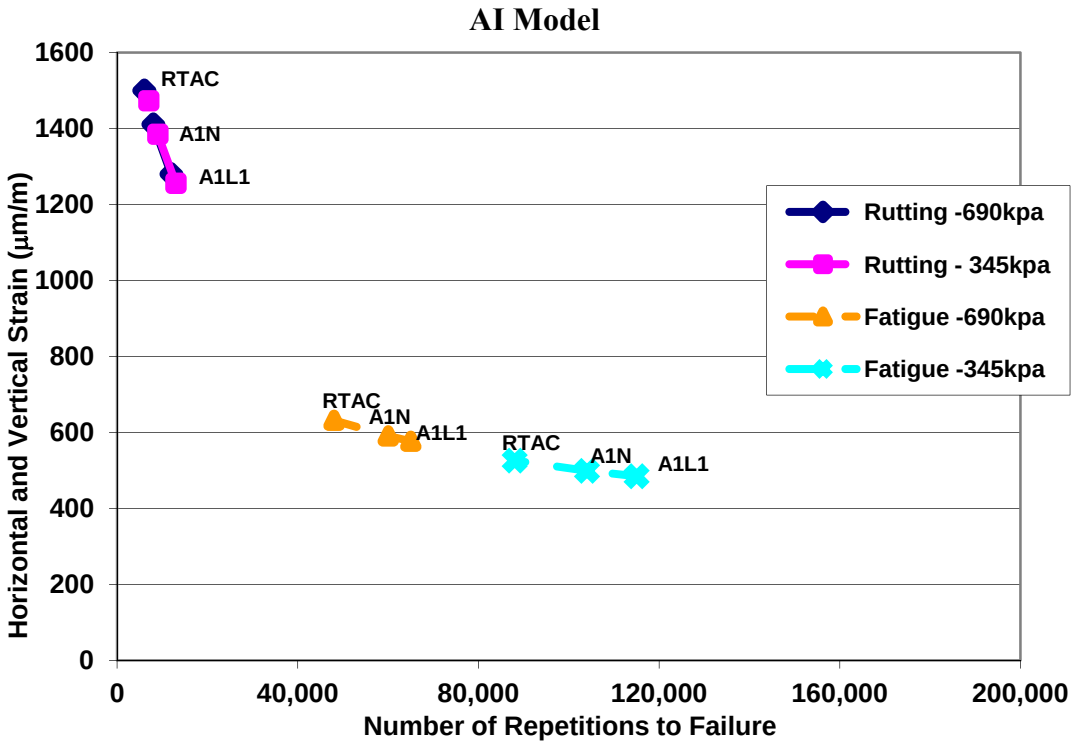

The figures show that the ESAL repetitions to rutting failure were more sensitive to load increases that caused changes in the vertical strains, than by load increases that caused changes in horizontal strains.

For example, the slope of the AI model fatigue line (Figure 7.8) from RTAC to A1L1 loads at 690kPa tire pressure was relatively flat (0.003 microstrain/repetition), indicating low sensitivity to changes in strain on the fatigue repetitions. The slope of the AI fatigue line at 345kPa tire pressure was also relatively flat, indicating low sensitivity to changes in strain on the fatigue repetitions. While the slopes were similar, the predicted ESAL repetitions to fatigue failure at 345kPa tire pressure were higher that the 690kPa tire pressure over the same load levels.

For rutting, the slope of the AI model rutting line from RTAC to A1L1 loads at 690kPa tire pressure (Figure 7.8) was much steeper (0.03 microstrain/repetition), indicating higher sensitivity to changes in strains on rutting failure. The slope of the rutting line at 345kPa tire pressure was the same as 690kPa tire pressure, indicating little difference between the ESAL repetitions to rutting failure over the same loads and vertical strains.

The slopes of the lines for the Local model ESAL predictions for rutting and fatigue failures (Figure 7.7) were similar to the AI model, despite the different in the magnitude of the ESAL predictions.

The graphs show the positive impact of lower tire pressure on ESAL repetitions to fatigue failure. Alternatively it also showed the negative impact of increased loading on the ESAL repetitions to rutting failure, which was only marginally offset by reducing the tire pressure.

Figure 7.9 shows the Local and AI model predicted ESAL repetitions to rutting failure at the B-Train Drive Axle and B1L2 to A1N loads for the spring conditions on PR 304. The plot also shows the calibrated vertical strains from the FEM (Table 7.2) versus the Local

and AI model ESALs (Table 7.16 and Table 7.4) for the load increase, from B1L2 to B1N, and B1N to A1N.

FIGURE 7.9: Local and AI Model Predicted Repetitions to Rutting Failure at B-Train Drive Axle at B1L2 to A1N Loads for Spring Conditions on PR 304

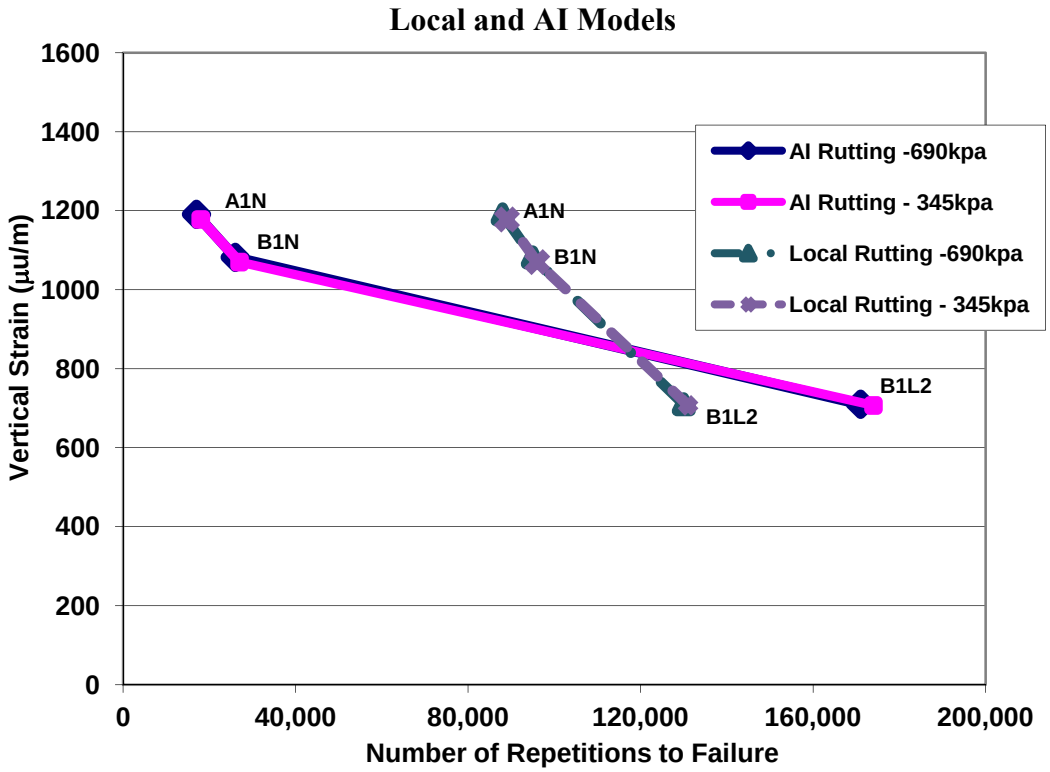

The graph shows that the ESAL repetitions to rutting failure on PR 304 was also sensitive to changes in vertical strains caused by the load increase from B1L2 to A1N.

The slope of the AI model rutting line (Figure 7.9) for B1N to A1N loads was steep (0.012 microstrain/repetition), indicating high sensitivity to changes in strains caused by the load increase. The slope of the AI model rutting line from B1L2 to B1N loads was flatter (0.002 microstrain/repetition), indicating lower sensitivity to changes in strains caused by that load increase. This major change in slope was due to the very low B1L2

load. The much lower B1L2 load produced lower vertical strains and higher ESAL repetitions to rutting failure.

The slope of the AI model rutting line at 345kPa tire pressure was the same as 690kPa tire pressure, with little difference between the ESAL repetitions to rutting failure over the same loads. This also showed the negative impact of increased loading on the ESAL repetitions to rutting failure, which was only marginally offset by reducing the tire pressure.

STATISTICAL T-TEST ANALYSIS OF LOCAL, AI, AND MEPDG FAILURE PREDICTIONS

A statistical t-test was conducted to determine whether the means of the Local, AI, and MEPDG predictions were statistically different at the 95% confidence limit. The t-test of the means of paired Local, AI, and MEPDG predicted ESAL repetitions to fatigue and rutting failure were tested at the null hypothesis to determine if the difference in means were not statistically different from zero (i.e. H=0, the null hypothesis) at 95% confidence limits. For the t-test, if t-critical was greater than the calculated t-statistic at 95% confidence limit, it could be concluded that the means of the two model results were not statistically different from zero.

Table 7.17 presents the t-test parameters from the Local, AI, and MEPDG predicted ESAL repetitions to fatigue and rutting failure for the B-Train maximum loads and spring

conditions on PTH 11 and PR 304. The p-value, which is the probability that t-critical was greater that the observed t-statistic, is also presented.

TABLE 7.17: T-test Parameters from Local, AI, and MEPDG Model Predicted ESAL Repetitions to Fatigue and Rutting Failure at B-Train Maximum Loads for Spring Conditions on PTH 11 and PR 304

Model Comparison	Failure Mode	t-Statistic	t-Critical (2-tailed)	Probability (ρ<0.05) (2-tailed)	Pass/Fail Null Hypothesis
PTH 11					
Local-AI	Fatigue	3.98	2.11	0.0010	Rejected
	Rutting	251.14		0.0000	Rejected
Local-MEPDG	Fatigue	8.65		0.0000	Rejected
	Rutting	65.65		0.0000	Rejected
AI-MEPDG	Fatigue	40.73		0.0000	Rejected
	Rutting	12.82		0.0000	Rejected
PR 304					
Local-AI	Rutting	70.92	2.20	0.0000	Rejected
Local-MEPDG	Rutting	7.67		0.0000	Rejected
AI-MEPDG	Rutting	9.78		0.0000	Rejected

The results show that the t-statistics for each model comparison were greater than t-critical, and the null hypothesis was rejected. Therefore, it was concluded that the Local, AI, and MEPDG model predictions were statistically different, at the 95% confidence level.

One explanation for the big difference between the Local model predictions and the AI and MEPDG models is the Local model was developed and calibrated for weak low volume pavements in a specific region with unique responses of the pavement at that

location. Re-calibration of the Local model with a larger data set of low volume pavements responses would be advantageous.

However Wardle et al [2003] argues that agreement should not be expected between predicted repetitions to failure from different models. Wardle et al compared the predictions of several rutting failure models and found no agreement between the strain predictions. Because each failure criterion was derived in the context of its own detailed procedure, Wardle et al noted that the models will only produce consistent predictions when used as part of the same procedure.

However, for a given pavement the Local, AI or MEPDG model could be used to predict the relative change in repetitions to failure under different loading and tire pressure conditions. Using the Local, AI or MEPDG models to compare absolute repetitions to failures for different pavements with different materials and layer thicknesses could result in an overestimation of fatigue failure or underestimation of rutting failure, or vice versa.

7.4 DAMAGE RATIO ANALYSIS

Damage models are based on the cumulative damage concept, which predict the ESAL repetitions to failure using critical strains and material properties in a pavement. Damage is computed on a period, for a given load repetition, and accumulated using Miner's Hypothesis, up to a damage value of 1.0 for each failure mode.

Damage ratios were computed at the B-Train maximum allowable and SWR loads and high and low tire pressures for the spring conditions on PTH 11 and PR 304. The damage

ratio was computed by dividing the expected B-Train ESAL repetitions during the spring period to the predicted ESAL repetitions to failure. Based on industry expectations, approximately 600 B-Train trips were estimated during the last month (May) of the SWR period on PTH 11 and PR 304. This equated to around 1200 Drive single axle repetitions, 1800 Trailer1 single axle repetitions, and 1200 Trailer2 single axle repetitions. The damage ratios for the B-Train Drive, Trailer1, and Trailer2 axle groups were accumulated to obtain a total damage ratio for the vehicle.

Table 7.18 presents the computed B-Train damage ratios from the Local model predicted ESAL repetitions to fatigue and rutting failures at the maximum allowable and SWR loads for the spring conditions on PTH 11.

TABLE 7.18: B-Train Damage Ratios from Local Model Predicted ESAL Repetitions to Fatigue and Rutting Failures at Maximum Allowable and SWR Loads for Spring Conditions on PTH 11

Load Level	Orientation	Damage Ratio from Local Model Repetitions							
		Drive		Trailer1		Trailer2		B-Train Total[1]	
		690 kPa	345 kPa	690 kPa	345 kPa	690 kPa	345 kPa	690 kPa	345 kPa
		Fatigue							
A1L1	Horizontal	0.015	0.012	0.023	0.020	0.014	0.012	0.051	0.044
A1N	Horizontal	0.015	0.012	0.025	0.022	0.017	0.015	0.057	0.049
RTAC	Horizontal	0.016	0.013	0.026	0.022	0.017	0.015	0.058	0.050
		Rutting							
A1L1	Vertical	0.014	0.014	0.020	0.020	0.014	0.014	0.049	0.049
A1N	Vertical	0.015	0.015	0.022	0.022	0.015	0.015	0.053	0.052
RTAC	Vertical	0.016	0.016	0.022	0.022	0.016	0.016	0.054	0.053

Note: [1]Excludes steering axle damage ratio

The results show that when the load was increased from A1L1 to RTAC, the Local model fatigue damage ratio increased by an average of 13%. The results also show that when the tire pressure was reduced, from 690 kPa to 345 kPa, the fatigue damage ratio decreased by an average of 15%.

For rutting, when the load was increased from A1L1 to RTAC, the Local model rutting damage ratio increased by an average of 13%. When the tire pressure was reduced, from 690 kPa to 345 kPa, the rutting damage ratio was decreased by an average of 0.5%.

Table 7.19 presents the computed B-Train damage ratio from the Local model predicted ESAL repetitions to rutting failure at the maximum allowable and SWR loads for the spring conditions on PR 304.

TABLE 7.19: B-Train Damage Ratios from Local Model Predicted ESAL Repetitions to Rutting Failure at Maximum Allowable and SWR Loads for Spring Conditions on PR 304

Load Level	Orientation	Damage Ratio from Local Model Repetitions							
		Drive		Trailer1		Trailer2		B-Train Total[1]	
		690 kPa	345 kPa	690 kPa	345 kPa	690 kPa	345 kPa	690 kPa	345 kPa
		Rutting							
B1L2[2]	Vertical	0.009	0.009	0.014	0.014	0.009	0.009	0.032	0.032
B1N	Vertical	0.013	0.013	0.018	0.018	0.012	0.012	0.043	0.042
A1N	Vertical	0.014	0.014	0.019	0.019	0.013	0.013	0.046	0.046

Note: [1]Excludes steering axle damage ratio
[2]Damage ratios for Trailer1 and Trailer2 estimated based on Drive axle strains

The results show that when the load was increased from B1N to A1N, the Local model rutting damage ratio increased by an average of 7%. When the tire pressure was reduced from 690kPa to 345kPa the rutting damage ratio decreased by an average of 0.5%.

COMPARISON OF LOCAL, AI, AND MEPDG DAMAGE RATIOS

A comparison of the damage ratios computed from the Local, AI, and MEPDG predicted ESAL repetitions to failure was made at the B-Train maximum allowable loads and tire pressures and spring conditions on PTH 11 and PR 304.

Table 7.20 and Table 7.21 present the computed B-Train damage ratios from the Local, AI, and MEPDG model predicted ESAL repetitions to failure at the maximum allowable and SWR loads and spring conditions on PTH 11 and PR 304, respectively.

TABLE 7.20: B-Train Damage Ratios from Local, AI, and MEPDG Model Predicted ESAL Repetitions to Fatigue and Rutting Failure at Maximum Allowable and SWR Loads for Spring Conditions on PTH 11

Load Level	Strain Orientation	Damage Ratio from Local, AI, and MEPDG Repetitions					
		Local		AI		MEPDG	
		B-Train Total[1]		B-Train Total[1]		B-Train Total[1]	
		690 kPa	345 kPa	690 kPa	345 kPa	690 kPa	345 kPa
		Fatigue					
A1L1	Horizontal	0.051	0.044	0.066	0.042	0.087	0.050
A1N	Horizontal	0.057	0.049	0.091	0.059	0.126	0.076
RTAC	Horizontal	0.058	0.050	0.098	0.062	0.138	0.080
		Rutting					
A1L1	Vertical	0.049	0.049	0.293	0.280	0.128	0.124
A1N	Vertical	0.053	0.052	0.460	0.436	0.203	0.190
RTAC	Vertical	0.054	0.053	0.539	0.505	0.233	0.224

Note: [1] Excludes steering axle damage ratio

TABLE 7.21: B-Train Damage Ratios from Local, AI, and MEPDG Model Predicted ESAL Repetitions to Rutting Failure at Maximum Allowable and SWR Loads for Spring Conditions on PR 304

Load Level	Strain Orientation	Damage Ratio from Local, AI, and MEPDG Repetitions					
		Local		AI		MEPDG	
		B-Train Total[1]		B-Train Total[1]		B-Train Total[1]	
		690 kPa	345 kPa	690 kPa	345 kPa	690 kPa	345 kPa
		Rutting					
B1L2	Vertical	0.032	0.032	0.025	0.024	0.009	0.009
B1N	Vertical	0.043	0.042	0.131	0.127	0.056	0.054
AIN	Vertical	0.046	0.046	0.217	0.209	0.095	0.092

Note: [1] Excludes steering axle damage ratio

The B-Train damage ratios from the Local, AI, and MEPDG models (given in Table 7.20 and Table 7.21) were normalized to provide a direct comparison of the results. The damage ratios on PTH 11 were normalized by dividing the B-Train total damage ratios at each load level by the A1N damage ratio. The damage ratios on PR 304 were normalized by dividing the B-Train total damage ratio at each load level by the B1N damage ratio.

Table 7.22 and Table 7.23 present the normalized B-Train damage ratios relative to the A1N and B1N maximum allowable loads for the spring conditions on PTH 11 and PR 304, respectively.

TABLE 7.22: Normalized B-Train Damage Ratio Relative to A1N Load for Spring Conditions on PTH 11

Load Level	Strain Orientation	Damage Relative to Normal Loads					
		Local		AI		MEPDG	
		690 kPa	345 kPa	690 kPa	345 kPa	690 kPa	345 kPa
		Fatigue					
A1L1	Horizontal	0.89	0.90	0.73	0.71	0.69	0.66
A1N	Horizontal	1.00	1.00	1.00	1.00	1.00	1.00
RTAC	Horizontal	1.02	1.02	1.08	1.05	1.09	1.05
		Rutting					
A1L1	Vertical	0.92	0.94	0.64	0.64	0.63	0.65
A1N	Vertical	1.00	1.00	1.00	1.00	1.00	1.00
RTAC	Vertical	1.02	1.02	1.17	1.16	1.15	1.18

TABLE 7.23: Normalized B-Train Damage Ratio Relative to B1N Load for Spring Conditions on PR 304

Load Level	Strain Orientation	Damage Relative to Normal Loads					
		Local		AI		MEPDG	
		690 kPa	345 kPa	690 kPa	345 kPa	690 kPa	345 kPa
		Rutting					
B1L2	Vertical	0.74	0.76	0.19	0.19	0.16	0.17
B1N	Vertical	1.00	1.00	1.00	1.00	1.00	1.00
A1N	Vertical	1.07	1.09	1.66	1.65	1.69	1.70

The results of the normalized damage ratio for PTH 11 show that the Local model had an average 10% reduction in B-Train fatigue damage at the A1L1 SWR load relative to the A1N normal load, and a 7% reduction in the B-Train rutting damage for the same change in loads. The Local model results also show that increasing the load from A1N to RTAC would result in an average 2% increase in both the B-Train fatigue and rutting damage relative to the A1N normal load.

The results of the AI and MEPDG normalized damage ratio for PTH 11 had an average 30% reduction in B-Train fatigue damage at the A1L1 SWR load relative to the A1N normal load, and a 36% reduction in B-Train rutting damage for the same load. The AI and MEPDG results also show that increasing the load from A1N to RTAC would result in an average 7% increase in B-train fatigue damage, and an average 17% increase in B-Train rutting damage relative to the A1N normal load.

For PR 304, the Local model normalized damage ratio for PR 304 show an average 25% reduction in B-Train rutting damage at the B1L2 SWR load relative to the B1N normal load. The Local model results also show that increasing the load from B1N to A1N would result in an average 8% increase in B-Train rutting damage relative to the B1N normal load.

The results of the AI and MEPDG normalized damage ratio for PR 304 had an average 82% reduction in B-Train rutting damage at the B1L2 SWR load relative to the B1N normal load. The AI and MEPDG results also show that increasing the load from B1N to A1N would result in an average 68% increase in B-train rutting damage relative to the B1N normal load. However, the changes in the AI and MEPDG normalized damage ratios for PR 304 appear to be unreasonable. A review of the results did not indicate an error in the data. It is possible that since the AI and MEPDG damage models were much more sensitive to the lower strains predicted on PR 304.

CHAPTER 8 - LIMITING FAILURE STRAINS AND STRAIN BASED DECISIONS FOR MANITOBA SWR POLICY

The carrying capacity of pavements is better characterized by the strains at critical locations in the pavement than by surface deflection [Huang, 2004]. Therefore an improved process that links SWR levels to the fundamental principles of limiting failure strains and pavement damage is required in Manitoba.

The Manitoba provincial road agency uses pavement deflections to regulate commercial vehicle weights on provincial roads during the spring period. The deflections are rebound of a pavement surface under a standard load. The SWR program uses a formula of 90% and 65% of the normal legal axle loads in an attempt to limit damage on weak pavements during the spring thaw. Table 8.1 presents the Manitoba SWR policy and maximum BBR deflection criteria. Strong pavements with BBR less than 1.5mm are not spring restricted. Moderately weak pavements, with BBR 1.5mm to 2.5mm, are Level 1 restricted at 90% of normal load. Very weak pavements with BBR greater than 2.5mm are Level 2 restricted at 65% of normal load.

Table 8.1: Manitoba SWR Policy and Maximum BBR Deflection Criteria

Manitoba SWR Policy	Maximum BBR Deflection (mm)
No restriction	<1.5
Level 1 restriction	1.5 - 2.5
Level 2 restriction	>2.5

Note: BBR=Benkelman Beam Rebound
SWR=spring weight restriction

Since the current system for establishing SWR damage in Manitoba is not based on limiting failure strains, but on deflections, a strain-based regime for the SWR period in Manitoba was developed in this thesis.

This chapter presents the limiting failure strains for PTH 11 and PR 304 based on the Local, AI, and MEPDG damage models. For this thesis, limiting failure strain was defined as the maximum horizontal or vertical strain to control rutting or fatigue failure at specified ESAL repetitions to failure. The chapter also presents and discusses a strain-based concept on how to manage the SWR regime in Manitoba based on the limiting strains from the Local damage model.

8.1 LIMITING FAILURE STRAINS FOR PTH 11 AND PR 304

The Local, AI, and MEPDG damage models were used to determine the limiting strains at failure on PTH 11 and PR 304. The limiting failure strains were calculated at low, medium, and high ESAL repetitions to failure, representing weak and strong pavements.

Table 8.2 presents the limiting failure strains computed from the Local, AI, and MEPDG models for the spring conditions on PTH 11 and PR 304. The fatigue and rutting limiting strains were computed from the Local models (Equations 7.1 and 7.2), the AI models (Equations 2.4 and 2.5), the MEPDG models (Equations 2.6 and 2.7), and the AC modulus for PTH 11 given in Table 6.1.

TABLE 8.2: Limiting Failure Strains Computed from Local, AI, and MEPDG Models for Spring Conditions on PTH 11 and PR 304

ESAL Repetitions to Failure	Limiting Failure Strain (μm/m)		
	Local Model	AI Model	MEPDG Model
Horizontal (Fatigue)			
50,000	911	613	576
100,000	483	496	484
1,000,000	-	246	270
Vertical (Rutting)			
50,000	2,525	932	1,124
100,000	1,008	800	970
1,000,000	-	478	620

Note: '-'=not applicable, ESAL beyond range of Local model calibration

The results show that the limiting strains at 100,000 ESALs from the Local, AI, and MEPDG models were 483 to 496μm/m for horizontal strains (fatigue failure), and 800 to1,008μm/m for vertical strain (rutting failure). While the slopes of the models differed, the equations appeared to intersect at about 100,000 ESAL repetitions to failure. The Local model limiting strains differed from the AI and MEPDG at the 50,000.

Nishizawa et el [1996] suggested limiting horizontal strains to less than 200μm/m (fatigue limit) to control fatigue cracking on thick asphalt pavements over 1 million ESAL.

Table 8.3 presents the limiting failure strains selected for the spring conditions on PTH 11 and PR 304. Since PTH 11 and PR 304 represent low volume roads with typical design of 100,000 ESALs, the limiting strains from the Local model were considered appropriate for PTH 11 and PR 304.

TABLE 8.3: Limiting Failure Strains for Spring Conditions on PTH 11 and PR 304

	Limiting Failure Strain (μm/m)	
	Horizontal	**Vertical**
PTH 11 & PR 304	483	1,008

Table 8.4 shows the Local model limiting strains versus the FEM predicted strains at the B-Train Maximum allowable and SWR loads on the drive axle and 690kPa tire pressure for the spring conditions on PTH 11 and PR 304. The FEM predicted and calibrated strains for PTH 11 and PR 304 were given in Table 7.1 and Table 7.2, respectively. The B-Train Drive axle was selected at 690kPa since that axle group governed the damage and produced the highest strains.

TABLE 8.4: Limiting Strains versus FEM Predicted Strains at B-Train Maximum Allowable and SWR Loads on Drive Axle and 690kPa Tire Pressure for Spring Conditions on PTH 11 and PR 304

B-Train Axle Group	Load Rating	Axle Load (kg)	Tire Load (kg)	Limiting Strains versus B-Train FEM Predicted and Calibrated Strains at 690kPa Tire Pressure (μm/m)			
				Horizontal Strain		Vertical Strain	
				Predicted	Limiting	Predicted	Limiting
PTH 11							
Drive	A1L1	14,400	1,800	577	483	-1280	-1008
	A1N	16,000	2,000	591		-1411	
	RTAC	17,000	2,125	632		-1500	
PR 304							
Drive	B1L2	9,425	1,178	n/a		-710	-1008
	B1N	14,500	1,813			-1082	
	A1N	16,000	2,000			-1190	

Note: n/a=not applicable

The results on PTH 11 shows that the FEM predicted and calibrated horizontal and vertical strains exceeded the limiting failure strains at all load levels for the spring conditions. Since the average measured fatigue cracking on PTH 11 was 6%, it was expected that the FEM horizontal strain at the SWR A1L1 load would have been lower than the limiting strain.

The results on PR 304 also show the FEM predicted and calibrated vertical strains exceeded the limiting strain for all load levels, except B1L2. The B1L2 SWR load level appeared to be conservative and produced strains well below the limiting strain.

Since the predicted strains on PTH 11 exceeded the limiting strain for the maximum allowable and SWR load levels and for two of the three loads on PR 304, it would appear that the current SWR loads regulating B-Train operations during the spring period are reasonable. The limiting failure strain analysis should be applied to other pavements to verify the findings.

8.2 STRAIN-BASED CONCEPT AND DECISION FOR MANITOBA SWR POLICY

Since pavement deterioration is related to critical strains, the strains can be used to evaluate pavement damage and bearing capacity during the spring thaw, instead of surface deflection. A strain-based concept on how to manage the SWR regime in Manitoba based on FEM strain predictions and the Local model limiting strains and predicted repetitions to failure is presented.

Figure 8.1 shows the schematic of the variation of pavement strength and determination of critical strains during the SWR period. The graph shows the variation of pavement strength with the seasons; through winter, early and late spring, summer and fall. If the critical strains can be determined at each location in the spring (partial SWR, full SWR, partial lifting SWR, and full lifting SWR), a rational method for spring load levels can be recommended. In order for the strain-based concept to be practical, the duration of the SWR period should be linked to a simple and readily usable methodology, such as Minnesota's "thawing index" procedure [MnDOT, 2009].

FIGURE 8.1: Schematic of Variation of Pavement Strength and Determination of Critical Strains during SWR Period

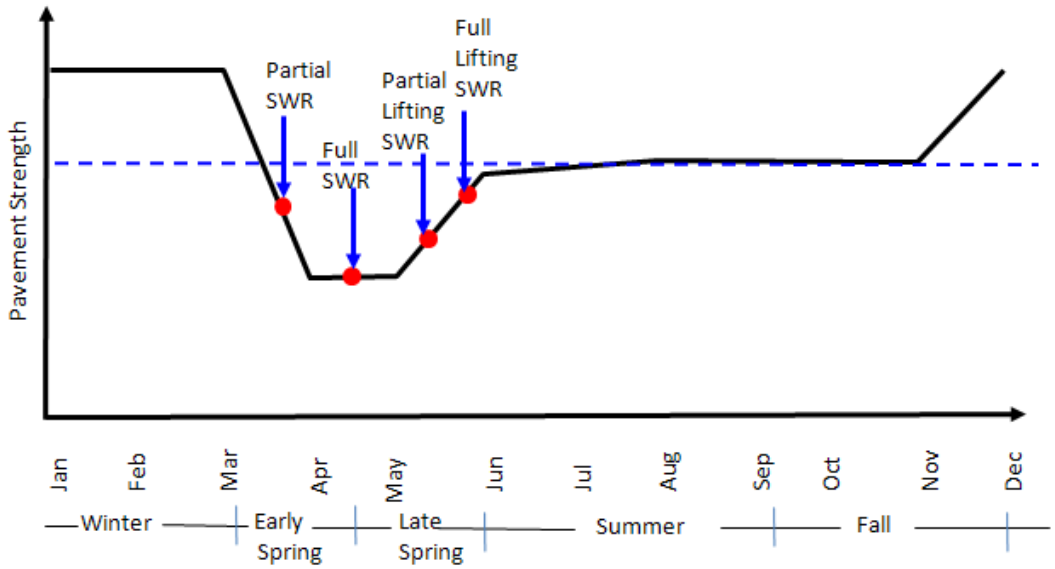

Figure 8.2 shows the flowchart of the strain-based concept to manage the level of SWR load levels in Manitoba.

FIGURE 8.2: Flowchart of Strain-Based Concept to Manage SWR Level in Manitoba

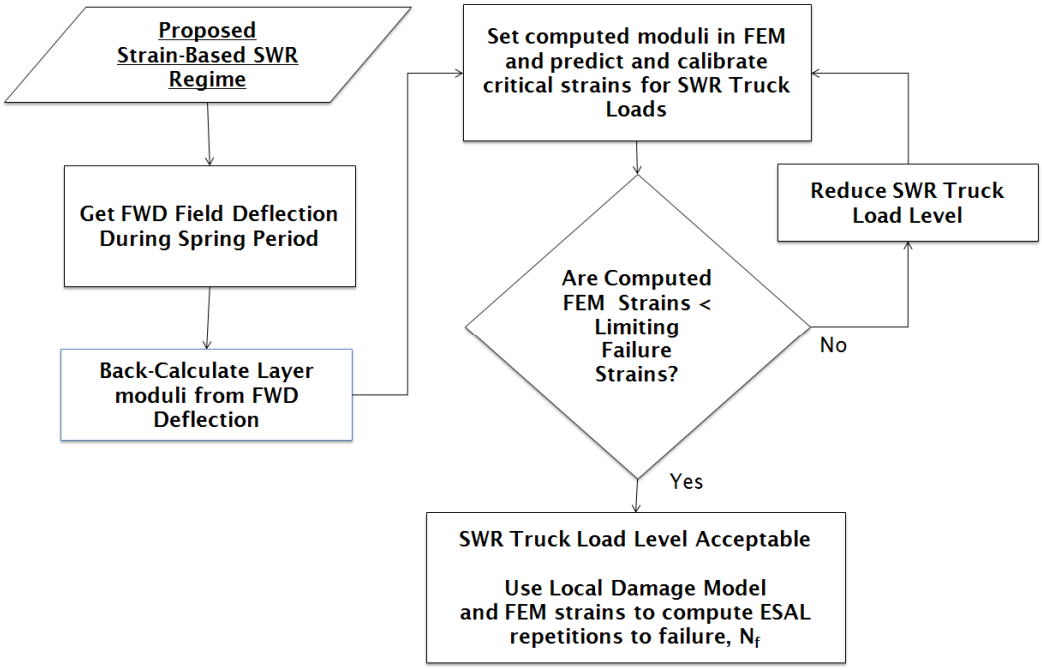

From the conceptual scheme, the FWD deflections could be obtained on a weekly basis and pavement strains predicted using the calibrated FEM at different periods during the spring thaw. The predicted strains can be compared to the limiting strain to determine acceptable load levels. Using the Local damage model to predict the cumulative ESAL repetitions to failure can relate the predicted strains to pavement damage. With that information, the SWR load levels can be determined so that the cumulative damage does not lead to unexpected failure of the pavement.

CHAPTER 9 - CONCLUSIONS AND RECOMMENDATIONS

Local calibrated mechanistic-empirical damage models were developed to predict fatigue and rutting failure on spring weight restricted (SWR) flexible pavements in Manitoba. The low volume Manitoba pavements on PTH 11 and PR 304 were instrumented with strain gauges and environmental sensors to measure pavement responses from a B-Train tractor double trailer at maximum and SWR loads and at two tire pressures (690kPa and 345kPa). The strains were measured during the spring thaw period. In addition, data from instrumented test sections from the Minnesota Road Research (MnROAD) low volume road was obtained to supplement the Manitoba data.

A three-dimensional finite element model (FEM) was calibrated with the measured strains and used to predict the strains at the B-Train maximum loads and tire pressures during the spring thaw. Local fatigue and rutting damage models were developed, calibrated, and validated using the FEM predicted strains and pavement distresses from the MnROAD low volume road. The Local model predictions were compared to the predictions of the Asphalt Institute (AI) and Mechanistic Empirical Design Guide (MEPDG) damage models. The Local damage models were used to assess the SWR loads that regulate commercial vehicle weights, based on limiting failure strain relationships between truck loads and damage.

The findings and conclusions from the research were as follows:

1. The FEM predicted strains confirmed that strains increased with increasing loads on PTH 11 and PR 304. For a 10% increase in load there was an approximate 10% increase in longitudinal and transverse strains at the bottom the AC layer on PTH 11 and an average 10% increase in the vertical strains at the top of the subgrade on both pavements. The B-Train dual tire arrangements created longitudinal strains at the bottom of the AC layer of PTH 11 that were 33% higher on average than the transverse strains.

   The FEM results also indicated that reducing tire pressure, from 690 kPa to 345 kPa, decreased the longitudinal and transverse tensile strains by an average of 15% on PTH 11. However, the same reduction in tire pressure did not significantly reduce the compressive strains at the top of the subgrade. Reducing the tire pressure from 690 kPa to 345 kPa decreased the vertical strain by an average of 1.5% on PTH 11 and PR 304.

   The results indicated that the calibrated FEM could be used to reliably predict strains for any low volume flexible pavement in Manitoba as a function of tire load, axle configuration, inflation pressure, and footprint contact area.

2. The FEM predicted strains were compared to the predicted strains from the KENLAYER layered elastic model. The KENLAYER predicted strains were an average 14% higher than the FEM predicted strains. Both models confirmed the similar trends of increasing strains at higher loads and higher tire pressure. The models also confirmed the positive impacts of reduced tire pressure on strains at the upper surface layer, but little impact on vertical strains at the top of the subgrade.

Based on the similar trends and magnitude of the FEM and KENLAYER strain predictions, KENLAYER could be calibrated and used for structural response modeling.

3. The Local, AI, and MEPDG damage models predicted ESAL repetitions to fatigue and rutting failure were compared. The Local model predicted ESAL repetitions to fatigue failure on PTH 11 were higher by an average of 20% and 37% (across all loads and axle groups) than the AI and MEPDG predictions, respectively. One explanation for the big difference between the Local model predictions and the other models was the Local model was developed and calibrated for weak low volume pavements in a specific region with unique responses of the pavements in that location.

   When the loads were increased by 13%, from A1L1 to RTAC on PTH 11 and at the same tire pressure, the Local, AI, and MEPDG predicted ESAL repetitions to fatigue failure decreased by an average of 13%, 33%, and 38% respectively. The Local, AI, and MEPDG predicted ESAL repetitions to rutting failure decreased by an average of 10%, 45%, and 45% respectively, for the same load increase.

   When the tire pressure was reduced from 690kPa to 345kPa over all loads and axle groups, the Local, AI, and MEPDG predicted ESAL repetitions to fatigue failure increased by an average 17%, 60%, and 74%, respectively. The Local, MEPDG, and AI predicted ESAL repetitions to rutting failure increased by an average 1%, 5%, and 5%, respectively, with the same reduction in tire pressure.

   The AI and MEPDG predictions indicated that reducing tire pressure had a significantly positive impact on fatigue performance, which could more than

compensate for an increase in loads by up to two levels for the spring condition. The Local model predictions were less sensitive to changes in tire pressure on fatigue performance because the Local model was developed only at 690kPa, which was the standard tire pressure on the MnROAD 5-axle semi trailer. The Local, AI, and MEPDG model predictions indicated that reduced tire pressure had minimal impact on rutting performance.

In general, for each 1% increase in load, there was an approximate 1% increase in the FEM horizontal and vertical strains, and an approximate 1.5% and 3% decrease in the ESAL repetitions to fatigue and rutting failures, respectively, for the AI and MEPDG models. For the Local model, there was an approximate 0.5% and 1.5% decrease in ESAL repetitions to fatigue and rutting failures, respectively, for each 1% increase in load. Therefore, a one fold increase in load can result in up to a three fold decrease in the predicted ESAL repetition to failure depending on the damage model. This is why a strain based SWR evaluation of damage is much more relevant than deflection.

4. A statistical analysis was conducted to determine whether the means of the Local, AI and MEPDG predicted ESAL repetitions to failure were statistically different. The results of the t-test indicated that the Local, AI, and MEPDG predicted ESAL repetitions to rutting and fatigue failures were statistically different at the 95% confidence level.

   However for a given pavement, the Local, AI, or MEPDG model could be used to assess the relative damage effects under different loading and tire pressure conditions. The use of either the local, AI or MEPDG to compare damage in different pavements

with different materials and layer thicknesses could result in an overestimation of fatigue damage or underestimation of rutting damage, or vice versa.

5. The Local, AI, and MEPDG damage models were used to determine the limiting failure strains at failure on PTH 11 and PR 304. The results show that the limiting strains at 100,000 ESALs from the Local, AI, and MEPDG models were at 483μm/m to 496μm/m for horizontal strains (fatigue failure), and 800μm/m to 1,008μm/m for vertical strain (rutting failure). The Local model limiting strains were different from the AI and MEPDG at the 50,000 ESAL level.

   The Local model limiting strains of 483μm/m for horizontal strains and 1,008μm/m for low volume roads with 100,000 ESALs can be used for PTH 11 and PR 304.

6. The Local model limiting failure strains for PTH 11 and PR 304 were compared to the FEM predicted and calibrated strains at the B-Train maximum allowable and SWR loads. The predicted strains on PTH 11 were higher than the limiting strains at all load levels, and at two of the three load levels on PR 304. The limiting failure strains should be validated with other pavements to verify the findings.

7. A strain-based concept on how to manage the SWR regime in Manitoba based on the limiting strains was developed for PTH 11 and PR 304. From the conceptual scheme, the strains at different periods in the pavement can be predicted during the spring thaw period using the calibrated FEM. The FEM predicted strain can be compared to the limiting strain. The FEM strains can be related to the damage experienced by the pavement using the Local damage model to predict the cumulative ESAL repetitions

to pavement failure. With that information, the SWR load levels can be determined so that the cumulative damage does not lead to unexpected failure of the pavement.

RECOMMENDED FUTURE RESEARCH

The following future research is proposed:

1. Instrument three additional low volume flexible pavements to validate the magnitude of the strains measurements during the spring.

2. Model the retrofit strain installation layout on PTH 11 with the FEM to verify strain calibration factors.

3. Further validate the coefficients of the Local damage model with a larger data set of low volume flexible pavement strains and rutting and fatigue data.

4. Calibrate and develop local coefficients for the MEPDG models and compare to the Local model predictions. Manitoba is currently evaluating MEPDG for future roadway design and analysis.

5. Validate the strain-based concept on how to manage SWR load levels on selected low volume roads. The limiting strain analysis should be validated with other pavements to verify the research findings.

REFERENCES

AASHTO (American Association of State Highways and Transportation Officials), (1962), "*The AASHTO Road Test - Report 5"*, Pavement Research, Highway Research Board

AASHTO (American Association of State Highways and Transportation Officials), (1993) "*Guide for Design of Pavement Structures*", Washington DC

AASHTO (American Association of State Highways and Transportation Officials), (2001) *"T256 – Standard Method of Test for Pavement Deflection Measurements"*, Highway Research Board

AI (Asphalt Institute), (1982), *"Research and Development of the Asphalt Institute Thickness Design Manual (MS-1)"*, Ninth Edition, Research Report, No. 82-1

ASTM (American Society for Testing and Materials), (2008), *"ASTM D5858 - Standard Guide for Calculating in Situ Equivalent Elastic Moduli of Pavement Materials Using Layered Elastic Theory"*

ASTM (American Society for Testing Materials), (2009), *"ASTM D4694 - Standard Test Method for Deflection with Falling-Weight-Type Impulse Load Device*

Baburamani, P., (1999) *"Asphalt Fatigue, Life Prediction Models – A Literature Review",* Research Report ARR 334, Australian Road Research Board (ARRB) Transport Research

Bao, W., (2000), *"Calibration of Flexible Pavement Structural Model using Mn/ROAD Field Data"*, Master of Science Thesis, University of Minnesota, Department of Civil Engineering

Bayat, A., Knight, M., and Adedapo, A., (2010), *"Flexible Pavement Response under Dynamic Wheel Loads – A CPATT Full Scale Instrumented Test Road"*, 8th International Transportation Specialty Conference, Canadian Society for Civil Engineering

Beranek, S., and Carpenter, S., (2009), *"Fatigue Failure Testing in Section F – A Report of the Findings of ICT-R39 Validation of Extended Life HMA Pavement Design Concepts",* Research Report ICT-09-058, Illinois Center for Transportation, University of Illinois at Urbana-Champaign

Berg, R. L., Bigl, R., Stalk, J., and Durell, G., (1996), *"Resilient Modulus Testing of Materials from MNROAD, Phase 1; Report #96-21",* US Army Cold Region Research and Engineering Laboratory, and Minnesota Department of Transportation

Bradley, A., (2006), *"Hauling with Full Axle Weights and Reduced Tire Pressures on Weight Restricted Roads in British Columbia"*, Transportation Research Record, No. 1967, Transportation Research Board

Bradley, A., and Shalaby, A., (2007), *"Extending the Spring Haul Season on Thaw-weakened Roads in Manitoba – Phase 1 Proposal"*, Report prepared for Manitoba Infrastructure and Transportation by the Department of Civil Engineering, University of Manitoba and FP Innovations

Brown, S., (1997), *"Achievements and Challenges in Asphalt Pavement Engineering"*, 8th International Conference on Asphalt Pavements, ISAP

Bullock, M., Tighe, S., and Bolduc, P., (2006), *"The Opportunities for Intelligent Transportation Systems to Assist with Spring Load Restrictions and Winter Weight Premiums",* Annual Conference of the Transportation Association of Canada

Burnham, T. R., Tewfik, A., and Srirangarajan, S., (2007), *"Development of a Computer Program for Selecting Peak Dynamic Sensor Responses From Pavement Testing, Final Report"*, Report prepared for the Minnesota Department of Transportation by the Department of Electrical and Computer Engineering, University of Minnesota

Carpenter, S., Ghuzlan, K., and Shen, S, (2003), *"Fatigue Endurance Limit for Highway and Airport Pavements"*, Paper#03-3428, Transportation Research Board Annual Meeting

Chapin, J., Pernia, J., Kjartanson, B., (2009) *"Seasonal Load Restrictions on Low Volume Highway: Pavement Strength Estimation"*, Annual Conference of the Transportation Association of Canada

Clayton, A., and McGregor, R., (2001) *"Harmonization of Spring Weight Restrictions and Winter Weight Premiums for Roads in the Prairie Region"*, Report Executive Summary, Report #ABTR/RD/RR-01/01, University of Manitoba and EBA Engineering Consultant Ltd

Clayton, A., Montufar, J., Regehr, J., Issacs, C., and McGregor, R., (2005), *"Aspects of the Potential Impacts of Climate Change on Seasonal Weight Limits and Trucking in the Prairie Region"*, Climate Change Impacts and Adaptation Directorate, Natural Resources Canada, Report by the University of Manitoba Transport Information Group, and EBA Engineering

Clayton, A., and McGregor, R., (2001), *"Harmonization of Spring Weight Restrictions and Winter Weight Premiums for Roads in the Prairie Region"*, Report Executive Summary, ABTR/RD/RR-01/01

Cline, T., and Worel, B., (2009), *"MnROAD Safer, Smarter, Sustainable Pavements through Innovative Research"*, Minnesota Road Research, Office of Materials,Version 1

Cowe-Falls, L., and Knoth, J., (2006), *"Pavement Response to Legal Overloads at the Nisku Test Road, Alberta"*, Annual Conference of the Transportation Association of Canada

Dai, S., Van Deusen, D., Beer, M., Rettner, D., and Cochran, G., (2000), *"Investigation of Flexible Pavement Response to Truck Speed and FWD Load through Instrumented Pavements"*, Minnesota Department of Transportation

Dai, S., and Zollars, J., (2002), *"Resilient Modulus of Minnesota Road Research Project Subgrade Soil"*, Transportation Research Record 1786, Transportation Research Board

Dorman, G., (1962), *"The Extension to Practice of a Fundamental Procedure for Design of Flexible Pavements"*, Proceedings of 1st International Conference of Structural Design of Asphalt Pavement

Duncan, J. C., (1968), "*Finite Element Analyses of Pavements"*, Highway Research Record No. 228, Highway Research Board, pp. 18-33

ELMOD5, (2007), *Software Version 5.1.72*, Dynatest International

Fernando, E. G., (2006), *"Determine Effects of Tire Size and Inflation Pressure on Tire Contact Pressure and Primary Pavement Response to Loading"*, Texas Transportation Institute, Texas A&M University, Project 0-4361

FHWA (Federal Highway Administration), (1990), *"Spring Load Restrictions"*, Pavement Newsletter No. 17, US Department of Transportation

FHWA (Federal Highway Administration), (2010), *"LTPP Protocol P07 - Test Method for Determining the Creep Compliance, Resilient Modulus and Strength of Asphalt Materials using the Indirect Tensile Test Device*"

Ghuzland, K.A., and Carpenter, S.H., (2003), *"Traditional Fatigue Analysis of Asphalt Concrete Mixtures"*, Transportation Research Board Annual Meeting CD-ROM

Groebner, D. F., Shannon, P. W., Fry, P. C., and Smith, K. D., (2008), *"Business Statistics: A Decision-Making Approach"*, Seventh Edition, Pearson Prentice Hall, Upper Saddle River, NJ.

Haas, R., Hudson, W.R., and Zaniewski, J., (1994), *"Modern Pavement Management"*, Krieger Publishing, Malabar

Hoegh, K., Khazanovich, L., and Jensen, M., (2010), *"Local Calibration of MEPDG Rutting Model for MnROAD Test Sections"*, Transportation Research Board Annual Meeting CD-ROM

Huang, Y. H., (2004), *"Pavement Analysis and Design,"* 2nd Edition, Pearson Prentice Hall, Upper Saddle River, NJ

Huen, K., Tighe, S., Mills, B., and Perchanok, M., (2006), *"Development of Tools for Improved Spring Load Restriction Policies in Ontario"*, Annual Conference of the Transportation Association of Canada

Johnson, S., (2006), *"Comparison of Nonlinear Finite Element Modeling Tools for Structural Concrete",* Department of Civil and Environmental Engineering, University of Illinois at Urbana-Champaign

Kavanagh, L., Shalaby, A., Liu, Q., Bradley, A., and Mercier, S., (2010), *"Data Analysis, Pavement Model Development and Calibration, and Rational Model for Lifting SLR in Manitoba, Interim Report #3"*, Report prepared for Manitoba Infrastructure and Transportation by the Department of Civil Engineering, University of Manitoba, and FP Innovations

Kavanagh, L., Shalaby, A., Liu, Q., Bradley, A., and Mercier, S., (2011), "*Recommendations to Improve the Productivity of the Manitoba Trucking Industry; Use of Tire Pressure Control Systems during SLR, and a Rational Method for Ending SLR, Final Report #4"*, Report prepared for Manitoba Infrastructure and Transportation by the Department of Civil Engineering, University of Manitoba, and FP Innovations

Kim, M. E. T., (2007), *"Nonlinear Pavement Foundation Modeling for Three-Dimensional Finite Element Analysis of Flexible Pavements"*, Transportation Research Board Annual Meeting CD-ROM

Kersten, M.S., and Skok E., (1968), *"Application of AASHTO Road Test Results to Design of Flexible Pavements in Minnesota",* Minnesota Department of Highways and University of Minnesota

Levinson, D., Marastenu, M., Voller, V., Margeau, I., Smalkowski, B., Hashami, M., Li, N., Corbett, M., and Lukanen, E., (2005), *"Cost-Benefit Study of Spring Load Restriction",* Minnesota Department of Transportation, Report Mn/RC-2005

Liu, Q., (2011), *"Instrumentation and Finite Element Simulation of Pavement Responses to Standard and Reduced Tire Pressure"*, M.Sc. Thesis, Civil Engineering Department, University of Manitoba, Winnipeg, Manitoba

Liu, Q., Kavanagh, L., and Shalaby, A., (2011), *"Impacts of Reduced Truck Tire Pressure on Strain Response of Low Volume Spring Restricted Roads in Manitoba, Canada"*, Transportation Research Record, Journal of the Transportation Research Board, No. 2203, Low Volume Roads, Volume 1, p.186-193

Liu, Q., and Shalaby, A., (2013), *"Simulation of Pavement Response to Tire Pressure and Shape of Contact Area"*, Canadian Journal of Civil Engineering, Volume 40(3), p.236-242

Lukanen, E.O., (2005), *"Load Testing of Instrumented Pavement Sections, Final Report"*, University of Minnesota, Department of Civil Engineering

Mabood, F., Tighe, S., Klement, T., Kazmierowski, T., and Mercier, S., (2008), *"Evaluating Tire Pressure Control Systems (TPCS) to Improve Productivity and Mitigate Pavement Damage"*, Conference of the Transportation Association of Canada

MIT (Manitoba Infrastructure and Transportation), (1964), *"Bituminous Paving Mixture Analysis"*, Materials Engineering

MIT (Manitoba Infrastructure and Transportation), (2008), "*Soil Survey Report"*, Materials Engineering

MIT (Manitoba Infrastructure and Transportation), (2009), *"Manitoba's 2009 Spring Road Restriction (SRR) Program"*, www.gov.mb.ca/mit/srr

MnDOT (Minnesota Department of Transportation), (2009), *"Policy and Process for Seasonal Load Limit Starting and Ending Dates"*, Minnesota Technical Memorandum No. 09-09-MAT-02

MnROAD (Minnesota Road Research), (2009), *"Providing Research Insight for a Safe, Efficient, and Cost-Effective Transportation System"*, National Research and Technology Center, Minnesota Department of Transportation

MnROAD (Minnesota Road Research), (2009), *"Semi Tractor Trailer Brief"*, Minnesota Road Research, Minnesota Department of Transportation

MnROAD (Minnesota Road Research), (2010), "*Low Volume Road Instrumentation"*, Minnesota Department of Transportation website, http://www.dot.state.mn.us/mnroad/instrumentation/pavementsensors.html

Monismith, C., Secor, K., and Blackmer, W., (1961), *"Asphalt Mixture Behavior in Repeated Flexure"*, Association of Asphalt Paving Technology, AAPT, Volume 30

Monismith, C., and Deacon, X., (1969), *"Fatigue of Asphalt Paving Mixtures"*, American Society for Civil Engineering (ASCE), Journal of Transportation Engineering, Volume 95

Montufar, J., Han, K., Lew, K., Clayton, A., Shalaby, A., McGregor, R., Sims, R., Palsat, D., and MacDonald, A., (2000), *"Study for the Harmonization of Spring Weight Restrictions and Winter Weight Premiums for Roads in the Prairie Region: Technical Rationale for Policies and Practices Relating to Winter Weight Premiums and Spring Weight Restrictions",* University of Manitoba, Transport Information Group, and EBA Engineering Consultants Ltd

Montufar, J., and Clayton, A., (2002), *"Seasonal Weight Limits on Prairie Region Highways: Opportunities for Rationalization and Harmonization"*, Canadian Journal of Civil Engineering, Volume 29, p.8-16

Moreno, A. M., (2000), *"Load Equivalency Factors from the Structural Response of Flexible Pavements"*, Master of Civil Engineering Thesis, Department of Civil Engineering, University of Minnesota

NCHRP (National Cooperative Highway Research Program), (2002) *"Simple Performance Test for Superpave Mix Design"*, NCHRP Report 465, Project 9-29, Transportation Research Board, Washington, DC

NCHRP (National Cooperative Highway Research Program), (2004) *"Finite Element Procedures for Flexible Pavement Analysis"*, NCHRP Final Document, Appendix RR, Transportation Research Board, Washington, DC

NCHRP (National Cooperative Highway Research Program), (2007), *"Mechanistic-Empirical Pavement Design of New and Rehabilitated Pavement Structures",* NCHRP Project 1-37A and NCHRP Project1-40A, Federal Highways Administration

NCHRP (National Cooperative Highway Research Program), (2010), *"Validating the Fatigue Endurance Limit for Hot Mix Asphalt"*, NCHRP Project 9-38, Transportation Research Board

Newcomb, D., and Birgisson, B., (1999) *"Measuring In Situ Mechanical Properties of Pavement Subgrade Soils"*, NCHRP Synthesis 278, Transportation Research Board

Nichizawa, T., Shimeno, S., Sekiguchi, M., (1996), *"Fatigue Analysis of Asphalt Pavements with Thick Asphalt Mixture Layers",* Proceedings, 8th International Conference on Asphalt Pavements, Seattle, Washington, pp.969-976

Odermatt, N., Janoo, V., and Magnusson, R., (1999), *"Analysis of Permanent Deformation in Subgrade Material Using a Heavy Vehicle Simulator",* International Conference in Accelerated Pavement Testing, Reno, Nevada

Ovik, J., Birgisson, B., and Newcomb, D., (2000), *"Characterizing Seasonal Variations in Pavement Material Properties for Use in a Mechanistic-Empirical Design Procedure"*, Final Report 1996-2000, Minnesota Department of Transportation

Papagiannakis, A.T., and Masad, E.A., (2008), *"Pavement Design and Materials"*, John Wiley and Sons, Inc.

Park, D. W., (2008), *"Prediction of Pavement Fatigue and Rutting Life Using Different Tire Types"*, Korean Society Civil Engineering Journal of Civil Engineering, pp. 297-303, 2008

Raad, L., Minassian, G., and Saboundjian, S., (1998), *"Mechanistic Evaluation of the Effect of Tire Inflation Pressure on Pavement Damage under Spring-Thaw Weakening"*, Transportation Research Board, Washington, DC

Rutherford, M.S., (1989), *"Pavement Response and Load Restrictions on Spring Thaw-Weakened Flexible Pavements"*, Transportation Research Record No. 1252, p.1-11

Schwartz, C., and Carvalho, R., (2007), *"Implementation of the NCHRP 1-37A Design Guide, Final Report, Volume 2: Evaluation of Mechanistic-Empirical Design Procedure",* Department of Civil and Environmental Engineering, University of Maryland

Shalaby, A., Law, T., and Kavussi, A., (2004), *"Comparing Back-Calculated and Lab Resilient moduli of Bituminous Paving Mixtures"*, Canadian Journal of Civil Engineering, Volume 31, p.988-996

SHRP (Strategic Highway Research Program), (2001), *"Distress Identification Manual for the Long Term Pavement Performance Project Protocol*", Federal Highway Administration

Smalkowski, B., Ning, L., and Levinson, D., (2006), *"Economic Effects of Lifting the Spring Load Restriction Policy in Minnesota"*, Journal of the Transportation Research Forum, pp. 45-56

Smith, D., (1993), *"Effects of Variable Tire Pressure on Road Surfacings, Volume II: Analysis of Test Results"*, Technical Report GL-93-20, US Army Corps of Engineers. Waterways Experiment Station, Vicksburg, MS., 84 p.

Soliman, H., (2010), *"Laboratory Determination of Resilient Modulus of Subgrade and Base Materials"*, Civil Engineering Department University of Manitoba

TAC (Transportation Association of Canada), (1997), *"Pavement Design and Management Guide"*

TI (Transport Institute), (2010), *"Manitoba Transportation Report"*, Transport Institute University of Manitoba

Timm, D. H., and Priest, A. L., (2004), *"Dynamic Pavement Response Data Collection and Processing at the NCAT Test Track"*, NCAT Report 04-03

Timoshenko, S., and Goodier, J., (1951), *"Theory of Elasticity"*, Professors of Engineering Mechanics Stanford University, McGraw Hill Inc., Second Edition

TXDOT (Texas Department of Transportation), (2008), *"Falling Weight Deflectometer"*, Technical Advisory

Ullidtz, P., (1998), *"Deterioration Models for Managing Flexible Pavement"*, Paper offered for Presentation at 78th Annual Meeting of the Transportation Research Board, Washington DC

Van Deusen, D., Schrader, C., and Johnson, G., (2002), *"Evaluation of Spring Thaw Load Restriction and Deflection Interpretation Techniques"*, International Society for Asphalt Pavements (ISAP), Ninth International Conference on Asphalt Pavement

Von Quintus, H. and Killingsworth, B., (1998) "*Analyses Relating to Pavement Material Characterizations and Their Effects on Pavement Performance"*, FHWA-RD-97-085, U.S. Department of Transportation, Federal Highway Administration, McLean, VA

Wang, F., and Machemehl, R., (2006), *"Predicting Truck Tire Pressure Effects Upon Pavement Performance"*, Report No. SWUTC/06/167864-1, Southwest Region University Transportation Center, Texas Transportation Institute, Texas A&M University System, College Station, Texas

Wardle, L., Youdale, G., and Rodway, B., (2003), *"Current Issues for Mechanistic Pavement Design"*, AARB Transport Research

Willis, J., and Timm, D., (2008), "*Repeatability of Asphalt Strain Measurement under Full Scale Dynamic Loading"*, Transportation Research Record, No 2087, Transportation Research Board, pp.40-48

Wu, H., (2001), *"Parallel Methods for Static and Dynamic Simulation of Flexible Pavement Systems"*, Doctoral Dissertation, University of Washington

Wu, Z., and Hossain, M., (2003), *"Pilot Instrumentation of a Superpave Test Section at the Kansas Accelerated Testing Laboratory"*, Final Report No. KTRAN:KSU-98-2, Kansas State University, A cooperative Transportation Research Program between Kansas State University and Kansas Department of Transportation

Yapa, K. A. S., and Lytton, R. L., (1988), *"A simplified Mechanistic Rut Depth Prediction Procedure for Low-Volume Roads"*, FHWA/TX-89/473-1, Texas Transportation Institute, Texas A&M University

Yoder, E., and Witczak, M., (1975), *"Principles of Pavement Design"*, Second Edition, Wiley

APPENDICES

APPENDIX A

Manitoba SWR Zones, Maximum Allowable and SWR Axle Weights

Manitoba Infrastructure and Transportation (MIT) manages approximately 18,700 km of primary Provincial Trunk Highways (PTH), and secondary Provincial Roads (PR) in Manitoba. Of this amount, 12,000 km are bituminous and AST surfaced roads, 700 km are concrete surfaced roads, and 6,000 km are gravel roads [MIT, 2009]

Based on Manitoba's Spring Road Restriction Program, approximately 4,800 km of the 12,000 km of bituminous and AST paved roads are annually affected by SWR. Gravel and concrete surfaced roads are not subject to SWR.

Manitoba's vehicle weight regulations are based on three weight classes which are applied to a PTH or PR road. The weight classes are RTAC (vehicles that meet national requirements defined in the Roads and Transportation Association of Canada (RTAC) memorandum of Understanding), A1, and B1 weights. RTAC weights are at the highest load levels, followed by A1 and B1 weights, respective.

MIT has two climatic zones and two levels of SWR. Because of differing thaw rates, the province has been divided into two zones; Zone 1 (south) and Zone 2 (north). The SWR start and end dates are by climatic zones. In climatic Zone 1, SWR is applied earlier, and is removed earlier, than Zone 2.

The two levels of SWR are Level 1 and Level 2. Level 1 is at 90 % of the normal axle weights and is usually applied on Class A1, and Class B1 roadways. As the road structure gets weaker, and deflections increase, the next level of restriction is imposed. Level 2 SWR is at 65 % of the normal axle weights and is usually applied on Class A1 and Class B1 roadways.

Table A-1 presents the Manitoba climatic zones and SWR start and end dates.

Table A-1: Manitoba Climatic Zones and SWR Start and End Dates [after MIT, 2009]

Climatic Zone	SWR[1] Start Date	SWR[1] End Date
Zone 1	Mar 18, 2010	May 26, 2010
Zone 2	Mar 25, 2010	May 31, 2010

Note: [1] Spring Weight Restriction

Figure A-1 shows the two Manitoba climatic SWR zones.

Figure A-1: Manitoba Climatic SWR Zones [after MIT, 2009]

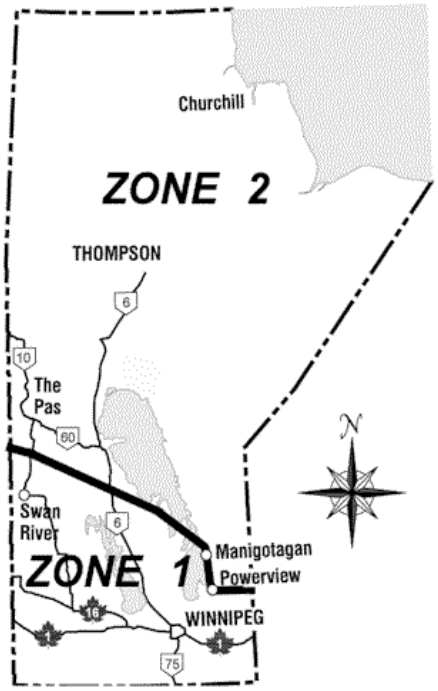

Table A-2 presents the Manitoba maximum allowable and SWR axle weights. The weights are by RTAC, A1, and B1 roads and different axle groups.

Table A-2: Manitoba Maximum Allowable and SWR Axle Weights [after MIT, 2009]

MANITOBA MAXIMUM ALLOWABLE and SWR AXLE WEIGHTS (kilogram)				
Axle Loading	**Steering Axle**	**Single Axle**	**Tandem Axle**	**Tridem Axle**
RTAC normal	5,500	9,100	17,000	23,000
A1 normal	5,500	9,100	16,000	23,000
A1 90%	5,500	8,190	14,400	20,700
A1 65%	3,575	5,915	10,400	14,950
B1 normal	5,500	8,200	14,500	20,000
B1 90%	5,500	7,380	13,050	18,000
B1 65%	3,575	5,330	9,425	13,000

Note: [1] Spring Weight Restriction

APPENDIX B

Minnesota SWR Zones, Maximum Allowable and SWR Axle Weights

Minnesota public highway system has approximately 217,000 km of roads. MnDOT administers approximately 9% of this system. The road system is divided into 10-ton, 9-ton, 7-ton, and 5-ton roads that designate the maximum allowable load on any single axle. The 10-ton roads generally have good structural capacity and are not affected by SWR [Levinson, 2005].

Minnesota roadways are generally categorized into two specific groups. The main group consists of all State Trunk Highways, all paved County and County State-Aid Highways, and other routes. These roads are commonly referred to as 10-ton routes. Minnesota statutes provide for maximum loads which may be carried upon any wheel, any single axle, any group of consecutive axles, and the gross vehicle weight [MnROAD, 2009].

There are about 62,750 kilometers of paved roads in Minnesota that do not meet the 10-ton spring load design standard and are restricted to lower loads during the spring period. Included in these restricted roads are about 2,575 kilometers of State Trunk Highways, 37,975 kilometers of county state aid highways, 3,860 kilometers of municipal state aid city roads, and roughly 17,700 kilometers of other local roads [MnROAD, 2009].

In the spring of each year, 9-ton roads are restricted to 7-ton and 5-ton normal weights for groups of two or more consecutive axles. The starting and end dates for the restrictions are determined for each of the six climatic or frost zones in Minnesota.

Table B-1 presents the Minnesota climatic zones and SWR start and end dates.

Table B-1: Minnesota Climatic Zones and SWR Start and End Dates [after MnROAD, 2009]

Climatic Zone	SWR[1] Start Date	SWR[1] End Date
North	Mar 09, 2010	May 03, 2010
North-Central	Mar 09, 2010	Apr 26, 2010
Central	Mar 09, 2010	Apr 19, 2010
Metro	Mar 08, 2010	Apr 12, 2010
South	Mar 08, 2010	Apr 12, 2010
Southeast	Mar 08, 2010	Apr 12, 2010

Note: [1] Spring Weight Restriction

Figure B-1 shows the Minnesota SWR zones due to the differing thaw rates.

Figure B-1: Minnesota SWR Zones [after MnROAD, 2009]

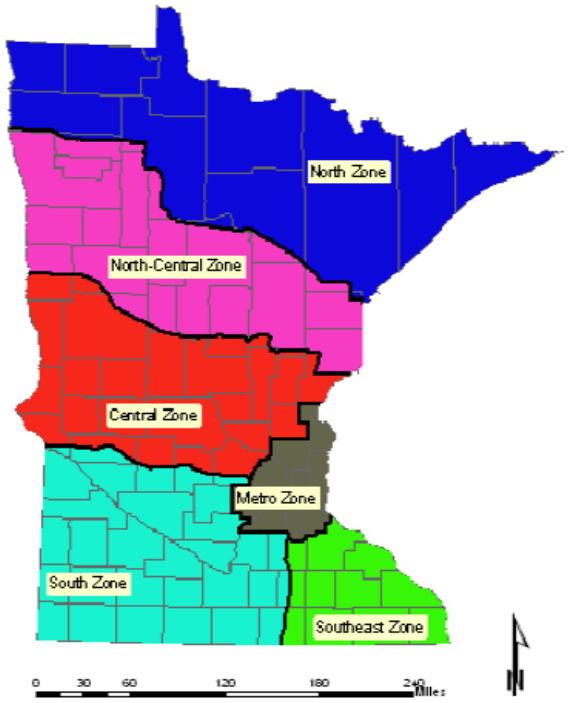

Table B-2 presents the Minnesota maximum allowable and SWR axle weights for a 5-axle semi trailer.

Table B-2: Minnesota Maximum Allowable and SWR Axle Weights

MAXIMUM ALLOWABLE AND SWR AXLE WEIGHTS (kilogram) for 5-axle Semi Trailer			
Axle Loading	**Steering Axle**	**Single Axle**	**Tandem Axle**
9-Ton Route (SWR) Reduced to 7-Ton Route Loads	4 080[1]	6,364	11 990
9-Ton Route - Normal	4 080	8 160	15 413
10-Ton Route - Normal	4 533	9 066	15 413

Note: [1]Maximum allowable 9-ton SWR steering axle = 4,080 kg

APPENDIX C

Manitoba B-Train Configuration and Dimensions

The test vehicle at the Manitoba sites was an 8-axle B-train.

Figure C-1 shows the Manitoba B-Train configuration.

Figure C-1 : Manitoba B-Train Configuration and Dimensions [after MIT, 2009]

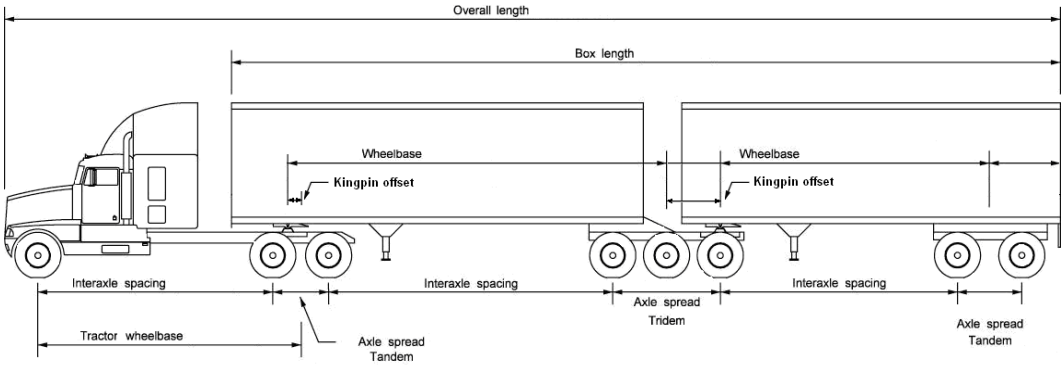

Table C-1 presents the Manitoba B-Train dimensions.

Table C-1 : Manitoba B-Train Dimensions

Parameters	Length (m)
Overall length	23.83
Box (trailer) length	20.00
Tractor wheelbase	5.36
Tractor axle spread (tandem)	1.32
Tractor interaxle spacing	4.70
Lead semi-trailer wheelbase	8.27
Lead semi-trailer axle spread (tridem)	3.04
Lead semi-trailer interaxle spacing	6.19
Lead semi-trailer kingpin offset	0.76
Second semi-trailer wheelbase	7.62
Second semi-trailer axle spread (tandem)	1.52
Second semi-trailer interaxle spacing	6.10
Second semi-trailer kingpin offset	0.76

Table C-2 presents the Manitoba maximum allowable and SWR load limits for each axle group of the 8-axle B-Train (i.e. steering, drives, lead and rear trailers, respectively).

Table C-2: Manitoba Maximum Allowable and SWR Load Limits - 8-Axle B-Train

Spring Weight Restriction Rating	Maximum Allowable Axle Group Load Limits 8-Axle B-Train (kilogram)				
	Steering Axle	Drive Tandem Axle	Front Trailer Tridem Axle	Rear Trailer Tandem Axle	GVW[1]
B1 Level 2	3 575	9 425	13 000	9 425	35 425
B1 Level 1	5 500	13 050	18 000	13 050	47 630
B1 Normal	5 500	14 500	20 000	14 500	47 630
A1 Level 1	5 500	14 400	20 700	14 400	55 000
A1 Normal	5 500	16 000	23 000	16 000	56 500
RTAC Normal	5 500	17 000	23 000	17 000	62 500

Note: [1]Gross Vehicle Weight

APPENDIX D

MnROAD 5-Axle Semi Trailer Configuration and Dimensions

The control vehicle at the MnROAD low volume test road is a 5-axle semi trailer.

Figure D-1 shows the MnROAD 5-axle semi trailer configuration and dimensions.

Figure D-1: MNROAD 5-Axle Semi Trailer Configuration and Dimensions [after Cline et al , 2009]

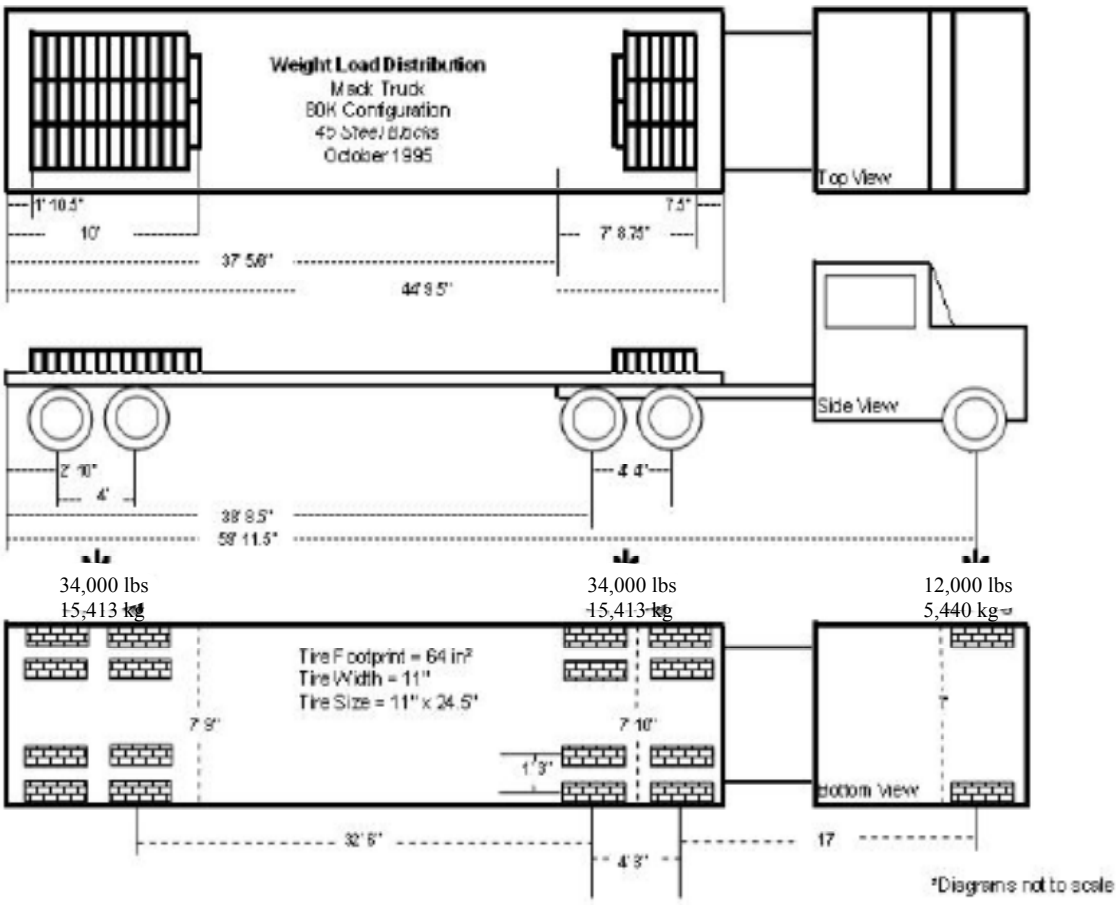

Note: Truck Dimensions in imperial units

Table D-1 presents the Minnesota maximum allowable and SWR load limits for the 5 axle semi trailer group (i.e. steering, drive, and trailer).

Table D-1: Minnesota Maximum Allowable and SWR Load Limits for 5-Axle Semi Trailer

Spring Weight Restriction Rating	Maximum Legal and SWR Axle Group Load Limits (kg) 5-Axle Semi Trailer				
	Steering Axle	Tandem Drive Axle	Tandem Trailer Axle		GVW[1]
10-Ton Route Normal	4,533	15,413	15,413		35,359
9-Ton Route Normal	4,080	15,413	15,413		34,906
9-Ton Route SWR[2] (7-Ton loads)	4,080 [3]	11,990	11,990		28,060

Note: [1]Gross Vehicle Weight,
[2] Spring Weight Restriction
[3] Maximum allowable 9-ton SWR steering single axle = 4,080 kg

APPENDIX E

MnROAD Instrumentation Layout for Asphalt Strain Gauge, Vertical Pressure Gauge, and Thermocouple Gauge

Bituminous strain gauges, dynamic soil pressure gauges, and thermocouple gauges were embedded throughout the pavement and subgrade layers to measure horizontal pavement strains and vertical soil pressures due to the semi trailer loads for Cells 26A, 27A, and 28A at the MNROAD low volume road test site.

The bituminous strain gauges were placed horizontally at the bottom of the asphalt layer in both longitudinal (LE) and transverse directions (TE) to measure tensile strains at the bottom of the AC layer, in both the 80KIP and 102KIP lanes.

The vertical pressure gauges (PK) were placed at the top of the subgrade to measure vertical pressures on the subgrade due to loading. The thermocouples were installed at the centerline of the 80KIP lane to measure layer temperatures, in the middle of the outer wheelpath and at the edge of the shoulder.

For the 80KIP lane, the sensors were placed at three locations under the wheelpath of each lane, one in the inner edge of the wheelpath (LE1/TE1/PK1), one in the center of the wheelpath (LE2/TE2/PK2), and one at the outer edge of the wheelpath (LE3/TE3/PK3).

For the 102KIP lane, the sensors were placed at the same offsets but designated LE4/TE4/PK4 at the inner edge of the wheelpath, LE5/TE5/PK5 at the center of the wheelpath, and LE6/TE6/PK6 at the outer edge of the wheelpath.

Table E-1 presents the typical MnROAD longitudinal and transverse bituminous strain gauge locations and sensor layout information under the AC layer of Cell 26A. The sensor offsets were measured from the centerline between the two lanes, and the sensor depth measured from the surface of the pavement. The negative offset (-) represented the 80KIP lane and positive (+) offset represented the 102KIP lane.

Table E-1: MnROAD Longitudinal (LE) and Transverse (TE) Bituminous Strain Gauge Locations - Cell 26A

CELL	MODEL	STATION	SEQUENCE	SENSOR ID	SENSOR OFFSET		SENSOR DEPTH	
		(Feet)	(SEQ)		(Feet)	(Meter)	(Inch)	(mm)
26A	TE	17180	1	26TE001	-8.5	-2.6	6.4	163
26A	TE	17180	2	26TE002	-9.5	-2.9	6.5	165
26A	TE	17180	3	26TE003	-10.5	-3.2	6.6	168
26A	TE	17180	4	26TE004	8.6	2.6	5.4	137
26A	TE	17180	5	26TE005	9.5	2.9	5.4	137
26A	TE	17180	6	26TE006	10.5	3.2	5.2	132
26A	LE	17185	1	26LE001	-8.5	-2.6	6.1	155
26A	LE	17185	2	26LE002	-9.5	-2.9	6.1	155
26A	LE	17185	3	26LE003	-10.5	-3.2	6.2	158
26A	LE	17185	4	26LE004	8.5	2.6	5.4	137
26A	LE	17185	5	26LE005	9.5	2.9	5.2	132
26A	LE	17185	6	26LE006	10.5	3.2	5.2	132

Figure E-1 shows the MnROAD longitudinal and transverse bituminous strain gauge locations and sensor layout under the AC layer of Cell 26A.

Figure E-1: MnROAD Longitudinal (LE) and Transverse (TE) Bituminous Strain Gauge Locations - Cell 26A

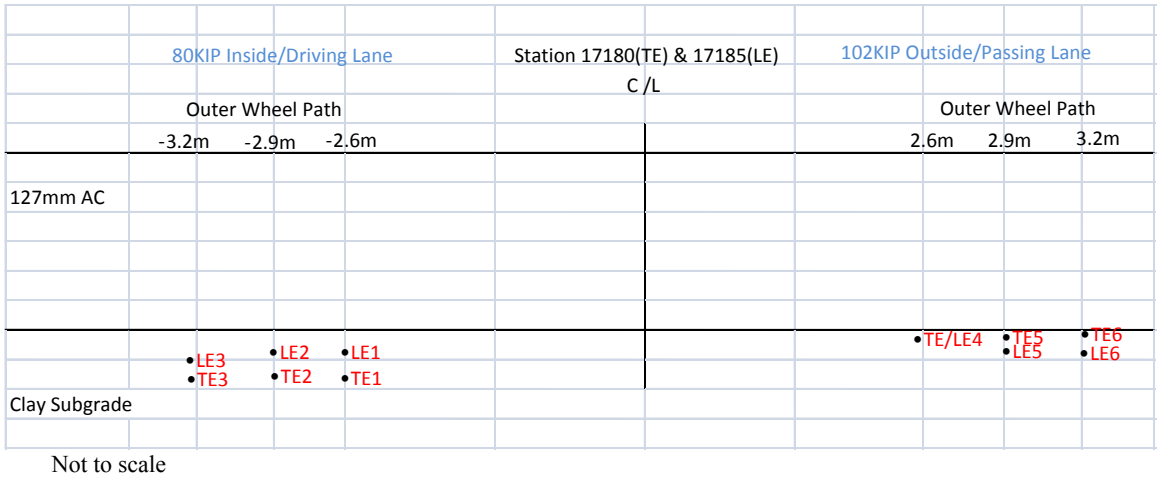

Not to scale

Table E-2 presents the typical MnROAD vertical dynamic pressure gauge location and sensor layout information at the top of the subgrade for Cell 26A. The sensor offsets were also measured from the centerline between the two lanes, and the sensor depth measured from the surface of the pavement. The negative offset (-) represented the 80KIP lane and positive (+) offset represented the 102KIP lane.

Table E-2: MnROAD Vertical Dynamic Pressure (PK) Gauge Location - Cell 26A

CELL	MODEL	STATION	SEQUENCE	SENSOR ID	SENSOR OFFSET		SENSOR DEPTH	
		(Feet)	(SEQ)		(Feet)	(Meter)	(Inch)	(mm)
26	PK	17184	1	26PK001	-8.5	-2.6	7.7	195
26	PK	17184	2	26PK002	-9.5	-2.9	7.7	195
26	PK	17184	3	26PK003	-10.5	-3.2	8.2	207
26	PK	17184	4	26PK004	8.5	2.6	7.2	183
26	PK	17184	5	26PK005	9.5	2.9	6.8	174
26	PK	17184	6	26PK006	10.5	3.2	7.1	180
26	PK	17184	7	26PK007	-9.7	-2.9	12.1	308

Figure E-2 shows the MnROAD vertical dynamic pressure gauge location and sensor layout at the top of the subgrade for Cell 26A.

Figure E-2: MnROAD Vertical Dynamic Pressure Gauge (PK) Locations - Cell 26A

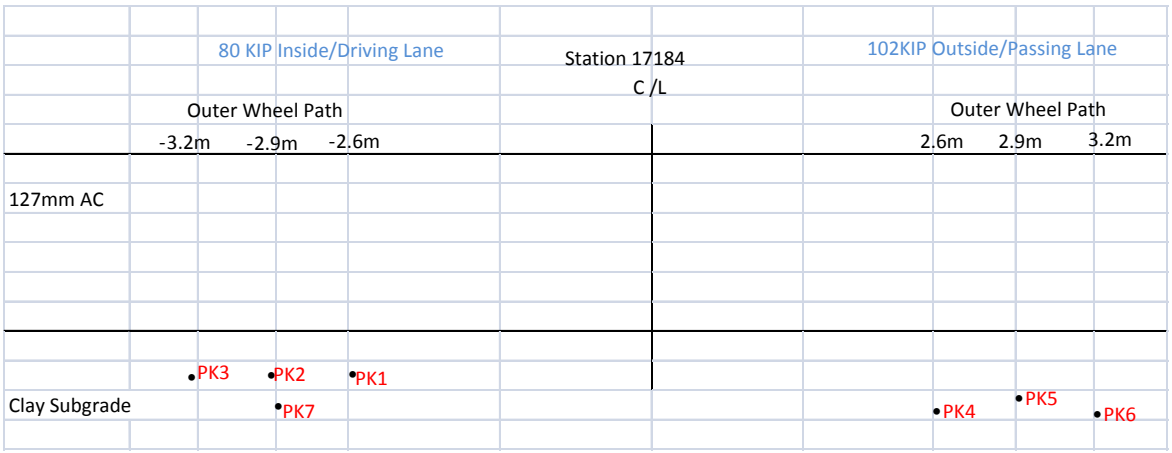

Not to scale

Table E-3 presents the MnROAD thermocouple (TC) locations and gauge layout information in the structure for Cell 26A. Only the locations under the center of the outer wheelpath were selected from the database.

Table E-3: MnROAD Thermocouple (TC) Gauge Location - Cell 26A

CELL	MODEL	STATION	SEQUENCE	SENSOR ID	SENSOR OFFSET		SENSOR DEPTH	
		(Feet)	(SEQ)		(Feet)	(Meter)	(Inch)	(mm)
26	TC	17197	11		-9.5	-2.9	1.1	28
26	TC	17197	12		-9.5	-2.9	3.4	86
26	TC	17197	13		-9.5	-2.9	6.2	157
26	TC	17197	14		-9.5	-2.9	11.8	300
26	TC	17197	15		-9.5	-2.9	17.8	452
26	TC	17197	16		-9.5	-2.9	23.8	605
26	TC	17197	17		-9.5	-2.9	35.8	909
26	TC	17197	18		-9.5	-2.9	47.8	1,214
26	TC	17197	19		-9.5	-2.9	59.8	1,519
26	TC	17197	20		-9.5	-2.9	95.8	2,433

Figure F-3 shows the MnROAD thermocouple (TC) locations and gauge layout under the center of the outer wheelpath of Cell 26A.

Figure E-3: MnROAD Thermocouple (TC) Gauge Locations - Cell 26A

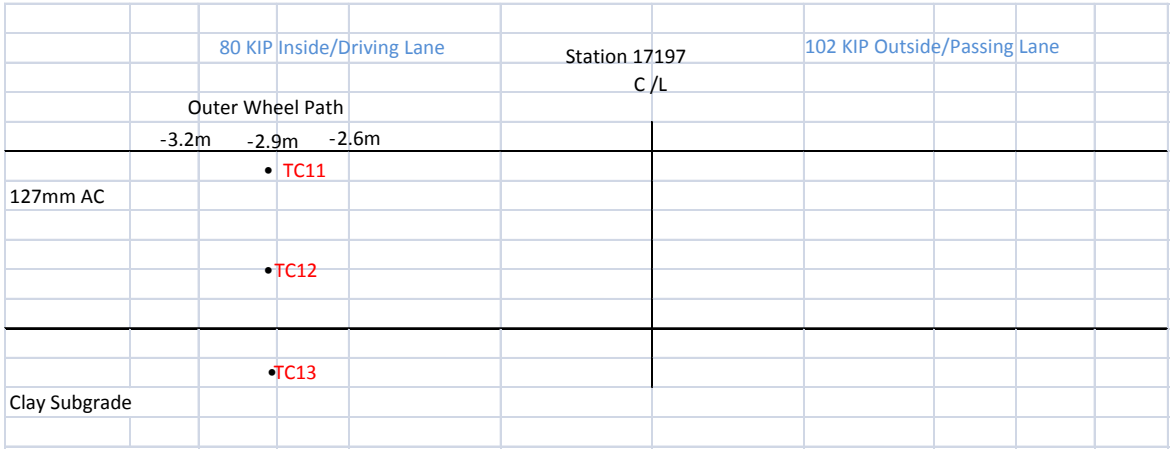

APPENDIX F

MnROAD Measured Peak Longitudinal and Transverse Strains, Vertical Subgrade Pressures, and Pavement Temperatures, from Early to Late Spring – Cell 26, Cell 27, and Cell 28

The longitudinal and transverse strain and vertical subgrade pressures for early to late spring were obtained from the MnROAD database for Cells 26-A, 27-A and 28-A. By 1999 only a few cells had strain gauges that provided meaningful data.

The data from 1996 was the latest available from the database for the selected cells. There were significanlty more pavement response data available for the 80KIP lane than the 102KIP lane in the database for these early cells at the low volume road. The strain data for all 5 axles of the semi trailer, taken from early to late spring of 1996, are presented.

For Cell 26-A, Figures F-1 and F-2 show the measured peak longitudinal and transverse strains for the 80KIP and 102KIP lanes from the early to late spring (March to May) of 1996. Figures F-3 and F-4 shows the measured peak vertical pressure at the top of the subgrade for the 80KIP and 102Kip lanes, respectively.

For Cell 27-A, Figures F-5 and F-6 show the measured peak longitudinal and transverse strains for the 80KIP and 102KIP lanes from the early to late spring (March to May) of 1996. Figures F-7 and F-8 shows the measured peak vertical pressure at the top of the subgrade for the 80KIP and 102Kip lanes, respectively.

For Cell 28-A, Figures F-9 and F-10 show the measured peak longitudinal and transverse strains for the 80KIP and 102KIP lanes from the early to late spring (March to May) of 1996. There were no measured peak vertical pressure available for Cell 28-A.

Figures F-11, F-12, and F-13 show the measured temperature profiles throughout the pavement structures on Cell 26-A, Cell 27-A and Cell 28-A respectively.

Figure F-1: Cell 26-A – Measured Peak Longitudinal and Transverse Strains (LE2, TE2) - All Axles of Semi Trailer - Early to Late Spring – Center of Outer Wheelpath - 80KIP Lane

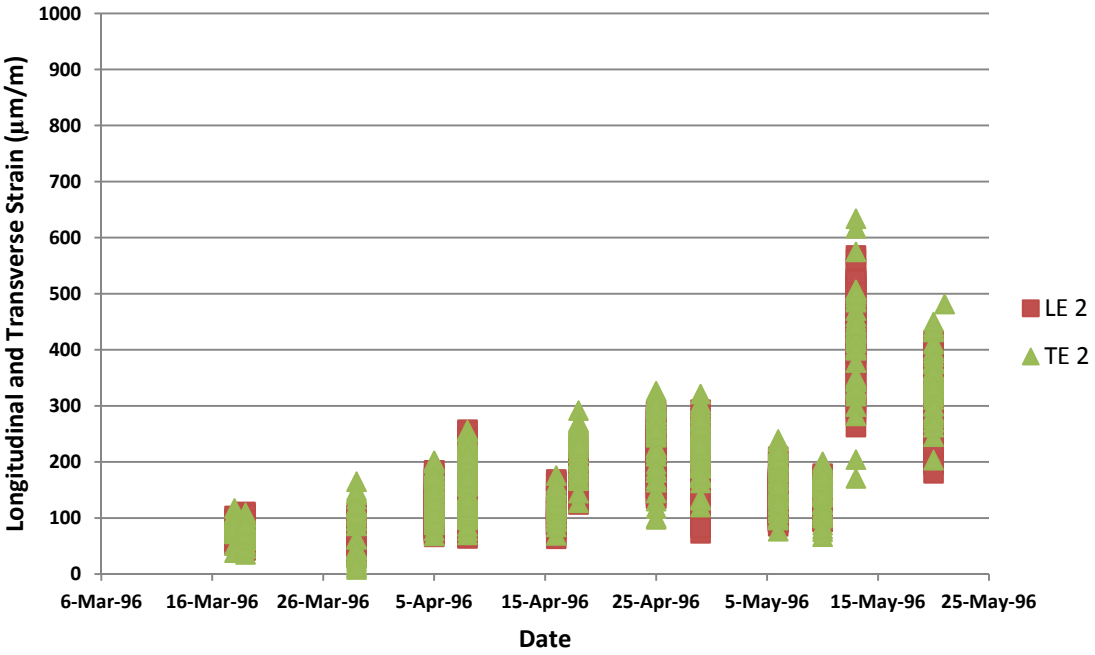

Figure F-2: Cell 26-A – Measured Peak Vertical Subgrade Pressure (PK2) - All Axles of Semi Trailer - Early to Late Spring –Center of Outer Wheelpath - 80KIP Lane

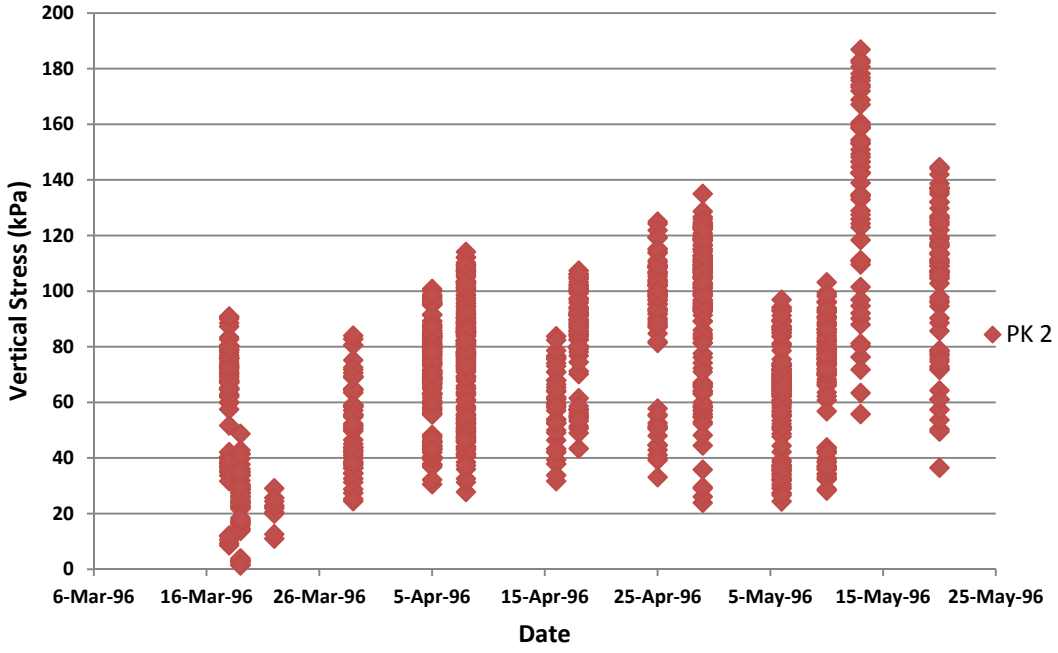

Figure F-3: Cell 26-A – Measured Peak Longitudinal and Transverse Strains (LE5, TE5) - All Axles of Semi Trailer - Early to Late Spring – Center of Outer Wheel Path - 102KIP Lane

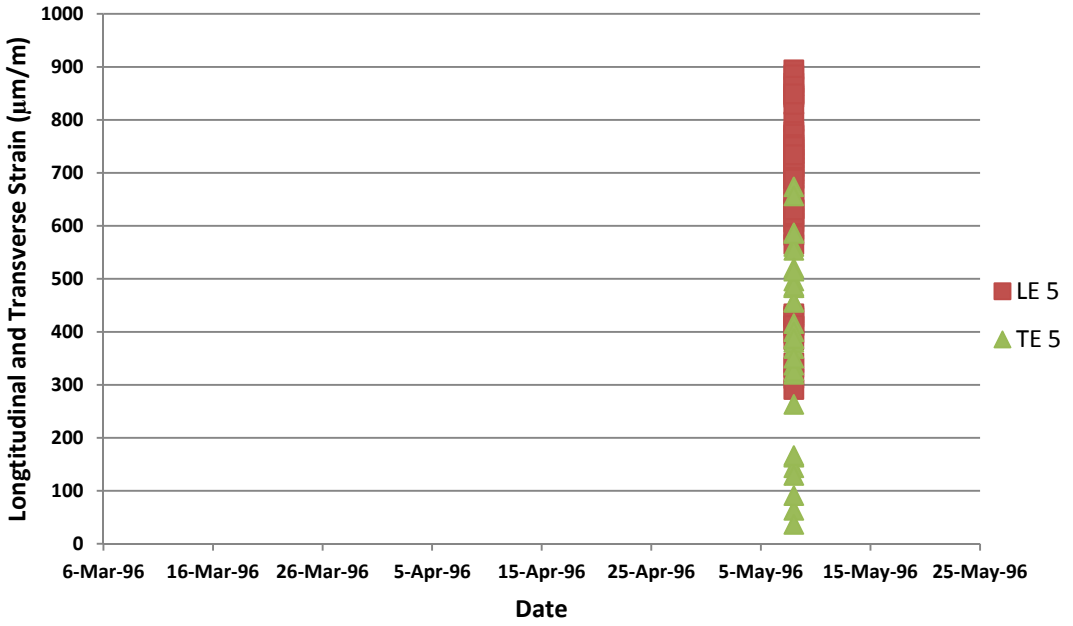

Figure F-4: Cell 26-A – Measured Peak Vertical Subgrade Pressure (PK5) - All Axles of Semi Trailer - Early to Late Spring – Center of Outer Wheelpath - 102KIP Lane

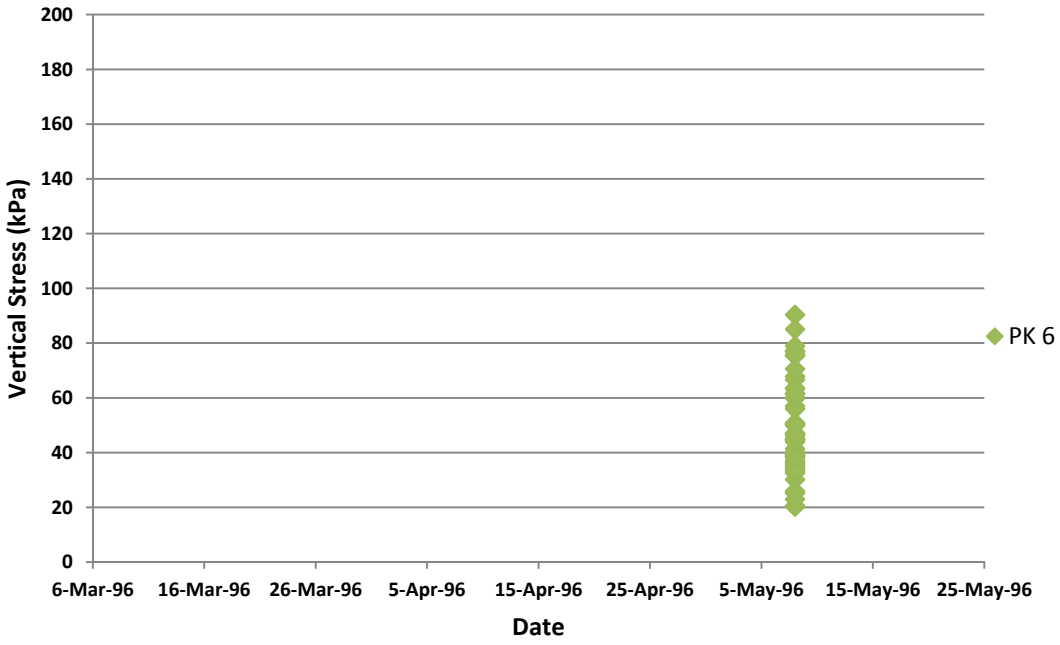

Figure F-5: Cell 27-A – Measured Peak Longitudinal and Transverse Strains (LE2, TE2) - All Axles of Semi Trailer - Early to Late Spring – Center of Outer Wheelpath - 80KIP Lane

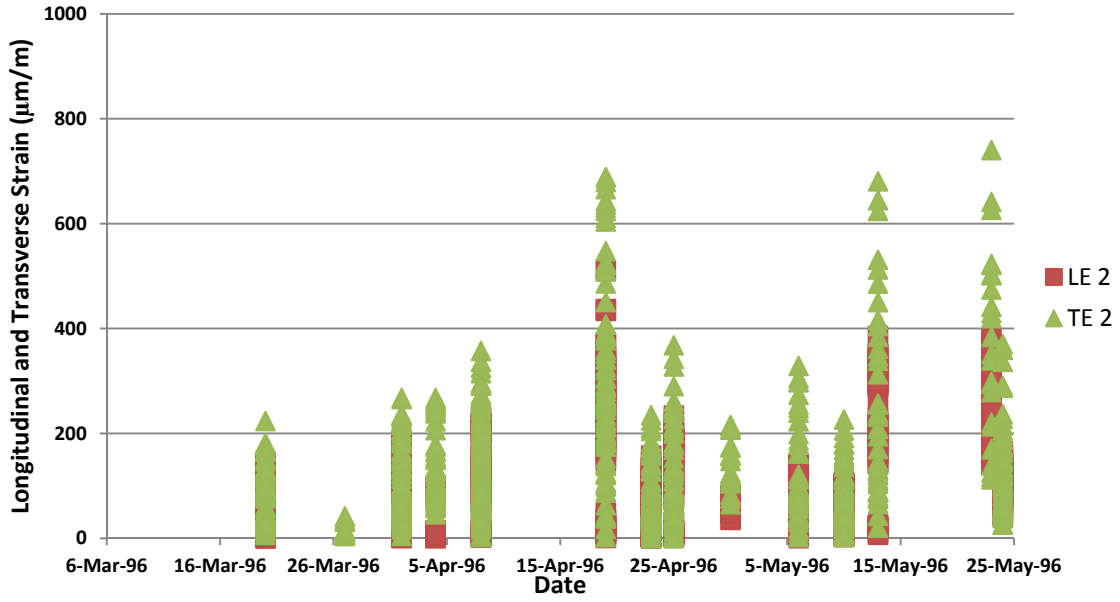

Figure F-6: Cell 27-A – Measured Peak Vertical Subgrade Pressure (PK2) - All Axles of Semi Trailer - Early to Late Spring – Center of Outer Wheelpath - 80KIP Lane

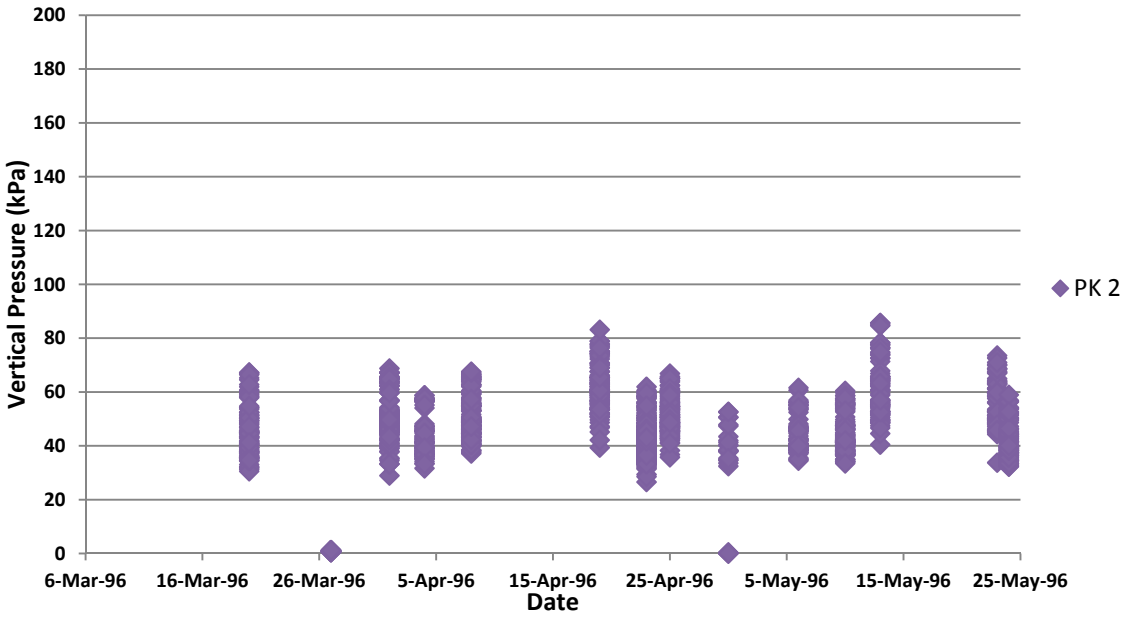

Figure F-7: Cell 27-A – Measured Peak Longitudinal and Transverse Strains (LE5, TE5) - All Axles of Semi Trailer - Early to Late Spring – Center of Outer Wheelpath - 102KIP Lane

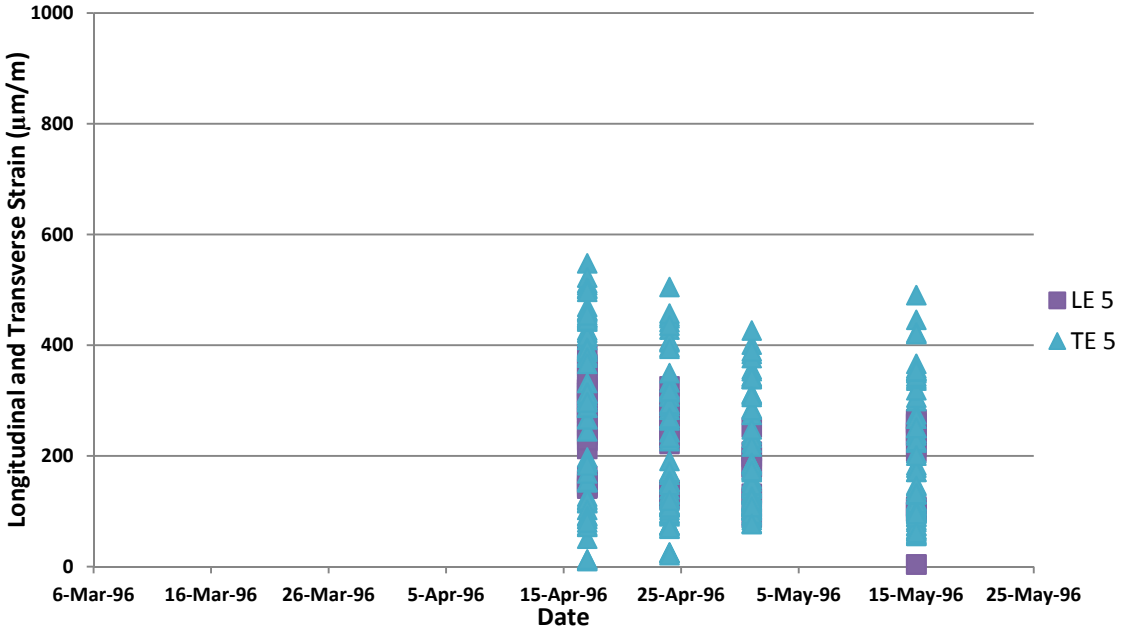

Figure F-8: Cell 27-A – Measured Peak Vertical Subgrade Pressure (PK5) - All Axles of Semi Trailer - Early to Late Spring – Center of Outer Wheelpath - 102KIP Lane

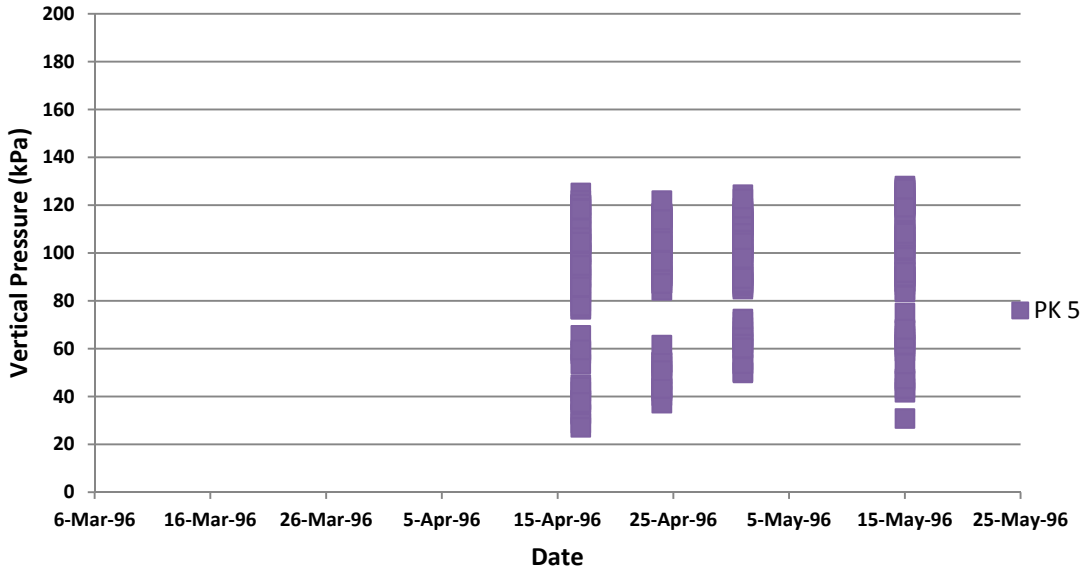

Figure F-9: Cell 28-A – Measured Peak Longitudinal and Transverse Strains (LE2, TE2) - All Axles of Semi Trailer - Early to Late Spring – Center of Outer Wheelpath - 80KIP Lane

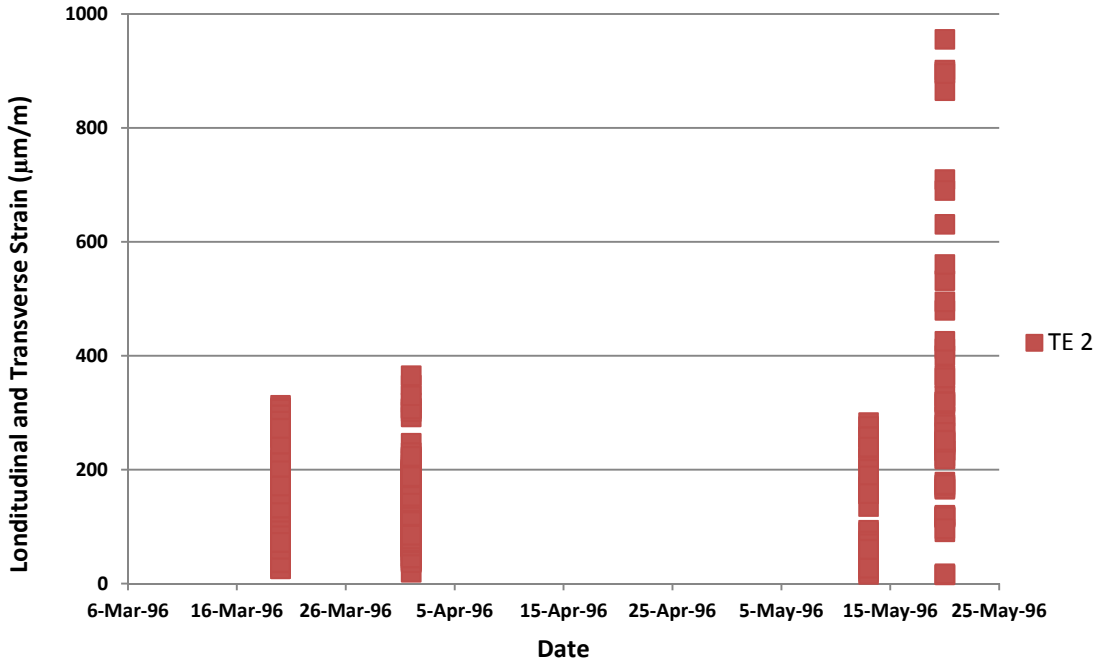

Figure F-10: Cell 28-A – Measured Peak Longitudinal and Transverse Strains (LE5, TE5) – All Axles of Semi Trailer – Early to Late Spring – Center of Outer Wheelpath - 102KIP Lane

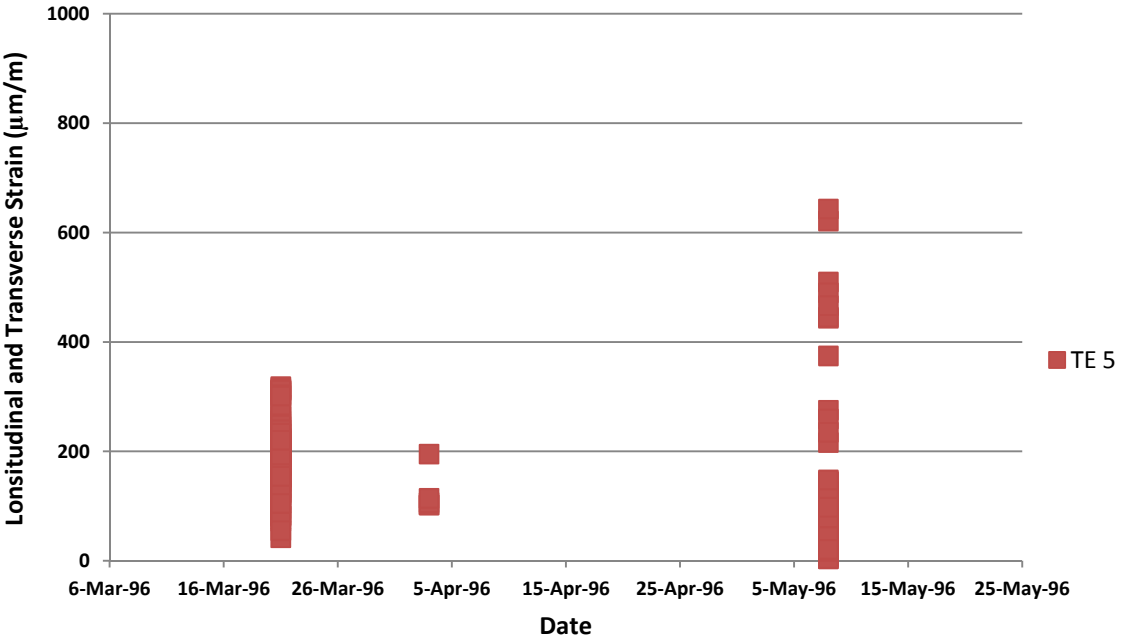

Figure F-11: Cell 26-A – Measured Pavement Temperature (TC) by Depth – Center of Outer Wheelpath (Station 171+96.81 – Hour 1400) - Early to Late Spring – 80 KIP Lane

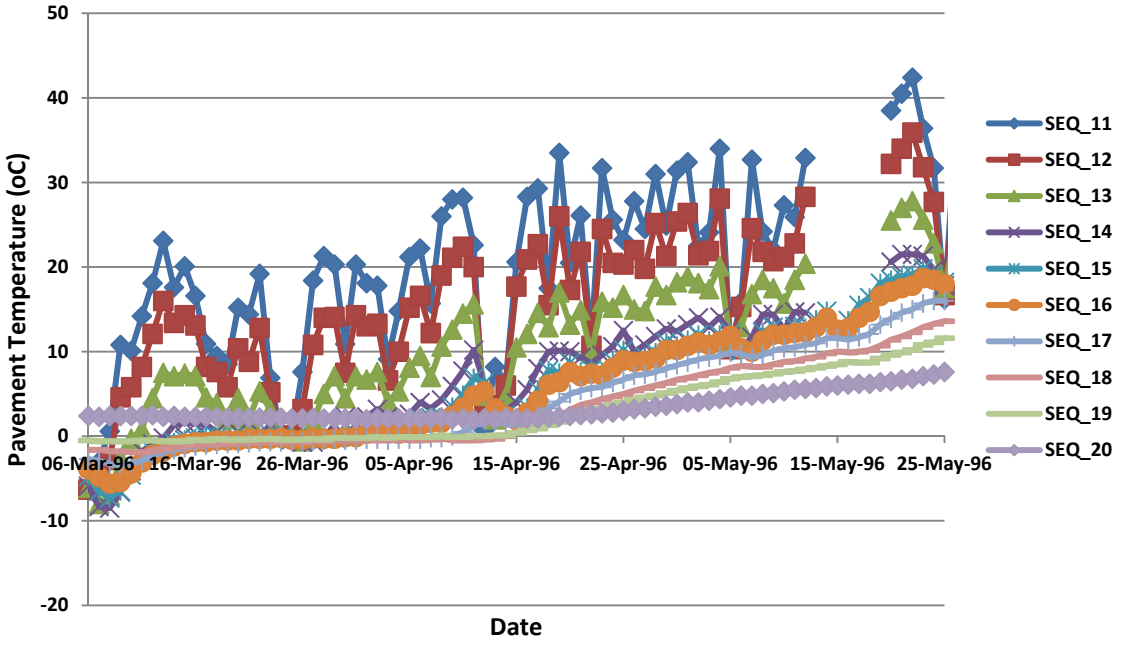

Figure F-12: Cell 27-A – Measured Pavement Temperature (TC) by Depth – Center of Outer Wheelpath (Station 171+05.67 – Hour 1400) - Early to Late Spring – 80KIP Lane

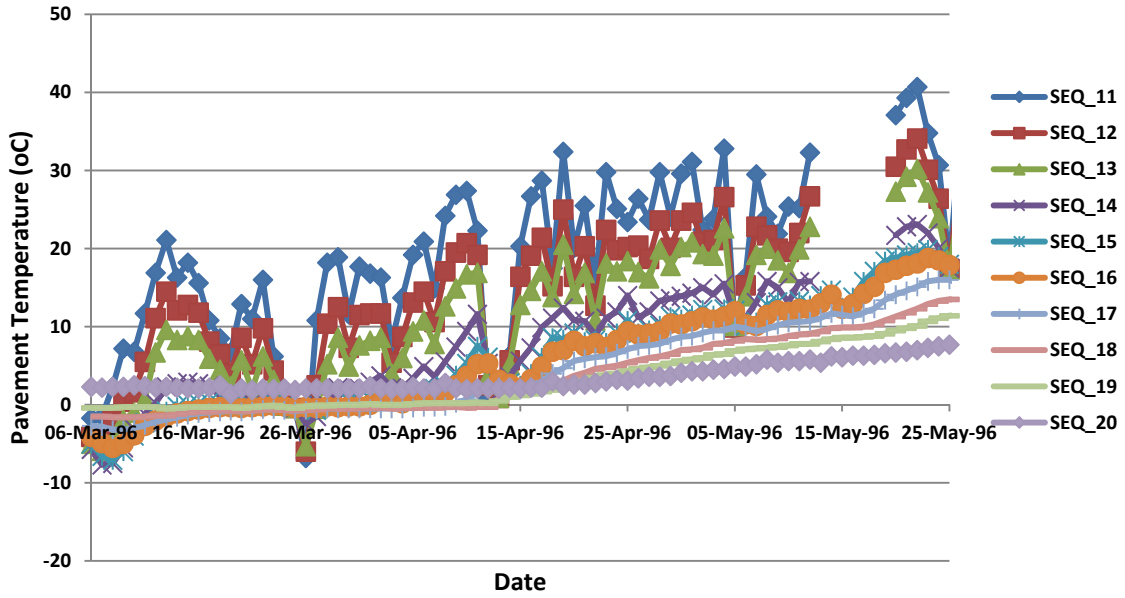

Figure F-13: Cell 28-A – Measured Pavement Temperature (TC) by Depth – Center of Outer Wheelpath (Station 182+65.66 – Hour 1400) - Early to Late Spring – 80KIP Lane

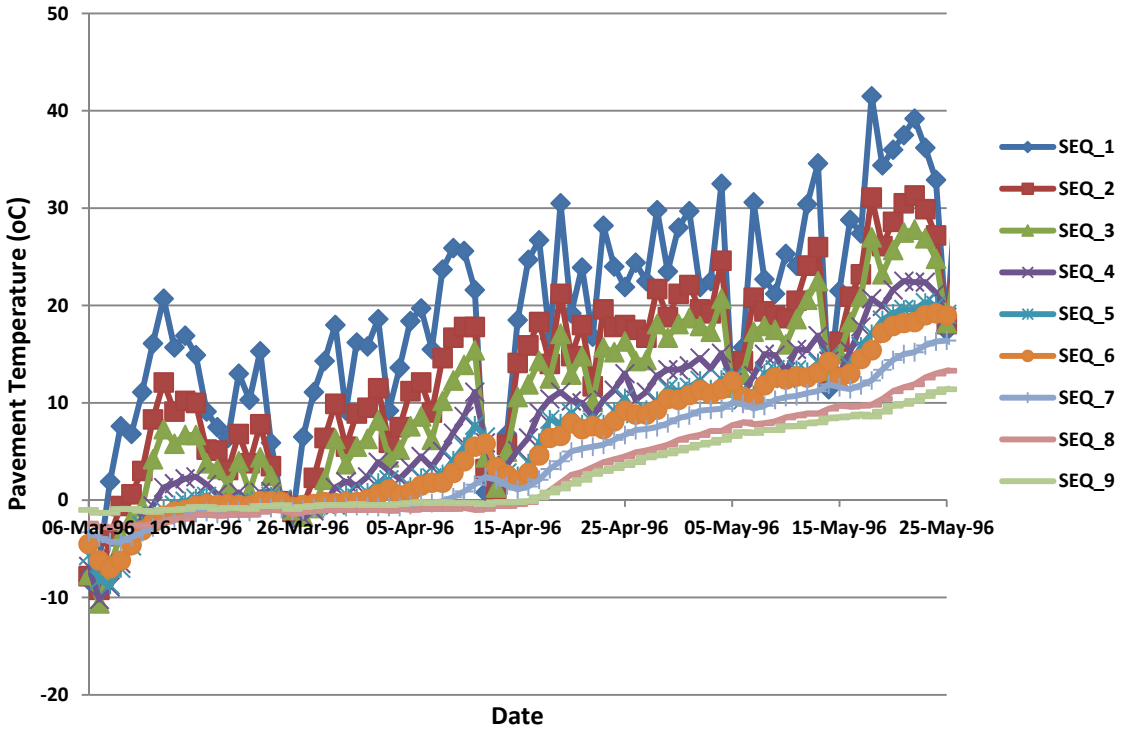

APPENDIX G

Minnesota Criteria for Defining Early and Late Spring Season, Freezing Index and Thawing Index at MnROAD and Manitoba Sites

MnROAD collects pavement response data from embedded sensors in each pavement cell on the low volume road during the early spring, late spring, summer, and fall of each year.

Minnesota defines early spring as when the thawing index (TI) reaches 15^{o}C-days, which is a when spring load restriction levels in Minnesota are in placed. TI is the cumulative number of average daily air temperature above 0^{o}C after the winter freeze. In the early spring, the base is thawing but the subgrade is frozen. The early spring ends typically after 28 days. Minnesota defines late spring as the end of early spring and the period when the base recovers and the subgrade thaws. Late spring ends when the average 3-day mean daily air temperature is greater than 17^{o}C [Ovik et al, 2000].

Table G-1 presents the Minnesota criteria for determining the duration of early and late spring. The spring layer modulus, relative to the fall standard modulus, is also presented.

Table G-1: Minnesota Criteria for Early and Late Spring

	Early Spring	Late Spring
	Base thaws, Subgrade frozen	Base recovers, Subgrade thaws
Start	TI>15^{o}C_Days	End of early Spring
End	Approximately 28 days	3-day T_{avg}>17^{o}C
Modulus		
AC	High	Standard
Base	Low	Low
Subgrade	High	Low

Note: TI=thawing index,
T_{avg}=average air temperature;
Modulus = relative to fall standard modulus [Ovik et al, 2000]

The equation for calculating the cumulative thawing index (CTI) is shown in Equation G-1. [Source: Minnesota Technical Memorandum No. 09-09-MAT-02 "Policy and Process for Seasonal Load Limit Starting and Ending Dates", June 2009]

To calculate the CTI, the freezing index is multiplied by a refreeze factor of 0.5. This is used to account for the partial phase change of water from a liquid to a semi-solid during temporary refreeze events.

$$CTI_n = \Sigma \text{ Daily Thawing Index} - (0.5 \times \text{Daily Freezing Index}) \qquad (G\text{-}1)$$

• When $\left(\frac{Tmax+Tmin}{2} - T_{reference}\right) < 0°C$; And $CTI_{n-1} \leq 0.5 \times \left(0^oC - \frac{Tmax+Tmin}{2}\right)$,
Daily Thawing Index = 0°C-day, and Daily Freezing Index = 0°C-day.
(Significant thawing has not yet occurred)

• When $\left(\frac{Tmax+Tmin}{2} - T_{reference}\right) > 0°C$;
Daily Thawing Index = $\left(\frac{Tmax+Tmin}{2} - T_{reference}\right)$, and Daily Freezing Index = 0°C-day.
(The pavement structure is thawing)

• When $\left(\frac{Tmax+Tmin}{2} - T_{reference}\right) < 0°C$; And $CTI_{n-1} > 0.5 \times \left(0^oC - \frac{Tmax+Tmin}{2}\right)$,
Daily Thawing Index = 0°C-day, and Daily Freezing Index = $\left(0^oC - \frac{Tmax+Tmin}{2}\right)$.
(The pavement structure is refreezing)

Where: CTI_n = cumulative thawing index calculated over 'n' days (°C-day),
CTI_{n-1} = cumulative thawing index for the previous day,
$T_{maximum}$ = Maximum daily air temperature (°C),
$T_{minimum}$ = Minimum daily air temperature (°C), and
$T_{reference}$ = Reference air temperature (see Table G-2) (°C).

Minnesota resets the CTI to zero on January 1.

Minnesota uses a reference temperature to account for the increasing intensity of the sun during the spring thaw period. As the sun's daily duration and intensity increases the air temperature at which thawing may occur in the pavement's structure reduces.

Table G-2 presents the Minnesota reference temperature used when calculating the cumulative thawing and freezing index. The adjustment for the increase in solar intensity uses a freezing temperature depression of 1.5°C during the first seven days of February and a depression of 0.5°C per week from then until the end of the season.

Table G-2: Minnesota Reference Temperature used when calculating the Cumulative Thawing and Freezing index

Date	Reference Temperature (°C)
January 1 – January 31	0
February 1 – February 7	-1.5
February 8 – February 14	-2.0
February 15 – February 21	-2.5
February 22 – February 28	-3.0
March 1 – March 7	-3.5
March 8 – March 14	-4.0
March 15 – March 21	-4.5
March 22 – March 28	-5.0
March 29 – April 4	-5.5
April 5 – April 11	-6.0
April 12 – April 18	-6.5
April 19 – April 25	-7.0
April 26 – May 2	-7.5
May 3 – May 9	-8.0
May 10 – May 16	-8.5
May 17 – May 23	-9.0
May 24 – May 30	-9.5
June 1-December 31	0

Table G-3 presents the Manitoba and MnROAD sites early and late spring dates based on Minnesota reference temperatures and criteria for calculating thawing and freezing index. The dates are based on average air temperatures obtained for each year from weather stations at or near the sites, the reference temperatures and freezing and thawing index equations, and the Minnesota start and end criteria for early and late spring.

Table G-3: Manitoba and MnROAD Sites Early and Late Spring Dates based on Minnesota Reference Temperatures and Criteria for Calculating Thawing and Freezing Index

	Minnesota Criteria	Early and Late Spring Dates		
		Cell 26-A, Cell 27-A, Cell 28-A (1996)[1]	Cell 33-B (2001)	PTH 11 and PR 304 (2009)[2]
Early Spring[3]	Start - *TI>15°C_Days*	March 12	March 16	March 21
	End- *Approximately 28 days*	April 8	April 10	April 17
Late Spring[4]	Start- *End of early Spring*	April 8	April 10	April 17
	End- *3-day T_{avg}>17°C*	May 16	April 28	May 26
Freezing Index (FI)	Degree_Days_°C	1,230	1,058	1,790

Note: [1]Air Temperature from MnROAD weather station
[2]Air Temperature from Great Falls weather station (5 km South of Pine Falls)
[3] Base Thaws, Subgrade Frozen
[4] Base Recovers, Subgrade Thaw
TI=thawing index,
T_{avg}=average air temperature

Figures G-1, G-2, and G-3 show plots of the freezing and thawing indices and late and early spring dates for the MnROAD and Manitoba test sites, respectively.

Figure G-1: Freezing and Thawing Indices and Late and Early Spring Dates for MnROAD Cell 26, Cell 27, Cell 28

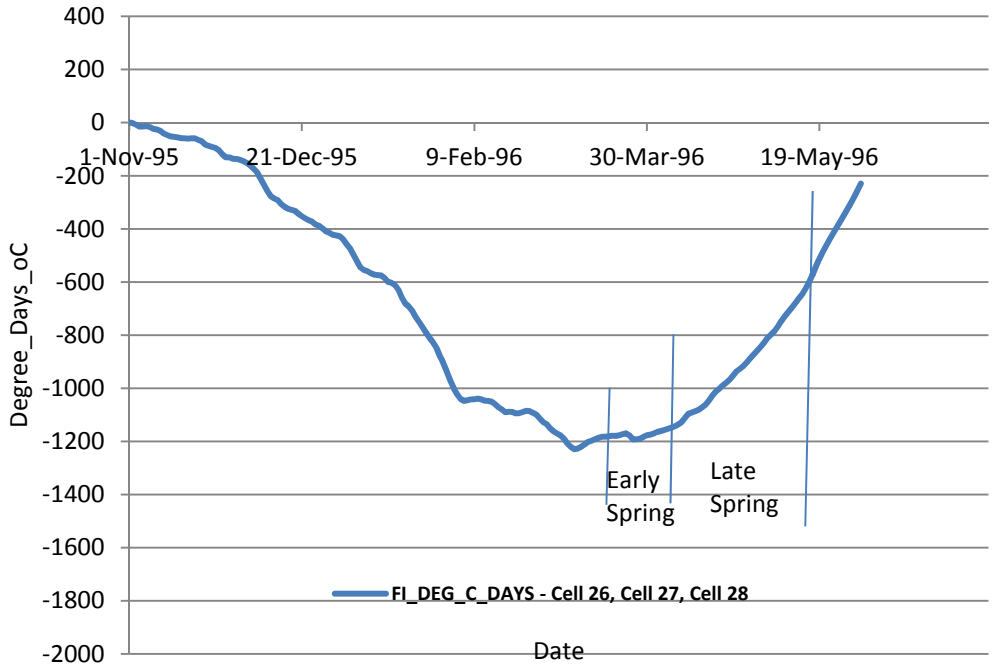

Figure G-2: Freezing and Thawing Indices and Late and Early Spring Manitoba PTH 11 and PR 304

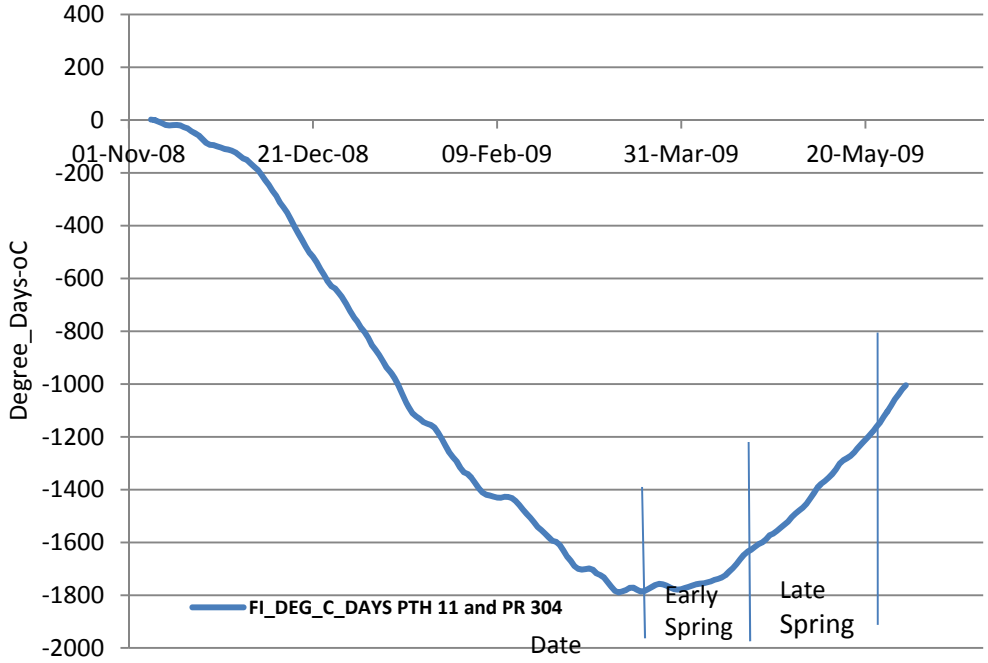

Figure G-3: Freezing and Thawing Indices and Late and Early Spring MnROAD Cell 33-B